



LUND UNIVERSITY

Quantum memory development and new slow light applications in rare-earth-ion-doped crystals

Li, Qian

2018

Document Version:

Publisher's PDF, also known as Version of record

[Link to publication](#)

Citation for published version (APA):

Li, Q. (2018). *Quantum memory development and new slow light applications in rare-earth-ion-doped crystals*. [Doctoral Thesis (compilation), Atomic Physics]. Atomic Physics, Department of Physics, Lund University.

Total number of authors:

1

Creative Commons License:

CC BY-NC

General rights

Unless other specific re-use rights are stated the following general rights apply:

Copyright and moral rights for the publications made accessible in the public portal are retained by the authors and/or other copyright owners and it is a condition of accessing publications that users recognise and abide by the legal requirements associated with these rights.

- Users may download and print one copy of any publication from the public portal for the purpose of private study or research.
- You may not further distribute the material or use it for any profit-making activity or commercial gain
- You may freely distribute the URL identifying the publication in the public portal

Read more about Creative commons licenses: <https://creativecommons.org/licenses/>

Take down policy

If you believe that this document breaches copyright please contact us providing details, and we will remove access to the work immediately and investigate your claim.

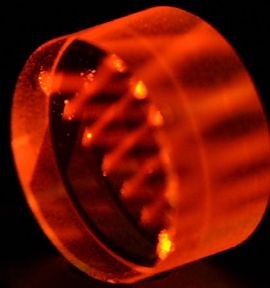
LUND UNIVERSITY

PO Box 117
221 00 Lund
+46 46-222 00 00

Quantum memory development and new slow light applications in rare-earth-ion-doped crystals

QIAN LI

DEPARTMENT OF PHYSICS | FACULTY OF ENGINEERING | LUND UNIVERSITY



QUANTUM MEMORY DEVELOPMENT AND NEW SLOW LIGHT APPLICATIONS IN RARE-EARTH-ION-DOPED CRYSTALS

Qian Li

Doctoral Thesis
2018



QUANTUM MEMORY DEVELOPMENT AND NEW SLOW LIGHT APPLICATIONS IN
RARE-EARTH-ION-DOPED CRYSTALS

pp.iii-99 © Qian Li 2018

Paper **I** ©2013 American Physical Society

Paper **II** ©2013 American Physical Society

Paper **III** ©2015 American Physical Society

Paper **IV** ©2016 American Physical Society

Paper **V** ©2016 Optical Society of America

Paper **VI** ©2016 Springer Nature

Faculty of engineering

Department of Physics

Lund University

Lund Reports on Atomic Physics, LRAP 544 (2018)

ISBN 978-91-7753-616-1 (print)

ISBN 978-91-7753-617-8 (pdf)

ISSN: 0281-2762

Printed in Sweden by Media-Tryck, Lund University
Lund, 2018

ABSTRACT

When doped into solid state transparent crystals, rare-earth ions can have optically excited states with milliseconds coherence time and up to six hours coherence time for hyperfine levels after being cooled down to liquid helium temperature. This long coherence property makes them unique as solid state material and attractive for quantum information applications.

The rare-earth ions have narrow homogeneous linewidths on the order of \sim kHz. When doped into a crystal, the lattice structure is slightly distorted due to the size mismatch between the dopant and the host ions, resulting in slight differences in the local crystal fields at the dopant sites. Therefore, the resonance frequencies of the rare-earth ions are shifted relatively, resulting in an inhomogeneously broadened absorption profile, typically on the order of a few GHz. This provides the possibility of addressing each group of ions individually and engineering the absorption profile for different purposes by optical pumping using a narrow linewidth laser, and makes rare-earth-ion-doped crystals suitable for ensemble based quantum memories.

Quantum memories are vital components for developing long-distance quantum communication. Part of this thesis project focused on making quantum memories with high efficiency and long storage time, especially using materials with low optical depth. To achieve this goal, a low finesse, unsymmetrical cavity was employed and experiments were carried out at (or close to) the impedance matched condition. Atomic frequency comb (AFC) protocol proposed for such an inhomogeneously broadened system was used to store coherent light for a certain time. 56% overall efficiency was achieved, and the main limiting factor for reaching even higher efficiency was the inefficient coupling between incoming light and the cavity mode. Other possible loss mechanisms were analyzed as well.

Long-time, on-demand, quantum memory experiments were conducted with the help of two efficient radio-frequency rephasing pulses. Storage time was extended from microseconds to milliseconds after compensating (most of) the residual earth magnetic field in the lab. The opportunities and challenges of combining the

cavity assistant quantum memory and the long time, on demand quantum memory were analyzed and possible solutions were proposed.

Another part of the thesis project involves slow light-based applications in rare-earth-ion-doped crystals. The strong slow light effect at the presence a spectral hole is due to the fact that the light interacts with the absorbing ions outside the spectral hole off-resonantly, and most of the light energy is stored inside the ions as a polarization. For example, with a group velocity of 300 km/s, 99.9% of the pulse energy is stored in the ions when the pulse propagates inside the crystal. The slower the light propagates, the more energy is stored inside the medium. Based on this, a frequency shifter that is capable of shifting the light frequency of ± 4 MHz was demonstrated, and frequency shift up to GHz was proposed. Group velocity control by a factor of 20 and pulse compression in time by a factor of 2 were also demonstrated. The frequency shift and group velocity of the light are solely controlled by the external electric field, which makes them ideal for weak light situation. The unique property of such a frequency shifter and group velocity controller is that they could be made to accept light from an arbitrary incoming angle and polarization, for example, scattered light.

POPULAR SCIENCE

As humans, we learn through statistics, whether consciously or unconsciously. We observe, search our databases for similar behavior, and characterize whether the phenomena match or relate to what we already knew. This is why when it comes to quantum mechanics, people find it difficult to accept. Because it contradicts our common sense.

In quantum mechanics, for example, an atom could be in a superposition state, which means it could be in state $|0\rangle$ and state $|1\rangle$ simultaneously. What makes it even more puzzling is the fact that when we want to make a measurement to see which state the atom is in, instead of obtaining the actual state, i.e. the superposition state, it returns only one of the states, with a certain probability, because the superposition state collapses randomly to that state. This is completely different from our daily experience, where, for example, a TV is either ‘on’ (in state 1), or ‘off’ (in state 0); it cannot be both ‘on’ and ‘off’ at the same time. Moreover, the state it is in does not depend on whether we are watching or not. Such behavior of the atom, though feels weird at the beginning, has been demonstrated and verified by countless experiments over the past century.

The quantum computer is one application that takes advantage of the superposition, as well as the entanglement property (which is a consequence of superposition) of quantum mechanics. So does quantum communication which creates a secure information transfer channel, where, if a third party tries to eavesdrop (measure the quantum state being transferred), the quantum state of the information collapses and the sender and receiver will be able to detect it. In both quantum computation and long distance quantum communication, there is a need for quantum memories, which could be used to take in the quantum information, hold it for a certain time and release it at a later time, with high fidelity and efficiency.

Quantum memories are essential components of mature quantum computation, for example, to store intermediate computational results for a certain time, just like the classical memory to a classical computer. They are also a vital part of the quantum repeaters that are used in long-distance quantum information dis-

tribution, just like the classical repeaters in classical communication. However, unlike classical memories, which use the ‘measure and then repeat’ method to duplicate data, and classical repeaters, which use ‘measure and amplify’ method to boost the signal, quantum memories cannot measure the input data, because it collapses the quantum information, and its efficiency has to be high because any trace of the information that is not stored or is left inside the memory represents a loss of information.

Obtaining high efficiency for the quantum memories requires that the physical system used for the memory could couple strongly to the light (on which the quantum information is encoded). However, to maintain the fragile superposition property, the memory has to interact only weakly with the rest of the universe. These two requirements seem to be contradictory because things that interact strongly with light tend to be affected easily by the environment. This could be solved by using atoms (ions) that interact weakly with the surrounding, but use a lot of them, so-called an ensemble of atoms (ions). In this thesis, quantum memories use such ensembles of rare-earth ions (RE ions) doped into transparent crystals were demonstrated. The long coherence time (up to milliseconds, which is very long on a quantum scale) of such RE ions makes them suitable for quantum computation and quantum memories.

Besides quantum memories, slow light effects were also studied in such crystals. Light, as an electromagnetic wave, propagates at a speed of $c = 299792458$ m/s in vacuum. However, light travels slower in a medium. One way of understanding this slowing down effect is from the light matter interaction point of view. Inside a material, there are numerous atoms (or ions) made of a nuclear core and the surrounding electron cloud. When light propagates inside a medium, its electric field displaces the electron cloud of the atoms, causing it to oscillate. Therefore, part of the light energy is stored inside the atom. Oscillating electrons emit light, and the light that the electron sends out in some cases lags in phase compared with the incoming light field. Interference between the remaining light field and the newly emitted light field makes the crest of the light move slightly slower. The closer the light frequency to the resonance frequencies of the atoms, the stronger the interaction and the larger the fraction of pulse energy stored inside the medium. When the light propagates at less than 300 km/s, more than 99.9% of light field energy is stored inside the medium. We use such phenomena to control the group velocity of the light, shift the frequency of light, and narrow the cavity linewidth when there is a slow light material enclosed in the cavity.

LIST OF PUBLICATIONS

This thesis is based on the following papers, which will be referred to in the text by their roman numerals.

- I Efficient quantum memory using a weakly absorbing sample**
M. Sabooni, Q. Li, S. Kröll and L. Rippe.
Phys. Rev. Lett. **110**, 133604 (2013).

- II Spectral engineering of slow light, cavity line narrowing, and pulse compression**
M. Sabooni, Q. Li, R. K. Mohan, L. Rippe and S. Kröll.
Phys. Rev. Lett. **111**, 183602 (2013).

- III Slow-light-based optical frequency shifter**
Q. Li, Y. Bao, A. Thuresson, A. Nilsson, L. Rippe and S. Kröll.
Phys. Rev. A **93**, 043832 (2016)
Synopsis of paper selected for online display of APS Physics.

- IV Using electric fields for pulse compression and group-velocity control**
Q. Li, A. Kinos, A. Thuresson, L. Rippe and S. Kröll.
Phys. Rev. A **95**, 032104 (2017)
Synopsis of paper selected for online display of APS Physics.

- V Development and characterization of high suppression and high tendue narrowband spectral filters**
A. Kinos, Q. Li, L. Rippe and S. Kröll.
Applied optics **55**, 10442 (2016).

VI Fast all-optical nuclear spin echo technique based on EIT

A. Walther, A. N. Nilsson, Q. Li, L. Rippe and S. Kröll.
Eur. Phys. J. D **70**, 166 (2016).

ABBREVIATIONS

AFC	Atomic Frequency Comb
CRIB	Controlled Reversible Inhomogeneous Broadening
DDS	Direct Digital Synthesizer
EIT	Electromagnetic Induced Transparency
EOM	Electro-Optical Modulator
FID	Free Induction Decay
FWHM	Full Width at Half Maximum
GEM	Gradient Echo Memory
NMR	Nuclear Magnetic Resonance
PBS	Polarization Beam Splitter
PD	Photo Diode
PDH	Pound-Drever-Hall frequency locking
PSHB	Persistent Spectral Hole Burning
RASE	Rephased Amplified Spontaneous Emission
RE ions	Rare-Earth ions
RF	Radio Frequency
ROSE	Revival Of Silenced Echo
UOT	Ultrasound Optical Tomography
ZEFOZ	Zero First Order Zeeman
ZCT	Zero crossing temperature
Pr	Praseodymium
Eu	Europium
Er	Erbium
Y ₂ SiO ₅	Yttrium Orthosilicate

CONTENTS

Abstract	iii
Popular Science	v
1 Introduction	1
1.1 A brief overview of the project	2
1.2 Outline of the thesis	3
2 Light matter interaction	5
2.1 Two level system and Bloch sphere	5
2.2 The Bloch equations	6
2.2.1 The Bloch equations in another form	7
2.2.2 Pulse area	7
2.3 Coherent transients	8
2.3.1 Free induction decay	8
2.3.2 Photon echo	9
3 Rare-earth-ion-doped crystals	11
3.1 Energy level of rare-earth ions	11
3.1.1 Coherence time and homogeneous linewidth	14
3.1.2 Inhomogeneous linewidth	15
3.2 Hyperfine level	15
3.3 Spectral hole burning	16
3.4 Transition strength	17
3.5 Static dipole moment and Stark effect	17
3.6 $\text{Pr}^{3+}:\text{Y}_2\text{SiO}_5$ and $\text{Eu}^{3+}:\text{Y}_2\text{SiO}_5$	18
4 Slow light effect related phenomena	21
4.1 Phase velocity and group velocity	21
4.2 Slow light inside a spectral hole	23
4.2.1 Energy perspective	23
4.3 Cavity linewidth narrowing	24
4.4 Group velocity control and pulse compression	29
4.4.1 Crystal and E field	29
4.4.2 Experimental setup	29
4.4.3 Group velocity control	30
4.4.4 Pulse compression	31
4.5 Frequency shifter	32
4.5.1 Specially prepared structure	32
4.5.2 Frequency shift of the ions and the structure	33
4.5.3 Frequency shift of light	33
4.5.4 Energy distribution in the ions	34
4.5.5 Transient frequency shift	34
4.5.6 Efficiency	35
4.5.7 Higher frequency shift	35

4.6	Summary and outlook	36
5	Quantum memories	39
5.1	Ensemble based quantum memories	41
5.1.1	AFC	41
5.1.2	CRIB and GEM	43
5.2	Cavity enhanced quantum memory	45
5.2.1	Impedance matched cavity	45
5.3	Quantum memory using asymmetric low finesse cavity	47
5.3.1	Experimental setup	49
5.3.2	2 mm cavity crystal quantum memory	49
5.3.3	Impedance match	50
5.3.4	Quantum memory	50
5.4	Long time on demand quantum memories	52
5.5	Quantum memories in a 0.8 mm cavity	57
5.6	Conclusion and outlook	60
A	Experimental system	63
A.1	The light source	63
A.1.1	External stabilization system	64
A.1.2	Pulse-shaping system	67
A.2	The cryostat	67
B	Zero crossing temperature measurement	69
B.1	Laser stabilized to a Fabry-Pérot cavity	70
B.1.1	The 606 cavity	71
B.1.2	The 370 cavity	72
B.1.3	ULE glass	72
B.2	Zero crossing temperature measurement	73
B.2.1	Setup	74
B.2.2	The 606 cavity	78
B.3	Residual frequency drift	80
B.4	Conclusion and outlook	81
	Comments on the Papers	83
	Acknowledgements	87
	References	88

Papers

I	Efficient quantum memory using a weakly absorbing sample	103
II	Spectral engineering of slow light, cavity line narrowing, and pulse compression	111
III	Slow-light-based optical frequency shifter	119
IV	Using electric fields for pulse compression and group-velocity control	129
V	Development and characterization of high suppression and high tendue narrowband spectral filters	139
VI	Fast all-optical nuclear spin echo technique based on EIT	149

INTRODUCTION

Quantum mechanics is a well-established theory that describes the physical laws at the atomic scale, and superposition as a fundamental property of a quantum system has been demonstrated and verified. If we are brave enough to accept this premise, we will find a lot of quantum mechanical phenomena do not seem to be that weird anymore.

For example, in a classical computer that we rely so heavily on, every bit has two possible states, 0 and 1 and it could only be in one of these two states at a time. However, in a quantum computer, the information carrier, a qubit, can be in both state $|0\rangle$, state $|1\rangle$ and the superposition state of $|0\rangle$ and $|1\rangle$. If we have two bits, say, control bit in state 1, and target bit in state 0, after a so called Control-NOT operation (the XOR gate), the target bit changes from state 0 to state 1. However, in a quantum computer, when the control qubit is in a superposition state of $|0\rangle + |1\rangle$ and the target qubit is in state $|0\rangle$, the Control-NOT operation yields the following result:

$$(|0\rangle + |1\rangle) |0\rangle \xrightarrow{\text{Control NOT}} (|00\rangle + |11\rangle). \quad (1.1)$$

We see that the target qubit is also in a superposition state of being in $|0\rangle$ and $|1\rangle$ at the same time. Moreover, we cannot write this output state as two separate qubit states; their states are somehow linked, which is called an entanglement state. Even if we send them far apart, one stays on Earth and the other one goes to the Moon, for example, and if we measure the state of one of the qubits and get the result of $|0\rangle$, we will immediately know that if we measure the state of the other qubit, the output will be $|0\rangle$ with certainty.

However, to maintain the superposition state, the qubit has to keep its phase information throughout the entire computation time. This might be difficult if the computation is very complicated

and needs input from different stages where significant delay might occur. One way to solve this problem is to use quantum memories, which could store the intermediate computation result and release it whenever the next part of the computation process needs it.

The other major application of quantum memory is the long-distance quantum communication. To distribute the quantum information world-widely, we need a continental quantum network. Photons, which are ideal quantum information carriers, suffer from losses when sent through an optical fiber. To build such long distance quantum networks, quantum repeaters are needed. However, unlike the classical repeater, which could measure the state of the input signal, amplify it, and send it out again, the quantum repeater has to work differently since it is impossible to measure an arbitrary quantum state precisely or replicate it perfectly due to the quantum non-clone theorem [1]. Most approaches to quantum repeaters require the use of quantum memories that could store the quantum information of a photon until the entanglements between all quantum repeaters are well established.

Most quantum mechanical effects happen on a microscopic scale; however, we do see it on the macroscopic scale as well. One of the best known examples is the laser, which is widely used nowadays, from state-of-the-art quantum physics research to computer chips fabrication, from the cutting and welding of metals to delicate eye surgery, from the detection of gravitational waves to supermarket bar code readers, to name but a few.

The feature that makes lasers so unique and powerful is the coherence property of the emitted photons. All photons emitted from the laser have the same frequency, waveform and phase. If atoms are in phase with each other, they emit coherent light. This coherence information is the key property used in this thesis.

1.1 A brief overview of the project

One thing about working in research is that you are not always sure where you will land from the very beginning, because you are heading toward an area where nobody has been before and it is difficult to predict what you will see. This could be painful for some people, but it is also what makes research attractive: there are always possibilities for new discoveries, there will be a lot of surprises along the way, and maybe one of them will be fascinating enough to change your research direction.

The initial goal of this thesis work was to improve the efficiency and extend the storage time of quantum memories in rare-earth-ion-doped crystals. The first two years was focused on enhancing quantum memory efficiency using an unsymmetrical cavity and extending the storage time of the quantum memories. We were able to boost the memory efficiency of a crystal from about 1% to

56% and increase storage time from microseconds to milliseconds. We believe there is still room for improvement.

In our experiment of the cavity assisted quantum memory, we found an extremely interesting phenomenon: the linewidth of the cavity mode narrowed from \sim GHz to \sim MHz, which was nothing that we had seen before. We soon discovered that it was caused by the slow light effect due to the engineering of the absorption profile of the crystal. Later, my research shifted to investigating the applications of such slow light effect in our crystals. Besides cavity linewidth narrowing, optical frequency shifting and group velocity control based on the slow light effect were demonstrated as well.

1.2 Outline of the thesis

The thesis is structured as follows: Chapters 2 and 3 give the background necessary and relevant to the project, and lay the foundation for understanding the experiments and discussion presented in Chapters 4 and 5. There are two appendices, A and B, Appendix A describes the setup used for our experiments, and Appendix B presents a small experimental project that was useful for the experiments we conducted in our group.

Chapter 2 describes the coherent interaction between a laser field and a two-level atomic system, it introduces the optical Bloch equation, the Bloch sphere and Bloch vector, which help visualize the interaction process.

Chapter 3 presents the spectroscopic properties of the rare-earth ions doped crystals with a focus on the properties of a particular material, $\text{Pr}^{3+}:\text{Y}_2\text{SiO}_5$.

Chapter 4 presents three slow light related experiments in rare-earth-ion-doped crystals: cavity linewidth narrowing, optical frequency shift, and group velocity control.

Chapter 5 focused on all the quantum memory-related work, where two-level quantum memories with the assistant of the unsymmetrical cavity and three-level quantum memory with long time, on-demand readout are experimentally demonstrated.

Appendix A describes the experimental setup we have in the lab: an external laser stabilization system, a pulse shaping system, and a helium bath cryostat.

Appendix B presents an experiment aiming at finding the zero crossing temperature of the two external cavity in our lab.

LIGHT MATTER INTERACTION

In this chapter, I will describe the interaction of a two-level atom with coherent radiation. A semiclassical treatment was used, i.e., the light radiation field is treated as a classical electric field while the atom is treated quantum mechanically. In Section 2.1, the Bloch representation of an atomic state is introduced and followed by Bloch equations that describe the coherent process when a two-level system is driven by coherent light in Section 2.2. At the end, two coherent transient phenomena are discussed. We will see that the Bloch picture is an intuitive and powerful tool to help us understand the light matter interaction process and how the state evolves under a certain external field.

2.1 Two level system and Bloch sphere

An arbitrary state of a two-level atomic system could be written as the superposition of the two states, ground state $|1\rangle$ and excited state $|2\rangle$, as follows (the global phase factor of the state is ignored since it has no observable effect [2]):

$$|\psi\rangle = c_1 |1\rangle + c_2 |2\rangle e^{-i\omega_0 t}, \quad (2.1)$$

where ω_0 is the angular frequency at which the electron cloud oscillates and it corresponding to the energy difference between the two states, $\omega_0 = (E_2 - E_1)/\hbar$; c_1 and c_2 are the probability amplitudes for finding the atom at the corresponding level and $|c_1|^2$ and $|c_2|^2$ represent the probability of finding the system in state $|1\rangle$ and $|2\rangle$ respectively. Therefore, if we sum up all the probabilities, it has to be 1,

$$|c_1|^2 + |c_2|^2 = 1, \quad (2.2)$$

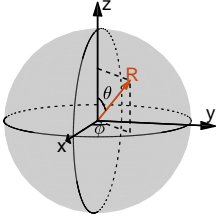


Figure 2.1. The Bloch sphere and a vector inside it describing a state that could be characterized by two parameters, θ , and ϕ .

because the electron has to be somewhere. We could rewrite Equation (2.1) as

$$|\psi\rangle = \cos\left(\frac{\theta}{2}\right) |1\rangle + \sin\frac{\theta}{2} |2\rangle e^{-i\phi}, \quad (2.3)$$

where θ and ϕ are real numbers. The advantage of this way of expressing the state is that the state could be visualized in a spherical coordinate system as a vector on the unit sphere defined by the two parameters, as shown in Figure 2.1. This is called Bloch sphere representation, and an arbitrary state could now be represented by a vector originating from the center and pointing to the Bloch sphere as

$$\mathbf{R} = (u, v, w). \quad (2.4)$$

This is known as Bloch vector. The states $|1\rangle$ and $|2\rangle$ are now represented by vectors pointing to the south and north poles of the Bloch sphere, respectively. A 50/50 superposition state of $|1\rangle$ and $|2\rangle$ corresponds to a vector at the equator plane, and the exact position on the equator depends on the phase factor, ϕ , between these two states.

So far, the states that we have discussed are pure states, which means that they are fully known, and the vector length is $|\mathbf{R}| = u^2 + v^2 + w^2 = 1$. A state that is not fully known is called a mixed state, it could be represented by a vector pointing inside the Bloch sphere, i.e., the length of the vector is less than 1, and $u = v = w = 0$ describes a completely mixed state.

2.2 The Bloch equations

The Bloch equations could be used to describe the time evolution of an arbitrary atomic state under interaction with an external field. It was first developed by Felix Bloch [3] to describe the nuclear spin state driven by radiofrequency electromagnetic fields and later suggested by Feynman et al. that it could be adapted for use in any two-level problems [4].

The derivation of the optical Bloch equations for an atomic system from Schrödinger equation could be found in Ref. [5]. There are different forms of Bloch equation that are useful for different purposes. One way of writing Bloch equation is shown below:

$$\begin{cases} \dot{u} = -\frac{1}{T_2}u - \Delta v + \Omega_{im}w, \\ \dot{v} = \Delta u - \frac{1}{T_2}v + \Omega_{re}w, \\ \dot{w} = -\Omega_{im}u - \Omega_{re}v - \frac{1}{T_1}(w + 1), \end{cases} \quad (2.5)$$

where T_1 and T_2 are the lifetime and coherence times of the excited state and $\Delta = \omega_0 - \omega$ is the frequency detuning between the atomic transition frequency, ω_0 , and the frequency of the optical driving field, ω . Ω_{re} and Ω_{im} are the real and imaginary parts of the

complex Rabi frequency (Ω), which describes the coupling strength between the external field and atomic field as follows:

$$\Omega(t) = \frac{\boldsymbol{\mu}_{12} \cdot \boldsymbol{\varepsilon}(t)}{\hbar} = \Omega_{re} + i\Omega_{im}, \quad (2.6)$$

where $\boldsymbol{\varepsilon}(t)$ is the complex amplitude of the electromagnetic field, including the phase variations, and $\boldsymbol{\mu}_{12}$ is the transition dipole moment between the two states.

2.2.1 The Bloch equations in another form

Equation (2.5) is useful to calculate the evolution of the state mathematically while it is difficult to see what is happening during the interaction process from those equations alone. We could write the Bloch equations in another form to obtain an intuitive picture of the dynamic of the Bloch vector under certain external field as

$$\dot{\mathbf{R}} = \mathbf{W} \times \mathbf{R} - \left(\frac{1}{T_2}u, \frac{1}{T_2}v, \frac{1}{T_1}(w+1) \right). \quad (2.7)$$

The first part of the right side of the equation shows that the Bloch vector, \mathbf{R} , rotates around another vector, $\mathbf{W} = (-\Omega_{re}, \Omega_{im}, \Delta)$, which contains all the parameters of the external field and represents the coupling between the light and atoms. The frequency of the rotation is given by the length of the vector, $|\mathbf{W}| = \sqrt{\Omega_{re}^2 + \Omega_{im}^2 + \Delta^2}$. The second part describes the shrinking of the Bloch vector, T_1 makes it shrink downwards toward the ground state ($w = -1$ in this case) and T_2 makes it decrease in the uv -plane toward the w -axis.

To visualize the movement of the Bloch vector on the Bloch sphere, we consider a short time t which is much shorter than the relaxation time, T_1 and T_2 , such that we could ignore the last term in Equation (2.7) and assume that the external field is constant over this time period; thus, \mathbf{W} is constant. These lead to

$$\frac{d}{dt}(\mathbf{R} \cdot \mathbf{W}) = 0, \quad (2.8)$$

which means that the $\mathbf{R} \cdot \mathbf{W} = |\mathbf{R}||\mathbf{W}|\cos(\beta)$ is a constant, where β is the angle between $|\mathbf{R}|$ and $|\mathbf{W}|$. Since $|\mathbf{R}|$ and $|\mathbf{W}|$ are both constant, then the angle between \mathbf{R} and \mathbf{W} , β is constant, which means that the Bloch vector, \mathbf{R} , spins around \mathbf{W} on the Bloch sphere. Figure 2.2 shows the evolution of the Bloch vector under a certain external field.

2.2.2 Pulse area

The Rabi frequency has the unit of rad/s, which quantifies how fast a resonant external field makes the Bloch vector spin. Thus,

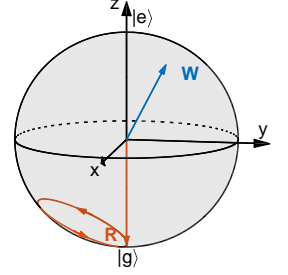


Figure 2.2. The movement of Bloch vector driven by a certain field. Because of the detuning between the driving field and the resonance frequency of the atom, the Bloch vector no longer goes to $w=1$.

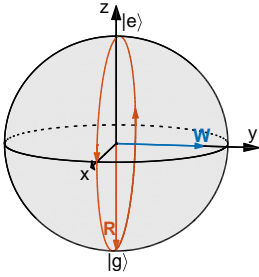


Figure 2.3. The effect of a π pulse drives a Bloch vector originally pointing straight down to pointing straight up; thus, inverse the population from one state to the other. If the pulse stops halfway, the Bloch vector then ends up on the equator plane, which represents a 50/50 superposition of the two states.

for a pulse with time duration of t , the total angle that the Bloch vector changes due to the external field is given by

$$\Theta = \int_0^t \Omega_{re}(t') dt'. \quad (2.9)$$

Θ is called the pulse area, it is the angle through which the Bloch vector turns. The most commonly used terms are $\pi/2$ and π pulses. For an atom, initially in its ground state driven by an on-resonance field, a $\pi/2$ pulse put it into a 50/50 superposition state while the π pulse excites the atom fully to the excited state. For the same driving field, the pulse areas are not the same for two different transitions. This is because the different transition dipole moments associated with the transitions result in different Rabi frequencies for the same driving field (see Figure 2.6): thus, resulting two different pulse areas for the same driving field. Both of these pulses are used in the photon echo sequences discussed in Section 2.3.2. The effect of $\pi/2$ and π pulses acting on a ground state is shown in Figure 2.3.

2.3 Coherent transients

The light emitted from an ensemble of atoms depends largely on their coherence property, i.e., their phase relations. When atoms emit incoherently, i.e., there is no phase correlation of the emitted light from different atoms, the intensity of the emission is proportional to the number of atoms; spontaneous emission is a good example. However, when the atoms emit coherently, i.e., the phase of the emitted light fields are the same and they interfere constructively, the intensity of the emission is proportional to the number of atoms squared. In this case, the emission is enhanced proportionally to the number of atoms in the ensemble.

The coherent emission is transient in a medium where the resonance frequency of the emitters shift relative to each other (an inhomogeneously broadened system), such as a Doppler-broadened gas or rare-earth-ion-doped crystals. This is because the emitters emit in phase for only a limited time before they dephase due to the frequency difference. In this section, we will focus on two coherent transient effects, *free induction decay* and *photon echo*.

2.3.1 Free induction decay

When a narrow linewidth laser coherently interact with an inhomogeneously broadened line, and saturate a narrow frequency interval within it and then if the laser is suddenly switched off, the coherence it build up during the interaction time evolves freely and will give out an emission that is in the same direction of the excitation beam while decay with time.

The decay time of the FID, τ_{FID} , is proportional to the coherence time of the system that the laser is interacting with, and can be written as [6]:

$$\tau_{FID} = \frac{T_2}{1 + \sqrt{\Omega T_1 T_2 + 1}}, \quad (2.10)$$

where T_1 and T_1 are the life time and coherence time of the excited state and Ω is the optical Rabi frequency. If the inhomogeneous absorption linewidth is much wider than the Fourier width of the exciting pulse, the duration of the FID is roughly equal to the duration of the pulse.

2.3.2 Photon echo

A photon echo was first observed in a Ruby crystal [7], where a burst of light was emitted at time $\approx \tau_s$ after irradiation by two successive Ruby-laser pulses separated by τ_s . The term *photon echo* is suggested based on the corresponding spin echo phenomenon observed in nuclear magnetic resonance (NMR) experiments [8]. Here we consider a photon echo process from an inhomogeneously broadened atomic ensemble excited by a fixed frequency.

As we discussed in the last section, the short light pulse put the atoms in a superposition state (ideally in the uv -plane) and they are in phase at the beginning: $\phi = 0$ at $t = 0$ for all the atoms. Then they dephase quickly from each other due to their different oscillation frequencies. At time t_{12} , the phase of the atom i is $\phi_i = \Delta_i t_{12}$, where Δ_i is the detuning between the frequency of the excitation light and the oscillation frequency of the atom. We send in another pulse, which should ideally be a π pulse, and rotate the Bloch sphere 180° around the u -axis. This would invert the phase evolution of the atoms at time t_{12} and the phase of atom i changes to $\phi_i = -\Delta_i t_{12}$. If we wait the same time t_{12} , the phase of the atom i becomes $\phi_i = -\Delta_i t_{12} + \Delta_i t_{12} = 0$. Thus, all atoms are in phase again and emit coherently, sending out an ‘echo’ at time t_{12} after the second pulse. The emission of the photon echo is a coherent effect; thus, the echo signal depends on the phase memory (T_2) of the atoms. The longer the waiting time, t_{12} , the smaller the echo. The pulse sequence for the photo echo process is shown in Figure 2.4.

The two pulse photon echo technique has been studied extensively for classical information storage due to its high bandwidth and efficiency [9]. Unfortunately, it is not suitable for quantum storages [10, 11]. The inversion pulse (a bright π pulse) causes gain and spontaneous emission which contributes to the noise signal, the signal to noise ratio is too low when one tries to detect an echo at the single photon level (however, one technique, revival of the silenced echo (ROSE), is proposed to address this problem [12]).

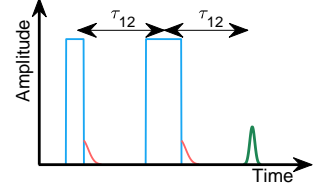


Figure 2.4. Two-pulse photon echo sequence: The first $\pi/2$ pulse (shown as the first blue trace) puts the atoms in a superposition state with the same phase and the atoms start to emit coherently (the emission is shown as the red trace after the pulse). However, since they have different oscillation frequencies, they dephase quickly, causing a decrease in the emission. The second π pulse with twice the pulse duration and same field amplitude as the first π pulse (shown as the second blue pulse) inverts the phase of all the atoms, which will be in phase again after a time equal to the two pulses, τ_{12} , and emit an echo (shown as the green trace).

Several protocols have been proposed aiming at bypassing the second bright π pulse, such as controlled reversible inhomogeneous broadening (CRIB) [13, 14], gradient echo memory (GEM) [15, 16] and atomic frequency comb (AFC) quantum memory [17–19]. The reshape could be done by external electric or magnetic field as in CRIB and GEM or by carefully preparing a periodic comb structure in a frequency domain with teeth separation of Δ , as in AFC. If the atoms in an AFC structure are excited coherently, they emit light when they are in phase; the first one happens at time $t = \frac{2\pi}{\Delta}$. The AFC quantum memory will be discussed more in Chapter 5.

RARE-EARTH-ION-DOPED CRYSTALS

Rare-earth elements include scandium and yttrium, as well as the 15 lanthanides, according to the International Union of Pure and Applied Chemistry (IUPAC). Despite the name, most of the rare-earth elements are not really rare, but they tend to occur together in nature and are difficult to separate. The first rare-earth-element, yttrium, was named after the village in Sweden where it was found, Ytterby. Some of the other rare-earth elements were named in a similar manner or after the scientists who discovered or elucidated them. Their positions in the periodic table are shown in Figure 3.1.

The rare-earth-ion-doped crystals have attracted a lot of attention in the past decade as promising candidates for quantum computing [20–22] and quantum memories [16, 23], mainly because of their very long coherence time for both the excited state and ground states.

The materials used throughout the experiment presented in this thesis are rare-earth-ion-doped crystals (REICs), $\text{Pr}^{3+}:\text{Y}_2\text{SiO}_5$ to be more specific. In this Chapter, I will present some relevant properties of the rare-earth-ion-doped crystals; more detailed information about such materials can be found in Ref. [24].

3.1 Energy level of rare-earth ions

The electronic structure configuration of the lanthanide elements, with minor exceptions of La, Ce, and Gd, is $[\text{Xe}]6s^24f^n$. When doped into a solid material, they tend to lose the two 6s electrons and one 4f electron to form trivalent ions (they can lose two electrons and form divalent ions as well), called rare-earth ions (RE ions), such as Pr^{3+} . The trivalent lanthanide ions have a Xenon core and the valence electrons in the 4f subshell.

Figure 3.2 shows the radial charge density as a function of the radius, r , for the 4f, 5s, 5p, and 6s orbitals for Gd^{3+} calculated by

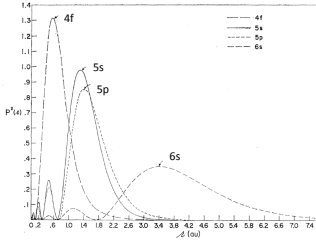


Figure 3.2. The radial charge density, $P^2(r)$ as a function of radius, r , for the 4f, 5s, 5p, 6s orbitals of Gd^+ from Ref. [25]. This figure is reprinted with permission.

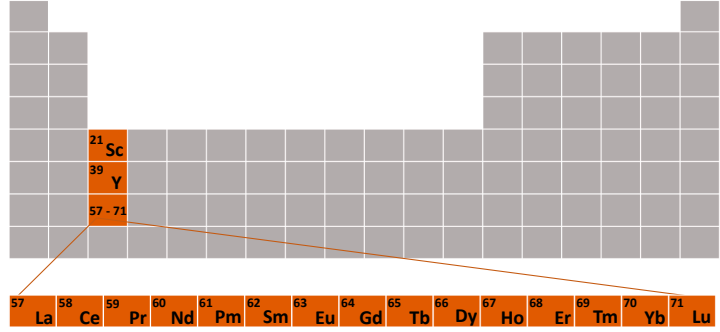


Figure 3.1. The location of the rare-earth elements in the periodic table.

Freeman and Watson [25]; we can see that the electrons in the 4f subshell are spatially shielded from the surrounding environment by the outer 5s and 5p orbitals. This is similar to the other rare-earth ions and is the reason that the surrounding environment has such a small effect on the energy levels of the 4f-subshell.

The calculated $4f^n$ energy levels of the trivalent rare-earth ions in a LaF_3 crystal were first published by Dieke et.al. in 1963, sometimes referred to as the Dieke diagram. It has been reprinted several times. Figure 3.3 shows one version from reference [26] with minor modifications. The energy levels of the rare-earth ions in other host materials may shift by a few hundreds of cm^{-1} , but the structures are similar.

Transitions within the 4f-subshell are forbidden for free ions since the electric dipole transition requires a change of parity. However, when doped into a non-centrosymmetric crystal, the low symmetry crystal field breaks the symmetry of the electron wavefunction and the transitions are weakly allowed, giving rise to a permanent electric dipole moment (static dipole moment) of each state [27, 28]. This is why the 4f-4f transitions have very long coherence times and their linewidths are typically a few kHz at cryogenic temperatures.

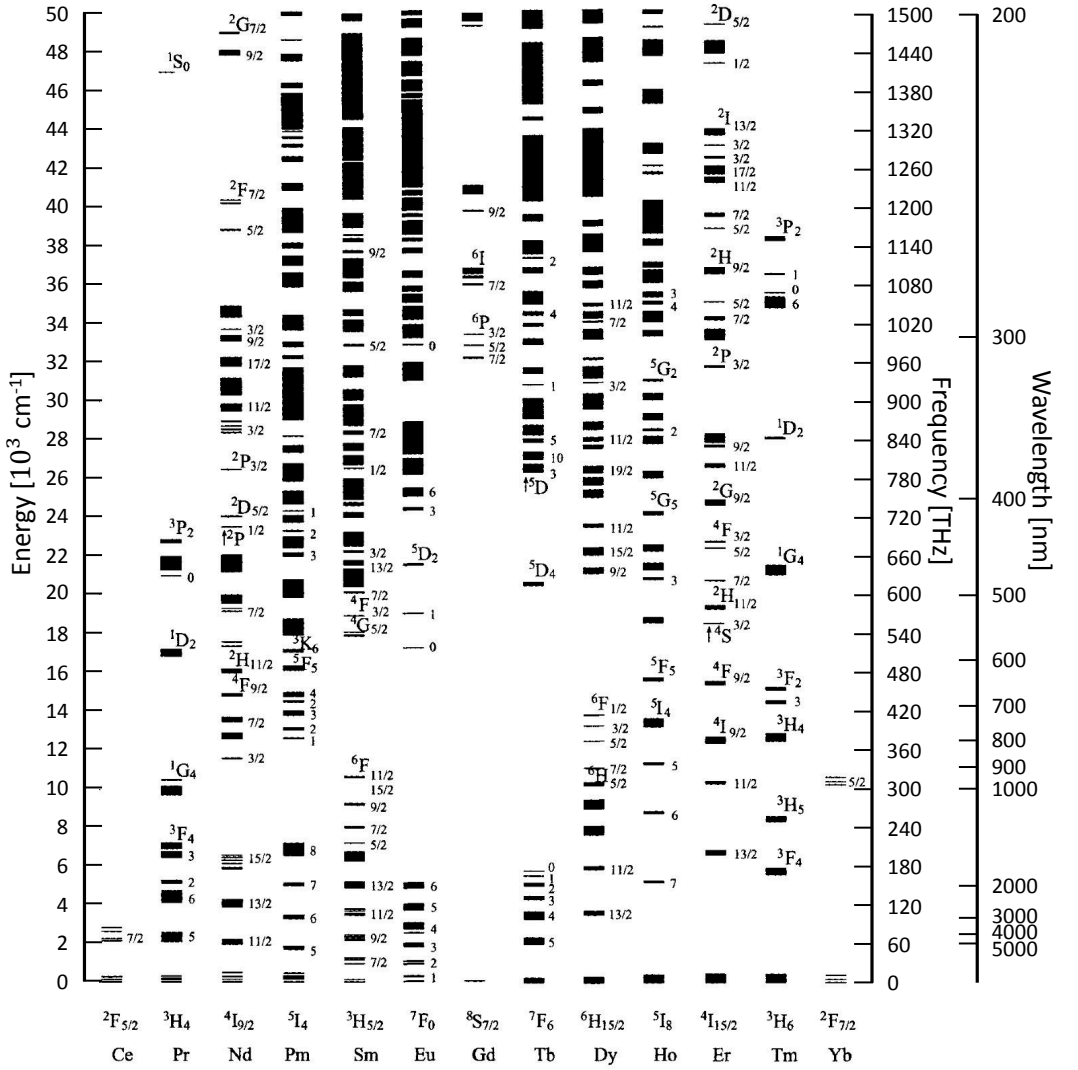


Figure 3.3. Calculated diagram of the $4f^n$ energy levels of the trivalent rare-earth ions in a LaF_3 crystal. It is a slightly modified version from reference [26] with permission.

3.1.1 Coherence time and homogeneous linewidth

Two different time constants are associated with one excited state: the lifetime of the state, T_1 , and the coherence time of the state, T_2 . The lifetime describes how long the atom stays in the excited state before it decays to the ground state, while the coherence time describes how long the superposition state keeps its phase information. The lifetime sets the upper boundary of the coherence time, $T_2 \leq 2T_1$, since the phase information is lost if the system decays to its ground state.

An atom in a superposition state oscillates at a frequency ω_0 , which depends on the energy level separation between the excited state and the ground state, $\omega_0 = \frac{E_e - E_g}{\hbar}$. The energy levels of these two states are affected by the surrounding electric field. For example, when the spin of a close by atom flips, the field changes slightly, shift the energy levels and altering the oscillation frequency of the state. Since this spin flip is a random process and unknown to us, the phase information we have about the state is not accurate anymore. Similarly, if a nearby atom is excited from the ground state to the excited state, the surrounding electric field changes and causes a phase change in the system because of the permanent electric dipole moment is different between these two states. The loss of phase information of a state is called dephasing (decoherence); if we know the cause, we can compensate for the dephasing and increase the coherence time of the states.

When an atom in a superposition state emits a photon, the frequency of the emitted photon will be the same as the frequency separation of the two states. Since the energy of the two states changes, the frequency of emitted photon will have a certain width instead of a perfectly monochromatic emission. The frequency width of such an emission, the homogeneous linewidth, can be calculated from the coherence time, T_2 according to

$$\Gamma_h = \frac{1}{\pi T_2}. \quad (3.1)$$

Coherence times of up to 30 seconds have been measured in $\text{Pr}^{3+}:\text{Y}_2\text{SiO}_5$ for the hyperfine ground states using decoupling sequences (bang-bang pulses) [29]; the lifetimes of these states are shown to be about 20 min with a small magnetic field [30]. Coherence time up to six hours by employing dynamic decoupling pulses at ZEFOZ point [31] and an extremely long lifetime of the nuclear spin state of 23 days are measured in $\text{Eu}^{3+}:\text{Y}_2\text{SiO}_5$. As for the optical transitions, coherence time of 112 μs at zero magnetic field and a lifetime of 164 μs have been demonstrated in $\text{Pr}^{3+}:\text{Y}_2\text{SiO}_5$; the coherence time could be extended to 152 μs when applying a field of 7.7 mT [32]; coherence times up to several milliseconds have been measured in $\text{Eu}^{3+}:\text{Y}_2\text{SiO}_5$ [33] and $\text{Er}^{3+}:\text{Y}_2\text{SiO}_5$ [34].

3.1.2 Inhomogeneous linewidth

When doped into an inorganic crystal, each individual rare-earth ion has a well-defined center frequency and a narrow homogeneous linewidth. However, because of the size mismatch of the dopant ions and the host ions that are substituted, the doping distorts the crystal lattice randomly and the individual ions are located in slightly different surroundings and feel different crystal fields. This causes a random shift of the center frequency of the ions, resulting in an absorption profile that is much wider than the homogeneous linewidth, Γ_h . This is referred to as the inhomogeneous linewidth; Γ_{in} . Figure 3.4 illustrates how this inhomogeneous broadening happens.

The inhomogeneous linewidth varies from crystal to crystal and depends on many factors, such as doping concentration, crystal quality, and external static pressure. Typically the inhomogeneous linewidth is a few GHz [34]. For the crystal used in this thesis, 0.05% $\text{Pr}^{3+}:\text{Y}_2\text{SiO}_5$, the typical linewidth is 5 - 10 GHz.

Since the inhomogeneous linewidths ($\sim \text{GHz}$) are typically 10^6 times wider than the homogeneous linewidths ($\sim \text{kHz}$), it is possible to address different ensembles of ions individually using different laser frequencies with narrow bandwidths, e.g., by spectral hole burning, to be discussed in Section 3.3. This offers attractive possibilities for data storage and quantum computing.

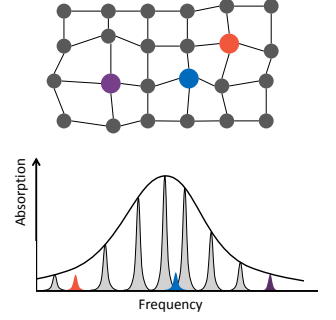


Figure 3.4. Illustration of the inhomogeneous broadening; when doped into a crystal, the rare-earth ions randomly replace some of the host ions; due to the size mismatch between the dopant ion and the host ion, the crystal lattice is distorted, affecting the local electric field the dopant ions feel and shifting their resonance frequency slightly. At the end, even though each dopant ion absorbs at a certain frequency, the ensemble forms a broad absorption profile.

3.2 Hyperfine level

Even though the surroundings have little effect on the rare-earth ions, the energy level structure of the states does depend on the host material and the symmetry of the site in which the rare-earth ions have replaced the host ions. For rare-earth ions with nuclear spins greater than $1/2$, the energy levels are split into hyperfine levels by second-order hyperfine and quadrupole interactions. Typical hyperfine level splittings range from a few MHz to a few GHz. The hyperfine structure of praseodymium (Pr^{3+}), when doped into Y_2SiO_5 at site 1 as used in this thesis, is shown in Figure 3.5. The Pr^{3+} (there is only one naturally abundant isotope, ^{141}Pr) has nuclear spin of $I = \frac{5}{2}$, and the $^3\text{H}_4$ and $^1\text{D}_2$ levels each splits into three hyperfine states with $m_I = \pm\frac{5}{2}, \pm\frac{3}{2}, \pm\frac{1}{2}$, respectively. At thermal equilibrium, all three ground states are equally populated and can be coupled to all three excited states. Therefore, a single radiation field drives all nine transitions at the same time in different ensembles of ions within the inhomogeneous bandwidth [35].

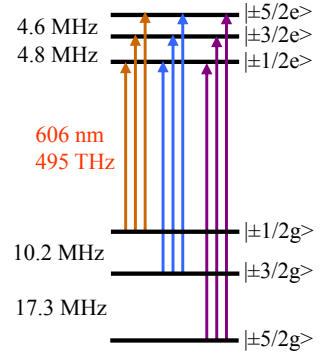


Figure 3.5. Hyperfine structure for the $^3\text{H}_4 - ^1\text{D}_2$ transition in $\text{Pr}^{3+}:\text{Y}_2\text{SiO}_5$ at site 1.

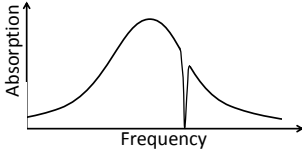


Figure 3.6. Spectral hole burning in a inhomogeneously broadened absorption spectrum. Atom/ions that absorb at specific frequencies are burned away by a laser beam.

3.3 Spectral hole burning

When a material with inhomogeneously broadened absorption profile is illuminated by a laser beam with frequency ν_0 and a linewidth that is narrower than the inhomogeneous linewidth of the spectrum, certain frequency components are bleached, leading to increased transmission at these frequencies. This is referred to as spectral hole burning and is shown in Figure 3.6.

Consider the $^3H_4 - ^1D_2$ transition of Pr^{3+} . Due to the different combinations of the ground state and excited state hyperfine levels and the inhomogeneous broadening effect, there are 9 possible transitions (from 9 groups of Pr^{3+} ions) that have the same transition frequency at the same time. If we have a laser with a linewidth comparable to the homogeneous linewidth of the Pr^{3+} ion, we can use it to interact with Pr^{3+} ions that have one transition (out of their nine transitions) that is resonant with the laser; those Pr^{3+} ions will be excited. Since there are three ground states, when those ions decay, they have a certain probability of relaxing to a hyperfine state different from the one that they originally came from, decreasing the absorption at the laser frequency. This process is called spectral hole burning and the region with less absorption is called a spectral hole. Since there are three states that can be excited from the same ground state, the absorption from the state where the ions were originally to the other two excited states will decrease as well; they are called side-holes. The other transitions from the two ground states that now have more populations have more absorption than before and create anti-holes. The structure of spectral holes and anti-holes could be used to study the energy level of the hyperfine structure.

The lifetime of the spectral hole depends on how fast the hyperfine states relax. Since the hyperfine state has a lifetime as long as $\sim 100s$ for $Pr^{3+}:Y_2SiO_5$, it is sometimes referred to as a persistent hole.

By scanning the laser in frequency and repeating the hole burning process many times, it is possible to create a wide hole with almost no absorption, referred to as a spectral pit. The maximum pit width is determined by the hyperfine splittings. For $Pr^{3+}:Y_2SiO_5$, the widest spectral pit we could create is 18 MHz, which is the separation of the ground state minus the separation of the excited state.

After the spectral pit is created, a group of ions with a selected frequency could be burnt back into the pit by using a spectrally narrow laser. This is referred to as peak creation; we could isolate one group of ions from the other ions and control the phase evolution of these ions precisely. Spectral hole burning (pit creation) and peak creation are the techniques we used in this thesis; for example, in the quantum memory project discussed in Chapter 5. More information about what pulse parameters and sequences to

g e	$\pm 1/2$	$\pm 3/2$	$\pm 5/2$
$\pm 1/2$	0.56	0.38	0.06
$\pm 3/2$	0.39	0.60	0.01
$\pm 5/2$	0.05	0.02	0.93

Table 3.1: The relative oscillator strength for the 3H_4 - 1D_2 transition between the ground and excited state hyperfine levels.

use for the pit, peak creation are found in Ref. [36]. A typical spectral pit with one group of ions inside is shown in Figure 3.7. The ions are at their $|\frac{1}{2}g\rangle$ state, while the three peaks correspond to the transitions from $|\frac{1}{2}g\rangle$ to $|\frac{1}{2}e\rangle$, $|\frac{3}{2}e\rangle$ and $|\frac{5}{2}e\rangle$, respectively. The height of the peaks depends on the oscillator strength of the corresponding transition (see next section).

3.4 Transition strength

Transition strength (oscillator strength) describes how easy it is to drive a transition. A higher transition strength means the transition could be driven in a shorter time with a given amount of laser power and that the transition has a higher absorption coefficient and greater spontaneous emission, thus a shorter lifetime, than transitions with lower transition strength under the same conditions.

The transitions in rare-earth ions are weaker than the allowed electronic transitions, which is why the rare-earth ions has long lifetimes and coherence times. Typical values for the oscillator strength of rare-earth ions range from $f = 1.3 \times 10^{-8}$ for $\text{Eu}^{3+}:\text{Y}_2\text{SiO}_5$ [37] to $f = 8 \times 10^{-6}$ for $\text{Nd}^{3+}:\text{YVO}_4$ [34]. The relative oscillator strength of the 3H_4 - 1D_2 transition in $\text{Pr}^{3+}:\text{Y}_2\text{SiO}_5$ is shown in Table 3.1.

The oscillator strength is proportional to the square of the transition dipole moment [38], and the transition dipole moment, μ_{ge} , for Pr^{3+} when doped into Y_2SiO_5 , lies in the D1-D2 plane with an angle of about 15.5° from the D2 axis, where D1, D2 (and b) are the three principal axes of the host material Y_2SiO_5 [24]. Figure 3.8 shows the transition dipole moment orientation relative to the principal axes of the host. To excite a transition, the incoming light field has to have one component along the transition dipole moment.

3.5 Static dipole moment and Stark effect

When atoms or ions are present in an electric field, their energy levels shift relative to the original levels due to the interaction of their static dipole moment with the electric field. This is called

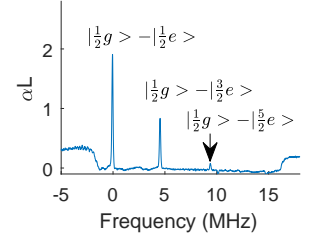


Figure 3.7. A typical spectral pit with one group of ions at their $\frac{1}{2}g$ state in $\text{Pr}^{3+}:\text{Y}_2\text{SiO}_5$ at site 1.

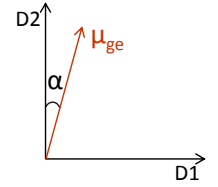


Figure 3.8. Transition dipole moment of Pr^{3+} . It almost lies in the D1-D2 plane and has an angle of $\sim 15.5^\circ$ with the D2 axis.

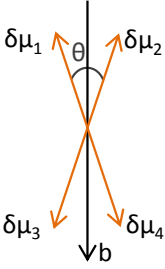


Figure 3.9. A schematic drawing showing the different static dipole moment orientations between the excited and ground states ($\delta\mu$) for the $^3\text{H}_4 - ^1\text{D}_2$ transition in $\text{Pr}^{3+}:\text{Y}_2\text{SiO}_5$. The magnitude of $\delta\mu$ is $111.6 \text{ kHz}/(\text{V}\cdot\text{cm}^{-1})$, oriented in one of the four possible directions, where $\theta = 24.8^\circ$.

the (DC) Stark effect, and the frequency shift is referred to as the Stark shift.

Because the static electric dipole moment of the ground state, μ_g , differs from that of the excited state, μ_e , the resonant frequency of the atoms or ions experiences a net Stark shift of in the presence of an external electric field.

$$\Delta_s = \frac{(\mu_e - \mu_g) \cdot \mathbf{E}}{\hbar} = \frac{\delta\mu \cdot \mathbf{E}}{\hbar}, \quad (3.2)$$

where \mathbf{E} is the applied electric field and $\delta\mu$ is the difference between the excited and ground state static dipole moments (not to be confused with the transition dipole moment).

For $\text{Pr}^{3+}:\text{Y}_2\text{SiO}_5$, there are four possible $\delta\mu$ orientations for Pr^{3+} , as shown in Figure 3.9; all four orientations of $\delta\mu$ have an angle of $\theta = 12.4^\circ$ relative to the b axis of the crystal; the magnitude of $\delta\mu/\hbar$ is $111.6 \text{ kHz}/(\text{V}\cdot\text{cm}^{-1})$ [39, 40]. If we apply an external field along the symmetry axes of the dipole moments, $\delta\mu_{1,2,3,4}$, i.e., along the b axis of the crystal or the direction perpendicular to it, two effective Stark shift coefficients appear with the same magnitude but opposite signs. As a result of this, half of the ions with the positive Stark coefficient will be the frequency shift from ν_0 to $\nu' = \nu_0 + |\Delta_s|$, while the other half of the ions, with the negative Stark coefficient, will be frequency shift from ν_0 to $\nu' = \nu_0 - |\Delta_s|$. If the external field is applied not along the symmetry axes, one could get four different frequency shifts.

3.6 $\text{Pr}^{3+}:\text{Y}_2\text{SiO}_5$ and $\text{Eu}^{3+}:\text{Y}_2\text{SiO}_5$

As discussed in Section 3.1.1, the random spin flips in the surrounding atoms could cause decoherence of the rare-earth ions and reduce the coherence time. Y_2SiO_5 is a good candidate for host material due to its low nuclear magnetic moment, which minimize the effect of decoherence caused by spin-flip from the host ions. There are two inequivalent yttrium sites that the rare-earth ions could occupy when doped into Y_2SiO_5 crystal, referred to as site 1 and site 2. The sites give rise to slightly different energy levels in the dopant ions.

Pr^{3+} and Eu^{3+} are similar in many ways. Both of them are non-Kramers' ions (have an even number of $4f$ electrons after forming RE^{3+}) and have non-degenerate crystal field levels. Both of them have a nuclear spin of $5/2$ and have no first-order hyperfine splitting [44] and the second order hyperfine interaction splits each crystal field level into three doubly degenerated hyperfine level at zero magnetic fields. Both the $^3\text{H}_4 - ^1\text{D}_2$ transition in Pr^{3+} and the $^7\text{F}_0 - ^5\text{D}_0$ transition in Eu^{3+} have a long lifetime and long coherence time. The $^7\text{F}_0 - ^5\text{D}_0$ transition in Eu^{3+} has an even longer coherence time because both states have an angular momentum

	Pr (site 1)	Pr (site 2)	Ref
λ_{vac}	605.977 nm	607.934 nm	[32]
T_1 optical	164 μ s	222 μ s	[32]
T_2 optical (0 T)	114 μ s	318 μ s	[32]
T_2 optical (7.7 mT)	152 μ s	377 μ s	[32]
T_1 hyperfine	≈ 100 s	≈ 100 s	[35]
T_1 hyperfine (10 mT)	~ 20 minutes	-	[30]
T_2 hyperfine (80 mT)	42 s	-	[41]
Stark coefficient	112 kHz/(V \cdot cm $^{-1}$)	92.9 kHz/(V \cdot cm $^{-1}$)	[39]

Table 3.2: Some properties for the $^3H_4 - ^1D_2$ of Pr:Y₂SiO₅ at liquid helium temperatures.

	Eu (site 1)	Eu (site 2)	Ref
λ_{vac}	579.879 nm	580.049 nm	[33]
T_1 optical	1.9 ms	1.6 ms	[33]
T_2 optical (0 T)	1.5 ms	1.1 ms	[33]
T_2 optical (10 mT)	2.6 ms	1.9 ms	[33]
T_1 hyperfine	23 days	23 days	[37]
T_2 hyperfine (0 T)	19 ms (^{151}Eu)	-	[42]
T_2 hyperfine (1.35 T)	6 hours (^{151}Eu)	-	[31]
Stark coefficient	35 kHz/(V \cdot cm $^{-1}$)	17 kHz/(V \cdot ccm $^{-1}$)	[43]

Table 3.3: Some properties for $^7F_0 - ^5D_0$ of Eu:Y₂SiO₅ at liquid helium temperatures.

of $J = 0$ which means there is no first-order magnetic moment, making it less sensitive to fluctuations in the crystal field.

All the work done within the scope of this thesis used Pr³⁺:Y₂SiO₅, it is believed that with Eu³⁺:Y₂SiO₅ better results could be possible, because of the longer lifetime and coherence time in Eu³⁺:Y₂SiO₅, provided there is sufficient laser power and wide enough modulation range of the laser, given that Eu³⁺:Y₂SiO₅ has much lower oscillator strength and wider hyperfine splitting. Some of the properties related to the $^3H_4 - ^1D_2$ transition in Pr³⁺:Y₂SiO₅ and the $^7F_0 - ^5D_0$ transition in Eu³⁺:Y₂SiO₅ are summarized in Tables 3.2 and 3.3.

SLOW LIGHT EFFECT RELATED PHENOMENA

The slow light effect has attracted a lot of attention in recent years because of its applications in the optical delay line, data synchronization, optical communication, as well as many other applications. It also has uses in quantum computing and quantum communication; for example, ultraslow light would make photon-photon interaction possible, enabling a single-photon pulse to coherently manipulate the quantum state of the other one [45], slow light based quantum memories have been demonstrated [46]. Slow light effect in rare-earth-ion-doped crystals has been studied extensively and group velocity of light down to 45 m/s has been demonstrated in such a system [47].

This chapter focuses on the slow light effect caused by spectral engineering of the inhomogeneous profile in rare-earth-ion-doped crystals. The chapter is structured as follows: Section 4.1 introduces the phase velocity and group velocity of light in relation to the refractive index, Section 4.2 provides two ways of calculating group velocity inside a spectral hole, as well as how to interpret the slow light effect from an energy point of view. Sections 4.3, 4.4, 4.5 focus on three slow-light related phenomena: cavity linewidth narrowing, group velocity control and pulse compression, as well as slow-light based frequency shifting, which lead to the publications of Papers **II**, **IV**, and **III**, respectively.

4.1 Phase velocity and group velocity

The speed of light in vacuum is a universal constant, $c = 2.99792458 \times 10^8$ m/s. When an achromatic light wave propagates inside a material, it propagates at its phase velocity, v_p , which is slower than c . That is because the atoms inside the medium can

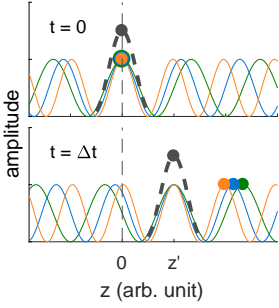


Figure 4.1. The propagation of a wave packet and some of the frequency components it contains.

be viewed as an atomic core surrounded by fast-moving electrons, the electrons feel the force of the electric field of the light and oscillate together with it. This makes the atoms act like an oscillating dipole, which sends out its own electric field. If we look at a point far away from the medium, the integrated electric field that the atoms send out is 90 degrees behind in phase with the driven light field. At the end, the two electric fields add together and it seems as though the light travels slower inside the material. This speed is called phase velocity which could be described by the refractive index n that depends on the property of material as $v_p = \frac{c}{n}$; for example, $n = 1.000293$ in air and $n = 1.33$ in water for incoming wavelength $\lambda = 589.29$ nm. The refractive index depends not only on the material property but on the frequency of the light as well, which is called dispersion.

Besides the phase velocity, there is another term that is often related to the light propagation inside a medium, which is the group velocity.

Since a perfect chromatic wave cannot be used to transmit information because no information can be coded onto it, when we say that an optical pulse that carries information propagates inside a material, we are referring to a wave packet that contains many different frequencies. The group velocity of the pulse describes the speed at which the 'maximum' of the light envelope is propagating, i.e., where all the frequency components interfere constructively. Since each frequency propagates at its own phase velocity, the 'maximum' of the envelope propagates at a group velocity that could be faster or slower than the phase velocity depending on the dispersion.

Figure 4.1 shows a schematic drawing of the propagation of an optical pulse, the dashed dark gray line represents the propagation of the wave packet at the group velocity, while the solid green, blue, and orange lines represent the propagation of some of the frequency components of this wave packet at phase velocity. The maximum of the wave packet, as well as one crest (labeled by a dot marker) from each of the three frequency components inside the wave packet, are at $z = 0$ at $t = 0$, as shown in the upper part of the figure. The maximum of the wave packet propagates to $z = z'$ at time $t = \Delta t$ while the three crests propagate to z_i , where $i = 1, 2, 3$, corresponding to the three frequency components. The group velocity for the wave packet and the phase velocity for the different frequency components are $v_g = \frac{z'}{\Delta t} = \frac{c}{n_g}$, and $v_{pi} = \frac{z_i}{\Delta t} = \frac{c}{n_i}$, respectively, where n_g is the group refractive index for this wave packet, while n_i ($i = 1, 2, 3$) is the refractive index for the three frequency components.

As discussed above, the group velocity of a light pulse through a material can be calculated as

$$v_g = \frac{c}{n_g}, \quad (4.1)$$

and n_g is calculated by

$$n_g = n + \nu \frac{dn}{d\nu}, \quad (4.2)$$

where n is the real part of the refractive index (used to calculate the phase velocity), which ranges for most materials from 1 to 4, while the dispersion part $\frac{dn}{d\nu}$ could be vary rapid in the vicinity of a material resonance. The group refractive index could be much bigger/smaller than 1 or even negative, depending on the dispersion. This results in a group velocity that is much smaller/bigger than c which we call slow light and fast light. The group velocity could even be negative, it still belongs to the fast light because a negative group velocity means the peak of the pulse propagates so fast that it comes out of a material even before it enters, sometimes it is referred to as backward light [48, 49]. Group velocities down to the human scale of about 17 m/s have been observed experimentally in ultracold atomic gas [50] and the same scale of group velocity has been demonstrated in rare-earth-ion-doped crystals as well [47].

4.2 Slow light inside a spectral hole

The strong slow light effect could be achieved by making $\frac{dn}{d\nu}$ large and positive (large normal dispersion) through engineering the absorption profile, as mentioned above, dispersion is much stronger in the vicinity of a material resonance. As shown in Figure 4.2, the refractive index changes dramatically over the narrow spectral hole region, leading to a strong slow light effect. For this spectral hole based slow light, the group velocity v_g could be estimated by [51, 52]

$$v_g \approx \frac{2\pi\Gamma}{\alpha}, \quad (4.3)$$

where Γ is the frequency width of the transmission window and α is the effective absorption coefficient outside the spectral hole. Thus, we can see intuitively how the spectral hole affects the group velocity, leading to the publication of Section 4.4.3, where the group velocity of the light is controlled solely by external fields that determine the width of the spectral hole.

4.2.1 Energy perspective

Another way of interpreting the slow light effect is from the energy point of view. When a light pulse propagates forward, the electromagnetic field is moving in space and time. Since the material

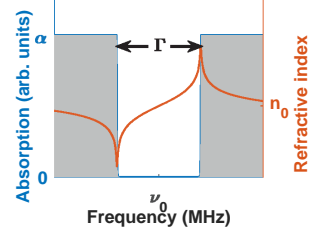


Figure 4.2. A spectral hole with a width of Γ and the dispersion of the refractive index associated with this structure. Due to the strong dispersion inside the spectral hole, the group velocity of the pulse propagating inside the spectral hole could be very low.

is made of atoms and molecules, the light interacts with them off-resonantly and lifts the Bloch vectors of the atoms slightly from their ground-state position. As a result, certain energy is stored in the material as atomic excitation. The Bloch vectors evolve in time, the atoms rephase at a later time and the energy stored inside the atoms return to the light field. The stronger the interaction, the more energy is stored in the material and the slower the light propagates [53–55].

For example, when a light field propagates inside the rare-earth-ion-doped crystal, it interacts with the host material and the doped ions at the same time, however, for the frequency region we are interested in here, the interaction of the light with the host atoms is more or less constant, while its interaction with the dopant ions depends heavily on the frequency of the light and the resonance frequency of the ions. Thus, it would be useful to separate these two interactions and denote the energy density stored inside the crystal to be the energy density stored inside the host atoms, U_{host} , and the energy density stored inside the ions, U_{ion} , respectively. There is another term, U_{vac} , denotes the energy density of the pure electromagnetic field.

Similar to Ref. [53], the energy flow across a unit cross section inside the crystal per unit of time could be written as $v_g(U_{\text{vac}} + U_{\text{host}} + U_{\text{ion}})$, which should be the same as the energy flow through a unit cross section per unit time outside the crystal, cU_{vac} . Thus, we have

$$v_g(U_{\text{vac}} + U_{\text{host}} + U_{\text{ion}}) = cU_{\text{vac}}, \quad (4.4)$$

$$v_g = \frac{c}{1 + \frac{U_{\text{host}}}{U_{\text{vac}}} + \frac{U_{\text{ion}}}{U_{\text{vac}}}} = \frac{c}{1 + \frac{U_{\text{med}}}{U_{\text{vac}}}}. \quad (4.5)$$

If there are no dopant ions or the frequency of light is very different than the resonance frequency of the ions such that $U_{\text{ion}} \approx 0$, we have $v_g = \frac{c}{1 + \frac{U_{\text{host}}}{U_{\text{vac}}}}$. If there is no dispersion from the host material, we have $v_g = v_p$ and the refractive index of the material could be written as $n = 1 + \frac{U_{\text{host}}}{U_{\text{vac}}}$.

From Equation (4.5), we could calculate that for a group velocity below 300 km/s, more than 99.9% of the total energy is stored in the medium.

4.3 Cavity linewidth narrowing

For a Fabry-Pérot cavity, the resonance of the cavity corresponds to the case when the incoming light field and the circulating field inside the cavity interfere constructively, which means they are in phase with each other. This happens when the round trip length of the cavity fits an integer number of the wavelength, $m(\lambda/2) = L$,

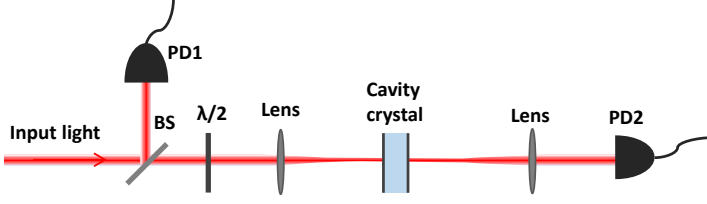


Figure 4.3. Experimental setup used for the cavity linewidth measurement. The incoming laser beam was split into two parts, one used as a reference beam while the other was focused inside the crystal, and detected by a photodetector (PD2). The polarization of the incoming light was along the D2 axis of the crystal by a $\lambda/2$ plate.

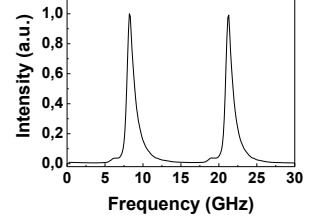


Figure 4.4. Cavity transmission at room temperature.

where m is an integer and the wavelength is $\lambda = c/(n\nu)$. Thus,

$$m \frac{c}{2L} = n\nu. \quad (4.6)$$

Differentiating Eq. 4.6 yields

$$\frac{c}{2L} \delta m = n \delta \nu + \nu \delta n. \quad (4.7)$$

Dividing the left (right) side of Eq. 4.7 by the left (right) side of Eq. 4.6 yields

$$\frac{\delta m}{m} = \frac{\delta \nu}{\nu} + \frac{\delta n}{n}, \quad (4.8)$$

where $n = n(\nu)$ is a function of frequency. Normally the relative frequency change is much faster than the refractive index change, $\delta \nu / \nu \gg \delta n / n$; thus, the frequency of the next cavity mode is far away in frequency from the current one. However, in the case of significant slow light effects $n \ll \nu (dn/d\nu)$, the second term on the right side of Eq. 4.8 is much larger than the first, and the cavity mode spacing is determined almost completely by the dispersion, while the effect of the relative frequency change is negligible.

The crystal we used here is a $L = 6$ mm, 0.05% $\text{Pr}^{3+}:\text{Y}_2\text{SiO}_5$. To make a cavity out of the crystal, the reflection coating was directly deposited onto the two surfaces of the crystal. One part of the crystal is left uncoated on both surfaces. The rest of the crystal was coated as follows: one of the surfaces was coated with a reflectivity of $R_1 = 95\%$, while the other surface was divided into two parts, one coated with the same reflectivity of $R_2 = 95\%$, the other with $R_2' = 99.7\%$. For investigation of the cavity mode narrowing, we used only the matched cavity part, where $R_1 = R_2 = 95\%$.

First, we measured the cavity mode spacing and cavity linewidth at room temperature at a wavelength where there should

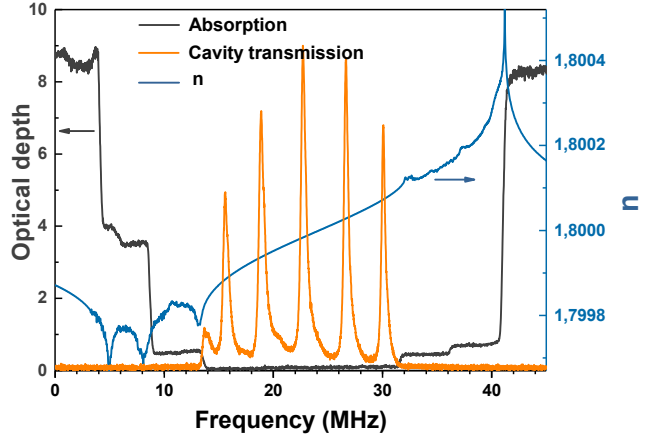


Figure 4.5. Cavity transmission and the dispersion at the presence of a spectral pit. The dark gray trace shows the estimated spectral structure inside the cavity, the blue trace is the calculated refractive index based on the Kramers-Kronig relation, and the orange trace shows the five cavity modes fitted inside an 18 MHz spectral pit.

be low absorption (around 620 nm) [56]. The cavity mode spacing is about $\delta\nu \approx 13$ GHz while the cavity linewidth is about $\gamma \approx 1$ GHz as shown in Figure 4.4, this is much wider than we expected. The cavity finesse was expected to be $F = \frac{\pi\sqrt{R}}{1-R} = 61$ for a matched cavity with $R = 0.95$, which would give the expected cavity linewidth of about 200 MHz. The main reason is the remaining absorption inside the crystal since there was still absorption at this wavelength and we could see the fluorescence from the ions. The transmission does not look symmetric and the tail on the high-frequency side is attribute to the higher order transverse modes in the cavity, while the small extra peaks to the left of the cavity modes come from the orthogonal light polarization, since the incoming light was polarized mainly along $D2$ but also contained a small $D1$ component, and $\text{Pr}^{3+}:\text{Y}_2\text{SiO}_5$ is a birefringent crystal with $n_{D1} = 1.7881$, $n_{D2} = 1.809$ [57, 58].

Optical pumping techniques were used to burn an 18 MHz wide spectral pit inside the ~ 9 GHz inhomogeneous absorption profile using a method similar to the one described in [59]. The experimental setup is shown in Figure 4.3, where the light propagated along the b axis of the crystal and the incoming light polarization was rotated to be along $D2$ by the $\lambda/2$ plate, a photodetector (PD2) was employed to measure the transmission through the cav-

ity crystal. The estimated spectral pit structure is shown as the black trace in Figure 4.5, while the blue trace shows the refractive index across the structure as calculated from the expected pit structure. A frequency chirped pulse was used to scan over the spectral pit, and 5 cavity modes were seen from PD2, shown as the orange trace in Figure 4.5. The cavity mode spacing and the linewidth were reduced to $\Delta \approx 3.5$ MHz and $\gamma \approx 600$ kHz respectively. The cavity linewidth and the mode spacing were further reduced by preparing a narrower spectral window of 1 MHz, for example. This resulted in a much steeper dispersion curve, which caused a stronger slow light effect and thus reduced the cavity linewidth further to about 30 kHz, as shown in Paper II. A reduction of the cavity linewidth of more than 10,000 was thus demonstrated.

In some sense, the slow light effect made the 6 mm long cavity behave like a very long cavity in the presence of a spectral hole (~ 45 m inside an 18 MHz pit and ~ 700 m inside a 1 MHz hole). If we send in a short pulse, we should be able to see the pulse bounces back and forth between the mirrors. We sent in a 20 ns long Gaussian pulse to the cavity in the presence of the 18 MHz spectral pit, while the center frequency of the Gaussian pulse was positioned in the center of the spectral pit. Figure 4.6 shows the transmitted light on the photodetector (PD2). The round trip time of the pulse is about 250 ns, which yields a group velocity of 48 km/s while the group velocity was measured to be about 10 km/s for a 3 MHz wide spectral structure.

Investigating the cavity linewidth narrowing is of great interest because of its wide-ranging applications. Here are a few examples. It was demonstrated in Ref. [60] that the weak spectral component outside the laser center frequency could be filtered away simply by sending the laser through a rare-earth-ion-doped crystal, reducing the laser phase noise by several tens of dB. Much narrower laser linewidth could be achieved by combing a similar cavity technique used here.

Spontaneous parametric down-conversion is widely used to generate entangled photon pairs and single photons. However, the frequency of the generated photon is too wide compared with the bandwidths of the quantum systems. One way to narrow the linewidth is to put the periodically poled nonlinear crystal inside a cavity. This configuration has two advantages: it enhances the efficiency of the conversion and the bandwidth of the photon emitted is the same as the cavity mode linewidth. However, the cavity mode and the bandwidth of the photon may still be too wide for certain applications. If a rare-earth-ion-doped crystal is combined with such a cavity, we could make it a slow light cavity and choose the parameters such that only one narrow cavity mode is within the transmission window, then we could narrow the cavity mode and the frequency width of the photon generated inside such a

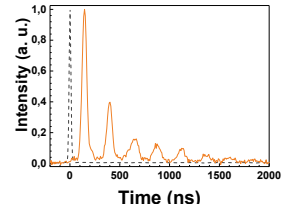


Figure 4.6. Light transmitted through a cavity (orange solid line) in the presence of an 18 MHz spectral pit when a 20 ns long pulse (dark gray dashed line) is sent into the cavity.

cavity to make it match well with the system. This would be ideal if the photons generated are used for a quantum system based on the same type of rare-earth-ion-doped crystals.

It could also be used to make high Q cavities. The Q value achieved in this cavity was 1.6×10^{10} in the presence of a 1 MHz spectral hole, while Q value up to 10^{11} has been measured in a crystalline CaF_2 whispering-gallery-mode (WGM) resonator, which was carefully polished and annealed [61]. WGM cavity made of rare-earth-ion-doped crystal with a Q value of 10^6 has been demonstrated [62], and it is reasonable to believe that the Q value could be increased by several orders of magnitude by combining with the slow light effect. If prepared more carefully, we might obtain a WGM cavity with an even higher Q value.

Mathematically speaking, Equation (4.6) shows that, in principle, there are different combinations of n and ν that match the same mode number m . In our slow light cavity, the two cavity modes to the left (right) inside the spectral pit in Figure 4.5 that are roughly 3.5 MHz apart have the same mode number as the two cavity modes below (above) the frequency of the inhomogeneous absorption line that is about 13 GHz apart. Thus, the slow light cavity described here could actually several cavity modes with the same mode number, which is not trivial for a conventional cavity.

4.4 Group velocity control and pulse compression

From Equation (4.3), we can see that the group velocity changes along with the width of the spectral hole; thus, it is possible to actively control the group velocity of the light propagating inside a spectral hole by control the width of the spectral hole. The hole width could be changed by shifting the resonance frequency of the ions by the Stark effect or the Zeeman effect, when applying an external electric field or magnetic field. Here we control the group velocity of light pulses via controlling the width of the hole by using the Stark effect.

As we discussed in Section 3.5, due to the symmetry of the electric dipole moment of the ions, there are two groups of ions with opposite sign of their Stark coefficient in the $\text{Pr}^{3+}:\text{Y}_2\text{SiO}_5$ crystal if an E field is applied along the b axis across the crystal (see Figure 3.9). Thus, the resonance frequency of half of the ions shifts to a higher frequency while that of the other half shifts to a lower frequency by the same amount when a certain external electric field is applied. Given a square hole structure from the beginning as shown in Figure 4.7 (a), a certain electric field results in a narrower hole structure, as in Figure 4.7 (b). The group velocity is reduced as the hole width narrows. Even though the effective absorption coefficient outside the hole is also reduced, at the maximum by a factor of 2, while the hole width could change much more than that. Thus, the group velocity decreases and we can control the group velocity straightforwardly by adjusting the strength of the electric field.

4.4.1 Crystal and E field

The crystal used in this experiment is a $10\text{ mm} \times 10\text{ mm} \times 6\text{ mm}$ ($D1 \times D2 \times b$) $0.05\% \text{ Pr}^{3+}:\text{Y}_2\text{SiO}_5$, it has two sets of electrodes directly deposited on its surfaces, as shown in Figure 4.8. The electric field at the center of the crystal along the light propagation axis simulated by COMSOL is shown in Figure 4.9. Because of the geometry of the electrodes, the electric field along the crystal is not quite homogeneous, it is lower at the edges and in the middle, however, it is within 95% if the light beam is within $\pm 1\text{ mm}$ of the center.

4.4.2 Experimental setup

We used an optical setup similar to the one for the cavity line narrowing experiment, except that the crystal is not a cavity but has electrodes on it, as shown in Figure 4.8 and a sketch of the setup is shown in Figure 4.10. A laser beam was split into two parts by a 90/10 beam splitter; the weaker one was detected by

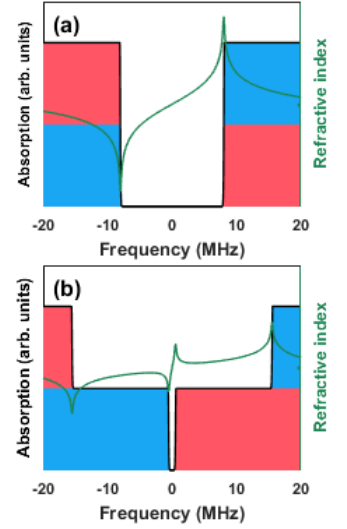


Figure 4.7. Sketch of the spectral structure before (a) and after (b) the 40 V external voltage is applied. Blue and red represent the ions with a positive and negative sign of Stark coefficient respectively, while the green trace shows the dispersion across the spectral structure.



Figure 4.8. The crystal used to make the frequency shifter. There are electrodes on its surfaces.

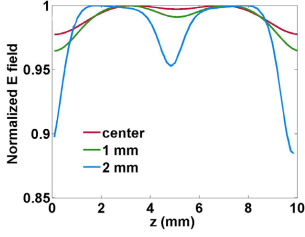


Figure 4.9. Electric field in the center of the crystal along the light propagation direction.

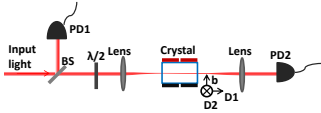


Figure 4.10. Simplified experimental setup for group velocity control.

a Thorlabs PDB150A photodetector (PD1) used as a reference beam to calculate the group delay of the pulse after crystal and to calibrate the laser intensity variations while the stronger beam was focused on the crystal and detected by another photodetector of the same model (PD2).

A 16 MHz spectral hole was created by sweeping the laser within ± 8 MHz around the center frequency (0 MHz). However, due to the inhomogeneity of the \mathbf{E} field, when a certain voltage was applied, the resonance frequency of the ions shifted differently depending on their location, which smoothed out the sharpness of the hole edge and induced some absorption close to the hole edge. To compensate for this effect, the structure preparation was optimized in the following way: 16 MHz, 8 MHz, 1 MHz and 500 kHz hole burning sequences were employed consecutively in the presence of 0, 20, 40 and 41.5 external voltages, followed by the 16 MHz hole burning sequence at 0 V at the end until a suitable hole structure with high transmission and sharp edge was achieved.

4.4.3 Group velocity control

We could see from Figure 4.7 that the dispersion curve for the 1 MHz hole at 40 V was much steeper than the 16 MHz hole at 0 V, which would result in a much slower group velocity for the narrower hole, as indicated in Equation (4.3).

After the preparation process, 16 Gaussian pulses with FWHM of 10 μs and cutoff duration of 100 μs were sent into the crystal successively at 16 different external fields (from 0 V to 42.5 V). The group velocity was calculated for each external field by measuring the delay between the transmitted pulses from the crystal and the reference beams, τ_d , and $v_g = \frac{L}{\tau_d}$. From Figure 4.11, we could see that the group velocity changed from 30 km/s at 0 V to 1.5 km/s at 42.2 V while maintaining a relative efficiency above 80%.

The slow light effect could be used as a delay line to hold the light for certain time for data synchronization or other applications. For an ordinary delay line that could delay a pulse for a certain time t , the fractional scattering loss of delaying time t is proportional to $I_s = 1 - e^{-\alpha_s l} = 1 - e^{-\alpha_s v_g t}$, where α_s is the scattering coefficient and l is the length the pulse has propagated. If a slow light delay line was used instead, the length of the delay line needed for the same delay time could be greatly reduced, thus reducing the scattering loss the light experiences during the delay process. Moreover, the slow light group velocity control is unique in the sense that it could be used as a tunable delay line that is controlled solely by an electric field; in some applications it could be an alternative to quantum memory.

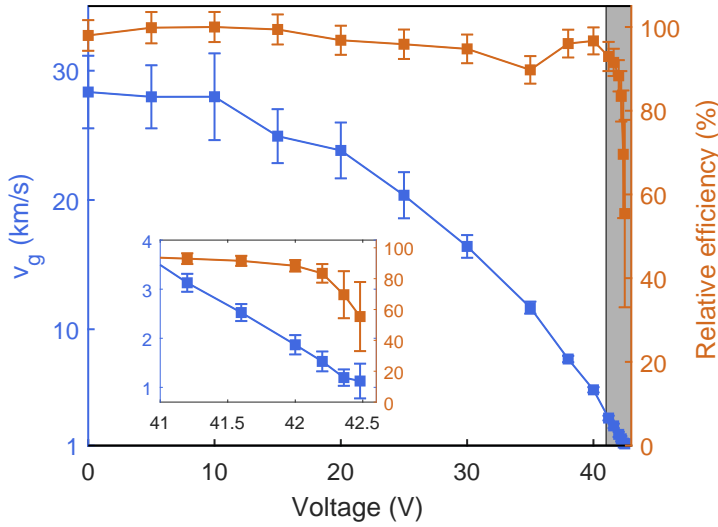


Figure 4.11. The group velocity (blue trace) and the efficiency (red trace) at different external voltages. The higher the external voltages, the lower the group velocity. The group velocity changed by a factor of 20 while keeping the relative efficiency at more than 80 %.

4.4.4 Pulse compression

Imagine a crystal that slows light down so much that the whole light pulse is compressed spatially and could fit inside it. When the light pulse is just about to exit the crystal, the slow light effect is switched off (or reduced, such that the group velocity increases), causing the pulse to come out much faster. The end of the pulse would spend much less time inside the crystal than the front. As a result, the pulse comes out of the crystal compressed in time.

A light pulse propagating inside the 16 MHz hole created initially has a group velocity of $\mathbf{v}_{g1} = L/\tau_1 \approx 29$ km/s, where τ_1 is the time it takes for the light pulse to propagate through the crystal. However, if an external voltage of $V = 40$ V is applied after preparation of the 16 MHz spectral hole (a sketch of the structure is shown in Figure 4.7 (b)), the pulse propagates at a group velocity of $\mathbf{v}_{g2} \approx 6.5$ km/s. In this case, a 1 μ s pulse that is about 300 m in vacuum is compressed to about 6.5 mm spatially, which fits well inside the 10 mm-long crystal. Therefore, if the pulse is sent to the crystal at an external voltage of 40 V and the external field is switched off just before it comes out, the pulse will be compressed. We can see this effect from Figure 4.12, where the black dashed trace is the reference of the input pulse and the blue trace

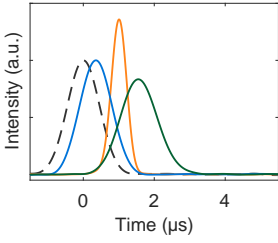


Figure 4.12. Pulse compression in time. A $1 \mu\text{s}$ -long pulse is sent into the crystal when $t = 0$ (dark gray dashed trace), transmitted from the crystal at $\tau_1 = 350\text{ns}$ when no external field is applied (blue trace) and at $\tau_2 = 1.54\mu\text{s}$ when 40 V is applied across the crystal (green trace). However, if the external voltage is 40 V when the pulse enters the crystal and $V = 0$ when the pulse exits the crystal, the pulse can be compressed in time (orange trace).

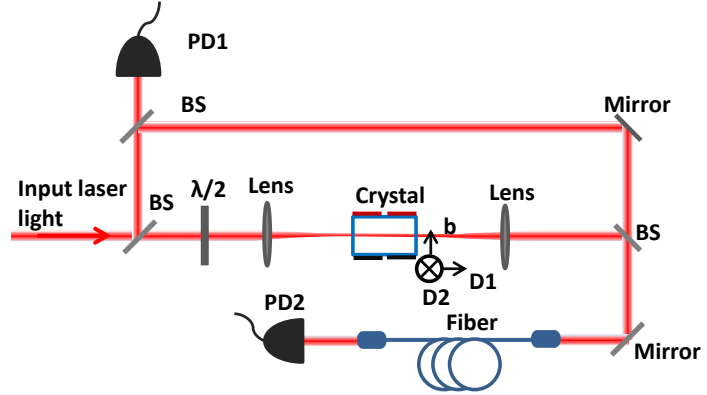


Figure 4.13. Experimental setup used to prepare the frequency shifter structure; the crystal has two sets of electrodes on its surfaces and the E field is along the b axis of the crystal.

is the output pulse when no external voltage is applied such that the pulse sees the structure shown in Figure 4.7 (a) inside the crystal. The green trace is when the pulse propagates at an external voltage of 40 V ; the spectral structure is shown as in Figure 4.7 (b). The orange trace, whose duration is greatly compressed, is when the external voltage is kept 40 V until the pulse is about to exit, then switched off. Therefore, the structure changed from Figure 4.7 (b) to Figure 4.7 (a) just before the pulse came out, compressing the pulse duration.

4.5 Frequency shifter

Since the slow light effect comes from the fact that the energy of the optical pulse is stored mainly inside the resonance centers via off-resonant excitation inside a slow light material, as was discussed in Section 4.2.1, if we change the frequency of the resonance centers while the light is still inside the material, we could in principle change the frequency of the light that comes out of the crystal. We will demonstrate this now.

4.5.1 Specially prepared structure

To shift the frequency of the light, it is crucial that all ions interacting with light off-resonantly have the same Stark coefficient. Optical pumping and the Stark effect were used to create a region in the frequency domain where only one such group of ions exist.

Figure 4.13 shows a sketch of part of the experimental setup. A laser beam was split into two parts, one focused into the crystal for preparation and later measurement, the other further split into two paths, one used as a reference beam to calibrate the intensity variation and the other as a local oscillator for frequency shift measurement. Both the experimental beam and the local oscillator were sent to a fiber; from the beating pattern of the two beams, one can analyze the frequency shift of the light that propagated through the crystal.

A sketch of how the absorption profile changed during the preparation process is shown in Figure 4.14. (a) shows that the ions were equally populated and absorption at all frequencies was the same at the beginning. An 18 MHz spectral pit was then created via optical pumping, as shown in (b). An external field was switched on; the resonant frequency of the two groups of ions Stark shifted to higher and lower frequency respectively, which split the spectral hole into two half holes, each half hole region containing ions with the same Stark coefficient, as shown in (c). At the end, optical pumping was utilized again to create a 1 MHz hole in one of the half holes. The final structure had a 1 MHz spectral hole surrounded by only one group of ions with the same Stark coefficient as shown in (d).

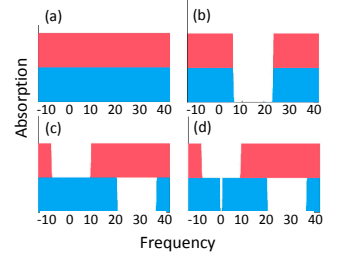


Figure 4.14. Step by step sketch of the absorption profile of the ions to create the frequency shifter. (a) before any hole burning, (b) A 16 MHz spectral hole was created, (c) After application of an external electric field, the red ions shift to lower frequency while the blue ions shift to higher frequency, and (d) a 1 MHz spectral hole was created at around 0 MHz. At the end, there is a 1 MHz spectral at 0 frequency with only the ions with the same Stark coefficient around it.

4.5.2 Frequency shift of the ions and the structure

A sketch of the frequency shifter structure created is shown in Figure 4.14 (d) as the structure around 0 MHz. To see the structure experimentally, a frequency chirped pulse with low amplitude was sent to the crystal after preparation, as shown as the black dashed trace in Figure 4.15. The αL at the absorption center of this crystal is estimated to be about 25; because of the high absorption of the ions, it is difficult to measure the αL exactly outside the frequency shifter structure.

Figure 4.15 (a) shows the spectral hole changes as the external voltage changes; the size of the frequency shift of the structures are proportional to the external voltages, just as it should be (see above).

4.5.3 Frequency shift of light

A 1 μ s-long Gaussian probe pulse originally centered at 0 MHz was sent through the crystal to measure the frequency shift of the light. Because of the slow light effect caused by the drastic dispersion in the spectral hole, it took the probe pulse 4 μ s to propagate through the crystal. To measure the frequency shift of the light, a square pulse with a frequency offset of 10 MHz relative to the probe pulse was sent out 4 μ s later as a local oscillator. Since the crystal is optically thick for the local oscillator, only the part that

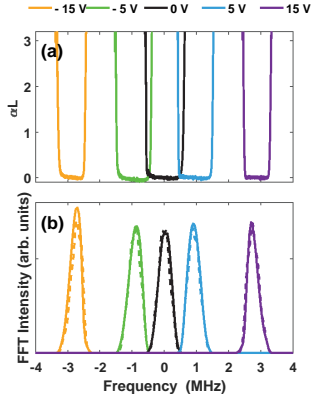


Figure 4.15. (a) Readout of the frequency shifter structure at different external voltages; the black dashed trace shows the original structure, and the others are the structures when different external voltages are applied. (b) The frequency of the light pulse out of the crystal at different external voltages when the incoming beam was centered at 0 MHz.

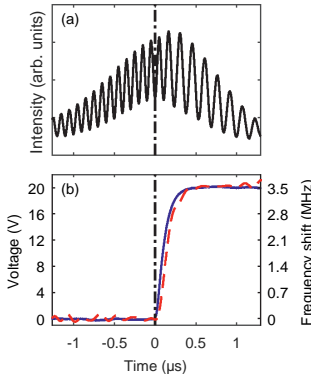


Figure 4.17. The beating pattern (a) and frequency of the probe pulse (b) changes when the external voltage changes.

bypassed the crystal reached the fiber and met the probe pulse at the detector. The frequency of the probe pulse can be mapped out from the beating pattern of the two pulses. Figure 4.15 (b) shows the frequency distribution of the light transmitted through the crystal at different electric fields; the solid traces show the experimental data, and the dashed traces show the simulated data from the modified Maxwell-Bloch (MB) simulator described in Section 4.5.4. They match quite well. Comparing Figure 4.15 (a) and (b), it is clear that the frequency of the light pulse follows the frequency shift of the ions, both of which are proportional to the electric field applied; this can be confirmed by the red trace in Figure 4.18.

4.5.4 Energy distribution in the ions

A modified version of the Maxwell-Bloch (MB) model was used to simulate the frequency shift process. The Stark effect was included in the MB model by shifting the resonance frequency of the ions at a certain time. Since there are two groups of ions with the same Stark coefficient but opposite signs, the simplest approach is to introduce two Bloch vectors (denoted \bar{r}^A and \bar{r}^B), where, at a particular time, τ_0 , the resonance frequency for \bar{r}^A and \bar{r}^B shifted by $+\Delta_s$ and $-\Delta_s$ respectively. More detailed information about the MB equation could be found in Paper III; the energy distribution of the pulse just before and after the application of the external electric field is shown in Figure 4.16 where the different colors show the amount of energy stored in the ions, which are normalized to the maximum energy stored inside the ions. Before the frequency shift, the spectral hole is centered around 0 MHz and most of the energy stored close to the hole edge and propagates forward, while after adding the external field, the center frequency of the ions moves to be around 3.8 MHz and the energy in the ions follows. Thus, the emitted light from the ions shifts its frequency as well.

4.5.5 Transient frequency shift

To see how the frequency of the light changes along with the external field, external voltage is applied when half the pulse propagates through the crystal while the other half remains outside. From Figure 4.17. The beating pattern for the second half of the pulse is clearly different from the first half; from the calculated instantaneous frequency in Figure 4.17, we see that the frequency of the light changes along with the external voltage with a delay of about 200 ns.

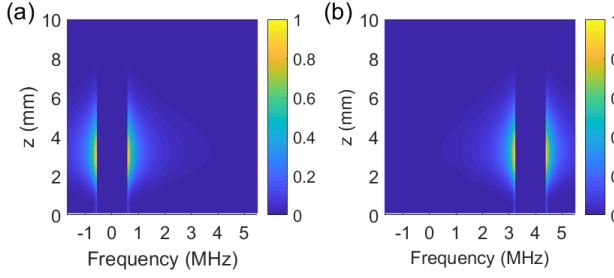


Figure 4.16. Energy distribution in the ions just before (a) and after (b) applying an electric field. The energy of the pulse is stored in the ions outside the 1 MHz transmission window, and the frequency shift of the ions shift the light frequency

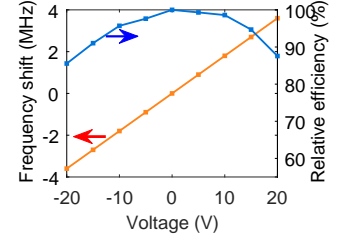


Figure 4.18. Frequency shift of the probe pulse and the relative efficiency of the frequency shift.

4.5.6 Efficiency

The relative efficiency of the frequency shift process is calculated by comparing the area of the transmitted pulse at different voltages with the area of the probe pulse when no external voltage is applied, i.e., $\eta_{rel} = \frac{\text{Energy}(V)}{\text{Energy}(V=0)}$, where $\text{Energy}(V)$ is the area of the transmitted pulse for a specific voltage (electric field), and $\text{Energy}(V = 0)$ is when no external field is applied. The signal is averaged 50 times to obtain a better signal to noise ratio. The blue trace of Figure 4.18 shows that the relative efficiency is more than 90% for a frequency shift less than ± 3 MHz. The efficiency drops when the frequency shift of the light becomes larger. This is mainly because of the narrowing of the spectral structure when a higher electric field is applied, as shown in Figure 4.15 (a). This narrowing of the spectral hole induces absorption of the pulse energy and reduces efficiency. The efficiency of the pulse propagated through a 1 MHz wide square hole is fundamentally limited by absorption of the Pr^{3+} ions, since they have a homogeneous linewidth of 1 kHz and induce absorption inside the spectral hole. However, this absorption in principle is quite low, 2 %. This means that the absolute efficiency of the frequency shift of the light can be quite high if the structure is fully optimized.

4.5.7 Higher frequency shift

This project demonstrated a maximum frequency shift of only about 7 MHz; however, it should be possible to extend the frequency shift to hundreds of gigahertz if a static E field is applied to separate the two groups of ions completely. Then we could do the hole burning and frequency shift in one group of ions; the frequency shift would be proportional to the added external field and

free of absorption from the other group of ions. The maximum shift is expected to be limited only by the breakdown voltage of the crystal, which is expected to be $\sim \text{MV/cm}$.

One unique feature of this frequency shifter is that it is controlled solely by the electric field as for the group velocity control; thus, it is especially suitable in weak light situations, for example, to shift the frequency of weak coherent light to match a particular quantum memory or to shift the spectra of the qubits for the readout process [63].

Another advantage of this frequency shifter is that it could work for scattered light if prepared properly and the acceptance angle could be as large as 2π . It has been shown that a band-pass filter prepared in the same material could work for light from multiple directions and the light could be transmitted and delayed if it matches the passband of the filter while not delayed but strongly attenuated if outside the passband and in the absorbing region [64, 65]. By adding an identical crystal immediately after the present one and rotating it around the light propagation axis by 90° relative to the first one, it could work for light with arbitrary polarization as well [66]. By using special anti-reflection coating techniques [67], the solid acceptance angle of such a device could be close to 2π ; once the light is inside the crystal, it is guided to the exit facet via total internal reflection and comes out from the opposite surface. This would be particularly useful in ultrasound optical tomography, assuming that light is iteratively sent to an ultrasound focus deep inside a scattering medium using phase conjugation mirrors [68]. However, since the light will be shifted by the ultrasound frequency each time it passes through the focus, one could argue that a frequency shifter, which works for randomly scattered light as demonstrated here, that is able to shift the light back to its original frequency will further improve the performance of such a scheme.

4.6 Summary and outlook

The strong dispersion caused by the engineering of the inhomogeneous absorption profile induces the slow light effect. Three phenomena related to this effect were investigated: cavity linewidth narrowing, group velocity control and the frequency shift of an optical pulse.

Because of the slow light effect, a 6 mm long cavity behaved like a 700 m long cavity. Five cavity modes were observed inside an 18 MHz transmission window at the center of the inhomogeneous absorption profile; cavity mode linewidth down to about 30 kHz was achieved in a 1 MHz spectral hole, while it was about 13 GHz without spectral hole burning; this makes the cavity Q value 1.6×10^{10} , which is almost comparable to the highest optical

cavity Q values demonstrated to date. It has quite a few applications, including boosting the Q value by inserting such a slow light material inside the cavity, generation of narrow bandwidth entanglement photon pairs for quantum information purposes, and use of such a slow light cavity instead of a conventional FP cavity as a reference cavity to stabilize the laser frequency. The quantum information group has a promising, ongoing project to use such a cavity to lock the laser frequency.

A group velocity change of a factor of 20 was achieved with the relative efficiency of more than 80% inside a spectral hole by tuning an external electric field. The same principle could be used to compress the time duration of an optical pulse. This tunable delay line might find its application as an alternative to quantum memories for some systems due to its high efficiency and tunable delay by using solely the electric field.

The frequency shift of about ± 4 MHz has been demonstrated, and the \sim GHz frequency shift has been proposed. The frequency shift is based on the fact that the energy of an optical pulse is stored mainly in the medium as atomic excitation when it propagates inside a slow light medium. The slower the group velocity, the larger the fraction of energy that is stored. For a group velocity less than 300 km/s, more than 99.9% of the pulse energy is stored in the medium. This makes high-efficiency frequency shifts possible. A frequency shift of the ions when the energy is stored in them results in the same frequency in the light emitted from the ions afterward. The frequency shift is proportional to the external electric fields. It is of particular interest to use this in a waveguide structure where the electrodes could be placed closely. Only a few tens of volts could shift the frequency of hundreds of MHz [69]

The last two applications have potential to work for scattered light, with random polarization and close to 2π incident angles. Besides that, since the group velocity and frequency shift were controlled only by an external electric field, it is particularly suitable for weak light fields, since no strong optical field is required for the application. Moreover, because it is a solid crystal-based system, it could also be integrated with other systems, which opens the possibility of on-chip applications.

QUANTUM MEMORIES

In classical communication and computation, we have bits as the carriers of information; a bit can be either 0 or 1, which could be the on or off signal of a transistor. Similarly, in the quantum world, we have quantum bits, “qubits”, carrying the information. The unique property of a qubit is that besides being in state 0 or 1 as the classic bits, it could be in state 0 and 1 simultaneously, which is called superposition; this makes quantum computers much more powerful than classical ones for certain problems. A qubit could be represented by a single photon (for example its two polarization) or a two-level quantum system of an ion.

A quantum memory is a device that could take in the quantum information, hold it in certain way and emit it after a certain desired time. Quantum memories could be used to store the intermediate computational results of a quantum computation and are an essential part of quantum repeaters, which are the key components in long-distance quantum communication.

The most common way of transmitting quantum information is to encode it onto a photon and send it through an optical fiber. However, due to absorption and scattering loss inside the fiber, the signal decreases exponentially as the distance increases. In classical communication, the communication distance could be increased by amplifying the signal in a repeater after propagating a certain distance and then sending it farther away. However, in the quantum world, there is no way of boosting a quantum superposition state to extend the communication distance, due to the no-cloning theorem [1]. Figure 5.1 shows the principle of how quantum repeaters are used to extend the communication distance. Each quantum repeater (also called a node, represented by the gray circles) contains an entangled photon pair generation source (the entangled photon pairs are denoted by $\bullet \circ$) and a multi-mode quantum memory device (denoted as green squares labeled QM). One

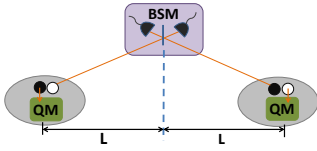


Figure 5.1. A schematic drawing of two adjacent nodes of a simplified quantum repeater; this way the communication length is extended (see text).

photon from each photon pair is sent towards the adjacent node via a quantum channel (most of the time, an optical fiber) while the other one is stored in quantum memory. Photons from the two nodes meet half way between the nodes and a Bell-state measurement (BSM) that consists of a beam splitter and two single-photon detectors is carried out. The pairwise entanglement between the photons and respective quantum memory is swapped to the entanglement between the two quantum memories in the two adjacent nodes. Thus, the entanglement is extended from L , the farthest distance a photon can travel before it is absorbed or scattered, to $2L$. The success of BSM heralds the establishment of entanglement between the two quantum memories, and the lifetime of the quantum memory has to be longer than the time it takes for the photons to travel halfway toward the adjacent node and for the heralding signal about the successful entanglement operation to travel back. The atomic excitation in the quantum memories can be converted into photons and sent to the next adjacent node to further extend the entanglement [70]. However, this is not as straightforward in reality; normally one needs to repeat the process many times before the entanglement between two nodes is successfully established. This requires even longer storage time for the quantum memory, especially for a long chain of quantum networks containing many quantum repeater nodes.

There are several factors to consider when building a quantum memory device that works in reality, such as fidelity [2], bandwidth, multi-mode capacity [71], efficiency, storage time and operational wavelength. Fidelity is a measure of how well the quantum state wavefunction of the re-emitted photon with the input photon. High bandwidth quantum memory with multi-mode capacity is necessary, since it improves the quantum information transmission rate. Long storage time makes long transmission distance possible and could hold the system longer for synchronization and the operation wavelength depends on the available transition of the material which is used for the quantum memory. Efficiency can be defined as the energy of the pulse that is re-emitted from the memory relative to the energy of the pulse that is sent into the memory. It also describes the probability that the stored information can be retrieved. High efficiency requires the photons being stored couples strongly with the quantum memories while the quantum memory devices interact only weakly with the rest of the universe. This could be done by using atoms/ions that interact only weakly with the surrounding but use a lot of them, which is called the ensemble approach.

In this chapter, I will start with some quantum memory protocols based on ensemble of ions with the focus on the quantum memory research conducted in Lund using atomic frequency comb (AFC). First, a theoretical background is given about the AFC

based quantum memory in Section 5.1.1 including how it works and the maximum efficiency to expect, as well as the main advantage of this technique compared with other methods. Section 5.2 introduces the impedance matched cavity and discusses why it could benefit quantum memory efficiency while Section 5.3 focusing on the two attempts towards high-efficiency quantum memory with the assistance of a low finesse asymmetric cavity. Section 5.4 talks about long storage time quantum memory project, where two highly efficient RF pulses were employed to compensate for the dephasing caused by the ground state hyperfine level inhomogeneous broadening.

5.1 Ensemble based quantum memories

A number of quantum memory protocols have been developed based on ensembles of ions, such as electromagnetic induced transparency (EIT) [72], controlled reversible inhomogeneous broadening (CRIB) [14, 73], gradient echo memory (GEM) [16, 74], atomic frequency comb (AFC) [17, 18] revival of silenced echo (ROSE) [12, 75], and rephased amplified spontaneous emission (RASE) [76, 77]. Among which, CRIB, GEM, AFC, ROSE and RASE are photon echo based quantum memories since they all store the incoming photon by letting it interact with the optical transition directly, and the collective rephasing of the atomic state causes the re-emission of the stored photon later. The AFC, CRIB and GEM techniques will be discussed briefly in this section with the focus on the AFC protocol.

5.1.1 AFC

The quantum memory research in this thesis was based on the atomic frequency comb (AFC) protocol proposed by Afzelus et al. in 2009 [18]. The AFC protocol is based on absorption of light by an ensemble of ions whose optical transition is inhomogeneously broadened. The ensemble approach is very useful in quantum memories due to the strong collective enhancement of the light-matter coupling [78].

The basic idea of AFC based quantum memories is shown in Figure 5.2, where $|g\rangle$ and $|s\rangle$ are ground state hyperfine or Zeeman states. The optical transition $|g\rangle - |e\rangle$ has a narrow homogeneous linewidth of γ_h and an inhomogeneous linewidth Γ_{in} while $\Gamma_{in} \gg \gamma_h$. This transition could be spectrally shaped such that the atomic density (as well as the absorption frequency) has a comb shape called atomic frequency comb. The comb can be characterized by the width of each peak δ , the separation between each tooth Δ and the finesse of the AFC, $F = \frac{\Delta}{\delta}$.

The atoms are initially in their ground state; when a single photon with FWHM of γ_p , which is wider than the separation

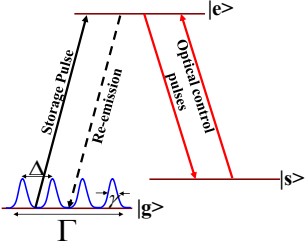


Figure 5.2. The principle of the AFC quantum memory scheme. An atomic comb structure with peak separation of Δ is prepared for the optical transition $|g\rangle - |e\rangle$. The incoming pulse with a frequency matching this transition would be absorbed, and re-emitted after time $t = \frac{1}{\Delta}$. A pair of optical control fields on $|e\rangle - |s\rangle$ could be applied to the coherently excited atoms before the rephasing at $t = \frac{1}{\Delta}$ happens and store the atomic excitation in the long-lived spin state $|s\rangle$. This enables a long storage time and on-demand readout of the input pulse.

of the AFC teeth while narrower than the FWHM of the AFC structure, is absorbed by the atoms at time $t = 0$, the photon is stored as a single excitation of one atom delocalized over all the atoms. The atomic state could be described by

$$|\psi\rangle = \sum_j c_j e^{i\delta_j t} e^{-ikz_j} |g_1 \dots e_j \dots g_N\rangle, \quad (5.1)$$

where $|g_j\rangle$, $|e_j\rangle$ and z_j represent the ground state, the excited state, the position of atom j , k is the wavenumber of the light field, and δ_j is the detuning of the atom relative to the laser frequency. The amplitude of this excitation c_j depends on the frequency and spatial position of the atom, as well as the amplitude of the incoming electric field.

The collective atomic state could also be understood as a coherent superposition of a large number of AFC atoms excited by a single photon; the light field is stored in a coherent superposition of the collective optical excitations delocalized over all the resonant atoms in the atomic frequency comb. Those atoms are initially in phase with each other after excitation. However, due to the frequency detuning, they dephase quickly. If we assume the AFC structure has very sharp peaks, the detuning δ_j could be written approximately as $\delta_j = m_j \Delta$, where m_j are integers. Then the collective state rephase after time $t = \frac{1}{\Delta}$, which leads to a coherent photon-echo [79] type re-emission. Figure 5.3, shows the phase evolution of the AFC peaks after a photon is absorbed until the re-emission of a photon.

However, the storage time of the photon is predetermined for the protocol described above; for the complete, long storage time and on-demand readout of the stored field, AFC scheme, the single collective excitation in $|e\rangle$ could be transferred to a long-lived ground state spin level $|s\rangle$ by a short optical control π pulse. This will temporarily “freeze” the phase evolution of the atoms. To retrieve the optical field, a second optical control π pulse could be sent in after time T_s and transfer the atomic excitation back to the excited state, $|e\rangle$. This resumes the phase evolution, and the total storage time would be extended to $T_s + \frac{1}{\Delta}$. Even though Δ is predetermined by the AFC structure, T_s could vary to fulfill the on-demand requirement to the quantum memory. T_s could be very long, limited solely by the coherence lifetime of the spin wave if the spin transition is only homogeneous broadened. If there is inhomogeneous broadening, the spin-echo technique such as RF rephasing pulses [80] or composite adiabatic pulses [81] could be used to extend the storage time.

If each peak has a certain optical depth of $d = \alpha L$, where α is the absorption coefficient of the material and L is the length of the material, the effective absorption depth for Gaussian shape AFC

peaks could be written as

$$d_{\text{eff}} = \frac{d}{F} \sqrt{\frac{\pi}{4 \ln 2}} \approx \frac{d}{F}, \quad (5.2)$$

It has been shown for an AFC based quantum memory with a forward readout configuration that the efficiency is limited to 54% due to re-absorption in the sample, while it can reach 100% with two counterpropagating control fields applied before re-emission of the echo [18]. The efficiency of an AFC-based quantum memory for the backward propagating mode could be written as [18]

$$\eta_{\text{AFC}} = (1 - e^{-\frac{d}{F}})^2 \eta_f, \quad (5.3)$$

where the first term depends on the coupling between the light and the atoms while the second term, $\eta_f = e^{-\frac{1}{F^2} \frac{\pi^2}{2 \ln(2)}}$, is the dephasing factor. As can be seen from this equation, a higher finesse would yield a smaller dephasing while sacrificing some absorption of the photon. Figure 5.4 shows the quantum memory efficiency for different AFC finesses at different optical depths. We could see that higher finesse is always better for a sufficiently high optical depth.

Even though all the equations and experiments were based on Gaussian type AFC peaks, it should be noted that a top hat type of AFC peaks would have better efficiency than a Gaussian type AFC peaks [82].

The main advantage of AFC-based quantum memory is the multimode capacity of the memory. The number of modes stored in the memory, N , using electromagnetically induced transparency (EIT) and off-resonant Raman-type memories scales as \sqrt{d} [83, 84] while controlled reversible inhomogeneous broadening (CRIB) scales slightly better since $N \sim d$ [84, 85], but it is eventually limited by the optical depth as well. However, in AFC, the multimode capacity is independent of optical depth, and multimode storage in AFC-based quantum memories has been demonstrated experimentally at the single photon level [17].

5.1.2 CRIB and GEM

As the name indicate, in the controlled reversible inhomogeneous broadening the dephasing caused by the inhomogeneous broadening is fully controlled and external electric field is used for this. The main procedure is shown in Figure 5.5 and described below.

- (i) Isolating one group of ions from the rest: remove all the absorbing ions within certain frequency interval and then burn back one group of ions with a certain transition frequency.

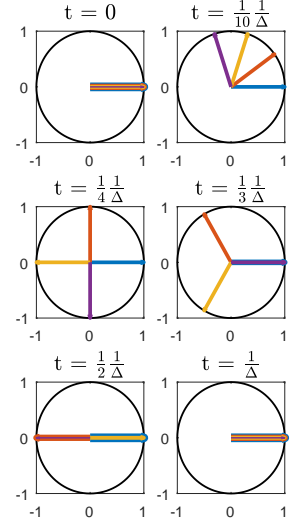


Figure 5.3. The phase evolution of four AFC peaks on the equator plane of the Bloch sphere from just been excited to the emission of the first echo.

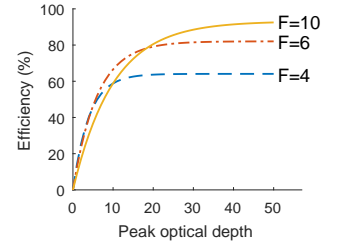


Figure 5.4. The efficiency of AFC-based quantum memory at different optical depths for different AFC finesses.

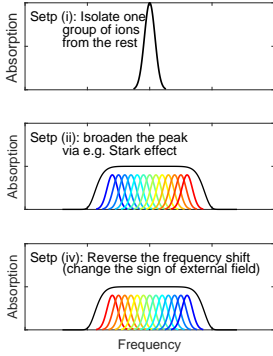


Figure 5.5. The absorption profiles in some step of the CRIB protocol.

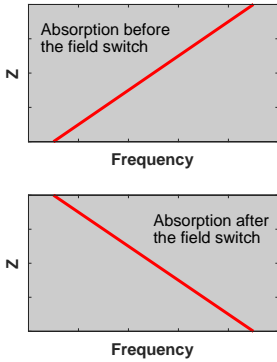


Figure 5.6. The longitudinal CRIB or GEM. The longitudinal CRIB or GEM, where different frequency components of the light is absorbed and emitted at different spacial location which eliminates the re-absorption.

- (ii) Apply a gradient external field, e.g. electric field. The resonance frequencies of the ions would shift relative to each other due to the linear Stark effect. The frequency shift is proportional to the strength of the electric fields the ions feel. In the end, the narrow absorption peak becomes much broader and it is ready for light storage now.
- (iii) Send in the light pulse to be stored at time $t = 0$, which creates the collective atomic coherence between the ground state and the excited state. The ions are in phase at the beginning, however they will start to accumulate different phase depending of their detuning due to the inhomogeneous broadening.
- (iv) After certain time $t = \tau$, the sign of the electric field is reversed, this will change the sign of the frequency shift, and the ions starts to rephase.
- (v) After the same time interval, at $t = 2\tau$, the ions will have the same phase again and emits the echo signal.

The efficiency of the CRIB protocol depends on the configuration of the external field. If the broadening is along the transverse direction, that is the direction perpendicular to the pulse propagation axis, the above mentioned procedure will result in an echo emitted in the forward direction. The time of the memory is limited by the coherence time in the excited state and the maximum efficiency is limited to 54% just like in the AFC case. Similar to the AFC protocol, the echo could be recalled in the backward direction with the help of two counterpropagating transfer pulses (that would transfer the coherence to another long lived ground state hyperfine level), the storage time could then be extended beyond the coherence time of the excited state and the efficiency could reach close to unity if the optical depth αL is high enough as given by

$$\eta = (1 - e^{-\alpha L})^2. \quad (5.4)$$

If the external electric field gradient is applied along the propagation direction of the pulse (as was proposed originally by Nilsson et al. [14]), such that different frequency component get absorbed at different position as shown in Figure 5.6, the re-absorption of the forward echo could be eliminated [74] and the efficiency could approach unity in both directions [86]. However, it should be noted that the echo recalled in the forward direction is associated with a frequency chirp [87]. This specific realization of CRIB is often referred to as gradient echo memory (GEM).

To date, the highest quantum memory efficiency is achieved in GEM, with 69% efficiency in a rare-earth-ion-doped crystal [16] and 87% efficiency in rubidium vapor [88].

5.2 Cavity enhanced quantum memory

It can be seen from Figure 5.4 that a high optical depth is required if one wants to obtain a high quantum memory efficiency. However, for some systems that are attractive otherwise, it might be very challenging to attain high optical depth, for example, the solid-state rare-earth-ion doped crystal. There are different ways to increase the optical depth of the quantum memory in order to improve efficiency, for example, use crystals with higher doping concentrations, increase the length of the crystal, and select ions that have higher oscillator strength. However, one can increase the doping concentration of the ions only to a certain level, beyond that, it only broaden the inhomogeneous linewidth instead of increase the optical depth [37]. A very long crystal is inconvenient and difficult to integrate with other quantum hardware. Furthermore, there are not many ions to choose from. and we would not want to exclude ions with very good coherence properties just because they have low oscillator strength.

One promising way to resolve this issue could be to enclose the crystal by an asymmetric cavity and work on the impedance matched condition. Impedance matching means that the transmission from the first mirror matches the loss inside the cavity (this loss comes from the absorption of the crystal and the second mirror transmission); in this case, there would not be any reflection from the cavity. If the second mirror is highly reflective (preferably 100% reflectivity) and the crystal absorption matches the transmission of the first mirror, nothing is transmitted through the cavity either. Thus, all energy would be absorbed by the crystal inside the cavity in this case.

5.2.1 Impedance matched cavity

Impedance matching was first used as a term in radio frequency electronics, where it refers to the condition that the reflected power from the load is minimum or the power transfer to the load is maximum. When used in an optical cavity, it means that the light reflected from the input mirror of a cavity is minimized by adjusting the reflectivity of the cavity mirrors, etc.

We will now consider a Fabry - P rot cavity composed of two mirrors, M_1 and M_2 , separated by L , with reflectivity R_1 and R_2 respectively, as shown in Figure 5.7. In order not to lose generality, the round-trip loss inside the cavity is set to be as $1 - R_2e^{2\alpha L}$. At the steady state, the circulating field just inside the input mirror of the cavity, E_{circ} , consists of two parts (see the black spot in Figure 5.7): the incoming field that transmitted through the input mirror $E_{\text{in}}t_1$ and the circulating field after one round trip (having passed through all the elements once inside the cavity and bounc-

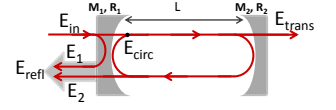


Figure 5.7. Impedance coupling of a Fabry - P rot cavity.

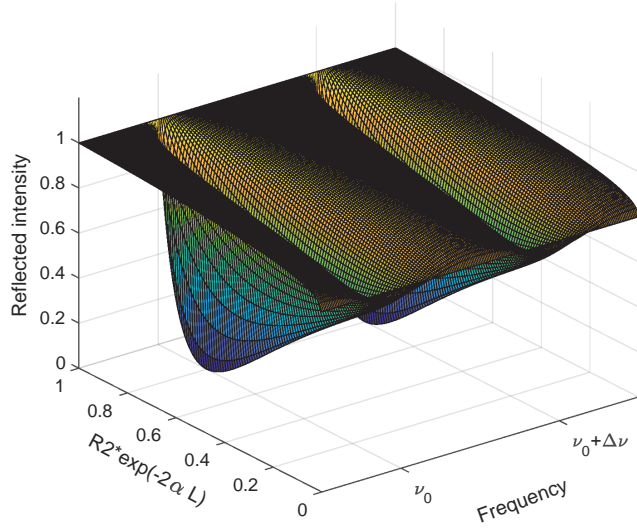


Figure 5.8. The reflected intensity as a function of the loss from the back mirror and the intracavity loss of a cavity and the frequency of the incoming light, normalized to the incoming intensity (see text).

ing through the two cavity mirrors) and returning to the same point, $E_{\text{circ}}e^{-2\alpha L - i\omega \frac{2L}{c}}$.

$$E_{\text{circ}} = E_{\text{circ}}r_2r_1e^{-2\alpha L - i\omega \frac{2L}{c}} + E_{\text{in}}t_1 \quad (5.5)$$

where $r_1 = \sqrt{R_1}$, $t_1 = \sqrt{1 - R_1}$ are the reflection and transmission coefficients for M_1 and r_2 and t_2 are the reflection and transmission coefficients for M_2 . From Equation (5.5), the circulating field inside the cavity and the transmitted field after the second mirror can be written as,

$$E_{\text{circ}} = \frac{E_{\text{in}}t_1}{1 - r_2r_1e^{-2\alpha L - i\omega \frac{2L}{c}}} \quad (5.6)$$

$$E_{\text{trans}} = E_{\text{circ}}t_2 \quad (5.7)$$

The reflected field, which consists of two parts, the directly reflected field from the front mirror $E_1 = -r_1E_{\text{in}}$ and the field leaking out from the circulating field inside the cavity $E_2 = E_{\text{circ}}t_1r_2e^{-2\alpha L - i\omega \frac{2L}{c}}$; the minus sign in E_1 represents the 180° phase shift of the reflected field relative to the incident field, since the field is reflected from a boundary with a higher refractive in-

dex. The reflected field can be expressed as,

$$E_{\text{refl}} = E_1 + E_2 \quad (5.8)$$

Depending on the reflected field, there could be three possible situations: under coupled, over coupled and impedance matched. Under coupling and over coupling are when the reflected field is dominated by the directly reflected field, E_1 , and the field that leaks out from the cavity, E_2 , respectively. Impedance matching is when the two fields E_1 and E_2 have the same amplitude, but the overall reflected field is zero since they have opposite phases and no power is reflected. They can be described by the following equations: $R_1 > R_2 e^{-2\alpha L}$, under coupled; $R_1 < R_2 e^{-2\alpha L}$, over coupled; and $R_1 = R_2 e^{-2\alpha L}$, impedance matched.

Figures 5.8 shows the reflected power as a function of the incoming light frequency and round-trip loss inside the cavity, including the back mirror transmittance and the absorption from the absorbing material inside a cavity when the front mirror reflectivity is $R_1 = 0.8$. ν_0 is the resonance frequency and $\Delta\nu = \frac{c}{2L}$ is the mode spacing of the cavity. Two special cases are shown in Figures 5.9 and 5.10, where Figure 5.9 shows the reflected intensity as a function of light frequency for an impedance matched cavity and Figure 5.10 shows the reflected intensity as a function of the round-trip loss inside the cavity, $1 - R_2 e^{-2\alpha L}$ when the light is on resonance with the cavity. We can see the reflected intensity goes to 0 only when the light is on resonance with the cavity and the cavity is impedance matched. Further, we note that if the reflectivity of the back mirror of the cavity is set to $R_2 = 1$ and we put one absorbing rare-earth-ion crystal inside the cavity and make sure that the round-trip absorption of the ions is matched with first mirror transmission, $1 - R_1 = 1 - e^{-2\alpha L}$, the cavity is still impedance matched. Since there is no reflection or transmission from the cavity, all incoming light would be absorbed by the ions. 100% energy transfer from the photon to the ions could be achieved; a weakly absorbing material inside an impedance matched cavity would behave like a highly absorbing material, which is required to obtain high quantum memory efficiency.

5.3 Quantum memory using asymmetric low finesse cavity

When the memory material is enclosed by an optical cavity and the impedance matched condition is fulfilled, quantum memory efficiency is theoretically predicted to be [89],

$$\eta = \left[\frac{2(\frac{d}{F})e^{-\frac{d}{F}}(1 - R_1)\sqrt{R_2}}{(1 - \sqrt{R_1 R_2}e^{-\frac{d}{F}})^2} \right]^2 \eta_f, \quad (5.9)$$

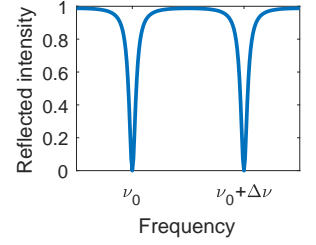


Figure 5.9. The reflected intensity as a function of the frequency of the incoming light for an impedance matched cavity, normalized to the incoming intensity.

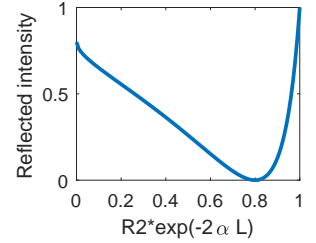


Figure 5.10. The reflected intensity as a function of the back mirror and intracavity loss of a cavity and the frequency of the incoming light, normalized to the incoming intensity.

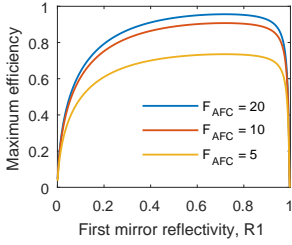


Figure 5.11. The maximum quantum memory efficiency at different first mirror reflectivities, R_1 , when ideal impedance match is achieved for all R_1 , as well as $R_2 = 0.998$ for finesse $F_{\text{AFC}} = 20$ (blue), $F_{\text{AFC}} = 10$ (red) and $F_{\text{AFC}} = 5$ (yellow) respectively.

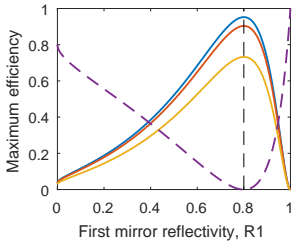


Figure 5.12. Maximum efficiency for quantum memory at different first mirror reflectivity when the effective absorption depth is set to $\tilde{d} = 0.11$ and $R_2 = 0.99997$ for finesse $F_{\text{AFC}} = 20$ (blue), $F_{\text{AFC}} = 10$ (red) and $F_{\text{AFC}} = 5$ (yellow) respectively. The dashed black trace shows the reflection from the cavity. Maximum efficiency is achieved when the impedance matching condition is fulfilled.

where η_f describes the reduction in efficiency due to the fact that the individual teeth of the frequency comb having finite width (AFC finesse not high enough), which leads to irreversible atomic dephasing. Figure 5.11 shows the maximum efficiency for quantum memory at different first mirror reflectivities, R_1 , assuming perfect impedance match, for different AFC finesse $F_{\text{AFC}} = 20$ (blue), $F_{\text{AFC}} = 10$ (red) and $F_{\text{AFC}} = 5$ (yellow) respectively, while R_2 is set to $R_2 = 0.997$ which is a realistic reflectivity attainable in practice. For an AFC finesse of $F = 10$, the maximum quantum memory efficiency is more than 90% for $R_1 = 0.58 \sim 0.83$.

In the case of high mirror reflectivities, for example, $\sqrt{R_1} \approx 1$ with $\epsilon \ll 1$, $R_2 = 1$, and when impedance matched, which is $e^{-2\frac{d}{F}} = R_1$. Then $e^{-2\frac{d}{F}} \approx 1 - 2\frac{d}{F} = R_1$ and $e^{-\frac{d}{F}} = |\ln(R_1)|$. We could rewrite Equation (5.9) as,

$$\eta \approx \sqrt{R_1} \eta_f \approx \eta_f. \quad (5.10)$$

From this, we could see that memory efficiency could theoretically reach unity given sufficiently high AFC finesse even without the counter-propagating control fields because of the constructive interference of the echo inside the cavity when it is impedance matched [23].

In the end, we decided to go for a crystal with reflectivity $R_1 = 0.80$ and $R_2 = 0.997$. In this case, we would need a single trip optical depth of $\tilde{d} = 0.11$ to obtain to the impedance matched condition. For this optical depth, the maximum efficiency of the quantum memory is a function of first mirror reflectivity and $R_2 = 0.997$ is shown in Figure 5.12 for different AFC finesse $F_{\text{AFC}} = 20$ (blue), $F_{\text{AFC}} = 10$ (red) and $F_{\text{AFC}} = 5$ (yellow), respectively. The dashed black trace shows the reflection. When $R_1 = 0.8$, the cavity is impedance matched and maximum efficiency is about 90.4% for $F_{\text{AFC}} = 10$.

In this thesis, the cavity assisted quantum memory experiment was conducted on two cavity crystals with different lengths, $L_1 = 2$ mm and $L_2 = 0.8$ mm, where the reflection coating was directly deposited on the two surfaces of the crystal with $R_1 = 0.8$ and $R_2 = 0.997$. The finesse of the two cavities can be calculated from

$$F_{\text{cav}} \approx \frac{\pi(R_1 R_2)^{\frac{1}{4}}}{1 - (R_1 R_2)^{\frac{1}{2}}} \quad (5.11)$$

disregarding absorption from the ions. The free spectral range are 42 GHz and 104 GHz for the 2 mm and 0.8 mm cavities respectively, calculated from

$$\Delta\nu_{\text{FSR}} = \frac{c}{2n_g L} = \frac{v_g}{2L}. \quad (5.12)$$

The full-width-at-half-maximum (FWHM) linewidth of the cavity mode would be calculated by

$$\delta\nu_c = \frac{\Delta\nu_{\text{FSR}}}{\mathcal{F}}. \quad (5.13)$$

This yields a cavity linewidth of ≈ 1.5 GHz and ≈ 3.7 GHz respectively for these two cavities.

However, $\text{Pr}^{3+}:\text{Y}_2\text{SiO}_5$ crystals have an inhomogeneous broadening of about 5 GHz (FWHM) around 606 nm at 2 K. This broadening is much smaller than the free spectral range of the cavity, and we have to be at cavity resonance with the correct absorption depth to fulfill the impedance matched condition, (as shown in Figure 5.8) which requires that the length of the cavities are tunable. Thus, the two surfaces of the cavity crystals are not completely parallel but have a small wedge such that the cavity length changes across the crystal. This ensures that the cavity mode could be tuned continuously to match the absorption of the ions for the impedance mating. However, to our surprise, the linewidth and free spectral range of the cavity narrow by about three orders of magnitude in the presence of a spectral pit, as discussed in Chapter 4. This is not detrimental to our experiment now but it posed an obstacle that we have to address if we want to create a long time on-demand quantum memory, which will be discussed further in Section 5.6

5.3.1 Experimental setup

Part of the experimental setup is shown in Figure 5.13 for impedance measurement of the cavity crystal and the quantum memory experiment. A frequency stabilized dye laser at 605.997 nm (in vacuum) was used as the light source. After passing two AOMs (not shown in the figure), the laser beam was split into two parts by a 50/50 beam splitter; one part was used as a reference beam to calibrate against the laser intensity variation and was measured by a photodiode (PD1), while the other part was focused by a lens with $f = 40$ cm into the cavity crystal to prepare the spectral structure and conduct the quantum memory experiment. 50% of the reflected light from the cavity crystal and the echo signal from the memory were directed to another photodiode (PD2). The polarization of the light was along the $D2$ axis of the crystal and propagated along the b axis of the crystal. The cavity crystal was immersed in liquid helium and cooled to 2.2 K.

5.3.2 2 mm cavity crystal quantum memory

Our first attempt for cavity assistant quantum memory used a 2 mm low finesse cylindrical cavity crystal, with reflection coating directly deposited onto both surfaces of the crystal, with $R_1 = 0.8$

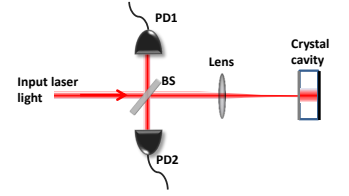


Figure 5.13. Sketch of the setup of the cavity assisted quantum memory. A laser beam was sent to a 50/50 beam splitter. One part of the beam was recorded by a photodiode (PD1) as a reference to calibrate the laser intensity fluctuation, and the other part was sent to the cavity crystal for the impedance matched quantum memory measurement. The reflection of the first surface of the cavity crystal and the AFC echo from the quantum memory propagate backward and 50% are reflected to another photodiode (PD2).

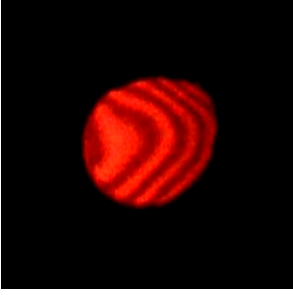


Figure 5.14. Interference pattern of the 2 mm cavity crystal before coating; photo by Mahmood Sabooni and Samuel Tornibue Kometa.

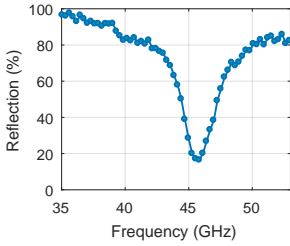


Figure 5.15. Impedance match measurement on the 2 mm cavity crystal. In the best case scenario, only 16% of the incoming light was directly reflected, which means that the best coupling efficiency we obtained was 84%.

and $R_2 = 0.997$ respectively. It is a 0.05% $\text{Pr}^{3+}:\text{Y}_2\text{SiO}_5$ crystal with a diameter of 12 mm. The cavity is along the b axis of the crystal, and the two surfaces of the crystal are not perfectly parallel to each other but with a small wedge. Figure 5.14 shows the interference pattern from the two surfaces of the 2 mm cavity crystal before coating; we could see that there are about 5 fringes at 606 nm, which means the difference in distance between the two surfaces is about $\Delta d = 4 \times \frac{\lambda}{2}/n$, and for $\lambda = 606$ nm and $n = 1.8$, $\Delta d = 670$ nm, corresponding to an angle of $\theta = 12$ arcseconds.

5.3.3 Impedance match

The impedance match of the cavity was first measured without the memory preparation, since it gave us an idea of the best coupling and set an upper bound for the memory efficiency we could expect. As we discussed before, to obtain the best impedance match, we have to tune the cavity length and scan the frequency at the same time.

An Attocube translation stage (Attocube system, ANC150) was used to translate the crystal such that the cavity length at the beam path could be changed. For each step, a weak Gaussian pulse with a duration of $\tau = 250$ ns and repetition rate of 10 Hz was sent to the cavity while the laser frequency slowly scanned over an 18 GHz frequency range for ~ 6 s. The reflection from the crystal on PD2 was calibrated by the reference on PD1. Then the signal area (PD2/PD1) was plotted against the frequency of the laser light. Figure 5.15 shows the best impedance match achieved where 84% of the input light was absorbed. Maximum coupling occurs about 45 GHz away from the inhomogeneous absorption center (at 605.977 nm in vacuum). We believe the 16% mismatch here is due mainly to the spatial mode mismatching because the curvature of the mirrors does not match that of the laser beam and the beam walk effect caused by the wedge between the two cavity mirrors.

5.3.4 Quantum memory

With the best impedance match in mind, a spectral pit (transmission window) and four AFC peaks were created inside the crystal, and quantum memory efficiency was measured and analyzed.

The optical transitions that of interest are shown in Figure 5.16. To perform the quantum memory experiment, a transmission window of about 18 MHz was first prepared within the inhomogeneous broadening, as in Ref. [59]. Due to strong dispersion over the spectral pit, the cavity linewidth narrowed from $\sim \text{GHz}$ to $\sim \text{MHz}$, as discussed in greater detail in Chapter 4. This makes the whole structure preparation process much more complicated and difficult to predict. After the transmission window was created, we

could see the cavity mode inside and adjust the crystal length to move the cavity mode to the place where we wanted the AFC peaks to be. Four AFC peaks were then created using complex hyperbolic secant pulses with chirp width of $f_{width} = 70$ kHz and temporal width of $t_{FWHM} = 16.8$ μ s (more information about the complex hyperbolic secant pulse can be found in Ref. [90]). Ions were pumped from $|1/2g\rangle$ to $|5/2e\rangle$; from $|5/2e\rangle$, they would have the highest probability of falling down to $|5/2g\rangle$ due to the high branching ratio for this transition.

The same pulse was repeated ~ 50 times with a waiting time of 500 μ s, creating one AFC peak. The whole process was then repeated 3 times but with the center frequency of the pulses changed consecutively by $\Delta = 0.9$ MHz to create other AFC peaks. Some 'clean wrong' pulses were employed afterwards to remove the extra ions in between the AFC peaks, which made the peaks narrower and yielded lower background absorption. At the end, four AFC peaks with finesses of about $F \approx 9$ (estimated) were created and the cavity mode was centered in the AFC peak structure.

The AFC structure consisted only of ions on $|5/2g\rangle$, and the optical depth of the peak could be as high as the αL , which is the optical depth before the structure preparation in the ideal case if all excited states are included. However, only the ions with transition $|5/2g\rangle - |5/2e\rangle$ were included, the maximum peak optical depth would be $0.93\alpha L$ since the branching ratio was 0.93 for this transition (see Table 3.1). The effective absorption depth for the AFC peaks was more than $0.93/F \approx 0.1$ times lower than without AFC preparation (assuming an AFC finesse of 10), which makes the impedance matching condition fulfilled at a frequency closer to the inhomogeneous line center after the AFC preparation than in Figure 5.15.

A weak Gaussian pulse with a duration of $\tau = 250$ ns matches the FWHM width of the AFC structure was sent to the crystal at $t = 0$, and after $t_s = \frac{1}{\Delta} = 1.1$ μ s the retrieved echo pulse was detected by PD2, as shown in Figure 5.17. To measure memory efficiency, the crystal was flipped 180° such that the second mirror with $R_2 = 0.997$ was facing the incoming Gaussian pulse and reflected it back to PD2 directly (the reflection is about 95% when on resonance and about 100% when off resonant). By comparing the pulse area of the echo and the directly reflected pulse after being calibrated by the reference detector PD1, the first echo efficiency is calculated to be about 56% while the efficiency for the same crystal under the same condition without cavity was estimated to be less than 1%.

Besides the first echo, we can see there are second and third echoes with combined efficiency of about 5 %. They are due to an inefficient rephasing process and could be reduced with a higher AFC finesse. The efficiency drop caused by the dephasing of the AFC structure is about 9% (for $F_{AFC} = 9$), and 24% of the incom-

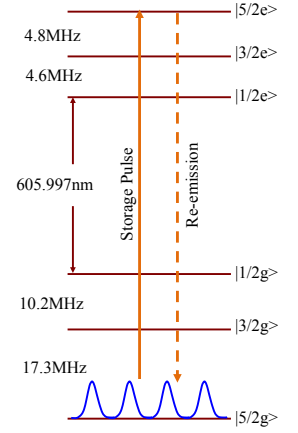


Figure 5.16. Hyperfine splitting of the ground state and excited state of the $^3H_4 \rightarrow ^1D_2$ transition of site 1 in $Pr^{3+}:Y_2SiO_5$. The AFC peaks were created on the $|5/2g\rangle$ state, and the storage pulse and echo coupled the states of $|5/2g\rangle - |5/2e\rangle$.

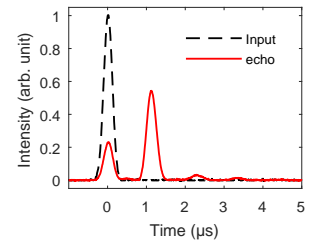


Figure 5.17. Quantum memory signal from the 2 mm cavity, Black dashed line, the input signal to the cavity to be stored; the red solid trace, the signal on the reflected detector (PD2). The first red peak is the direct reflected light while the rest of the peaks are the echoes. The efficiency of the first echo is estimated to be 56%.

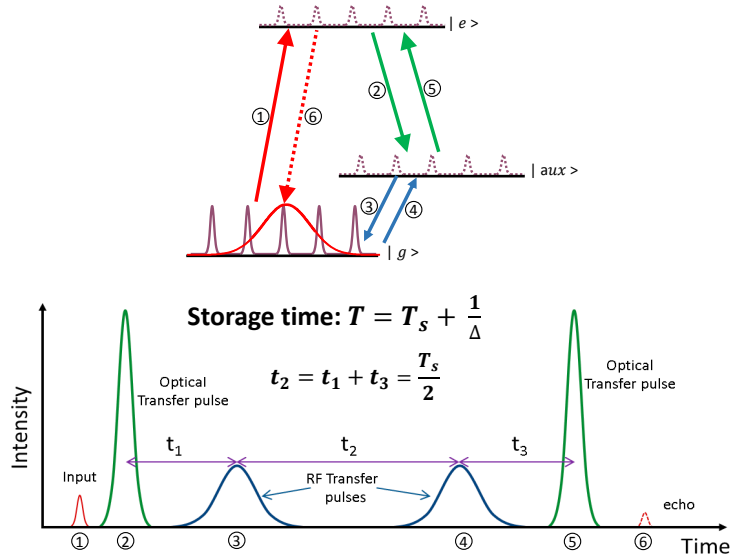


Figure 5.18. Long time, on demand quantum memory using AFC protocol. Upper part: the levels involved in the spin storage process. Lower part: the pulse sequence for the light storage.

ing light is not absorbed by the crystal due to the spatial mismatch; possibly the impedance matching condition is not fulfilled as well. About 3% of the loss is due to back mirror reflectivity not being 100% and the remaining 3% could be caused by some other losses (for example, background absorption) inside the cavity crystal.

5.4 Long time on demand quantum memories

As we discussed before, the storage time of the two-level AFC quantum memory is predetermined, but it could be made much longer and on-demand by using two optical control pulses to transfer the state to and back from an auxiliary spin state, which is referred as to three-level quantum memory or spin-wave storage. The pulse sequence and the energy levels involved for the spin wave storage are shown in Figure 5.18. After the preparation of the AFC structure, the storage photon is sent in, puts the ions to a superposition state between $|g\rangle$ and $|e\rangle$ just as in the two level case. Before the echo comes, one bright optical π pulse (the first green pulse) transfers all the ion in the excited state ($|e\rangle$) to another auxiliary state ($|aux\rangle$, which could be a ground state hyperfine level in the rare-earth ions). The phase evolution of the

excited state will then be ‘frozen’ until another bright optical π pulse (the second green pulse) transfers everything back, then the phase evolution continues. The total storage time will be $T_s + \frac{1}{\Delta}$, where T_s is the time separation of the two optical π pulse. In this case, the memory efficiency is limited by the decoherence and dephasing in the hyperfine state could be extended by a pair of RF rephasing pulses (blue ones), and time separation of the two RF pulses has to be the same as the sum of the time separation of the first optical π pulse and the first RF pulse and the second RF pulse to the second optical π pulse. Furthermore, Fraval et al. show that the spin coherence time can be extended to 82 ms by applying a specific magnetic field [91] and that using dynamic decoupling methods can further extend the coherence time to 30 s [29]. It seems quite promising to realize a quantum memory with a long storage time.

In this section, I will discuss the work we did on the long storage time quantum memory. We used a 1 mm long $\text{Pr}^{3+}:\text{Y}_2\text{SiO}_5$ crystal to do the spin wave storage and applied two RF refocusing pulse to increase the spin coherence time. The effect of the residual Earth magnetic field was observed and compensated for.

For this experiment, 10 AFC peaks with separation of $\Delta = 200$ kHz and $\delta \approx 80$ kHz were created in the $|3/2g\rangle$ state after the pit creation. The black trace in Figure 5.23 (most of it overlapping with the red trace) shows the original AFC structure. After the creation of the AFC peaks, a Gaussian pulse with $t_{FWHM} = 500$ ns was sent in for storage. Two optical control pulses were then employed to transfer the atomic excitation to and from a spin state with a time separation of T_{sw} . Since the structure we wanted to transfer was as wide as 2 MHz, two “sechscan” (complex hyperbolic secant scan) pulses with a frequency width of 2.6 MHz, duration of 2 μs and $t_{FWHM} = 500$ ns were used for optical transfer. The efficiency of the echo signal was measured as a function of T_{sep} , as shown in Figure 5.19

The solid squares were the data measured experimentally; it is a bit surprising that the first few data points for $T_{sw} < 12$ μs behaved differently than we expected and it is not clear why. We tried to fit the data for $T_{sw} > 12$ μs with a Gaussian shape inhomogeneous broadening, using the spin dephasing given by [92]

$$\eta_{sw}(T_{sw}) = e^{-\gamma_{spin}^2 T_{sw}^2 \pi^2 / 2 \ln 2}, \quad (5.14)$$

and we obtained a linewidth of 16.2 kHz, which is narrower than the literature value of 23 kHz - 30 kHz reported in Ref. [35, 93]. This could be due to the property variations in different crystals. The three-level efficiency at $T_{sw} = 0$ μs was extrapolated to be $\eta_{sw}(0) = 2.75\%$, while the two-level efficiency measured to be about 4%. This yielded an efficiency of about 83% for each optical control pulse, which is not as high as the group had demonstrated

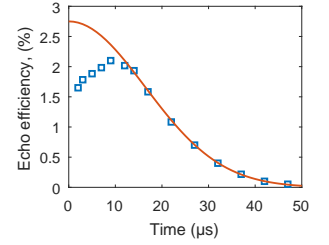


Figure 5.19. Echo efficiency when changing the time separation of the two optical control pulses (the two green pluses in Figure 5.18; no RF pulse in this case). The square data are experimental data, while the solid line is the fitted data with the spin state linewidth $\gamma = 16.23$ kHz.

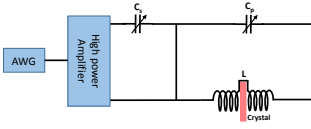


Figure 5.20. The circuit designed to generate the RF pulses. The crystal is placed in the middle of the coils, and adjustable capacitors are in parallel and series with the coils to fine tune the resonance frequency.

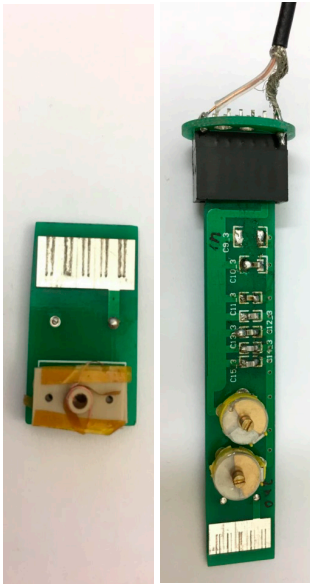


Figure 5.21. A photo of the final circuits used for this experiment. The crystal and coils are mounted on the small circuit board, inserted in the sample chamber and cooled down to 2 K, while all the capacitors are outside the cryostat to fine tune the resonance frequency since it shifts after cooling down.

before [22]. However, we have to consider that the frequency width of the AFC structures was 2 MHz, and the main reason for the low transfer efficiency was insufficient laser power for the transfer pulse since we could not increase the time duration of the pulse. One might obtain a higher transfer efficiency if a pinhole were added into the light path to look only at the center of the focus inside the crystal where the intensity is higher and more homogeneous. Thus, this is not a fundamental limit and one could do better with a more powerful laser.

The exponential decay of the quantum memory efficiency is due to the inhomogeneous broadening of the hyperfine state, which is estimated to be 16.2 kHz, as discussed above. To compensate for this dephasing, one could apply two RF pulses tuned to be resonant with the transition between the two hyperfine states to rephase the ions. The RF magnetic field could be generated by a current that runs through a coil wound around the sample, as shown in Figure 5.20. An alternating current through a coil generates an RF field perpendicular to the static magnetic field.

An LC circuit was designed by former PhD students in the group with coils around the crystal and capacitors, both in parallel and series with it, as shown in Figure 5.20. A photo of the circuits used for the experiment can be seen in Figure 5.21. The coils were made by 4 turns of wires from each side of the crystal (see Figure 5.20). The diameter of the opening for light propagation is about 2 mm, as shown in the left photo in Figure 5.21. A circuit simulation program (quite universal circuit simulation, QUCS) was used to choose the capacitance and inductance to make sure the resonance frequency of the circuit was around 10.2 MHz. After the circuit had been made, it was tested at room temperature to evaluate its resonance frequency and Q value. A typical waveform reflected from the circuit is shown in Figure 5.22. The smallest reflection we obtained was about 4% around 10.2 MHz, which means the energy transfer from the source to the load was about 96% and the linewidth of the resonance was about 0.5 MHz, which is enough since the frequency width we would like to address is about 26 kHz. The Q value of the circuit was about $Q = \frac{f_0}{\Delta f} = \frac{10.2\text{MHz}}{0.5\text{MHz}} \approx 20$.

The first version of the circuit was designed to have the crystal, the coils and the circuit on the same circuit board. However, when we put the crystal together with the circuit down to the sample chamber and cooled them to 2 K, the capacity and inductance changed slightly such that the resonance frequency altered as well. To this end, the circuit was split into two parts, where the coils and the crystal were on one circuit board and sent down to the cryostat, while all the capacitors were connected outside the sample chamber via a feedthrough. In this way, we could fine tune the resonance frequency back to 10.17 MHz by tuning the two adjustable capacitors.

The RF pulses used here were sechyp pulses with a center fre-

quency at 10.17 MHz and a frequency width of 350 kHz. The time duration was 60 μs , while the FWHM was 15 μs . To make sure the pulse area was correct, we read out the structure after applying one and two RF pulses and compared the structure with the original AFC structure. We changed the amplitude of the RF pulses until the AFC structure after two RF pulses looked the same as the original one, which means the RF pulses applied would correspond to π pulses.

Figure 5.23 shows the readout of the structure when no RF (Two RF, channel off), one RF (One RF, channel on), and two RF (Two RF, channel on) pulses were applied. Ten AFC peaks was originally created on the $|3/2g\rangle$ state, which is shown as the black trace; when one RF pulse was applied, the AFC structures were transferred from $|3/2g\rangle$ to the $|1/2g\rangle$ state. However, since RF pulses are not selective, everything is swapped at $|3/2g\rangle$ to $|1/2g\rangle$ and vice versa. Thus, all the AFC peaks should be transferred to $|1/2g\rangle$; when we read out the structure, we were expecting to see three AFC comb structures from the $|1/2g\rangle$ state, corresponding to $|1/2g\rangle - |1/2e\rangle$, $|1/2g\rangle - |3/2e\rangle$ and $|1/2g\rangle - |5/2e\rangle$. From the blue trace in Figure 5.23, we could clearly see the $|1/2g\rangle - |3/2e\rangle$ and $|1/2g\rangle - |5/2e\rangle$ transition at around 5 and 10 MHz, while the $|1/2g\rangle - |1/2e\rangle$ transition was buried inside other classes of ions and difficult to resolve (the αL was too high and the transmission through the crystal was too low compared with the noise level, so it is not shown in the data). If another RF pulses was applied afterwards, the AFC combs again transferred back to its original state, as shown by the red trace in the figure, almost identical to the black trace. By comparing the area of the AFC peaks at $|3/2g\rangle - |1/2e\rangle$ around 10 MHz, one RF pulse efficiency is estimated to be about 99.7%.

The full spin-wave storage with two RF pulses to compensate for the dephasing of the spin states was carried out afterward. The storage time was extended much longer after we applied the RF repulsing pulse. However, to our surprise, there were oscillations in the echo efficiency, as shown in the blue trace in Figure 5.24. Similar oscillation has been observed before [80], and it turns out that it was due to the interference caused by the splitting of the hyperfine level by the Earth's magnetic field. That field was around 50.20 μT , with a declination of $3^\circ 6' 16''$ and inclination of $70^\circ 1' 19''$ at Malmö, Sweden, in January 2013 (the vertical component, the north component and the east component were 47.18 μT , 17.13 μT and 0.93 μT respectively).

To compensate for the Earth's magnetic field, we could use Helmholtz coils, which are basically two identical circular solenoids with radiuses R that are placed symmetrically along a common axis with a separation of $d = R$. For a group of Helmholtz coils,

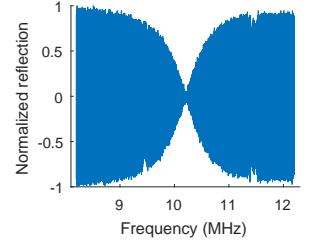


Figure 5.22. The reflected waveform when the input signal to the RF circuit scans from 8.3 to 12.2 MHz. The circuit has a resonance frequency at 10.2 MHz, and the Q value for this circuit is about 20.

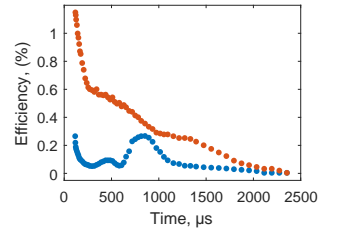


Figure 5.24. Efficiency of the echo before (blue) and after (orange) compensation for the Earth's magnetic field.

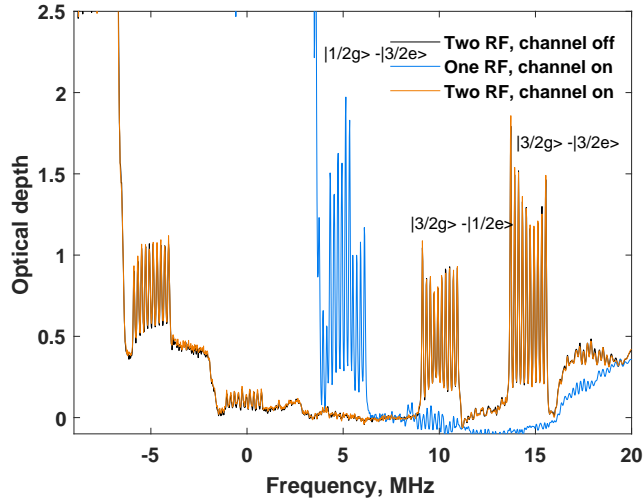


Figure 5.23. Readout of the AFC structure before and after applying one and two RF transfer pulses, showing that the RF pulses were π pulses. By comparing the AFC peaks area before and after two RF transfer pulses, the efficiency of one RF pulse was estimated to be about 99.7%.

the field at their midpoint can be calculated by

$$B = \left(\frac{4}{5}\right)^{\frac{3}{2}} \frac{\mu_0 n I}{R}, \quad (5.15)$$

where $\mu_0 = 4\pi \times 10^{-7} \text{ T} \cdot \text{m/A}$ is the permeability constant, n is the number of turns in one coil and I is the current that runs through the coil. We made two pairs of Helmholtz coils along the z-axis (vertical direction) and the x-axis (light propagation direction), with $n = 10$, $R \approx 0.17 \text{ m}$. The light propagation direction was about 40° to the horizontal component of the Earth's magnetic field. Based on an approximation, we would need a current of $I_z = 0.89 \text{ A}$ and $I_x = 0.32 \text{ A}$ to compensate for the Earth's magnetic field on these two axes.

The echo efficiency after compensating for the biggest of the Earth's magnetic field is shown as the orange trace in Figure 5.24; it seems that some magnetic field are still left, which is not surprising since there is one component along the y-axis that we didn't compensate for and the currents we applied on the other two axes were not precisely measured.

Even though there were remaining issues with the residual magnetic field, the primary goal of this experiment, to test and optimize the RF rephasing pulses, has been achieved successfully. Due

to the tight lab schedule, we have to switch to other experiments and maybe come back to this in a later time (in Paper VI we developed a method to compensate for the Earth's magnetic field in real time for all three axes, which was quite convenient). Our next step was to combine the cavity quantum memory with the spin wave storage to get high efficiency and on demand readout.

5.5 Quantum memories in a 0.8 mm cavity

After demonstrating the cavity enhanced quantum memory in Section 5.3.2, as well as the possibility of the on-demand long storage time in another crystal in Section 5.4, we decided to go one step further, combine these two techniques and do a spin wave storage in a cavity crystal. In this section, I will discuss the attempt to reach higher quantum memory efficiency, thoughts about doing a spin wave storage in a cavity and associated challenges.

As we could see from Figure 5.17 the quantum memory data of the 2 mm cavity crystal, the major loss of energy (about 24%) never got into the crystal; this could have two causes. First, spatial mismatch with the cavity because the curvature of the cavity mirrors does not match the wavefront of the light. This is to be expected since the cavity has two flat surfaces, which do not match the curvature of the focused laser beam, and the surfaces are not parallel but at an angle of $\theta = 12$ arcseconds, which would cause beam walk when laser field bouncing between the mirrors. Second, absorption of the ions still does not match the mirror reflectivity, which is the requirement for fulfilling the impedance matched condition. To further improve efficiency, we would need a better cavity and make sure to work at the impedance matched condition.

To overcome both of these two issues at the same time, we would need to have a perfect cavity with two mirrors at a certain curvature to support a stable Gaussian and a continuously adjustable length. This is not easy to achieve. Besides, we would also like to perform an on-demand quantum memory experiment on this new crystal and apply RF rephasing π pulses to compensate for the hyperfine state dephasing, as we did in Section 5.4; this would require a thin crystal in order to have a sufficient and homogeneous RF field inside the crystal.

In the end, we decided to go for a crystal of $10\text{ mm} \times 10\text{ mm} \times 0.8\text{ mm}$ with the same reflectivity as the 2 mm one and ideally with the two surfaces polished to a wedge of $\theta = 5$ arcseconds, which means the thickness change over the whole crystal is about 250 nm, corresponding to a 450 nm optical length. This way we would be able to change more than one cavity mode if we scan across the crystal (to make sure that we have the cavity mode covering the AFC peaks as well as the storage pulse).

A special crystal holder was designed to conduct the on-demand

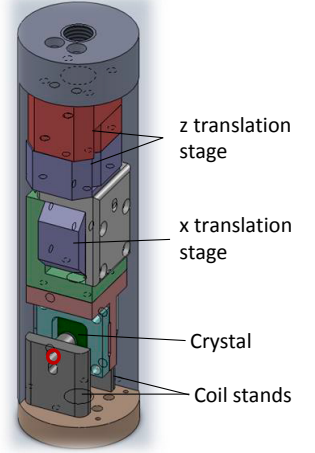


Figure 5.25. The holder designed for the 0.8 mm cavity crystal with the ability to carry out three level spin storage and compensate for the dephasing of the spin levels. It is capable of scanning the crystal both vertically and horizontally using two Attocubes (along the z and x axes).

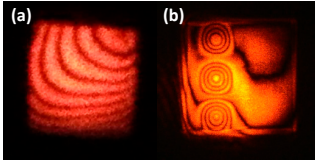


Figure 5.26. Interference pattern from the 0.8 mm crystal before (a) and after polish (b).

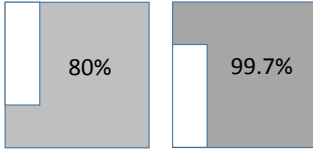


Figure 5.27. The coating on the two surfaces of the 0.8 mm cavity crystal. Top view facing an 80% reflection coated surface.

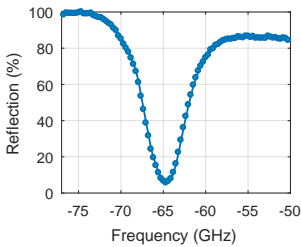


Figure 5.28. Impedance match measurement on the 0.8 mm cavity crystal. The reflection signal goes down to 5%, which means the coupling efficiency is 95%.

quantum memory experiment on the crystal shown in Figure 5.25. With this design, it was possible to scan the whole cavity to get to the impedance match condition. The crystal is shown as the dark green part and mounted on two Attocube translation stages: one used to scan the crystal in a vertical direction (to vary the crystal length), and the other to scan the crystal horizontally to move the crystal sideways and enable us to work with either the wedge part or the microcavity part. The upper part of the holder, contains the Attocubes and the crystal, hangs from the top, while the lower part, consist two dark gray stands before and after the crystal is used to support the coils to generate the RF field, sits on the bottom plate of the holder. The laser beam propagates through the small hole marked as a red circle. This arrangement makes it possible to have the coils fixed while adjusting the laser beam and scanning the crystal independently.

The crystal, ordered from Scientific Materials Corporation, had a wedge of about 25 arcseconds initially, which was way too much for our purposes. It was sent to LightMachinery for a better polish. Since the crystal was big and we were aware that the coupling to the wedged part would never be perfect, we decided to make three microcavities, one surface is flat and the other surface with a radius of curvature of $R \approx 0.7$ mm, which corresponds to a beam radius of about $50 \mu\text{m}$. These three microcavities have slightly different cavity lengths ($l, l + 70\text{nm}$ and $l + 140\text{nm}$). It is not guaranteed that we could obtain perfect impedance match since the cavity length is fixed. Although it cannot be changed continuously, these three microcavities provide at least an opportunity to investigate perfect spatial light coupling and possible impedance match at the same time. Figure 5.26 shows the interference pattern from the two surfaces of the 0.8 mm crystal before (a) and after (b) polish. We can see that the thickness difference across the crystal is much smaller after polish and three microcavities are on the left side of the crystal, as can be seen from Figure 5.26 (b).

The crystal was then sent to Optida for coating; the reflectivities are 80 % and 99.8 % for the front and back surfaces respectively. The coating was designed such that there are three parts (either the front surface, rear surface or neither surface is coated) close to one edge of the crystal, the rest of the crystal are fully coated. This design makes it possible to investigate the coating properties from on each surface and the properties of the bare crystal.

The first attempt focused on testing the impedance match of the cavity, as was done for the 2 mm cavity crystal. It turned out that we could reach 95% of cavity coupling even at the wedged part, as shown in Figure 5.28. The optimum impedance match was found at about 65 GHz from the inhomogeneous absorption center.

A spectral pit and four AFC peaks were prepared with similar

parameters as used for the 2 mm cavity crystal. Figure 5.29 shows the AFC structure prepared on the $|5/2g\rangle$ state of the crystal in the region where no coating is on either side of the crystal surfaces. We have $\Delta = 0.9$ MHz and $\delta \approx 90$ kHz (see Figure 5.2), which yields an AFC finesse of $F_{\text{AFC}} \approx 10$. A Gaussian pulse with $t_{\text{FWHM}} = 250$ ns and frequency match $|5/2g\rangle - |5/2e\rangle$ was sent to the cavity; the direct reflection and the echo after $t = \frac{1}{\Delta} = 1.1$ μs was observed in the reflected detector, as shown in Figure 5.30. Comparing it with the echo we obtained for the 2 mm cavity crystal in Figure 5.17, it is obvious that the ratio between the echo and the directly reflected light is much higher for this cavity (3.38 VS 2.45). However, the estimated memory efficiency was only around 40-50% in this crystal, which means that some energy coupled into the cavity was not emitted back via echo but lost somewhere.

A great deal of effort was devoted to finding out why we did not obtain higher efficiency while the echo was obviously much higher than the reflected input light. We suspect some loss mechanisms were in the cavity apart from absorption of the Pr^{3+} ions. Thus, we tune the laser to around 615 nm, which is 10 nm from the inhomogeneous absorption, such that there should not be any absorption from the Pr^{3+} ions at 2 K and the bulk loss of host crystal is not expected to be higher than $7 \times 10^{-4} \text{cm}^{-1}$ [94].

Since we achieved a decent quantum memory efficiency in the 2 mm cavity crystal but failed in this 0.8 mm cavity crystal, we started to investigate the extra polishing process only for this 0.8 mm crystal. It was polished by aluminum oxide particles about 50 nm in size using the fluid jet polishing technique; according to the technician, the polishing process may leave some residue in the material. The surface roughness is normally about 1 nm for this method; however, it depends on the hardness of the crystal and how much material needs to be removed. We had the technician from LightMachinery measure the surface roughness with their white light ZYGO (a white light interferometer system for surface characterization) and it turned out that the RMS surface roughness was about 3 nm with quite a few pit and dirt particles on the surfaces, could be under, inside or on top of the coating. A typical image from the measurement is shown in Figure 5.32 (a) and the surface height variation across the middle line in the image is shown in (b). The surface RMS roughness is about 3 nm; the black dots are big dirt particles that were removed.

The total integrated scatter (TIS) from a surface with RMS roughness d for incoming light wavelength λ could be calculated from the following equation [95],

$$\text{TIS} = 1 - e^{-\left(\frac{4\pi d}{\lambda}\right)^2}. \quad (5.16)$$

Given an RMS surface roughness of about $d = 3$ nm for $\lambda = 606$ nm light, the total integrated scattering is 0.385% on each surface

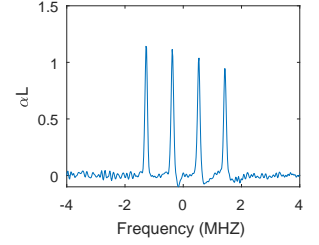


Figure 5.29. AFC structure of the 0.8 mm crystal when running at the transparent part with the same parameters as used with cavity.

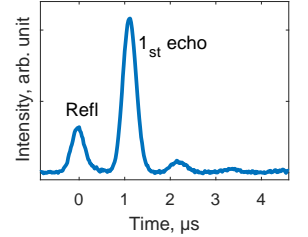


Figure 5.30. Signal on the photodetector 2 (PD2). The first peak is the directly reflected part of the input light to be stored, while the second one is the echo from the AFC memory. The ratio between the first echo and the direct reflection is 3.38, which is much better than what we obtained for the 2 mm cavity crystal.

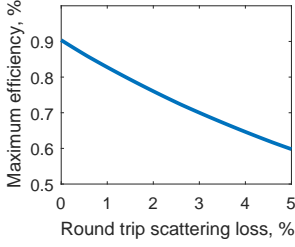


Figure 5.31. Maximum AFC quantum memory efficiency in an impedance matched cavity with (scattering) loss on the surfaces.

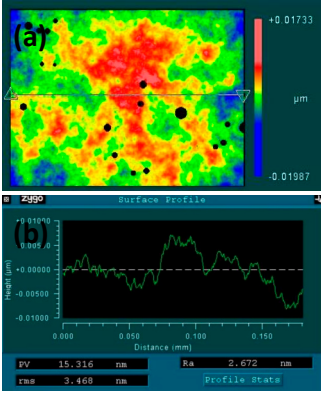


Figure 5.32. The surface roughness measurement data from LightMachinery. (a) shows the image of one part of the crystal surfaces; the black dots are big (dirt) particles that were removed from the data. (b) shows the height variation of the middle line across the image. The RMS surface roughness is about 3 nm on this crystal.

of the cavity, which makes the intra-cavity round-trip loss about 0.77%.

We modified Equation (5.9) to include a round-trip scattering loss s to the equation by replacing R_2 with $R_2(1-s)$; the maximum efficiency for an impedance matched cavity with $\Delta = 0.9$ MHz and $F = 10$ is shown in Figure 5.31. From our calculation, the efficiency drop caused by this surface roughness is about 8.4%, which does not explain all of the loss; there must be other loss that is not clear to us yet.

Since the two-level quantum efficiency is much less than we would expect and we failed to identify all the reasons for the low efficiency, we did not proceed to the spin wave storage in the impedance matched cavity. My suggestion to other PhD students who might want to pursue this research would be to investigate how well one could prepare a spectral pit in the presence of the cavity mode, how much background absorption comes from the pit, how much background absorption is between the AFC peaks as the first step, identify the possible sources of the extra loss and try to minimize them. If possible, a simulation of how the cavity mode changes during the optical pumping process, how efficient the optical pumping pulse is when the frequency is on resonance and out of resonance with the cavity, the standing wave effect inside the cavity and how it affects the quantum memory would help us understand the whole process much better.

5.6 Conclusion and outlook

So far, we have demonstrated the cavity enhanced quantum memory efficiency at (close to) the impedance matched condition. We demonstrated that our RF rephase pulses for the long time quantum memory are quite efficient. However, we were not able to show the spin wave storage in an impedance matched cavity. I would like to mention a few issues in case similar work is done in the cavity in the future. One challenge of this project is that due to the slow light effect caused by the strong dispersion across the transmission window inside the crystal, the cavity modes are only about few MHz while the optical control pulses and storage pulse are 10.2 MHz apart. This means that if we tune the cavity mode over the storage pulse to obtain impedance matching, the control pulses (at 10 MHz) are out of resonance with the cavity and the transfer efficiency is really low due to poor coupling with the cavity. Quantum memory efficiency would be low as well.

One possible way to solve this problem is to broaden the cavity linewidth such that it covers both frequencies. From Equation (5.13), it seems that this could be achieved either by lowering the reflectivity of the first mirror, which reduces the finesse of the cavity (R_2 should still be as high as possible in order to obtain

high efficiency for the memory), or by increasing the mode spacing which, in principle could be done by increasing the group velocity of the light inside the spectral pit or by reducing the cavity length. However, the second method would not really work, as the first mirror reflectivity sets the effective absorption depth of the cavity that bounds the absorption coefficient and the cavity length together and the absorption coefficient affects the group velocity of the pulse. To have an idea of how they affect each other, let's start with a simple estimation.

The group velocity inside a spectral pit can be approximated with equation [51]

$$v_g = \frac{2\pi\Gamma}{\alpha'}, \quad (5.17)$$

where Γ is the spectral width of the transmission window and α' is the absorption coefficient immediately outside the spectral transmission window. When the impedance matched condition is fulfilled, $1 - R_1 = 1 - e^{-\tilde{\alpha}L} = 1 - e^{-2\alpha L/F_{\text{AFC}}}$ where αL is the peak absorption depth of the AFC peaks and $\tilde{\alpha}$ is the effective absorption coefficient of the AFC peaks, as we discussed earlier. In the ideal case, α could reach $0.93\alpha'$ if the ions with $|5/2g\rangle - |5/2e\rangle$ transition matching this frequency are all burned back there. In reality, α could be much lower than $0.93\alpha'$. Here we just assume $\alpha = N\alpha'$, where N is a positive number smaller than 0.93 for later calculation. Thus, when the impedance matched condition is fulfilled, we have $L = -\frac{\ln R_1 F_{\text{AFC}}}{2N\alpha'}$. The Equation (5.12) can be written as:

$$\Delta_{\text{FSR}} = \frac{v_g}{2L} = \frac{2\pi N\Gamma}{F_{\text{AFC}}|\ln(R_1)|}, \quad (5.18)$$

which shows that the cavity mode spacing is affected only by the first mirror reflectivity, the finesse of the AFC peaks and the width of the spectral pit and cannot be changed by the length of the cavity.

Combining these two equations with Equations (5.11), (5.12) and (5.17), assuming $R_2 = 1$, Equation (5.13) can be written as

$$\delta\nu_c = \frac{\Delta\nu_{\text{FSR}}}{F_{\text{cav}}} = \frac{2N\Gamma(1 - R_1^{\frac{1}{2}})}{F_{\text{AFC}}|\ln(R_1)|R_1^{\frac{1}{4}}} \quad (5.19)$$

It seems that the cavity linewidth is affected only by the first mirror reflectivity, the finesse of the AFC peaks and the width of the spectral pit. The length of the cavity does not change the cavity linewidth, since the free spectral range and the finesse of the cavity are connected via the impedance matching condition. Figure 5.33 shows the cavity linewidth inside a spectral pit at different first mirror reflectivities, assuming perfect impedance matching to the AFC structures ($\Gamma = 18\text{MHz}$, $F_{\text{AFC}} = 10$ and $N = 0.5$ for this plot). For first mirror reflectivity $R_1 > 0.3$, the cavity linewidth stays almost the same.

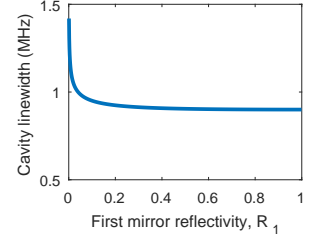


Figure 5.33. Cavity linewidth inside a pit when the impedance match condition is fulfilled. It is affected only by the first mirror reflectivity, R_1 .

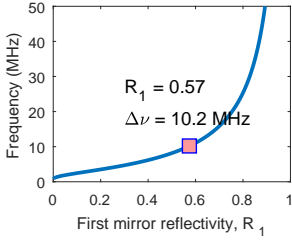


Figure 5.34. Cavity free spectral range when impedance match condition is fulfilled in the presence of spectral pit and AFC peaks. It depends only on the first mirror reflectivity, R_1 .

This is a very rough calculation, but it shows that it is not that simple to broaden the linewidth of the cavity to make it cover both the storage frequency and the optical control pulse frequency at the same time. It could be changed only slightly by modifying the cavity reflectivity.

An alternative approach is to adjust the cavity free spectral range inside the pit to about 10.2 MHz such that one mode matches the storage frequency and the next one matches the control pulse frequency. As we discussed earlier, the free spectral range of the cavity is (for a given finesse of the AFC peaks and a given width of the spectral pit) affected only by the first mirror reflectivity, as shown in Equation (5.18). Figure 5.34 shows that two cavity modes could cover both frequencies for a mirror reflectivity of about $R_1 = 0.57$ with $F_{\text{AFC}} = 10$ and $N = 0.5$.

However, the problem is that, since the storage and control pulses are at different cavity modes, the circulating field from the optical control pulses would have one more node than that from the storage pulse due to the standing wave pattern inside the FP cavity, which might lead to low transfer efficiency at some places. This brings up the option of using a whispering gallery mode (WGM) cavity, since the effective reflectivity of the WGM cavity could be adjusted there and the field inside the cavity is a traveling wave instead of a standing wave.

The third possibility is send the optical control pulse from the side of the crystal. This way we avoid the problem of mode matching both the control and storage pulse at the same time and there will not be any node in the transfer efficiency. The drawback is that the area of the control pulse has to be big enough to cover the whole cavity length along the light propagation direction, which would require a much higher laser intensity to ensure efficient transfer of the atomic excitation.

There are other possibilities. For example, if instead of depositing the cavity mirrors directly onto the crystal surfaces, one could use two separate mirrors and put the crystal in between them (or one mirror on the crystal and the other on a separated mirror outside the cryostat) such that the storage pulse still at the cavity mode while the control pulse is sent to the crystal with a small angle relative to the cavity mode and overlaps with the storage pulse on the crystal. This is what Jobez et al. tried in Ref. [96] with 53% two-level storage efficiency at 2 μs storage time and 12% three-level storage efficiency for 16 μs storage time. However, there one struggles with cavity stability and the mode overlap of the control pulse and the storage pulse.

EXPERIMENTAL SYSTEM

To manipulate the state of the ions, we need a light source with a frequency that matches the resonance frequency of the ions and that has a long coherence time. Thanks to former and current members of the group, the whole system was fairly well established when I started and works well most of the time. You could find a very good description and overview of the system in Refs. [97–99]. I will review the experimental system briefly to make this thesis complete and easier to understand.

A.1 The light source

The laser used for this thesis project is a ring cavity dye laser (Coherent 699-21) pumped by a 6W neodymium laser at 532 nm (Verdi V6). The dye used is Rhodamine 6G, which has an emission spectrum that covers both the $^3\text{H}_4 - ^1\text{D}_2$ transition at 606 nm of $\text{Pr}^{3+}:\text{Y}_2\text{SiO}_5$ and the $^7\text{F}_0 - ^5\text{D}_0$ transition around 580 nm of $\text{Eu}^{3+}:\text{Y}_2\text{SiO}_5$. With all the components inserted and optimized, it could yield a maximum output of about 1 W at 580 nm and 600 mW at 606 nm.

The dye laser comes with an internal cavity to stabilize the frequency to a linewidth of 1 MHz (about 500 kHz most of the time if everything works well). This means that the laser light has a coherence time of about one microsecond, which is much shorter than that of Pr^{3+} (150 μs [32]) and Eu^{3+} (2.6 ms [33]). Thus, we need an external locking system to accurately manipulate the state of the ions during their coherence time. If properly adjusted, we could scan the laser 30 GHz without mode hop using the control box, i.e., by tilting a galvo-mounted glass plate sitting in Brewster angle at the laser cavity.

A.1.1 External stabilization system

The Pound-Driver-Hall (PDH) technique is widely used to stabilize the frequency of laser by locking it to a stable cavity [100, 101]. It is employed here to lock our laser to an external Fabry-Pérot cavity made of low thermal expansion glass inside a cavity; the target linewidth of the laser with the external locking is 10 Hz. The advantage of the PDH locking is the fast response; it decouples the intensity fluctuation and frequency noise of the laser.

There is a really good introduction paper about PDH locking technique in Ref. [102], here I will offer only a conceptual description of how it works, for example, when there is a fast error in the laser beam.

For an impedance matched cavity at steady state, the cavity transmission is the same as the incoming light; the reflection from the first cavity mirror is zero because the field leaking out from the first mirror and the direct reflection of the incoming light cancel each other. If there is a fast phase change (frequency change) on the incoming laser beam, it takes as long as τ_c to see it in the reflection, where τ_c is the cavity field build-up time. However, we could see this change immediately from the reflected light since the directly reflected light field changes its phase right away and the field that leaks out of the cavity stays the same; the net field from these two will no longer be 0; the phase and intensity of this overall field contains all information of the error signal.

However, we cannot measure the phase of this error signal of the reflected light directly since the laser frequency is around 500 THz and no detector is fast enough for this. The easiest way to measure the frequency (phase) of this error signal is to beat it with a reference beam that is slightly shifted in frequency. This could be done by inserting an electro-optical modulator (EOM) in the laser beam before it enters the cavity. If the EOM is driven by a modulation signal at frequency ω_m , the light field after the EOM can be written as

$$\begin{aligned} E &= E_0 e^{-i[\omega t + m \sin(\omega_m t)]}, \\ &\approx J_0(m) E_0 e^{-i\omega t} \\ &\quad + J_1(m) E_0 e^{-i(\omega + \omega_m)t} - J_1(m) E_0 e^{-i(\omega - \omega_m)t} \\ &\quad + \text{higher order terms,} \end{aligned} \tag{A.1}$$

where ω is the frequency of the light, ω_m is the modulation frequency, E_0 is the amplitude of the incoming E-field, m is the modulation index that depends on the amplitude of the modulating field, and $J_n(m)$ are Bessel functions. When the modulation index is small, we could ignore the higher order terms, the field would be an overlapped field with a carrier and two sidebands at frequencies of ω , $\omega + \omega_m$ and $\omega - \omega_m$, respectively.

If the modulation frequency is high enough compared with the cavity linewidth, the two sidebands will be almost completely out of resonance with the cavity when the carrier is on resonance with and coupled into the cavity. The reflected fields constitute three components as well, the two sidebands that are 180° phase shifted compared with the incoming field and the field on the carrier frequency that contains the error signal we are interested in.

When the reflected fields are detected by a photodetector, it sees the beating of these three fields at the modulation frequency, ω_m , i.e., the frequency difference between the carrier and the sidebands and twice the modulation frequency, $2\omega_m$, the beating signal from the two carriers. Since we are interested in the field only at the carrier frequency, we could pick the signal at the modulation frequency out by a mixer with a reference signal from the same source that sends out the modulation signal to the EOM.

A frequency mixer is a device that takes in two inputs, normally one of them is the signal we are interested in, and the other one is the reference signal which is generally referred to as a local oscillator. The mixer produces new signals at the sum and difference frequencies of these two input fields. In this case, since the signal field and the local oscillator are at the same frequency, we obtain a DC signal (if the phases of the two signals are matched, otherwise some odd-looking error signals [103]) and a signal that oscillates at twice the modulation frequency. We could pick the DC signal up by a low pass filter and use it to compensate for the error in the laser. This was done by sending this DC signal to an EOM that sits inside the laser cavity after proper amplification.

The laser was locked to a spectral hole of the crystal initially [97, 98], where the frequency at which the laser could be locked is limited by the inhomogeneous linewidth of the crystal, since we cannot lock the laser if there is low absorption. To make the locking more flexible, an external Fabry-Pérot cavity made of low thermal expansion glass is used instead of the crystal [99]. However, the FP cavity has a free spectral range of about 3.3 GHz, which means that if we do not do anything, we could lock the laser only at discrete frequencies that are 3.3 GHz apart. To overcome this problem, we inserted a double pass AOM into the optical pass to shift the laser frequency. The center frequency of the AOM is about 1.1 GHz with a scanning range of about 1.5 GHz (double pass). This allows us to lock almost any frequency if we could use both the +1 and -1 order of the diffracted beam. However, currently we are only using the +1 order, which means we might not be able to lock the laser at any arbitrary frequency; but it is good enough for present purposes.

Figure A.1 shows a simplified sketch of the laser system, including an external laser stabilization system, and the pulse shaping system that will be discussed in the next section.

After coming out of the dye laser cavity, the laser light was sent

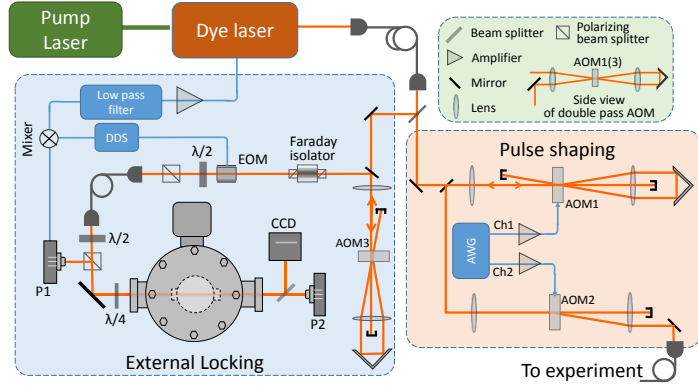


Figure A.1. Simplified sketch of the dye laser system. See text for more information

through a polarization maintaining fiber to clean up the spatial mode. Then it was split into two parts by a glass plate, about 2% of the light is directed to the stabilization system. The Faraday isolator after the double pass AOM 3 is used to block any light that is reflected back to the laser cavity, and the EOM is driven by a direct digital synthesizer (DDS) to modulate the light at about 50 MHz. The mode after the EOM is a bit elongated; a single mode polarization maintaining fiber is used to clean the mode, and a $\lambda/2$ plate is used before the fiber to match the polarization of the light with the polarization direction of the fiber. Another $\lambda/2$ plate is used to rotate the polarization of the light such that it matches one direction of the polarization beam splitter. Before entering the FP cavity that sits inside a vacuum chamber, the light was changed from linear polarization to circular polarization by a $\lambda/4$ plate, such that the reflected light after passing through the $\lambda/4$ plate twice could have a linear polarization perpendicular to the light before the $\lambda/4$ plate, and it will be directed on a low noise photodetector (P1) to generate the error signal. The signal transmitted through the cavity is split into two parts and detected by another photon detector (PD2) and a CCD camera, which record the transmitted light intensity and mode structure respectively.

The detected signal is mixed with the same modulation signal at a mixer, and the DC signal is picked up by a low pass filter and sent to an EOM and the control system of the laser after proper application.

A.1.2 Pulse-shaping system

To manipulate the state of the ions, we need to control the shape, frequency, phase and time duration of the light pulse with a high degree of precision. However, the light comes out of the dye laser is a continuous beam. Thus, we need a pulse shaping system to modulate the frequency and amplitude of the laser light which is done using AOMs.

As can be seen in Figure A.1, we use two AOMs for pulse shaping, one in a double pass configuration (to eliminate the spatial movement of the beam at different frequency) and the other in a single pass configuration. The double pass AOM (AOM 1) has a center frequency of 200 MHz and is capable of scanning 200 MHz (in double pass) in frequency, while the single pass AOM (AOM 2) has a center frequency of 360 MHz; the first order diffraction was sent through a single mode fiber to the experiment.

Both AOMs are controlled by an arbitrary waveform generator (Tektronix AWG520). The arbitrary waveform generator has two output channels, channel 1 and channel 2, which go to AOM1 and AOM2 respectively. It is capable of sending out two TTL signals associated with each channel, which could be used to synchronize other devices during the experiment.

A.2 The cryostat

In order to achieve long coherence time of the rare-earth ions, we need to lower the temperature to about liquid helium temperature, and a liquid helium bath cryostat from Oxford Instruments (Spectromag SM400) was used for this purpose. The crystal is immersed in the liquid helium; to avoid helium bubbles, the sample chamber is pumped to around 45 mbar and kept around 2.17 K. At this temperature, helium becomes superfluid and exhibits infinite thermal conductivity. The cryostat has four optical windows that permit access to the crystal from different directions. This cryostat is also equipped with superconducting magnets that allow delivery of a field up to 8 T along one direction.

ZERO CROSSING TEMPERATURE MEASUREMENT

To manipulate the quantum state of the ions for quantum memories and quantum computing, we need lasers that have good coherence properties, better than the coherence time of the ions that they interact with, which means that the linewidth of the lasers should be narrower than the homogeneous linewidth of the ions. Furthermore, it should be stable over the time that operations are carried out in order to address the same single ion and process data on it. To fulfill these requirements, we need to stabilize our lasers to an external frequency reference; Fabry-Pérot cavities (FP cavities) are good candidates for this purpose [100, 104]. Besides quantum information, stabilized lasers are a key component of optical atomic clocks [105], detection of gravitational waves [106] and precision tests of relativity [107]. The fractional frequency stability of the laser is limited by the fractional optical length stability of the FP cavity, which is fundamentally limited by the Brownian motion of the atom and molecular of the cavity material. A great deal of effort was devoted to reducing the thermal noise of the FP cavities: for example, choosing materials with low thermal expansion coefficients and operating the cavity at its zero crossing temperature (where the thermal expansion of the material is 0 to the first order).

To date, the most stable laser with frequency stability of 4×10^{-17} for integration times between 0.8 s and a few tens of seconds has been demonstrated using high-finesse, single-crystal silicon FP cavities cooled to 124 K which is their zero crossing temperature [108]. In this chapter, I describe the experiment we conducted to measure the zero crossing temperature of our two FP cavities, which are used to lock our lasers and investigate their stability. That was the only time the experiment was conducted

by the group; even though we are happy with the laser stability we have right now, we may need to come back later to measure the cavity parameters more precisely for further improvement. Thus, this chapter was written with the aim of providing a head start for a PhD student who follows up on this project.

B.1 Laser stabilized to a Fabry-Pérot cavity

If a laser is stabilized to an FP cavity, we can see what is affecting the stability of the laser by the following equations.

The resonance frequency, ν , of an FP cavity can be written as:

$$\nu = \frac{Nc}{2nL} \quad (\text{B.1})$$

where N is an integer known as mode order, c is the speed of light in vacuum, and n and L are the refractive index and the length of the FP cavity respectively. If we assume there is no dispersion in the FP cavity, the resonance frequency changes as the variation of the cavity length can be written as,

$$\Delta\nu = -\frac{Nc\Delta L}{2nL^2}. \quad (\text{B.2})$$

From Equations (B.1) and (B.2), we obtain,

$$\frac{\Delta\nu}{\nu} = -\frac{\Delta L}{L}. \quad (\text{B.3})$$

It is clear that for a laser locked against an FP cavity, the frequency stability of the laser is coupled to the fractional length stability of the cavity.

To attain a frequency stability of 10^{-14} , (5 Hz for our 606nm laser) using a 5 cm long cavity, the length variation has to be less than 5 fm, which is roughly the radius of a nucleus. Several factors can influence the length variation of a cavity: temperature variation, pressure variation, acoustic vibration, mechanical vibration and the inevitable Brownian motion of the atoms in the mirrors. Among which, the fundamental limit of how stable the length of a cavity could be is the Brownian motion of the atoms [109], while the other factors can potentially be reduced in various ways:

- (i) Put the cavity onto an active isolation platform, design the cavity geometry and mount it carefully such that the mechanical vibrations from the environment are isolated effectively.
- (ii) Put the cavity inside a vacuum chamber and keep the pressure low ($< 10^{-8}$ mbar). This not only protects the cavity from acoustic vibration but also gives a much more stable temperature and pressure control, which minimizes any refractive index fluctuation.

- (iii) Active temperature stabilization control to minimize the length variation due to temperature fluctuation.

To further reduce the length variation of the cavity, the cavity could be made out of materials with low thermal expansion coefficient, for example, ultra low expansion (ULE) glasses (or some other low expansion glass such as ZERODUR or CLEARCERAM-Z). These materials have a zero crossing temperature at around room temperature such that to the first order the length of the material does not change.

In our lab, we lock our lasers, one dye laser operating at 580-606 nm and one diode laser operating at around 370 nm, to two FP cavities respectively, and use all the above-mentioned methods to stabilize the locking cavity as much as possible. Both of those cavities use ultra low expansion (ULE) glass from Corning as a spacer with two cavity mirrors in optical contact with the ends. However, they have slightly different geometry designs, which will be described briefly below. A more detailed description of cavity parameters and mounting techniques can be found in [110] for the 370 cavity and [111] for the 606 cavity used here.

B.1.1 The 606 cavity

We will briefly describe the geometry of the 606 cavity used to lock the 606 nm laser in order to understand the later discussion better. As shown in Figure B.1, the cavity spacer has a spherical shape with one hole drilled through it for the laser light to pass; the cavity mirrors are in optical contact with the spacer at the two ends of the hole. The mirror substrates are made of fused silica with ULE compensation rings in optical contact with the back of the mirror substrates to minimize the mirror deformation [111, 112]. Another hole on the spacer perpendicular to the cavity is used for pumping vacuum inside it. The cavity spacer was mounted on a holder made from invar, which is nickel-iron alloy with a very low thermal expansion coefficient (1.3 ppm/K) in the temperature range for which the cavity is used. A great deal of effort was devoted to designing and mounting the cavity for satisfactory stability [113]. To minimize heat transfer from the surroundings to the cavity, three layers of aluminum heat shields are placed between the vacuum chamber and cavity with holes at the bottom of the heat shields to facilitate the vacuum pump. The Peltier element is placed underneath the radiation shield, while the temperature sensor is located inside the radiation shields and at the bottom of the vacuum chamber. A CAD model of the heat shield and the spacer mounted inside the vacuum chamber mode by former student Adam Wiman is shown in Figure B.1; more detailed information about this cavity can be found in Ref. [111].

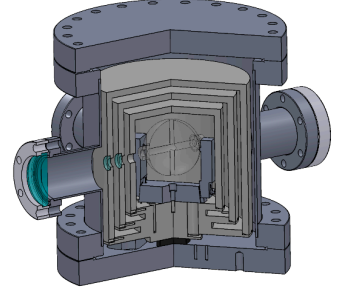


Figure B.1. CAD model of the 606 cavity and the heat shields inside the vacuum chamber. Three layers of aluminum heat shield are used to protect the cavity from fluctuations of the incident heat radiation of the environment (made by Adam Wiman).

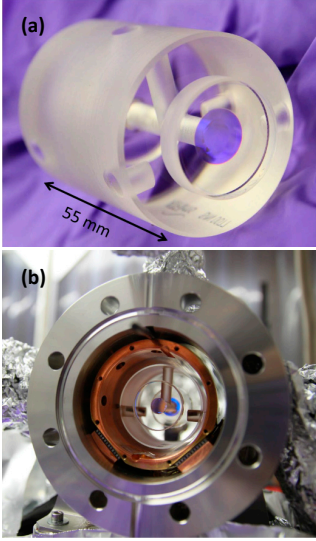


Figure B.2. (a) A photo of the 370 cavity; the cylindrical cavity spacer is made of ULE glass with one hole drilled along its axis for light propagation and a second one drilled perpendicularly for pumping vacuum. The two cavity mirrors are in optical contact with the end surfaces of the cylindrical spacer. (b) A photo of the vacuum chamber with the radiation shield, TECs, and the cavity mounted. (Photos by Yan Ying.)

B.1.2 The 370 cavity

The 370 cavity has a different design: a 55 mm long cylindrical shaped spacer is used instead of a spherical one. The mirrors are in optical contact with the end surfaces of the spacer. The cavity is suspended inside a copper radiation shield by spring wires, the outer surface of the radiation shield is gold-coated, which decrease the thermal transfer rate with the environment and improve the thermal stability of the cavity. The copper radiation shield sits on top of four TECs, which are mounted onto the copper adapters glued to the inner wall of the vacuum chamber. The gold coating makes the radiation shield more robust against the potential environmental temperature change, and the 4 TECs that are in contact with the radiation shield can compensate the possible temperature change and keep the cavity temperature stable. The vacuum chamber is more compact than the other 606 cavity: only 3 mm between the radiation shield and the vacuum chamber, which is the same distance the cavity spacer. Photos of the 370 cavity and the vacuum chamber assembly are shown in Figure B.2 (a) and (b) respectively. The temperature sensor for this cavity sits in one of the dents on the inside of the copper radiation shield.

The mirrors are high reflection coated both around 370 nm and in the range of 575 - 615 nm, allowing us to couple our dye laser to this cavity to measure the zero crossing temperatures of both cavities and analyze their relative stability. There are more details about the 370 cavity design in Chapter 5 of Ref. [110].

B.1.3 ULE glass

As mentioned earlier, one issue that affects the long-term stability of the cavities is the thermal expansion of the cavity spacer due to temperature variations over time. Different types of spacer materials are developed with very low thermal expansion coefficients, some even showing zero thermal expansion around room temperature. The one made by Corning is called ultra low expansion (ULE) glass. ULE is a Titania doped silicate glass with the unique characteristic that its coefficient of thermal expansion (CTE) is very close to 0 ppb/K around room temperature (0 ± 30 ppb/ $^{\circ}$ from 5 $^{\circ}$ to 35 $^{\circ}$, with 95% confidence level, ULE Corning Code 7972 Ultra Low Expansion Glass) and zero at the zero crossing temperature, denoted by T_c .

Figure B.3 shows the CTE and thermal expansion of the ULE glass versus temperature. At around 20 $^{\circ}$, the thermal expansion of the piece of glass tested is zero and the instantaneous CTE crosses zero at this temperature. Even though T_c is normally below room temperature, it varies from boule to boule, heavily dependent on the external stress in the glass [112]. The aim of this experiment is to determine the zero crossing temperature of the two cavity

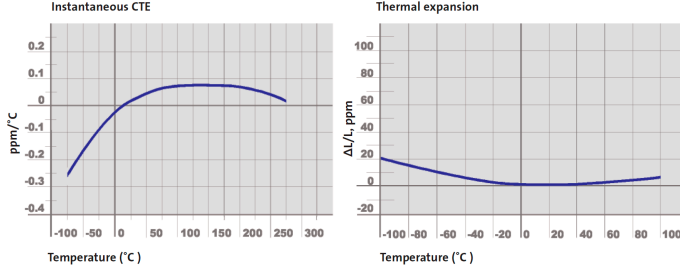


Figure B.3. Thermal expansion and its coefficient $\Delta L/L$ of a piece of ULE glass from Corning.

spacers used in our cavities for later reference and estimate their stability over temperature variations.

B.2 Zero crossing temperature measurement

It is estimated that the thermal expansion of the ULE glass has quadratic dependence over the temperature [114], which can be described by the following equation,

$$\frac{\Delta L}{L} = \alpha(T - T_c)^2 \quad (\text{B.4})$$

According to Equation (B.3), the resonance frequency of the cavity spacer at certain temperature T_s could then be written as,

$$\nu' = \nu_c + \Delta\nu = \nu_c - \beta(T_s - T_c)^2 \quad (\text{B.5})$$

where $\beta = \alpha\nu_c$. Moreover,

$$d\nu' = -2\beta(T_s - T_c) \quad (\text{B.6})$$

which can be used to calculate the frequency stability of the cavity at different temperatures. If we could vary the temperature of the spacer and measure the resonance frequency of the cavity at the same time, we could map out the zero crossing temperature in a straightforward manner. However, we do not have a temperature sensor at the cavity spacer, and the only places we could measure the temperature are the places where we have our sensors, both of them are away from the spacer. We could make a scientific estimate of the spacer temperature by the following heat transfer equations.

If the temperature of the radiation shield is different from the cavity spacer, the rate of heat flow between them is:

$$\Delta Q/\Delta t = AK\Delta T/x = AK(T_{rs} - T_s)/x, \quad (\text{B.7})$$

where ΔQ is the heat transferred over the time Δt ; ΔT is the temperature difference between the radiation shield and the cavity spacer; A is the surface area of the cavity spacer; K is the thermal conductivity factor of the medium between the radiation shield and the spacer (vacuum in our case); x is the distance between the radiation shield and the cavity spacer; and T_{rs} and T_s are the temperature of the radiation shield and the cavity spacer respectively. Assuming the cavity spacer has a mass of m and heat capacity of C , the temperature change of the spacer is ΔT_s , where

$$\Delta T_s = \frac{\Delta Q}{mC} \quad (\text{B.8})$$

From Equations (B.7) and (B.8), the temperature change of the cavity spacer can be written as:

$$\frac{dT_s}{dt} = \frac{-AK\Delta T/x}{mC} = \frac{1}{\tau_s}(T_{rs} - T_s) \quad (\text{B.9})$$

where $\tau_s = \frac{AK}{xmC}$ is the time constant of the cavity spacer.

Thus, if we change the temperature change of the cavity and record the reading from the sensor and the resonance frequency change of the cavity, we could fit the data by Equations (B.5) and (B.9); it is possible to map out the zero crossing temperature, the time constant, the coefficient of thermal expansion and the actual temperature of the spacer to calculate the frequency stability of the cavity at different temperature from Equation (B.6).

B.2.1 Setup

To measure the zero crossing temperature and estimate the stability of the cavities, we need a reference to compare with. A stabilized laser is a very good candidate for this purpose.

Our lab has two cavities and a laser stabilized against the 606 cavity. It is natural to use the stabilized laser to measure the relative frequency shift of the cavities when the temperature of one of them changes while that of the other one is fixed if the laser is coupled to both of them at the same time. If we assume that the resonance frequency change is due solely to the temperature change of the cavity, we could map out the zero crossing temperature of both cavities, as discussed at the end of the last section. A simplified sketch of our experimental setup is shown in Figure B.4. One part of the laser beam, beam path 1, is used for laser stabilization (illustrated by the shaded area). The laser is locked to one of the cavity modes of the 606 cavity, which is also used for all other experiments presented in this thesis. The other part of the

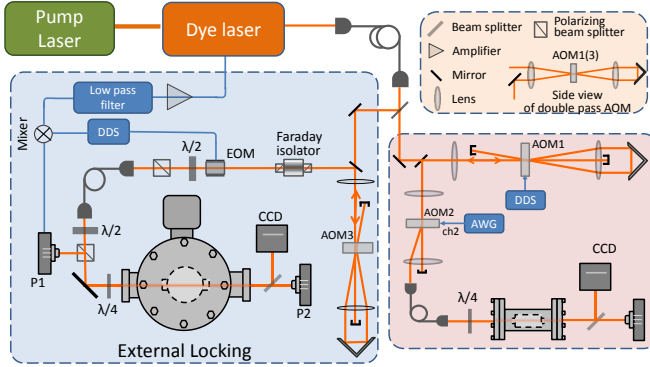


Figure B.4. A simplified sketch of the cavity zero crossing temperature measurement. The beam path1 of a 606 dye-laser is used to lock the laser to a ULE cavity (606 cavity). The laser was first sent through a double pass AOM (AOM1), which works at around 1.1 GHz, and sent to an EOM. The EOM was controlled by the RF signal from a DDS; it could add a phase modulation to the laser light to induce two frequency components (sidebands) 50 MHz from the center frequency of the laser (carrier). After passing through a polarizing beam splitter, the linearly polarized light was made circularly polarized by means of a $\lambda/4$ wave plate and coupled into a FP cavity. The transmitted light intensity was recorded by a photo detector (PD1) and the mode structure was monitored via a CCD camera (CCD1). The reflected beam was rotated back to linearly polarized light after passing through the $\lambda/4$ wave plate, but the polarization was with 90 degrees relative to the incoming laser light, so it would be reflected to a photo detector (PD3) by the polarizing beam splitter. Since both the sidebands and the carrier are reflected, the detector measures the beating frequency at 50 MHz (beating from carrier and sidebands) and 100 MHz (beating from the two sidebands). It was then sent to a mixer, where it was compared with the reference signal, the 50 MHz RF signal that is phase locked to the signal sent to the EOM. We obtained a DC signal and another one at twice the modulation frequency; the DC signal was picked up by a low pass filter as an error signal and sent to the laser cavity after amplification to correct any frequency or phase errors. More information about the locking cavity can be found in Appendix A. The path 2 was sent to a double pass AOM (AOM2) and coupled to the 370 cavity after a fiber; the transmission and the transmitted mode structures were recorded.

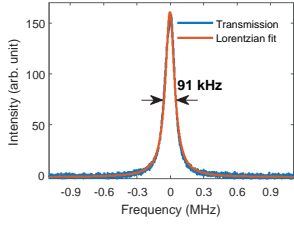


Figure B.6. Transmission from the 370 cavity when scanning the laser frequency. The blue trace is the raw data from experiment and the orange one is the Lorentzian fitting; the linewidth of the transmitted light is about 100 kHz at this wavelength.

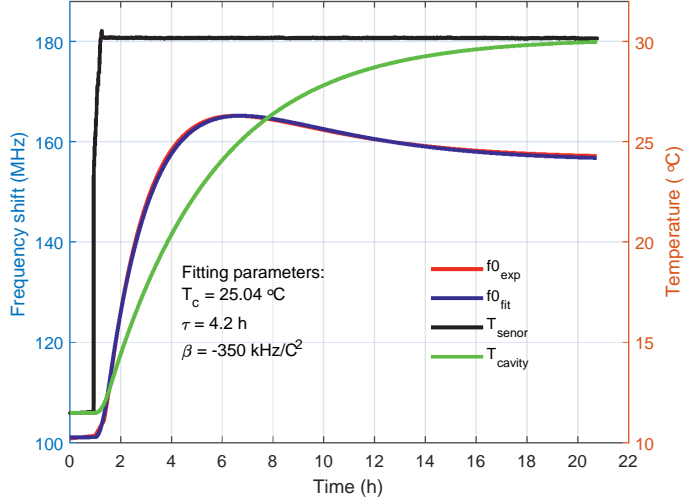


Figure B.5. The 370 cavity response when a temperature change was made. The orange trace is the temperature reading from the sensor while the green one is the cavity spacer temperature estimated using the fitting parameters listed in the figure. The red and blue traces are the center frequencies of the cavity transmission experimentally measured and fitted respectively.

laser beam, beam path 2, was directed to the 370 cavity after passing through a double pass AOM (AOM2) with center frequency of about 200 MHz, which is controlled by another homemade DDS (DDS2) capable of scanning 100 MHz with a step size of 5 Hz in 2 seconds. The transmitted light was recorded by a photo detector (PD2); the mode structure can be seen from the CCD camera (CCD2). Since both cavities have a free spectral range of approximately 3 GHz (about 3.3 GHz for the 606 cavity and 2.7 GHz for 370 cavity), a 1.1 GHz double pass AOM (AOM1) was used to make sure the laser was resonant with both cavities simultaneously.

Before starting the measurement, the laser was locked to the 606 cavity and the temperatures were fixed at 17° and 11.5° for the 606 cavity and the 370 cavity respectively for days to make sure the cavity temperatures were at equilibrium. The 606 cavity temperature was then kept the same while the setting point of the 370 cavity temperature controller was changed from 11.5° to 30°. The transmitted light from the 370 cavity was recorded and a Lorentzian curve was fitted to the transmission signal. The center frequency and linewidth of the Lorentzian fitting were saved for later analysis. A typical transmission curve of the 370 cavity is

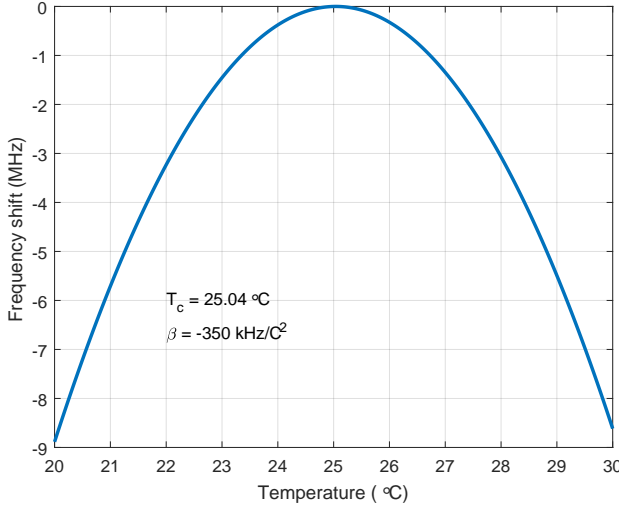


Figure B.7. The resonance frequency change of the 370 cavity at different temperatures. 0 MHz corresponds to the center frequency of the cavity when it is at its zero crossing temperature.

shown in Figure B.6; the linewidth of the cavity transmission is about 100 kHz at this wavelength, 606 nm, which yields a cavity finesse of about 27 000.

About 5 hours later, the turning point of the frequency was observed, which means that the cavity had passed its zero crossing temperature; we continued to measure for about 15 hours until the resonance frequency of the cavity stopped changing, which means that the cavity had reached the set temperature. All the saved data (time, resonance frequencies of the cavity, temperatures of the sensor) were then used as input to a simulation program based on Equations (B.9) and (B.5), which tried to estimate the zero crossing temperature of the cavity T_c , the time constant of the heat transfer β , the offset frequency ν_c and the estimated temperature of the spacer T_s .

The experimental and simulated data are plotted together in Figure B.5, where the red and blue are the experimental center frequency of the 370 cavity resonance and the fitted center frequency, using the parameters listed in the figure and Equations (B.9) and (B.5). The simulation returned a zero crossing temperature for the 370 cavity at $T_c = 25.1^\circ$ and a time constant of $\tau = 4$ hours.

Figure B.7 shows the resonance frequency change of the 370 cavity at different temperatures using the simulated parameters

shown in Figure B.5. The 0 MHz corresponds to the center of the resonance frequency when the cavity is at its zero crossing temperature. The sensitivity of the resonance frequency of the cavity at a certain temperature can be easily estimated. Using Equation (B.6), it can be calculated that if the cavity is 1° off from its zero crossing temperature, the frequency drift is 750 Hz/mK.

B.2.2 The 606 cavity

After determining the zero crossing temperature of the 370 cavity, the 370 cavity was set to that temperature, 25.1° , and the 606 cavity was set to 30° ; they were left for one day until their temperatures stabilized. A temperature step was then made on the 606 cavity. Since the laser was locked on that cavity, the laser frequency changed along with that of the cavity spacer; we could measure the frequency shift by looking at the transmitted frequency change of the 370 cavity. Since the 370 cavity was set to its zero crossing temperature, its absolute resonance frequency should be more or less constant; a frequency shift of Δf measured on the 370 cavity would actually mean a frequency shift of $-\Delta f$ on the 606 cavity caused by the temperature change. Thus, if we use the measured frequency change of Δf to fit the 606 cavity, it should have the opposite sign of β as the 370 cavity, which means the opening of the quadratic curve should be facing upwards instead of downwards as in the case of the 370 cavity.

The zero crossing temperature of the 606 cavity is much lower than we had expected; we did not observe any turning point of the frequency shift until the cavity temperature of the 606 cavity was around 8° . The laser unlocked a couple of times during data acquisition, so we had to cut away some data points when the laser was unlocked and replace them with linear interpolation before running the simulation.

Figure B.8 shows one of the experimental data recordings where the temperature of the 606 cavity was changed from 7.2° to 8.5° and after about 20 hours, it was changed back to 6.5° . This way, we were sweeping the cavity temperature to pass the zero crossing temperature twice. The red trace is the experimental frequency shift, while the blue one is the simulated curve using the parameters listed in the figure; we could clearly see a mismatch between the two curves, partly due to the spike at the beginning. As discussed earlier, the quadratic response of the resonance frequency versus frequency should be facing upwards for the 606 cavity; however, the spike on the frequency curve at the beginning when the temperature of the cavity was set to 8.5° from 7.2° shows an opposite response from the spacer. This spike might be caused by the response from the cavity mirror coating, as observed in Ref. [114]. The change in frequency is about 140 kHz; according to Equation (B.3), this corresponded to a length change of 1.4×10^{-11}

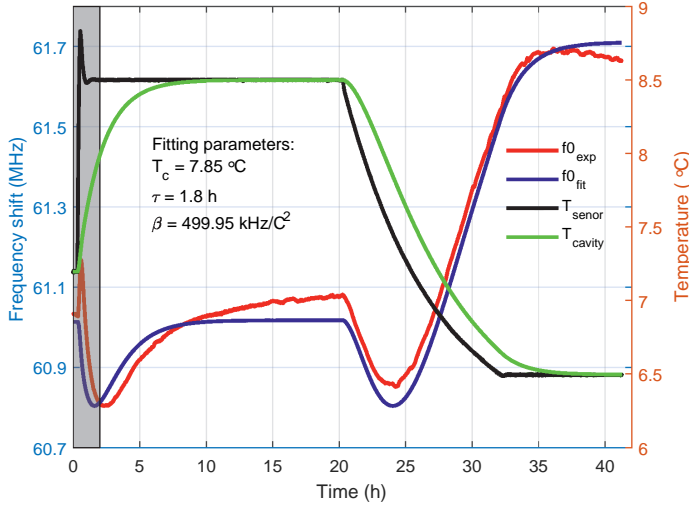


Figure B.8. The temperature of the 606 cavity was changed from 7.2° to 8.5° and then to 6.5° again. The red curve is the change of resonance frequency caused by the temperature change, and the orange trace is the temperature at the sensor point inside the 606 cavity. The blue and green traces are the simulated frequency change and spacer temperature using the parameters listed in the figure.

over the 1.6 K temperature change. This corresponds to a mirror coating with a thickness of 20 μ m and a thermal expansion coefficient of $0.44 \times 10^{-6}/\text{K}$. An expansion of the spike is shown in Figure B.9

Besides the first spike, there was some slow frequency drift even when the cavity was at a fixed temperature: for example, at 8.5° between hours 10 and 20, and at 6.5° after hour 35. However, the resonance frequency drifts upwards at 8.5° and downwards at 6.5°. The drift is on the order of 10 kHz/hour. The existence of the first spike and the drift affect the simulated parameter; thus, we tried to just fit the data when the cavity passed its zero crossing temperature the second time, as shown in Figure B.10; this one seems to fit quite well.

The resonance frequency change of the 606 cavity is plotted in Figure B.11 using the same parameters as in Figure B.10. The 0 MHz is the resonance frequency of the cavity at its zero crossing temperature. It can be calculated that if the cavity is 1° off from its zero crossing temperature, the frequency drift is 1 kHz/mK.

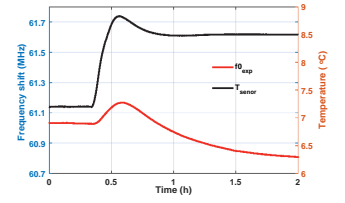


Figure B.9. An expanded view of the resonance frequency change of the cavity and the temperature change of the sensor (the gray part marked in Figure B.8).

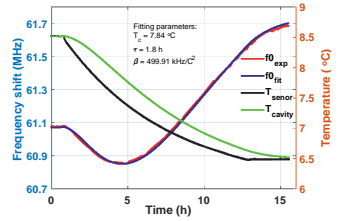


Figure B.10. The 606 cavity response and the simulated response when the temperature was changed from 8.5° to 6.5°. The black curve is the change of resonance frequency caused by the temperature change, and the orange trace is the temperature at the sensor point inside the 606 cavity. The blue and green traces are the simulated frequency change and spacer temperature using the parameters listed in the figure.

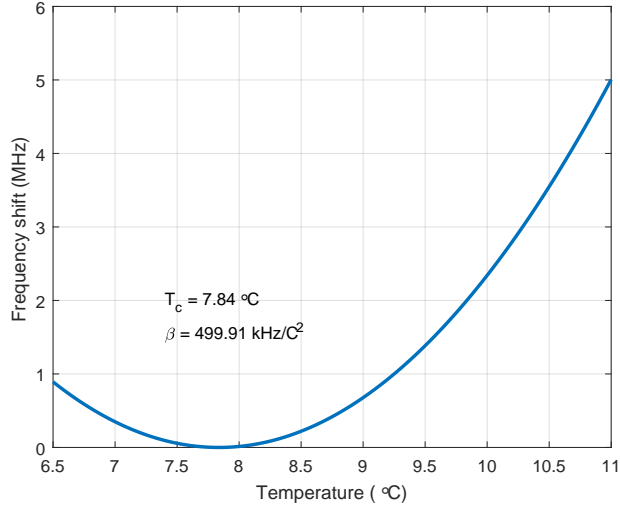


Figure B.11. The resonance frequency change of the 606 cavity at different temperatures, where the 0 MHz corresponds to the resonance frequency when the cavity is at its zero crossing temperature.

B.3 Residual frequency drift

As discussed above, one reason for the mismatch between the experimental data and our simulated data is the frequency drift in the system even when temperatures should be stable for both cavities. The drift is on the order of 9 kHz/hour (2.5 Hz/s); we are not sure what caused the drift. Below I listed some possible reasons for the frequency drift.

(i) Aging of the cavity spacer.

The ULE that makes the cavity spacer is still glass. The atoms and molecules inside glass are out of equilibrium and not in their lowest energy state. Thus, glasses age, which means that their physical properties change over time when they try to regain their equilibrium state, which has to be taken into consideration in applications like glass fibers and optical components made out of glass [115]. In our case, the length of the ULE cavity spacer changes over time and induces a resonance frequency shift of the cavity. It has been shown for another cavity that the frequency drift caused by the aging of the glass is about 60 mHz/s [116]. However, our drift was more like 2-3 Hz/s, which is two orders higher than the drift caused by pure glass aging.

- (ii) Temperature change due to the room temperature variation.

The lab is temperature stabilized at around 23.5° ; however, we did not monitor the temperature around the cavity to see how stable it was. It is possible that the room temperature increased in the daytime during data acquisition; thus, even though the temperature around the sensor was stable, the large volume of the cavity compartment suggests that the temperature of the spacer might have increased slightly. Since we are about 1 K away from the zero crossing temperature, the frequency drift was about 1 kHz/mK such that if the temperature of the spacer changed by 10 mK in an hour, it should be enough to explain the drift observed in the frequency change. Furthermore, the frequency drifts upwards when the cavity is about 8.5° and downwards when the cavity is about 6.5° . If the spacer temperature increases slightly relative to the sensor temperature, this is what we would expect since the zero crossing temperature of the cavity is around 7.8° . When the temperature is at 8.5° , the resonance frequency increases while the temperature increases; when the cavity temperature is around 6.5° , the resonance frequency decreases while the cavity temperature increases.

Apart from all the drift and the spike in Figure B.8, the fact that the two minimum frequencies of the cavity shifted by about 50 kHz is still difficult to explain. Because the minimum frequencies occur when the cavity reaches its zero crossing temperature, the cavity should have the same length for those two incidents. In principle, this can be explained by the drift of the other cavity; for example, the 370 cavity drifted 50 kHz over the two incidents. However, the temperature variation is only about 0.02 K during the two incidents, as seen in Figure B.12.

To explain the 50 kHz drift we observed in the measurement, we would need either a temperature change of 0.5 K when the 370 cavity is set to its zero crossing temperature or a temperature change is 0.02 K when the cavity temperature is about 4° off from its zero expansion temperature. We do not believe that either one is true, which leaves the reason for the frequency drift unknown.

B.4 Conclusion and outlook

We have measured the zero crossing temperatures of the 606 and 370 cavities to be around 7.8° and 25.1° with $\pm 0.2^{\circ}$ accuracy.

The big difference in the zero crossing temperature of these two cavities may be caused by the deformation of the mirror of the 606 cavity because of the different thermal coefficient of the mirror and the spacer [112]. Unfortunately, some drift in the system is unknown; due to lack of experimental time, we were not able to

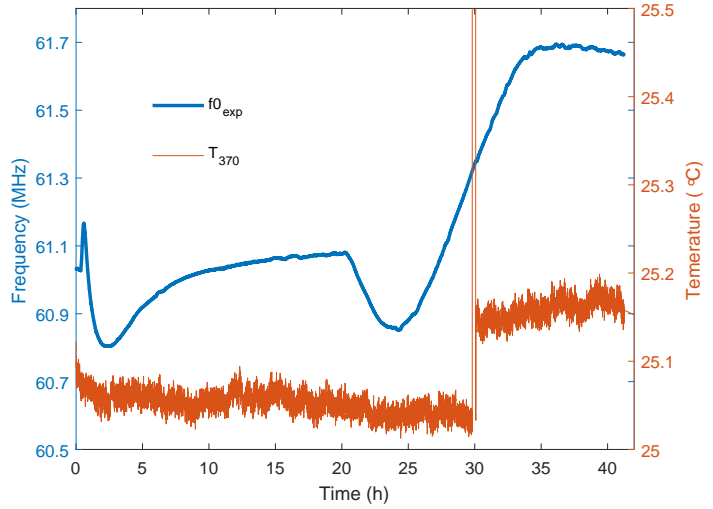


Figure B.12. The frequency change of the 606 cavity and the temperature of the 370 cavity when the 606 cavity temperature was changed.

investigate this problem further to obtain more precise zero crossing temperatures. For future reference to address this problem, it would be good to have another temperature sensor close to the two cavities to make sure the environmental temperature around the cavity does not change too much during the measurement if further measurement will be carried out. It would be useful to figure out where the drift comes from and try to make the same measurement again to obtain more precise zero crossing temperatures for both cavities. An alternative way of determining the zero crossing temperature could be to measure a few points around the zero crossing temperature, and interpolate the zero crossing temperature from those data points as in Ref. [114], provided that the problem of the frequency drift in the system is addressed properly.

COMMENTS ON THE PAPERS

I Efficient quantum memory using a weakly absorbing sample

M. Sabooni, Q. Li, S. Kröll and L. Rippe.
Phys. Rev. Lett. **110**, 133604 (2013).

In this paper we demonstrated the best storage and retrieval efficiency (56%) based on the AFC protocol so far. It was achieved with the assistance of a low finesse, unsymmetrical cavity, and by working at the impedance matched condition. The cavity assisted quantum memory reduces the requirement of high optical depth for high memory efficiency and opens the possibility of using materials with excellent coherent properties but low optical depth, such as $\text{Eu}^{3+}:\text{Y}_2\text{SiO}_5$. I participated in all the experiments and was involved in all the discussions about the data analysis and the manuscript.

II Spectral engineering of slow light, cavity line narrowing, and pulse compression

M. Sabooni, Q. Li, R. K. Mohan, L. Rippe and S. Kröll.
Phys. Rev. Lett. **111**, 183602 (2013).

Because of the slow light effect induced by the sharp dispersion across the spectral hole prepared inside a rare-earth-ion-doped crystal, the cavity mode spacing, as well as the cavity linewidth were narrowed by more than 4 orders of magnitude and the Q value of the cavity was increased by the same orders. This was two orders of magnitude larger than previously demonstrated. We argue that extraordinarily high Q cavities could be achieved by this technique, especially in a whispering gallery mode cavity, and a laser locked to the narrow cavity mode of such a slow light cavity might reach exceptional stability.

I performed all the experiments together with Mahmood Sabooni and was involved in all the discussions about the data analysis and the manuscript.

III Slow-light-based optical frequency shifter

Q. Li, Y. Bao, A. Thuresson, A. Nilsson, L. Rippe and S. Kröll.

Phys. Rev. A **93**, 043832 (2016)

Synopsis of paper selected for online display of APS Physics.

A solid state optical frequency shifter was demonstrated. The frequency of light was shifted by ± 4 MHz experimentally, and the possibility of obtaining a frequency shift of \sim GHz was discussed. The frequency shift was achieved through the combination of the slow light effect and the DC Stark effect; the frequency shift was proportional to the strength of the external electric field. Such a frequency shifter could be made to work for light with arbitrary polarization and the solid acceptance angle could be close to 2π . I participated in the planning and designing of the experiment, and carried out all the experiments. I came up with the idea of separating the two groups of ions for the experiment and I evaluated all the data. I wrote the manuscript.

IV Using electric fields for pulse compression and group-velocity control

Q. Li, A. Kinos, A. Thuresson, L. Rippe and S. Kröll.

Phys. Rev. A **95**, 032104 (2017)

Synopsis of paper selected for online display of APS Physics.

In this paper, we demonstrated a device that was capable of controlling the group velocity of a light pulse by a factor of 20 with a relative efficiency better than 80% and little distortion. The group velocity was fully controlled by the external electric field via the DC Stark effect. We also showed that, with the same principle, such a device could also be used to compress the pulse in time. A factor of 2 pulse compression in time was demonstrated.

I participated in the planning and all the experiments, evaluated the data and wrote the manuscript.

V Development and characterization of high suppression and high tendue narrowband spectral filters

A. Kinos, Q. Li, L. Rippe and S. Kröll.

Applied optics **55**, 10442 (2016).

A narrow-band (~ 0.5 MHz) spectral filter with high suppression (53.4 ± 0.7 dB at 1.25 MHz from the center) was developed in $\text{Pr}^{3+}:\text{Y}_2\text{SiO}_5$ targeting applications of ultrasound optical tomography (UOT). Simulations were performed to better understand absorption/suppression as a function of the incident angle and light polarization in such an absorbing, birefringent material.

I participated in most of the experimental work, was involved in the discussions for simulations and data analysis, as well as the manuscript.

VI Fast all-optical nuclear spin echo technique based on EIT

A. Walther, A. N. Nilsson, Q. Li, L. Rippe and S. Kröll.

Eur. Phys. J. D **70**, 166 (2016).

In this paper, an all-optical Raman spin echo technique using electromagnetically induced transparency (EIT) was demonstrated. The technique could be applied to a mixed state without prior preparation. Two applications were demonstrated and the potential applications were discussed.

I participated in parts of the experiment and was involved in the discussions about the manuscript.

ACKNOWLEDGEMENTS

This thesis would not have been possible without the help I received during my PhD studies. I would like to take this opportunity to express my sincere gratitude to all the people whom I have had the privilege to learn from and work with, especially my supervisors, colleagues, friends, and family members who have supported me in different ways.

First and foremost, I would like to thank my supervisor, Stefan Kröll, for giving me the opportunity to work with those fascinating ions, for always being there to help and having time for discussion, for taking every questions raised seriously, and for being nice to me even when I made silly mistakes that I should not have.

I am very grateful to my co-supervisors, Lars Rippe, for always being very understanding, not only scientifically but in other aspects too, for all the ideas you have and all the interesting topics you brought up; Nina Reistad, for being nice and always making time for me; Hugues de Riedmatten, for giving me the chance to work in your lab on the photon-pair source for three weeks in the sunny May weather in Barcelona.

I would like to thank group members, Andreas Walther, for always being able to explain a difficult topic in a way that I could follow; Ying Yan, Jenny Karlsson and Mahmood Sabooni, for guiding me in the field and teaching me how to use all the equipment, for all the discussions we had, and for willing to help whenever I needed; Diana Serrano, for always being brave enough to express yourself and for all the times we spent together, Chunyan Shi, for being the first one to read through the 1st draft of my chapters, it must have been very painful and I am truly sorry for that; Adam Kinos, for always able to make discussions in an organized way, for all the trips we went on together, and for your attitude towards work and life; you have influenced me in many ways.

Thanks to all the current and former members of the group for establishing and maintaining such an amazing system, so that I could focus on my project and go further along my way. I would also like to thank the new members of the group, Sebastian Horvath, Alexander Bengtsson, Mohammed Alqedra, Hafsa

Syed, Meng Li, Mengqiao Di and Vassily Kornienko, it was very pleasant to work with you and you will make the group even better.

Many thanks to the students whom I had the privilege to supervise, Yupan Bao and Ivan Sytsevich, for all the work we did together and for teaching me how to be a supervisor. It is so nice to see both of you here pursuing your PhD at the Physics Department, I wish you the best of luck in the future.

I am also grateful to other people at the Atomic Physics Division who helped me on more specific things, Camilla Nilsson and Anne Petersson Jungbeck for helping with all the administrative issues, Harriett Lindahl and Jakob Testad for handling all the financial issues; Bertil Hermansson and Åke Johansson for fixing my computer and especially Åke for spending almost an entire week migrating my computer to the new system; Lars Engström for planning and keeping track of doctoral teaching; and Leif Magnusson and Stefan Schmiedel for always having liquid helium available, even on very short notice.

Many thanks to Daniel Rieländer at ICFO for letting me work on your photon-pair generation source, and thanks to all the other members in the group, you made my stay a pleasant memory.

I would like to thank my friends, especially Xiaofen Zhang for being around during all these years, from Shandong to Shanghai, from Denmark to Sweden, I am so lucky to have an old friend so close on my way; Xiaodan Pang, for making this possible; Mengqin Shen, Zheming Li, you were my spiritual consolation whenever I felt it was so tough to raise two children. Thanks Fangfang Yang and Jianfeng Zhou, Chunlin Yu and Mingtang Den for the trip we took together to Gran Canaria, it was such a pleasant journey.

I am very grateful to my family and my extended family for their support on every decision I made, especially my mother-in-law for helping me out with the children while this thesis was being written.

Finally, I would like to thank my husband, Chengjun, for your unconditional love, for always believing in me even when I had doubts about myself, and for taking my side without knowing what it was all about. I would not have gotten this far without you. Thanks my sons, Lucas for those numerous fundamental physical/philosophical questions you raised, which takes more than a doctoral degree to answer, and Max for being so cute right now, which really brightens up my day. I love you.

REFERENCES

1. W. K. Wootters and W. H. Zurek. *A single quantum cannot be cloned*. Nature **299**, 802–803 (1982).
2. M. A. Nielsen and I. Chuang. Quantum computation and quantum information (2002).
3. F. Bloch. *Nuclear induction*. Physical review **70**, 460 (1946).
4. R. P. Feynman, F. L. Vernon Jr and R. W. Hellwarth. *Geometrical representation of the Schrödinger equation for solving maser problems*. Journal of Applied Physics **28**, 49–52 (1957).
5. C. J. Foot. *Atomic physics*. OUP Oxford (2004).
6. R. Macfarlane and R. Shelby. *Spectroscopy of solids containing rare earth ions*. Elsevier Science Publisher (1987).
7. I. D. Abella, N. A. Kurnit and S. R. Hartmann. *Photon Echoes*. Phys. Rev. **141**, 391–406 (1966). URL <https://link.aps.org/doi/10.1103/PhysRev.141.391>.
8. E. L. Hahn. *Spin echoes*. Physical review **80**, 580 (1950).
9. C. S. Cornish, W. Babbitt and L. Tsang. *Demonstration of highly efficient photon echoes*. Optics letters **25**, 1276–1278 (2000).
10. J. Ruggiero, J.-L. Le Gouët, C. Simon and T. Chanelière. *Why the two-pulse photon echo is not a good quantum memory protocol*. Phys. Rev. A **79**, 053851 (2009). URL <https://link.aps.org/doi/10.1103/PhysRevA.79.053851>.
11. N. Sangouard, C. Simon, J. Minář, M. Afzelius, T. Chanelière, N. Gisin, J.-L. Le Gouët, H. de Riedmatten and W. Tittel. *Impossibility of faithfully storing single photons with the three-pulse photon echo*. Phys. Rev. A **81**, 062333 (2010). URL <https://link.aps.org/doi/10.1103/PhysRevA.81.062333>.
12. V. Damon, M. Bonarota, A. Louchet-Chauvet, T. Chaneliere and J. Le Gouët. *Revival of silenced echo and quantum mem-*

- ory for light. *New Journal of Physics* **13**, 093031 (2011).
13. S. Moiseev and S. Kröll. *Complete reconstruction of the quantum state of a single-photon wave packet absorbed by a Doppler-broadened transition*. *Physical review letters* **87**, 173601 (2001).
 14. M. Nilsson and S. Kröll. *Solid state quantum memory using complete absorption and re-emission of photons by tailored and externally controlled inhomogeneous absorption profiles*. *Optics communications* **247**, 393–403 (2005).
 15. A. Alexander, J. Longdell, M. Sellars and N. Manson. *Photon echoes produced by switching electric fields*. *Physical review letters* **96**, 043602 (2006).
 16. Y. L. Morgan P. Hedges, Jevon J. Longdell and M. J. Sellars. *Efficient quantum memory for light*. *Nature* **7465**, 1052 (2010). URL <http://www.nature.com/nature/journal/v465/n7301/abs/nature09081.html>.
 17. H. De Riedmatten, M. Afzelius, M. U. Staudt, C. Simon and N. Gisin. *A solid-state light–matter interface at the single-photon level*. *Nature* **456**, 773–777 (2008).
 18. M. Afzelius, C. Simon, H. de Riedmatten and N. Gisin. *Multimode quantum memory based on atomic frequency combs*. *Phys. Rev. A* **79**, 052329 (2009). URL <https://link.aps.org/doi/10.1103/PhysRevA.79.052329>.
 19. M. Sabooni, Q. Li, S. Kröll and L. Rippe. *Efficient quantum memory using a weakly absorbing sample*. *Physical review letters* **110**, 133604 (2013).
 20. N. Ohlsson, R. K. Mohan and S. Kröll. *Quantum computer hardware based on rare-earth-ion-doped inorganic crystals*. *Optics communications* **201**, 71–77 (2002).
 21. J. Longdell, M. Sellars and N. Manson. *Demonstration of conditional quantum phase shift between ions in a solid*. *Physical review letters* **93**, 130503 (2004).
 22. L. Rippe, B. Julsgaard, A. Walther, Y. Ying and S. Kröll. *Experimental quantum-state tomography of a solid-state qubit*. *Phys. Rev. A* **77**, 022307 (2008). URL <https://link.aps.org/doi/10.1103/PhysRevA.77.022307>.
 23. M. Tittel Wolfgang, Afzelius, T. Chaneliere, R. L. Cone, S. Kröll, S. A. Moiseev, M. Sellars et al. *Photon-echo quantum memory in solid state systems*. *Laser & Photonics Reviews* **4**, 244–267 (2010).
 24. G. Liu and B. Jacquier. *Spectroscopic properties of rare earths in optical materials*. *Springer Series in Material Science* (2005).

25. A. J. Freeman and R. Watson. *Theoretical investigation of some magnetic and spectroscopic properties of rare-earth ions*. Physical Review **127**, 2058 (1962).
26. W. Carnall, G. Goodman, K. Rajnak and R. Rana. *A systematic analysis of the spectra of the lanthanides doped into single crystal LaF₃*. The Journal of Chemical Physics **90**, 3443–3457 (1989).
27. B. Henderson and G. F. Imbusch. *Optical spectroscopy of inorganic solids* volume 44. Oxford University Press (2006).
28. A. Kaplyanskii. *Linear Stark effect in spectroscopy and luminescence of doped inorganic insulating crystals*. Journal of luminescence **100**, 21–34 (2002).
29. E. Fraval, M. Sellars and J. Longdell. *Dynamic decoherence control of a solid-state nuclear-quadrupole qubit*. Physical review letters **95**, 030506 (2005).
30. N. Ohlsson, M. Nilsson and S. Kröll. *Experimental investigation of delayed self-interference for single photons*. Phys. Rev. A **68**, 063812 (2003). URL <http://link.aps.org/doi/10.1103/PhysRevA.68.063812>.
31. M. Zhong, M. P. Hedges, R. L. Ahlefeldt, J. G. Bartholomew, S. E. Beavan, S. M. Wittig, J. J. Longdell and M. J. Sellars. *Optically addressable nuclear spins in a solid with a six-hour coherence time*. Nature **517**, 177–180 (2015).
32. R. W. Equall, R. L. Cone and R. M. Macfarlane. *Homogeneous broadening and hyperfine structure of optical transitions in Pr³⁺:Y₂SiO₅*. Phys. Rev. B **52**, 3963–3969 (1995). URL <https://link.aps.org/doi/10.1103/PhysRevB.52.3963>.
33. R. W. Equall, Y. Sun, R. Cone and R. Macfarlane. *Ultraslow optical dephasing in Eu 3+: Y₂SiO₅*. Physical review letters **72**, 2179 (1994).
34. Y. Sun, C. Thiel, R. Cone, R. Equall and R. Hutcheson. *Recent progress in developing new rare earth materials for hole burning and coherent transient applications*. Journal of luminescence **98**, 281–287 (2002).
35. K. Holliday, M. Croci, E. Vauthey and U. P. Wild. *Spectral hole burning and holography in an Y₂SiO₅:Pr³⁺ crystal*. Phys. Rev. B **47**, 14741–14752 (1993). URL <https://link.aps.org/doi/10.1103/PhysRevB.47.14741>.
36. A. Amari, A. Walther, M. Sabooni, M. Huang, S. Kröll, M. Afzelius, I. Usmani, B. Lauritzen, N. Sangouard, H. De Riedmatten et al. *Towards an efficient atomic frequency comb quantum memory*. Journal of Luminescence

- 130**, 1579–1585 (2010).
37. F. Könz, Y. Sun, C. Thiel, R. Cone, R. Equall, R. Hutcherson and R. Macfarlane. *Temperature and concentration dependence of optical dephasing, spectral-hole lifetime, and anisotropic absorption in Eu 3+: Y₂SiO₅*. Physical Review B **68**, 085109 (2003).
 38. R. C. Hilborn. *Einstein coefficients, cross sections, f values, dipole moments, and all that*. American Journal of Physics **50**, 982–986 (1982).
 39. F. R. Graf, A. Renn, U. P. Wild and M. Mitsunaga. *Site interference in Stark-modulated photon echoes*. Phys. Rev. B **55**, 11225–11229 (1997). URL <https://link.aps.org/doi/10.1103/PhysRevB.55.11225>.
 40. S. E. Beavan, E. A. Goldschmidt and M. J. Sellars. *Demonstration of a dynamic bandpass frequency filter in a rare-earth ion-doped crystal*. JOSA B **30**, 1173–1177 (2013).
 41. G. Heinze, C. Hubrich and T. Halfmann. *Stopped Light and Image Storage by Electromagnetically Induced Transparency up to the Regime of One Minute*. Phys. Rev. Lett. **111**, 033601 (2013). URL <http://link.aps.org/doi/10.1103/PhysRevLett.111.033601>.
 42. A. Arcangeli, M. Lovrić, B. Tumino, A. Ferrier and P. Goldner. *Spectroscopy and coherence lifetime extension of hyperfine transitions in ¹⁵¹Eu³⁺:Y₂SiO₅*. Phys. Rev. B **89**, 184305 (2014). URL <http://link.aps.org/doi/10.1103/PhysRevB.89.184305>.
 43. F. R. Graf, A. Renn, G. Zumofen and U. P. Wild. *Photon-echo attenuation by dynamical processes in rare-earth-ion-doped crystals*. Physical Review B **58**, 5462 (1998).
 44. R. Macfarlane and R. Shelby. *Coherent transient and hole-burning spectroscopy of rare earth ions in solids*. In *Modern Problems in Condensed Matter Sciences* volume 21 pages 51–184. Elsevier (1987).
 45. M. D. Lukin and A. Imamoglu. *Nonlinear Optics and Quantum Entanglement of Ultraslow Single Photons*. Phys. Rev. Lett. **84**, 1419–1422 (2000). URL <http://link.aps.org/doi/10.1103/PhysRevLett.84.1419>.
 46. K. Kutluer, M. F. Pascual-Winter, J. Dajczgewand, P. M. Ledingham, M. Mazzera, T. Chanelière and H. de Riedmaten. *Spectral-hole memory for light at the single-photon level*. Phys. Rev. A **93**, 040302 (2016). URL <https://link.aps.org/doi/10.1103/PhysRevA.93.040302>.
 47. A. V. Turukhin, V. S. Sudarshanam, M. S. Shahriar, J. A.

- Musser, B. S. Ham and P. R. Hemmer. *Observation of Ultra-slow and Stored Light Pulses in a Solid*. Phys. Rev. Lett. **88**, 023602 (2001). URL <https://link.aps.org/doi/10.1103/PhysRevLett.88.023602>.
48. C. G. B. Garrett and D. E. McCumber. *Propagation of a Gaussian Light Pulse through an Anomalous Dispersion Medium*. Phys. Rev. A **1**, 305–313 (1970). URL <https://link.aps.org/doi/10.1103/PhysRevA.1.305>.
 49. G. M. Gehring, A. Schweinsberg, C. Barsi, N. Kostinski and R. W. Boyd. *Observation of backward pulse propagation through a medium with a negative group velocity*. Science **312**, 895–897 (2006).
 50. L. V. Hau, S. E. Harris, Z. Dutton and C. H. Behroozi. *Light speed reduction to 17 metres per second in an ultracold atomic gas*. Nature **397**, 594–598 (1999).
 51. R. N. Shakhmuratov, A. Rebane, P. Mégret and J. Odeurs. *Slow light with persistent hole burning*. Phys. Rev. A **71**, 053811 (2005). URL <https://link.aps.org/doi/10.1103/PhysRevA.71.053811>.
 52. A. Walther, A. Amari, S. Kröll and A. Kalachev. *Experimental superradiance and slow-light effects for quantum memories*. Phys. Rev. A **80**, 012317 (2009). URL <http://link.aps.org/doi/10.1103/PhysRevA.80.012317>.
 53. E. Courtens. *Giant Faraday Rotations in Self-Induced Transparency*. Phys. Rev. Lett. **21**, 3–5 (1968). URL <https://link.aps.org/doi/10.1103/PhysRevLett.21.3>.
 54. R. Lauro, T. Chanelière and J. L. Le Gouët. *Slow light using spectral hole burning in a Tm^{3+} -doped yttrium-aluminum-garnet crystal*. Phys. Rev. A **79**, 063844 (2009). URL <https://link.aps.org/doi/10.1103/PhysRevA.79.063844>.
 55. R. Shakhmuratov. *The energy storage in the formation of slow light*. Journal of Modern Optics **57**, 1355–1365 (2010).
 56. K. D. Dorozynska. *Designing an Experiment to Investigate Slow Light Effects in Whispering Gallery Mode Resonators*. Master’s thesis Lund University (2015).
 57. M. Sabooni, A. N. Nilsson, G. Kristensson and L. Rippe. *Wave propagation in birefringent materials with off-axis absorption or gain*. Phys. Rev. A **93**, 013842 (2016). URL <https://link.aps.org/doi/10.1103/PhysRevA.93.013842>.
 58. R. Beach, M. D. Shinn, L. Davis, R. W. Solarz and W. F. Krupke. *Optical absorption and stimulated emission of neodymium in yttrium orthosilicate*. IEEE Journal of Quan-

- tum Electronics **26**, 1405–1412 (1990).
59. A. Walther, B. Julsgaard, L. Rippe, Y. Ying, S. Kröll, R. Fisher and S. Glaser. *Extracting high fidelity quantum computer hardware from random systems*. Physica Scripta **2009**, 014009 (2009).
 60. C. Thiel, T. Böttger and R. Cone. *Rare-earth-doped materials for applications in quantum information storage and signal processing*. Journal of luminescence **131**, 353–361 (2011).
 61. A. A. Savchenkov, A. B. Matsko, V. S. Ilchenko and L. Maleki. *Optical resonators with ten million finesse*. Opt. Express **15**, 6768–6773 (2007). URL <http://www.opticsexpress.org/abstract.cfm?URI=oe-15-11-6768>.
 62. D. L. McAuslan, D. Korystov and J. J. Longdell. *Coherent spectroscopy of rare-earth-metal-ion-doped whispering-gallery-mode resonators*. Phys. Rev. A **83**, 063847 (2011). URL <https://link.aps.org/doi/10.1103/PhysRevA.83.063847>.
 63. N. Sinclair, E. Saglamyurek, H. Mallahzadeh, J. A. Slater, M. George, R. Ricken, M. P. Hedges, D. Oblak, C. Simon, W. Sohler and W. Tittel. *Spectral Multiplexing for Scalable Quantum Photonics using an Atomic Frequency Comb Quantum Memory and Feed-Forward Control*. Phys. Rev. Lett. **113**, 053603 (2014). URL <https://link.aps.org/doi/10.1103/PhysRevLett.113.053603>.
 64. H. Zhang, M. Sabooni, L. Rippe, C. Kim, S. Kröll, L. V. Wang and P. R. Hemmer. *Slow light for deep tissue imaging with ultrasound modulation*. Applied physics letters **100**, 131102 (2012).
 65. A. Kinoshita, Q. Li, L. Rippe and S. Kröll. *Development and characterization of high suppression and high étendue narrowband spectral filters*. Applied optics **55**, 10442–10448 (2016).
 66. C. Clausen, F. Bussières, M. Afzelius and N. Gisin. *Quantum Storage of Heralded Polarization Qubits in Birefringent and Anisotropically Absorbing Materials*. Phys. Rev. Lett. **108**, 190503 (2012). URL <https://link.aps.org/doi/10.1103/PhysRevLett.108.190503>.
 67. X. Guo, H. Y. Zhou, S. Guo, X. X. Luan, W. K. Cui, Y. F. Ma and L. Shi. *Design of broadband omnidirectional antireflection coatings using ant colony algorithm*. Opt. Express **22**, A1137–A1144 (2014). URL <http://www.opticsexpress.org/abstract.cfm?URI=oe-22-104-A1137>.
 68. K. Si, R. Fiolka and M. Cui. *Breaking the spatial resolution*

- barrier via iterative sound-light interaction in deep tissue microscopy. *Scientific reports* **2** (2012).
69. S. R. Hastings-Simon, M. U. Staudt, M. Afzelius, P. Baldi, D. Jaccard, W. Tittel and N. Gisin. *Controlled Stark shifts in Er^{3+} -doped crystalline and amorphous waveguides for quantum state storage*. *Optics communications* **266**, 716–719 (2006).
 70. H.-J. Briegel, W. Dür, J. I. Cirac and P. Zoller. *Quantum Repeaters: The Role of Imperfect Local Operations in Quantum Communication*. *Phys. Rev. Lett.* **81**, 5932–5935 (1998). URL <https://link.aps.org/doi/10.1103/PhysRevLett.81.5932>.
 71. I. Usmani, M. Afzelius, H. De Riedmatten and N. Gisin. *Mapping multiple photonic qubits into and out of one solid-state atomic ensemble*. *Nature Communications* **1**, 12 (2010).
 72. M. Fleischhauer and M. D. Lukin. *Quantum memory for photons: Dark-state polaritons*. *Phys. Rev. A* **65**, 022314 (2002). URL <https://link.aps.org/doi/10.1103/PhysRevA.65.022314>.
 73. B. Kraus, W. Tittel, N. Gisin, M. Nilsson, S. Kröll and J. Cirac. *Quantum memory for nonstationary light fields based on controlled reversible inhomogeneous broadening*. *Physical Review A* **73**, 020302 (2006).
 74. G. Hétet, J. J. Longdell, M. J. Sellars, P. K. Lam and B. C. Buchler. *Multimodal Properties and Dynamics of Gradient Echo Quantum Memory*. *Phys. Rev. Lett.* **101**, 203601 (2008). URL <https://link.aps.org/doi/10.1103/PhysRevLett.101.203601>.
 75. M. Bonarota, V. Damon, T. Chanelière, J.-L. L. Gouët and M. F. P. Winter. *Revival of Silenced Echo for Optical Quantum Memories: Efficiency and Noise Level*. In *Research in Optical Sciences* page QW2A.6. Optical Society of America (2012). URL <http://www.osapublishing.org/abstract.cfm?URI=QIM-2012-QW2A.6>.
 76. S. E. Beavan, P. M. Ledingham, J. J. Longdell and M. J. Sellars. *Photon echo without a free induction decay in a double- Λ system*. *Optics letters* **36**, 1272–1274 (2011).
 77. S. E. Beavan, M. P. Hedges and M. J. Sellars. *Demonstration of Photon-Echo Rephasing of Spontaneous Emission*. *Phys. Rev. Lett.* **109**, 093603 (2012). URL <https://link.aps.org/doi/10.1103/PhysRevLett.109.093603>.
 78. L.-M. Duan, M. Lukin, J. I. Cirac and P. Zoller. *Long-distance quantum communication with atomic ensembles and linear*

- optics*. Nature **414**, 413–418 (2001).
79. T. Mossberg, A. Flusberg, R. Kachru and S. Hartmann. *Total scattering cross section for Na on He measured by stimulated photon echoes*. Physical Review Letters **42**, 1665 (1979).
 80. G. Heinze, A. Rudolf, F. Beil and T. Halfmann. *Storage of images in atomic coherences in a rare-earth-ion-doped solid*. Physical Review A **81**, 011401 (2010).
 81. D. Schraft, T. Halfmann, G. T. Genov and N. V. Vitanov. *Experimental demonstration of composite adiabatic passage*. Phys. Rev. A **88**, 063406 (2013). URL <https://link.aps.org/doi/10.1103/PhysRevA.88.063406>.
 82. M. Bonarota, J. Ruggiero, J. L. L. Gouët and T. Chanelière. *Efficiency optimization for atomic frequency comb storage*. Phys. Rev. A **81**, 033803 (2010). URL <https://link.aps.org/doi/10.1103/PhysRevA.81.033803>.
 83. M. Lukin. *Colloquium: Trapping and manipulating photon states in atomic ensembles*. Reviews of Modern Physics **75**, 457 (2003).
 84. J. Nunn, K. Reim, K. Lee, V. Lorenz, B. Sussman, I. Walmsley and D. Jaksch. *Multimode memories in atomic ensembles*. Physical review letters **101**, 260502 (2008).
 85. C. Simon, H. De Riedmatten, M. Afzelius, N. Sangouard, H. Zbinden and N. Gisin. *Quantum repeaters with photon pair sources and multimode memories*. Physical review letters **98**, 190503 (2007).
 86. W. Tittel, M. Afzelius, R. Cone, T. Chaneliere, S. Kröll, S. Moiseev and M. Sellars. *Photon-echo quantum memory*. arXiv preprint arXiv:0810.0172 (2009).
 87. S. A. Moiseev and N. M. Arslanov. *Efficiency and fidelity of photon-echo quantum memory in an atomic system with longitudinal inhomogeneous broadening*. Phys. Rev. A **78**, 023803 (2008). URL <https://link.aps.org/doi/10.1103/PhysRevA.78.023803>.
 88. M. Hosseini, B. M. Sparkes, G. Campbell, P. K. Lam and B. C. Buchler. *High efficiency coherent optical memory with warm rubidium vapour*. Nature communications **2**, 174 (2011).
 89. M. Afzelius and C. Simon. *Impedance-matched cavity quantum memory*. Phys. Rev. A **82**, 022310 (2010). URL <https://link.aps.org/doi/10.1103/PhysRevA.82.022310>.
 90. L. Rippe, M. Nilsson, S. Kröll, R. Klieber and D. Suter. *Experimental demonstration of efficient and selective population transfer and qubit distillation in a rare-earth-metal-ion-*

- doped crystal. Phys. Rev. A **71**, 062328 (2005). URL <https://link.aps.org/doi/10.1103/PhysRevA.71.062328>.
91. E. Fraval, M. J. Sellars and J. J. Longdell. *Method of Extending Hyperfine Coherence Times in $Pr^{3+}:Y_2SiO_5$* . Phys. Rev. Lett. **92**, 077601 (2004). URL <http://link.aps.org/doi/10.1103/PhysRevLett.92.077601>.
 92. N. Timoney, B. Lauritzen, I. Usmani, M. Afzelius and N. Gisin. *Atomic frequency comb memory with spin-wave storage in $^{153}Eu^{3+}:Y_2SiO_5$* . Journal of Physics B: Atomic, Molecular and Optical Physics **45**, 124001 (2012).
 93. B. S. Ham, P. Hemmer and M. Shahriar. *Efficient electromagnetically induced transparency in a rare-earth doped crystal*. Optics communications **144**, 227–230 (1997).
 94. H. Goto, S. Nakamura and K. Ichimura. *Experimental determination of intracavity losses of monolithic Fabry-Perot cavities made of $Pr^{3+}:Y_2SiO_5$* . Optics express **18**, 23763–23775 (2010).
 95. N. Anderson and R. Lalezari. *High-performance mirrors excel for intracavity applications*. Laser Focus World **48**, 48–53 (2012).
 96. P. Jobez, I. Usmani, N. Timoney, C. Laplane, N. Gisin and M. Afzelius. *Cavity-enhanced storage in an optical spin-wave memory*. New Journal of Physics **16**, 083005 (2014). URL <http://stacks.iop.org/1367-2630/16/i=8/a=083005>.
 97. L. Rippe. *Quantum computing with naturally trapped sub-nanometre-spaced ions*. PhD thesis Lund University (2006).
 98. A. Walther. *Coherent processes in rare-earth-ion-doped solids*. PhD thesis Lund University (2009).
 99. J. Karlsson. *Cerium as a quantum state probe for rare-earth qubits in a crystal*. PhD thesis Lund University (2015).
 100. R. Drever, J. L. Hall, F. Kowalski, J. Hough, G. Ford, A. Munley and H. Ward. *Laser phase and frequency stabilization using an optical resonator*. Applied Physics B **31**, 97–105 (1983).
 101. R. V. Pound. *Electronic frequency stabilization of microwave oscillators*. Review of Scientific Instruments **17**, 490–505 (1946).
 102. E. D. Black. *An introduction to Pound–Drever–Hall laser frequency stabilization*. American Journal of Physics **69**, 79–87 (2001).
 103. G. Bjorklund, M. Levenson, W. Lenth and C. Ortiz. *Frequency modulation (FM) spectroscopy; Theory of lineshapes*

- and signal-tonoise analysis*. Applied physics. B, Photophysics and laser chemistry **32**, 145–152 (1983).
104. B. Young, F. Cruz, W. M. Itano and J. Bergquist. *Visible lasers with subhertz linewidths*. Physical Review Letters **82**, 3799 (1999).
 105. N. Huntemann, C. Sanner, B. Lipphardt, C. Tamm and E. Peik. *Single-ion atomic clock with 3×10^{18} systematic uncertainty*. Physical review letters **116**, 063001 (2016).
 106. B. P. Abbott, R. Abbott, T. Abbott, M. Abernathy, F. Acernese, K. Ackley, C. Adams, T. Adams, P. Addesso, R. Adhikari et al. *Observation of gravitational waves from a binary black hole merger*. Physical review letters **116**, 061102 (2016).
 107. C. Eisele, A. Y. Nevsky and S. Schiller. *Laboratory test of the isotropy of light propagation at the 10^{-17} level*. Physical Review Letters **103**, 090401 (2009).
 108. T. Legero, D. Matei, S. Häfner, C. Grebing, R. Weyrich, F. Riehle, U. Sterr, W. Zhang, J. Robinson, L. Sonderhouse et al. *1.5 μm lasers with sub 10 mHz linewidth*. In *Lasers and Electro-Optics (CLEO), 2017 Conference on* pages 1–2. IEEE (2017).
 109. K. Numata, A. Kemery and J. Camp. *Thermal-noise limit in the frequency stabilization of lasers with rigid cavities*. Physical review letters **93**, 250602 (2004).
 110. Y. Yan. *Towards single Ce ion detection in a bulk crystal for the development of a single-ion qubit readout scheme*. PhD thesis Lund Univeristy (2013).
 111. A. Wiman. *Laser stablization to a low expansion Fabry-Pérot cavity*. Master’s thesis Lund University (2011).
 112. T. Legero, T. Kessler and U. Sterr. *Tuning the thermal expansion properties of optical reference cavities with fused silica mirrors*. JOSA B **27**, 914–919 (2010).
 113. D. R. Leibrandt, M. J. Thorpe, M. Notcutt, R. E. Drullinger, T. Rosenband and J. C. Bergquist. *Spherical reference cavities for frequency stabilization of lasers in non-laboratory environments*. Opt. Express **19**, 3471–3482 (2011). URL <http://www.opticsexpress.org/abstract.cfm?URI=oe-19-4-3471>.
 114. J. Alnis, A. Matveev, N. Kolachevsky, T. Udem and T. Hänsch. *Subhertz linewidth diode lasers by stabilization to vibrationally and thermally compensated ultralow-expansion glass Fabry-Pérot cavities*. Physical Review A **77**, 053809 (2008).
 115. A. Amir, Y. Oreg and Y. Imry. *On relaxations and aging*

-
- of various glasses*. Proceedings of the National Academy of Sciences **109**, 1850–1855 (2012).
116. M. Fischer, N. Kolachevsky, M. Zimmermann, R. Holzwarth, T. Udem, T. W. Hänsch, M. Abgrall, J. Grünert, I. Maksimovic, S. Bize et al. *New limits on the drift of fundamental constants from laboratory measurements*. Physical Review Letters **92**, 230802 (2004).

PAPERS

Efficient quantum memory using a weakly absorbing sample

M. Sabooni, Q. Li, S. Kröll and L. Rippe.

Phys. Rev. Lett. **110**, 133604 (2013).

Efficient Quantum Memory Using a Weakly Absorbing Sample

Mahmood Sabooni, Qian Li, Stefan Kröll, and Lars Rippe

Department of Physics, Lund University, P. O. Box 118, SE-22100 Lund, Sweden

(Received 29 December 2012; published 26 March 2013)

A light-storage experiment with a total (storage and retrieval) efficiency $\eta = 56\%$ is carried out by enclosing a sample, with a single-pass absorption of 10%, in an impedance-matched cavity. The experiment is carried out using the atomic frequency comb (AFC) technique in a praseodymium-doped crystal ($0.05\%\text{Pr}^{3+}:\text{Y}_2\text{SiO}_5$) and the cavity is created by depositing reflection coatings directly onto the crystal surfaces. The AFC technique has previously by far demonstrated the highest multimode capacity of all quantum memory concepts tested experimentally. We claim that the present work shows that it is realistic to create efficient, on-demand, long storage time AFC memories.

DOI: 10.1103/PhysRevLett.110.133604

PACS numbers: 42.50.Ct, 03.67.Hk, 42.50.Gy, 42.50.Md

A quantum memory that has the ability to map onto, store in, and later retrieve the quantum state of light from matter is an important building block in quantum information processing [1]. Quantum memories are expected to become vital elements for long distance quantum key distribution [2,3]. Quantum computing based on linear optics schemes [4], signal synchronization in optical quantum processing [5,6], the implementation of a deterministic single-photon source [7], and precision measurements based on mapping of the quantum properties of an optical state to an atomic ensemble [8] are other applications of quantum memories. For most of the applications mentioned, high performance will be required in terms of high efficiency [9,10], on-demand readout, long storage time [11,12], multimode storage capacity [13,14], and broad bandwidth [15].

Many protocols have been proposed to realize an efficient quantum memory; these include electromagnetically induced transparency (EIT) [16], off-resonant Raman interactions [17], controlled reversible inhomogeneous broadening (CRIB) [18–20], gradient echo memory (GEM) [21], and atomic frequency combs (AFC) [22]. The most impressive storage and retrieval efficiencies so far, 87% [9] and 69% [10], were achieved in hot atomic vapor and rare-earth doped crystals, respectively, using the GEM technique. Additionally, 43% storage and retrieval efficiency using EIT in a hot Rb vapor [23] and 35% using AFC in a rare-earth doped crystal [24] were attained.

The AFC technique [22] is employed in this Letter because the number of (temporal) modes that can be stored in a sample is independent of the optical depth (d) of the storage material, in contrast to other quantum memory approaches. An AFC structure consists of a set of (artificially created) narrow absorbing peaks with equidistant frequency spacing Δ and uniform peak width γ (see the inset in Fig. 3). An input (storage) field (at time $t = 0$) that spectrally overlaps the AFC structure will be absorbed and leave the absorbers (in our case the Pr ions) in a superposition state [22]. If the coherence time is long compared

to $1/\Delta$, a collective emission due to constructive interference (similar as for the modes in a mode-locked laser) will occur at time $t_{\text{echo}} = 1/\Delta$.

High storage and retrieval efficiency is one of the main targets of quantum memories and this relies on strong coupling between light and matter [1]. One approach for studying light-matter interaction is based on the high finesse cavity-enhanced interaction of light with a single atom [25,26]. Another alternative for increasing the coupling efficiency of a quantum interface between light and matter is using an optically thick free space atomic ensemble [1]. In this Letter, we combine the advantages of both approaches to implement an efficient quantum interface in a weakly absorbing solid state medium [27]. Within the ensemble approach several experimental realizations from room-temperature alkali gases [28], to alkali atoms cooled and trapped at temperature of a few tens or hundreds of microkelvin [29] have been investigated. Among the ensemble-based approaches impurity centers in a solid state crystal is a powerful alternative for quantum memories because of the absence of atomic movement.

The objective of this Letter is to demonstrate a quantum memory with high storage and retrieval efficiency, with the added benefit of being achievable in a weakly absorbing medium. Another benefit is the short crystal length (2 mm), and small physical storage volume ($\ll \text{mm}^3$). This can simplify the implementation of long-term storage in the hyperfine levels, as will be further discussed at the end of the Letter. For an AFC memory with no cavity and with emission in the forward direction, the maximum theoretical efficiency is limited to 54% [22]. Our work is based on the proposals in Refs. [30,31], where it is shown that close to unity storage and retrieval efficiency can be obtained, using an atomic ensemble in an impedance-matched cavity. A cavity can be impedance matched, by having the absorption per cavity round trip ($1 - e^{-2\alpha L}$) equal to the transmission of the input coupling mirror ($1 - R_1$), while the back mirror is 100% reflecting, which gives $R_1 = e^{-2\alpha L}$, where α is the absorption coefficient and L is the

length of the optical memory material. For this impedance-matching condition, all light sent to the cavity will be absorbed in the absorbing sample inside the cavity and no light is reflected.

The storage cavity is made up of a 2 mm long 0.05% $\text{Pr}^{3+}:\text{Y}_2\text{SiO}_5$ crystal; see Fig. 1. To reduce the complexity of the alignment and reduce losses, the crystal surfaces are reflection coated directly, rather than using separate mirrors. The two cavity crystal surfaces are not exactly parallel as shown in Fig. 1 ($\theta \approx 10$ arcsec). Part of the incoming field \vec{E}_{in} will be reflected (\vec{E}_{refl}) at the first mirror surface ($R1$), see Fig. 1. The field leaking out through $R1$ from the cavity, \vec{E}_{leak} , is coherently added to \vec{E}_{refl} such that $\vec{E}_{\text{out}} = \vec{E}_{\text{refl}} + \vec{E}_{\text{leak}}$. At the impedance-matched condition, \vec{E}_{refl} and \vec{E}_{leak} differ in phase by π and have the same amplitude $|\vec{E}_{\text{refl}}| = |\vec{E}_{\text{leak}}|$. This means that the light intensity at the reflection detector (PD3) should ideally vanishes if this condition is satisfied.

The cavity crystal (impedance matching) was first tested without memory preparation. The effective cavity length can be optimized by translating the cavity perpendicular to the beam propagation direction. Here a sub- μm accuracy (Attocube system, ANCz150) translation stage was used. Then, a weak Gaussian pulse ($\tau_{\text{FWHM}} = 250$ ns) with a

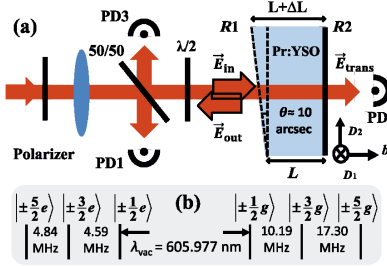


FIG. 1 (color online). (a) Part of the experimental setup. A frequency stabilized (< 1 kHz linewidth) dye laser at $\lambda_{\text{vac}} = 605.977$ nm is employed as light source. A 50/50 beam splitter splits off part of the input light onto a photo diode (PD1), to calibrate against variations in the input light intensity. Two other photo diodes monitor the transmitted (PD2) and the reflected (PD3) light from the cavity. The cavity length along the b axis is $L = 2$ mm and the crystal diameter in the (D_1, D_2) plane is 12 mm. b , D_1 , and D_2 are principal axes of the crystal [46]. A beam waist of about $100 \mu\text{m}$ is created at the crystal center via a lens with $f = 400$ mm. A half-wave plate ($\lambda/2$) is employed to align the polarization direction to a principal axis of the cavity crystal, which is immersed in liquid helium at 2.1 K. The input and output facet of the crystal has $R1 = 80\%$ and $R2 = 99.7\%$ reflectivity. A small part of the cavity crystal is left uncoated for measurements without a cavity effect. (b) The hyperfine splitting of the ground $|g\rangle$ and excited $|e\rangle$ state of the $^3H_4 - D_2$ transition of site I in $\text{Pr}^{3+}:\text{Y}_2\text{SiO}_5$ [38].

small pulse area and repetition rate of 10 Hz was injected into the cavity while the laser frequency was slowly scanned during ~ 6 s across the inhomogeneous Pr ion absorption line. To find the best impedance-matched point, the cavity crystal was translated in small steps perpendicular to the beam direction. For each step a 18 GHz laser scan was carried out. The calibrated reflected part of the input pulse (PD3/PD1) is plotted versus the frequency offset from the $\text{Pr}^{3+}:\text{Y}_2\text{SiO}_5$ inhomogeneous line center in Fig. 2, for the position where the highest absorption was obtained. This measurement shows that a maximum of about 84% of the input energy could be absorbed. This occurred about 45 GHz above the inhomogeneous broadening center frequency. This will set an upper limit for the achievable storage and retrieval efficiency in the present setup. Due to the absorption tailoring during the memory preparation (to be discussed below), the impedance-matching condition will be fulfilled closer to the inhomogeneous line center in the actual storage experiment, but the measurement establish the losses caused by spatial mode mismatching. In addition, in the present setup the dye laser is frequency stabilized against a Fabry-Pérot cavity using the Pound-Drever-Hall (PDH) locking technique [32,33]. This provide more freedom for locking the laser frequency further away from the inhomogeneous profile center compared to our earlier work [34] where stabilization based on hole burning was used. This has a

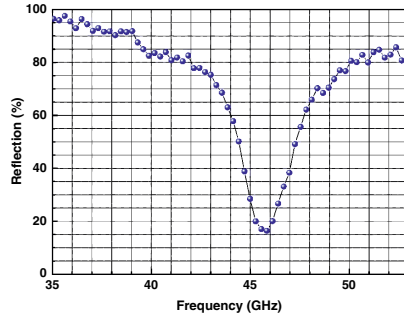


FIG. 2 (color online). The normalized reflected signal (PD3/PD1) is plotted against the frequency offset from the $\text{Pr}^{3+}:\text{Y}_2\text{SiO}_5$ inhomogeneous line center. The crystal was translated perpendicular to the input beam (see Fig. 1) and the graph is a frequency scan for the position that gave the best impedance matching. At the impedance-matching condition the reflected light detected at PD3 should vanish. The best impedance-matched condition without memory preparation (i.e., spectral manipulation by the absorption profile, see text) was a reflection of 16% (84% absorption), which was measured about 45 GHz above the inhomogeneous broadening center frequency that is located at 0 GHz in this figure.

large influence on improving the impedance-matching condition.

To demonstrate a quantum memory based on the AFC protocol, first, a transparent (nonabsorbing) spectral transmission window within the Pr ion absorption profile was created using optical pumping. An accurate description of the pulse sequences required for creating such a transparency window, which henceforth is called a spectral pit, is given in Ref. [24]. Because of the strong dispersion created by the spectral pit [35], the cavity free spectral range (FSR) and the cavity linewidth are reduced by 3–4 orders of magnitude [36]. The reduction can be understood as follows. The cavity FSR is $\Delta\nu_{\text{mode}} = \frac{c_0}{2L} \frac{1}{n_g}$ [37] where c_0 is speed of light in the vacuum, L is the cavity length, and n_g is the group refractive index. $n_g = n_r(\nu) + \nu \frac{dn_r(\nu)}{d\nu}$ and $n_r(\nu)$ is the real refractive index as a function of frequency ν . In case of no or constant absorption, the dispersion term is negligible compared to the real refractive index ($n_r(\nu) \gg \nu \frac{dn_r(\nu)}{d\nu}$). The FSR of this cavity with no absorbing material is about 40 GHz. In the presence of sharp transmission structures ($n_r(\nu) \ll \nu \frac{dn_r(\nu)}{d\nu}$) a dramatic reduction of the cavity FSR and the cavity linewidth can occur. In our case $\nu \frac{dn_r(\nu)}{d\nu} > 1000n_r(\nu)$ and the reduction is >3 orders of magnitude at the center of the inhomogeneous line. A more detailed description of the cavity FSR reduction is given in Refs. [34,36]. Translating the crystal perpendicular to the beam propagation direction will move the cavity transmission within the spectral pit due to the small wedge on the crystal.

After preparing the transparent (nonabsorbing) spectral transmission window, each AFC peak is created using a complex hyperbolic secant pulse (sechyp for short) with chirp width $f_{\text{width}} = 70$ kHz [38] and temporal width $t_{\text{FWHM}} = 16.8 \mu\text{s}$ [38]. This pulse excites ions from $|\pm \frac{5}{2}g\rangle \rightarrow |\pm \frac{5}{2}e\rangle$ state [see Fig. 1(a)]. From the $|\pm \frac{5}{2}e\rangle$ state, Pr ions will decay mostly to the $|\pm \frac{5}{2}g\rangle$ due to the high branching ratio for the $|\pm \frac{5}{2}e\rangle \rightarrow |\pm \frac{5}{2}g\rangle$ transition [39]. This pulse is repeated several (~ 50) times with a waiting time of $500 \mu\text{s}$ between each pulse. This process creates one AFC peak. Repeating this procedure with a consecutive change of center frequency of the sechyp pulse by Δ will create the other AFC peaks. The finesse of the AFC structure with peak width γ and peak separation Δ will be $F_{\text{AFC}} = \frac{\Delta}{\gamma}$.

As we discussed earlier, the absorption engineering of the Pr ions inside the cavity will directly affect the cavity modes via strong dispersion. Therefore, measuring the AFC structure properties in the cavity case is challenging. In order to at least to some extent estimate the AFC structure properties, the coating of a small part of the cavity crystal is removed, and the same preparation as for the memory is performed in this part. The remaining coating could affect the precision of this measurement through the cavity dispersion effect. The trace in Fig. 3 is recorded

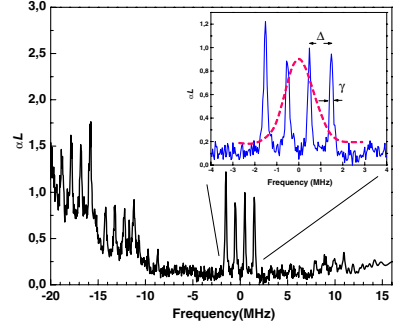


FIG. 3 (color online). The absorption profile created through the optical pumping process is shown. This measurement is done in a small part of the cavity crystal where the coating was removed. From the Pr inhomogeneous absorption profile, four AFC peaks, all absorbing on the $|\pm \frac{5}{2}g\rangle \rightarrow |\pm \frac{5}{2}e\rangle$ transition, are created. The spectral content of the storage pulse is shown schematically in the inset by the red dashed line across the AFC structure, which has peak width γ and peak separation Δ . The finesse of the AFC structure is $F_{\text{AFC}} = \frac{\Delta}{\gamma}$.

using a weak readout beam that is frequency chirped at a rate of $10 \text{ kHz}/\mu\text{s}$ across the frequency region of the AFC structure. The overall spectral structure is complicated and a detailed discussion of the spectrum is beyond the scope of the present Letter. The inset in Fig. 3 shows the spectral content of the storage pulse relative to the four AFC peaks. The cavity transmission linewidth is tuned to be at least as wide as the whole prepared AFC structure [34]. In this case it was ≈ 11 MHz wide.

The input pulse is stored using the $|\pm \frac{5}{2}g\rangle \rightarrow |\pm \frac{5}{2}e\rangle$ transition for ions initially in state $|\pm \frac{5}{2}g\rangle$. A Gaussian pulse with a duration of $\tau_{\text{FWHM}} = 250$ ns and small pulse area is employed as a storage pulse. The frequency of the storage pulse is tuned to the center frequency of an AFC structure with a peak separation $\Delta = 0.9$ MHz. The retrieved echo pulse is detected at detector PD3 after $1.1 \mu\text{s}$ as shown with black solid line in Fig. 4. In addition, multiple echoes are detected at times $2.2 \mu\text{s}$ and $3.3 \mu\text{s}$ which are probably due to multiple rephasing of the ensemble.

In order to assess the storage and retrieval efficiency, the intensity of the input storage pulse at the cavity crystal should be measured. To this end, the cavity crystal was turned $\sim 180^\circ$ such that the input storage pulse impinged on the $R2 = 99.7\%$ mirror, with no pit and peak creation active. In this way the input storage pulse is (almost completely) reflected and the signal on PD3, after calibrating using PD1, can be used as a reference value for the storage pulse input intensity, as shown by a red dashed line in Fig. 4. The pulse area of the first echo at $\approx 1.1 \mu\text{s}$

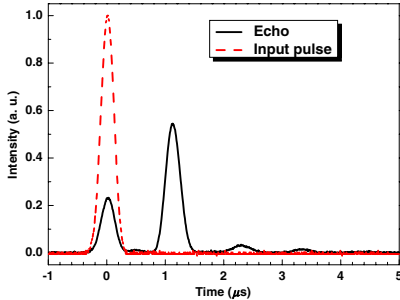


FIG. 4 (color online). The input storage pulse as a reference detected at PD3 (see text) is shown as a red dashed line. The retrieved echo pulse is detected at detector PD3 after $1.1 \mu\text{s}$ as shown with the black solid line. The area of the echo pulse at $1.1 \mu\text{s}$ divided by the reference signal pulse area gives a storage and retrieval efficiency of the memory of $\eta = 56\%$.

divided by the reference signal pulse area gives a storage and retrieval efficiency of the memory of $\eta = 56\%$ (four independent measurements gave values ranging from 55.5% to 56.8%). The leakage through the cavity detected on PD2 (see Fig. 1) during the storage is almost negligible ($\approx 1\%$ of the storage pulse).

The present result is lower than the best storage and retrieval efficiency achieved elsewhere [9,10]; however, it is the highest storage and retrieval efficiency based on the AFC protocol, which is presently the best multimode quantum state storage protocol [40], also in the cavity configuration [31]. The source of losses in the current setup can be estimated as about 16% related to the impedance mismatching, 5% associated with the multiple echoes, about 1% from transmission through the cavity, about 10% linked to the AFC finesse dephasing factor, and the rest possibly related to the crystal background absorption. By addressing these losses the efficiency could be improved. We estimate that the efficiency under the same conditions as in this experiment for a crystal in a single-pass configuration would be $<1\%$ [34]. Therefore the cavity configuration shows a significant enhancement compared to the bare crystal.

In order to obtain on-demand and long-term storage based on the AFC protocol [22], the ground-excited state superposition should be transferred to, and then brought back from, a spin-level superposition between two of the ground states [41]. The dephasing due to the spin state inhomogeneous broadening can be suppressed using radio-frequency (rf) spin-echo techniques. In addition, even longer ($> 60\text{s}$) storage time is possible by utilizing zero first-order Zeeman (ZEFOZ) shift [42] and spin-echo techniques to suppress slow variations of the spin transition frequencies [11,12]. Quantum memories in a smaller

physical volumes requires significantly lower rf power. Although the present result is 13% lower than the highest rare-earth crystal efficiency results so far [10], it is obtained in a crystal that is 10 times shorter. This may in practice significantly simplify long time, high efficiency spin storage, since too large volumes will require excessive rf powers to compensate for the spin inhomogeneous broadening. In addition, efficient quantum memories in a weakly absorbing media opens up the possibility of utilizing materials with low optical depth but good coherence properties (e.g., $\text{Eu}^{3+}:\text{Y}_2\text{SiO}_5$ [43]).

In summary, we have demonstrated a quantum memory with $\eta = 56\%$ storage and retrieval efficiency based on the AFC protocol. This is done in a weakly absorbing medium and short crystal length (2 mm) by utilizing an impedance-matched cavity configuration. This achievement, in addition to the storage and recall of weak coherent optical pulses [14,44], spin-wave storage demonstration [41], the best multimode quantum memory [13,14], and storage of entanglement [15,45] increases the possibility of creating an efficient, on-demand, long storage time, and multimode quantum memory based on the AFC protocol in the future.

This work was supported by the Swedish Research Council, the Knut & Alice Wallenberg Foundation, the Maja & Erik Lindqvists forskningsstiftelse, the Crafoord Foundation, and the EC FP7 Contract No. 247743 (QuRep) and (Marie Curie Action) REA Grant No. 287252 (CIPRIS).

- [1] K. Hammerer, A. S. Sørensen, and E. S. Polzik, *Rev. Mod. Phys.* **82**, 1041 (2010).
- [2] L. M. Duan, M. D. Lukin, J. I. Cirac, and P. Zoller, *Nature (London)* **414**, 413 (2001).
- [3] N. Sangouard, C. Simon, B. Zhao, Y. A. Chen, H. de Riedmatten, J. W. Pan, and N. Gisin, *Phys. Rev. A* **77**, 062301 (2008).
- [4] P. Kok, W. J. Munro, K. Nemoto, T. C. Ralph, J. P. Dowling, and G. J. Milburn, *Rev. Mod. Phys.* **79**, 135 (2007).
- [5] E. Knill, R. Laflamme, and G. J. Milburn, *Nature (London)* **409**, 46 (2001).
- [6] J. Nunn, N. K. Langford, W. S. Kolthammer, T. F. M. Champion, M. R. Sprague, P. S. Michelberger, X. M. Jin, D. G. England, and I. A. Walmsley, *arXiv:1208.1534v1* [Phys. Rev. Lett. (to be published)].
- [7] S. Chen, Y.-A. Chen, T. Strassel, Z.-S. Yuan, B. Zhao, J. Schmiedmayer, and J.-W. Pan, *Phys. Rev. Lett.* **97**, 173004 (2006).
- [8] A. I. Lvovsky, B. C. Sanders, and W. Tittel, *Nat. Photonics* **3**, 706 (2009).
- [9] M. Hosseini, B. M. Sparkes, G. Campbell, P. K. Lam, and B. C. Buchler, *Nat. Commun.* **2**, 174 (2011).
- [10] M. P. Hedges, J. J. Longdell, Y. Li, and M. J. Sellars, *Nature (London)* **465**, 1052 (2010).
- [11] J. J. Longdell, E. Fraval, M. J. Sellars, and N. B. Manson, *Phys. Rev. Lett.* **95**, 063601 (2005).
- [12] G. Heinze *et al.* (to be published).

- [13] M. Bonarota, J.L. Le Gouët, and T. Chanelière, *New J. Phys.* **13**, 013013 (2011).
- [14] I. Usmani, M. Afzelius, H. de Riedmatten, and N. Gisin, *Nat. Commun.* **1**, 12 (2010).
- [15] E. Saglamyurek, N. Sinclair, J. Jin, J.A. Slater, D. Oblak, F. Bussières, M. George, R. Ricken, W. Sohler, and W. Tittel, *Nature (London)* **469**, 512 (2011).
- [16] M. Fleischhauer and M.D. Lukin, *Phys. Rev. Lett.* **84**, 5094 (2000).
- [17] K.F. Reim, J. Nunn, V.O. Lorenz, B.J. Sussman, K.C. Lee, N.K. Langford, D. Jaksch, and I.A. Walmsley, *Nat. Photonics* **4**, 218 (2010).
- [18] S.A. Moiseev and S. Kröll, *Phys. Rev. Lett.* **87**, 173601 (2001).
- [19] M. Nilsson and S. Kröll, *Opt. Commun.* **247**, 393 (2005).
- [20] B. Kraus, W. Tittel, N. Gisin, M. Nilsson, S. Kröll, and J.I. Cirac, *Phys. Rev. A* **73**, 020302 (2006).
- [21] G. Hetet, J.J. Longdell, M.J. Sellars, P.K. Lam, and B.C. Buchler, *Phys. Rev. Lett.* **101**, 203601 (2008).
- [22] M. Afzelius, C. Simon, H. de Riedmatten, and N. Gisin, *Phys. Rev. A* **79**, 052329 (2009).
- [23] N.B. Phillips, A.V. Gorshkov, and I. Novikova, *Phys. Rev. A* **78**, 023801 (2008).
- [24] A. Amari, A. Walther, M. Sabooni, M. Huang, S. Kröll, M. Afzelius, I. Usmani, B. Lauritzen, N. Sangouard, H. de Riedmatten, and N. Gisin, *J. Lumin.* **130**, 1579 (2010).
- [25] J.M. Raimond, M. Brune, and S. Haroche, *Rev. Mod. Phys.* **73**, 565 (2001).
- [26] Y. Colombe, T. Steinmetz, G. Dubois, F. Linke, D. Hunger, and J. Reichel, *Nature (London)* **450**, 272 (2007).
- [27] A.V. Gorshkov, A. Andre, M.D. Lukin, and A.S. Sorensen, *Phys. Rev. A* **76**, 033804 (2007).
- [28] B. Julsgaard, J. Sherson, J.I. Cirac, J. Fiurasek, and E.S. Polzik, *Nature (London)* **432**, 482 (2004).
- [29] J. Simon, H. Tanji, J.K. Thompson, and V. Vuletic, *Phys. Rev. Lett.* **98**, 183601 (2007).
- [30] M. Afzelius and C. Simon, *Phys. Rev. A* **82**, 022310 (2010).
- [31] S.A. Moiseev, S.N. Andrianov, and F.F. Gubaidullin, *Phys. Rev. A* **82**, 022311 (2010).
- [32] R.W.P. Drever, J.L. Hall, F.V. Kowalski, J. Hough, G.M. Ford, A.J. Munley, and H. Ward, *Appl. Phys. B* **31**, 97 (1983).
- [33] D.R. Leibrandt, M.J. Thorpe, M. Notcutt, R.E. Drullinger, T. Rosenband, and J.C. Bergquist, *Opt. Express* **19**, 3471 (2011).
- [34] M. Sabooni, S.T. Kometa, S. Thuresson, A. Kröll, and L. Rippe, [arXiv:1212.3774](https://arxiv.org/abs/1212.3774) [New J. Phys. (to be published)].
- [35] A. Walther, A. Amari, S. Kröll, and A. Kalachev, *Phys. Rev. A* **80**, 012317 (2009); Correction: the expression for the group velocity needs to be corrected to $v_g = \frac{2\pi L}{\alpha}$ in subsection "IV.B. Slow light effects."
- [36] M. Sabooni *et al.* (in preparation).
- [37] A.E. Siegman, *Lasers* (University Science Books, Mill Valley, California, 1985).
- [38] L. Rippe, M. Nilsson, S. Kröll, R. Klieber, and D. Suter, *Phys. Rev. A* **71**, 062328 (2005).
- [39] M. Nilsson, L. Rippe, S. Kröll, R. Klieber, and D. Suter, *Phys. Rev. B* **70**, 214116 (2004); M. Nilsson, L. Rippe, S. Kröll, R. Klieber, and D. Suter, *Phys. Rev. B* **71**, 149902 (E) (2005).
- [40] J. Nunn, K. Reim, K.C. Lee, V.O. Lorenz, B.J. Sussman, I.A. Walmsley, and D. Jaksch, *Phys. Rev. Lett.* **101**, 260502 (2008).
- [41] M. Afzelius, I. Usmani, A. Amari, B. Lauritzen, A. Walther, C. Simon, N. Sangouard, J. Minar, H. de Riedmatten, N. Gisin, and S. Kröll, *Phys. Rev. Lett.* **104**, 040503 (2010).
- [42] M. Lovric, P. Glasenapp, D. Suter, B. Tumino, A. Ferrier, P. Goldner, M. Sabooni, L. Rippe, and S. Kröll, *Phys. Rev. B* **84**, 104417 (2011).
- [43] B. Lauritzen, N. Timoney, N. Gisin, M. Afzelius, H. de Riedmatten, Y. Sun, R.M. Macfarlane, and R.L. Cone, *Phys. Rev. B* **85**, 115111 (2012).
- [44] M. Sabooni, F. Beaudoin, A. Walther, N. Lin, A. Amari, M. Huang, and S. Kröll, *Phys. Rev. Lett.* **105**, 060501 (2010).
- [45] C. Clausen, I. Usmani, F. Bussières, N. Sangouard, M. Afzelius, H. de Riedmatten, and N. Gisin, *Nature (London)* **469**, 508 (2011).
- [46] Y.C. Sun, *Spectroscopic Properties of Rare-Earths in Optical Materials* edited by G. Liu and B. Jacquier, Springer Series in Material Science (Springer, Berlin Heidelberg, 2005), Chap. 7.

PAPER II

Spectral engineering of slow light, cavity line narrowing, and pulse compression

M. Sabooni, Q. Li, R. K. Mohan, L. Rippe and S. Kröll.

Phys. Rev. Lett. **111**, 183602 (2013).

Spectral Engineering of Slow Light, Cavity Line Narrowing, and Pulse Compression

Mahmood Sabooni,¹ Qian Li,¹ Lars Rippe,¹ R. Krishna Mohan,² and Stefan Kröll¹

¹Department of Physics, Lund University, Post Office Box 118, SE-22100 Lund, Sweden

²Spectrum Lab, Montana State University, Post Office Box 173510, Bozeman, Montana 59717, USA

(Received 12 April 2013; published 31 October 2013)

More than 4 orders of magnitude of cavity-linewidth narrowing in a rare-earth-ion-doped crystal cavity, emanating from strong intracavity dispersion caused by off-resonant interaction with dopant ions, is demonstrated. The dispersion profiles are engineered using optical pumping techniques creating significant semipermanent but reprogrammable changes of the rare-earth absorption profiles. Several cavity modes are shown within the spectral transmission window. Several possible applications of this phenomenon are discussed.

DOI: 10.1103/PhysRevLett.111.183602

PACS numbers: 42.50.Ct, 42.50.Pq, 42.79.Gn, 78.47.nd

Cavity-linewidth narrowing has been suggested to have great potential in many different areas such as laser stabilization [1,2], high-resolution spectroscopy [2], enhanced light-matter interaction, and compressed optical energy [3]. We show more than 4 orders of magnitude of cavity-linewidth narrowing, which, to the best of our knowledge, is more than 2 orders of magnitude larger than demonstrated with other techniques. Previously, 10 to 20 times linewidth narrowing has been shown using electromagnetic induced transparency [4–6], and recently, 2 orders of magnitude were shown using coherent population oscillation in combination with a cavity dispersive effect [7]. We also demonstrate several cavity modes within the slow light transmission window, something which we are not aware of having been demonstrated using electromagnetic induced transparency or coherent population oscillation. The present results are obtained using spectral hole burning in rare-earth-ion-doped crystals [8–10], and we discuss the properties and potential of slow light structures created with this method in these materials.

In this Letter, a cavity formed by depositing mirrors directly onto a praseodymium doped Y_2SiO_5 crystal and (near) persistent spectral hole burning is employed to create a very strong dispersion. A sharp dispersion slope reduces the photon group velocity and therefore increases the effective photon lifetime in the cavity compared to a nondispersive cavity (some times referred to as a cold cavity [11]).

Generally, the mode spacing in a Fabry-Perot cavity $\Delta\nu$ is given by [11]

$$\Delta\nu = \frac{c}{2L} \frac{1}{n_g(\nu)} = \frac{c}{2L} \frac{1}{n + \nu \frac{dn}{d\nu}} = \frac{v_g(\nu)}{2L}, \quad (1)$$

where c is the speed of light in vacuum, ν is the light frequency, n is the real part of the index of refraction (for the phase velocity), $v_g(\nu)$ is the group velocity, and $n_g(\nu)$ is the index of refraction for the group velocity. For the present work, it is useful to briefly analyze the mode spacing relation.

The resonance condition for a Fabry-Perot cavity of length L may be expressed as $m(\lambda/2) = L$, where m is an integer and the wavelength $\lambda = c/(n\nu)$. Thus,

$$m \frac{c}{2L} = n\nu. \quad (2)$$

Differentiating Eq. (2) gives

$$\frac{c}{2L} \delta m = n \delta \nu + \nu \delta n. \quad (3)$$

Dividing the left- (right-) hand side of Eq. (3) with the left- (right-) hand side of Eq. (2) yields

$$\frac{\delta m}{m} = \frac{\delta \nu}{\nu} + \frac{\delta n}{n}, \quad (4)$$

where $n = n(\nu)$ is a function of frequency. Normally, when the frequency is changed, $\delta\nu/\nu \gg \delta n/n$, but in the case of significant slow light effects, $n \ll \nu(dn/d\nu)$, and the second term on the right-hand side in Eq. (4) is much larger than the first. Thus, the cavity mode spacing is basically completely determined by the dispersion, while the impact of the relative change in the frequency is negligible. Below, it is shown how we modify the cavity absorption to enter this regime where the Fabry-Perot cavity mode spacing is completely determined by the frequency dispersion.

First, we examine the cavity transmission far away from the absorbing inhomogeneous Pr ion transition (nondispersive cavity). The crystal cavity is ≈ 6 mm long, the reflectivity was specified to $R_1 \approx R_2 \approx 95\%$, and Y_2SiO_5 has a real index of refraction of $n \approx 1.8$. The cavity mode spacing for this crystal is $\Delta\nu_{\text{nondispersive}} \approx 13$ GHz, and the transmission peak linewidth is $\delta\nu_{\text{nondispersive}} \approx 1$ GHz. A frequency scan across two cavity modes is shown in Fig. 1(a). The reason for the comparatively large cavity linewidth (low finesse) could be due to improper matching to the spatial cavity mode [12,13]. We expect that the high frequency wing of the cavity modes is due to higher order transverse modes in the cavity. The small extra peak to the left of the modes is the cavity mode for the orthogonal

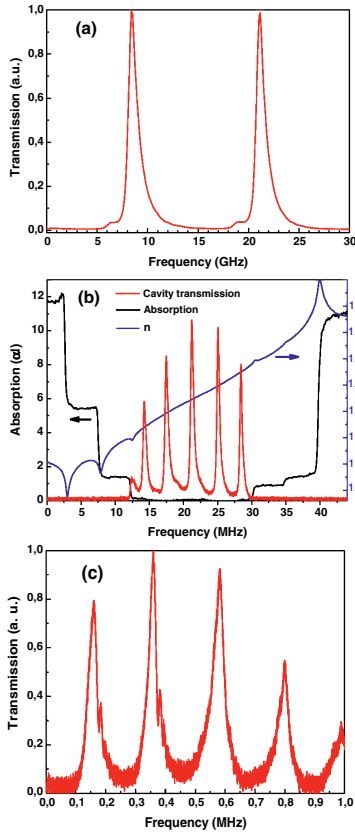


FIG. 1 (color online). (a) Nondispersive cavity transmission spectrum. (b) Cavity transmission spectrum (red trace) and the best guess for the absorption profile around the ≈ 18 MHz spectral hole (black trace) inside the cavity. The corresponding real refractive index n calculated from the black-trace absorption profile is shown as a blue trace. (c) Cavity transmission spectrum for the absorption profile in a ~ 1 MHz spectral hole.

polarization. The Y_2SiO_5 crystal is birefringent, and cavity modes for the two polarizations along the two principal axes will be displaced relative to each other [14]. Both modes are seen because the input polarization has a small angle relative to the D_2 (principal) axes [see Fig. 2(b)].

Second, persistent spectral hole burning is employed to manipulate the ion absorption distribution in the inhomogeneously broadened (~ 9 GHz) $^3H_4 \rightarrow ^1D_2$ transition of the

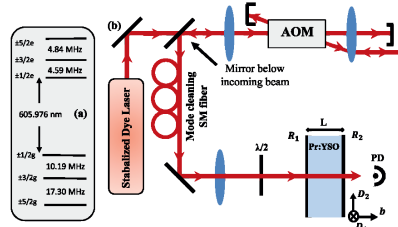


FIG. 2 (color online). Experimental setup. (a) The hyperfine splitting of the $^3H_4 \rightarrow ^1D_2$ transition of $\text{I Pr}^{3+} : \text{Y}_2\text{SiO}_5$ is shown [33,34]. (b) A double-pass AOM is employed to tailor the optical pulses out of the continuous output from a narrow ($< \text{kHz}$) linewidth laser. A PD monitors the light transmitted through the cavity. The specified reflectivity of the crystal input and output facets is $R_1 = R_2 = 95\%$. D_1 , D_2 , and b show the crystal principal axis orientations.

0.05% doped $\text{Pr}^{3+} : \text{Y}_2\text{SiO}_5$ crystal. A frequency stabilized dye laser [15,16] at $\lambda_{\text{vac}} = 605.976 \text{ nm}$ is used to remove the absorbing ions within an 18 MHz wide spectral region [black trace, Fig. 1(b)] by a series of laser pulses. The laser pulses optically pump the ions to the excited state, from where they decay back to one of the hyperfine ground levels [see Fig. 2(a)]. A typical value for the ground state hyperfine population decay is $\sim 40 \text{ s}$, while it could be 40 min in a weak magnetic field ($\approx 0.01 \text{ T}$) [17] and several weeks for other rare-earth-ion-doped crystals [18]. A detailed description of the procedure for creating a spectral transmission window can be found in Ref. [19]. An arbitrary-waveform-generator controlled double-pass acousto-optic modulator (AOM), which can tailor the light amplitude, phase, and frequency [see Fig. 2(b)] is used to form the necessary laser pulses. As is shown in Fig. 1(b), the modified ion absorption profile (black trace) has close to zero absorption within about 18 MHz. The absorption profile is taken in a part of the 6 mm crystal which is not reflection coated, i.e., outside the cavity. In this way, the frequency resolved absorption measurement can be recorded without being affected by the cavity mode structure. Admittedly, this can only be seen as an estimate of the absorption structure inside the cavity. Previously, we have measured the absorption αL in a 1 mm crystal of the same dopant concentration to be approximately equal to 2. The left axis in Fig. 1(b) has been scaled to be consistent with this value. In order to verify that absorption and scattering losses are indeed small in the 18 MHz transmission window, we compared the transmission through the crystal (without the cavity) in the black-trace spectral transmission region in Fig. 1(b), with the transmission through the crystal when the laser is detuned by about 4 nm from the 9 GHz inhomogeneous line center. It was not possible to detect a difference between the transmission in the 18 MHz

transmission region and when the laser was detuned about 4 nm (~ 4 THz) away from the absorption line. From this, we estimate that any absorption in the slow light transmission window is in any case below <0.1 dB/cm. The bulk loss in Y_2SiO_5 has previously been estimated to <0.003 dB/cm [20].

Experimental line narrowing data are shown in Figs. 1(b) and 1(c). In Fig. 1(b), there are five cavity transmission peaks within the ≈ 18 MHz transparent spectral region. The spectral width of the cavity transmission is reduced from $\delta\nu_{\text{nondispersive}} \approx 1$ GHz in the nondispersive cavity case [Fig. 1(a)] to $\delta\nu_{\text{dispersive}} \approx 600$ kHz in the dispersive cavity case. In Fig. 1(c), the transmission window is about a MHz, yielding a steeper dispersion curve, and the cavity linewidth is about 30 kHz, i.e., a reduction of about 30 000 relative to the nondispersive cavity linewidth. At the same time, the cavity mode spacing has decreased from 13 GHz to about 220 kHz (factor of 60 000).

Equation (1) shows that it is possible to control the cavity mode spacing by controlling the group refractive index $n_g(\nu)$. The (real part of the) refractive index can be calculated from the ion absorption frequency distribution $\alpha(\nu)$ via the Kramers-Kronig relations. This will give the dispersion and group refractive index. The refractive index as calculated from the absorption (black line) is shown by the blue line in Fig. 1(b). As shown in Fig. 1, the cavity mode spacing and cavity linewidth can be controllably varied over several orders of magnitude by engineering the ion absorption frequency distribution.

Although spectral hole burning based slow light structures have been discussed previously [8,9] and slow light structures in general have been analyzed extensively, e.g., Ref. [21] and references therein, we think it could be relevant to discuss the properties and potential of the absorption structuring techniques shown here. Because of the cavity-linewidth narrowing, the 6 mm long cavity can have a longitudinal mode spacing of ≈ 220 kHz, which in vacuum would correspond to that of a ≈ 700 m long cavity. The transversal part of the mode, however, still behaves as that of a 6 mm long cavity, which means that it is possible to combine a narrow beam with fairly even beam size with a small cavity mode spacing. The longitudinal and transversal cavity mode behaviors are thus decoupled by more than 4 orders of magnitude.

In order to further examine the cavity properties, a short pulse was sent into the cavity. The solid red trace in Fig. 3(a) shows the light transmitted to the photodiode (PD) for a 20 ns long input pulse (black dashed trace, centered at time $t = 0$). With an 18 MHz slow light transmission window, the 6 m long pulse is compressed to about 2.5 mm and bounces back and forth in the cavity with some light leaking out after each round trip. Figure 3(b) shows the corresponding data with a 3 MHz transmission window where the cavity round trip time is increased to well over a microsecond. The group velocity v_g is approximately given by [8,10]

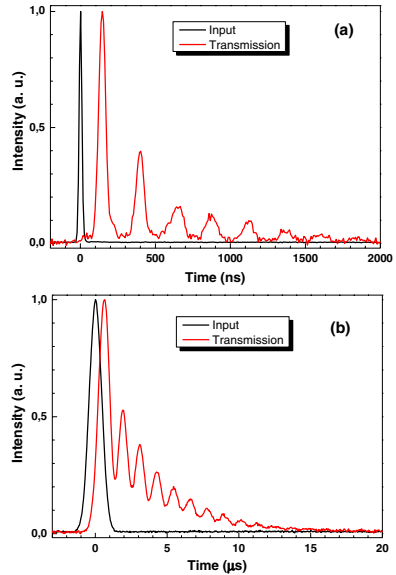


FIG. 3 (color online). Transmitted light to a PD (a) when a 20 ns long pulse (black trace, centered at time $t = 0$) is sent into the cavity in the presence of the ≈ 18 MHz spectral hole and (b) when a $1 \mu\text{s}$ long pulse (black trace, centered at time $t = 0$) is sent into the cavity in the presence of the ≈ 3 MHz spectral hole. Both signals are normalized.

$$v_g = \frac{2\pi\Gamma}{\alpha}, \quad (5)$$

where Γ is the spectral width of the transmission window and α is the absorption coefficient immediately outside the spectral transmission window (i.e., the effective absorption depth of the transmission window). In general, e.g., Ref. [9], the time-bandwidth product TB for any slow light structure of this type of length l approximately is

$$\text{TB} = \frac{l}{v_g} \Gamma = \frac{\alpha l}{2\pi}. \quad (6)$$

Thus, the bandwidth is determined by the transmission window Γ , which readily can be changed by a new optical pumping sequence. The group velocity is then determined by the absorption coefficient of the surrounding structure which, for a given crystal, can most easily be changed by moving the transmission window to different positions within the inhomogeneous line. The further out from the line center, the higher the group velocity. Finally, the time delay is then set by the crystal length. It is noteworthy that all

these parameters can be varied independently, which offers a good opportunity to test, for example, the nonlinear enhancement effects due to slow light in a well controlled environment. As an example, a $TB \approx 10$ for $\Gamma = 1$ MHz, $\alpha \approx 50 \text{ cm}^{-1}$, and $l = 12$ mm is reported in Ref. [22].

Potential applications of controlled spectral engineering of slow light structures in cavities will now be discussed. The fact that the lifetime of a light pulse in the cavity and the cavity Q value increase by several orders of magnitude is interesting because whispering gallery mode rare-earth crystal resonators with Q values in the 10^6 range have been demonstrated [23], and Q values up to 10^{10} are predicted [23]. These numbers could potentially be enhanced by 4 orders of magnitude by modifying the absorption profiles by optical pumping, as is done here. Also, the loss rate due to scattering in the cavity could be strongly reduced. For example, if the fractional scattering loss I_f for a pulse spending time t in the cavity is proportional to $1 - e^{-\alpha_0 l_0}$, where α_0 is the scattering coefficient and l_0 is the length traversed by the pulse, then we obtain $I_f = 1 - e^{-\alpha_0 l_0} = 1 - e^{-\alpha_0 v_g t}$, where v_g is the group velocity. Thus, if we would like to delay light by a given time t , a material with a low group velocity can strongly reduce scattering losses. In general, these types of slow light effects can be interesting for solid state materials that, as compared to vacuum or gas, will normally experience larger scattering.

It is also possible to dynamically tune the speed of light propagating through the material using an electric field. In noncentrosymmetric sites, the rare-earth ions have a permanent electric dipole moment which is different in the ground and excited states. This means that the ion transition frequency is shifted by an external electric field [24], an effect which, e.g., has been used when creating high efficiency quantum memories in these materials [25] or to move the transmission window in frequency [26]. Electric fields can equally well be used to change the width of the spectral transmission window [27] which changes the index of refraction. The group velocity can in this way readily be modulated at tens of MHz rates. As can be seen from Fig. 3, this rate can be much faster than the time it takes for the pulse to propagate through the cavity. Thus, it may be interesting to investigate the possibility to adiabatically tune the wavelength inside the cavity by modifying the refractive index, as is done in photonic crystal cavities, e.g., Ref. [28], but now on a time scale which differs by 6 orders of magnitude.

Low phase noise and very narrow linewidth laser systems have wide ranging applications as stable frequency references and sources. A passive laser line narrowing technique based on spectral hole burning was demonstrated recently. Selective filtering of weak spectral components outside the laser center frequency by transmitting the laser beam through a highly absorbing spectral hole burning material resulted in phase noise suppression by several tens of dB outside the central laser frequency [29]. Using the cavity

line narrowing techniques presented in this Letter, transmission windows narrower than the sub-kHz homogeneous lines of the material can be obtained. Further, the region outside the transmission window would be nontransparent, but light outside the center frequency is now reflected instead of being absorbed, which has several advantages.

Spontaneous parametric down-conversion is widely used in quantum optics and quantum information science as a source for entangled photon pairs and as single photon sources. It is often desirable to generate entangled photons with a very narrow bandwidth, for example, to match the bandwidth of an optical quantum memory or the bandwidth of an optical transition [30,31]. Photons with narrow bandwidth can be generated by cavity-enhanced spontaneous down-conversion, where a periodically poled nonlinear crystal is enclosed inside a cavity [32]. A rare-earth-ion-doped slow light cavity could be combined with a periodically poled nonlinear crystal. A single narrow cavity transmission peak could be created within the spectral transmission window of the rare-earth-ion-doped cavity crystal. Since the rare-earth-ion inhomogeneous absorption peak can be hundreds of gigahertz wide, this constitutes the only transparent region.

The present cavity has the unusual property of supporting several modes with equal wavelength but with different frequencies. From Eq. (2), it can be seen that for any mode number m , mathematically there is an infinite number of combinations of ν and n which will fulfil the equation. The present cavity indeed has more than one mode supported for certain mode numbers. For instance, in Fig. 1(b), the two first (last) modes, which are about 4 MHz apart, have the same mode number as the two cavity modes just below (above) the rare-earth absorption line, which are separated by about 13 GHz.

In conclusion, we have shown more than 4 orders of magnitude cavity-linewidth narrowing caused by off-resonant interaction with praseodymium ions doped in an inorganic crystal. Several cavity modes are shown within the 18 MHz slow light transmission window. The crystal can readily be reprogrammed by optical pumping or dynamically tuned by external electric fields to yield other cavity linewidths or light group velocities. It is suggested that the combination of slow light structures and whispering gallery modes in rare-earth crystal resonators might give exceptionally high-cavity Q values.

This work was supported by the Swedish Research Council, the Knut and Alice Wallenberg Foundation, the Crafoord Foundation, and the EC FP7 Contract No. 247743 (QuRep). The research leading to these results also received funding from the People Programme (Marie Curie Actions) of the European Union's Seventh Framework Programme FP7 (2007-2013) under REA Grant Agreement No. 287252 and Lund Laser Centre (LLC). Finally, we are grateful to Dr. Mikael Afzelius for several valuable discussions.

- [1] Y. Shevy, D. Shevy, R. Lee, and D. Provenzano, *Proceedings of the Conference On Optical Fiber Communication OFC Collocated National Fiber Optic Engineers Conference OFC-NFOEC* (IEEE, New York, 2010).
- [2] M. D. Lukin, M. Fleischhauer, M. O. Scully, and V. L. Velichansky, *Opt. Lett.* **23**, 295 (1998).
- [3] T. Baba, *Nat. Photonics* **2**, 465 (2008).
- [4] H. Wu, J. Gea-Banacloche, and M. Xiao, *Phys. Rev. Lett.* **100**, 173602 (2008).
- [5] J. Zhang, G. Hernandez, and Y. Zhu, *Opt. Lett.* **33**, 46 (2008).
- [6] H. Wang, D. J. Goorskey, W. H. Burkett, and M. Xiao, *Opt. Lett.* **25**, 1732 (2000).
- [7] P. Grinberg, K. Bencheikh, M. Brunstein, A. M. Yacomotti, Y. Dumeige, I. Sagnes, F. Raineri, L. Bigot, and J. A. Levenson, *Phys. Rev. Lett.* **109**, 113903 (2012).
- [8] R. N. Shakhmuratov, A. Rebane, P. Megret, and J. Odeurs, *Phys. Rev. A* **71**, 053811 (2005).
- [9] R. Lauro, T. Chaneliere, and J. L. Le Gouet, *Phys. Rev. A* **79**, 063844 (2009).
- [10] A. Walthers, A. Amari, S. Kröll, and A. Kalachev, *Phys. Rev. A* **80**, 012317 (2009); correction: the expression for the group velocity needs to be corrected to $v_g = (2\pi\Gamma/\alpha)$ in Subsec. IV.B.
- [11] A. E. Siegman, *Lasers* (University Science Books, Mill Valley, CA, 1985).
- [12] M. Sabooni, Q. Li, S. Kröll, and L. Rippe, *Phys. Rev. Lett.* **110**, 133604 (2013).
- [13] M. Sabooni, S. T. Kometa, A. Thuresson, S. Kröll, and L. Rippe, *New J. Phys.* **15**, 035025 (2013).
- [14] M. Sabooni, Ph.D. thesis, Lund University, 2013.
- [15] R. W. P. Drever, J. L. Hall, F. V. Kowalski, J. Hough, G. M. Ford, A. J. Munley, and H. Ward, *Appl. Phys. B* **31**, 97 (1983).
- [16] D. R. Leibrandt, M. J. Thorpe, M. Notcutt, R. E. Drullinger, T. Rosenband, and J. C. Bergquist, *Opt. Express* **19**, 3471 (2011).
- [17] N. Ohlsson, M. Nilsson, and S. Kröll, *Phys. Rev. A* **68**, 063812 (2003).
- [18] F. Konz, Y. Sun, C. W. Thiel, R. L. Cone, R. W. Equall, R. L. Hutcheson, and R. M. Macfarlane, *Phys. Rev. B* **68**, 085109 (2003).
- [19] A. Amari, A. Walthers, M. Sabooni, M. Huang, S. Kröll, M. Afzelius, I. Usmani, B. Lauritzen, N. Sangouard, H. de Riedmatten, and N. Gisin, *J. Lumin.* **130**, 1579 (2010).
- [20] H. Goto, S. Nakamura, and K. Ichimura, *Opt. Express* **18**, 23763 (2010).
- [21] R. W. Boyd, *J. Opt. Soc. Am. B* **28**, A38 (2011).
- [22] H. Zhang, M. Sabooni, L. Rippe, C. Kim, S. Kröll, L. V. Wang, and P. R. Hemmer, *Appl. Phys. Lett.* **100**, 131102 (2012).
- [23] D. L. McAuslan, D. Korystov, and J. J. Longdell, *Phys. Rev. A* **83**, 063847 (2011).
- [24] R. M. Macfarlane and A. J. Meixner, *Opt. Lett.* **19**, 987 (1994).
- [25] M. P. Hedges, J. J. Longdell, Y. Li, and M. J. Sellars, *Nature (London)* **465**, 1052 (2010).
- [26] S. E. Beavan, E. A. Goldschmidt, and M. J. Sellars, *J. Opt. Soc. Am. B* **30**, 1173 (2013).
- [27] M. Persson, Master's thesis, Lund University, 2001.
- [28] S. F. Preble, Q. F. Xu, and M. Lipson, *Nat. Photonics* **1**, 293 (2007).
- [29] C. W. Thiel, T. Bottger, and R. L. Cone, *J. Lumin.* **131**, 353 (2011).
- [30] C. Clausen, I. Usmani, F. Bussieres, N. Sangouard, M. Afzelius, H. de Riedmatten, and N. Gisin, *Nature (London)* **469**, 508 (2011).
- [31] E. Saglamyurek, N. Sinclair, J. Jin, J. A. Slater, D. Oblak, F. Bussieres, M. George, R. Ricken, W. Sohler, and W. Tittel, *Nature (London)* **469**, 512 (2011).
- [32] X. H. Bao, Y. Qian, J. Yang, H. Zhang, Z. B. Chen, T. Yang, and J. W. Pan, *Phys. Rev. Lett.* **101**, 190501 (2008).
- [33] R. W. Equall, R. L. Cone, and R. M. Macfarlane, *Phys. Rev. B* **52**, 3963 (1995).
- [34] L. Rippe, M. Nilsson, S. Kröll, R. Klieber, and D. Suter, *Phys. Rev. A* **71**, 062328 (2005).

PAPER III

Slow-light-based optical frequency shifter

Q. Li, Y. Bao, A. Thuresson, A. Nilsson, L. Rippe and S. Kröll.

Phys. Rev. A **93**, 043832 (2016)

Synopsis of paper selected for online display of APS Physics.

PHYSICAL REVIEW A **93**, 043832 (2016)

Slow-light-based optical frequency shifter

Qian Li,^{1,*} Yupan Bao,¹ Axel Thuresson,² Adam N. Nilsson,¹ Lars Rippe,¹ and Stefan Kröll¹¹Department of Physics, Lund University, P. O. Box 118, SE-22100 Lund, Sweden²Theoretical Chemistry, Lund University, P. O. Box 124, SE-22100 Lund, Sweden

(Received 7 February 2016; published 19 April 2016)

We demonstrate experimentally and theoretically a controllable way of shifting the frequency of an optical pulse by using a combination of spectral hole burning, slow light effect, and linear Stark effect in a rare-earth-ion-doped crystal. We claim that the solid angle of acceptance of a frequency shift structure can be close to 2π , which means that the frequency shifter could work not only for optical pulses propagating in a specific spatial mode but also for randomly scattered light. As the frequency shift is controlled solely by an external electric field, it works also for weak coherent light fields and can be used, for example, as a frequency shifter for quantum memory devices in quantum communication.

DOI: 10.1103/PhysRevA.93.043832

I. INTRODUCTION

Changing the passband of a filter changes its frequency response, that is, it changes which frequency components from a signal can pass through the filter. Here we demonstrate that it is possible to change the frequency of an optical signal when the passband of a filter is dynamically changed while light propagates through it.

Manipulation of the frequency of light during propagation was first proposed and experimentally demonstrated by dynamically changing the refractive index of the medium for a light pulse propagating inside a photonic crystal cavity [1–3]. Later, it was realized in a photonic crystal waveguide by the aid of slow light effects [4,5]. The physical mechanism behind those frequency conversion processes can be seen as the adiabatic tuning of an oscillator, which is basically analogous to the classical phenomenon of sliding a finger along a guitar string after it has been plucked or tuning a cavity by moving the end mirror of the cavity. The refractive index changes were achieved at the presence of another strong optical field, and the relative frequency shift was proportional to the relative refractive index change, $\Delta\nu/\nu = -\Delta n/n$. However, in the present work, a different physical mechanism for a frequency shift is demonstrated.

Previously, a spectral filter prepared in a rare-earth-ion-doped crystal with an on-off ratio of about ~ 60 dB has been experimentally demonstrated [6]. This work showed that the passband of the filter can be dynamically changed by combining spectral hole burning with a linear Stark effect [6]. A filter prepared in such a crystal by spectral hole burning induces sharp dispersion across the spectral hole, and hence the group velocity of an optical pulse propagating inside the crystal will be greatly slowed down and the pulse will be compressed spatially [7–10]. Further study reveals that, in contrast to the structural slow light effect [4,5,11,12], the slow light effect caused by spectral engineering of the absorption profile originates from the reversible energy storage between the light and the absorbing ions in the medium via off-resonant interaction [11,13–16]. The energy of the input pulse is distributed between the polarization of the ions, U_{med} ,

and the electromagnetic field, U_{em} , in the material, and the group velocity of the pulse, v_g , can be written as [15,16]

$$v_g = \frac{c/n}{1 + U_{\text{med}}/U_{\text{em}}}, \quad (1)$$

where n is the refractive index of the medium and c is the speed of light in a vacuum. Therefore, the group velocity of the pulse decreases with the increase of the fraction of energy accumulated in the medium. In the case of extreme slow light effects, almost all energy will be temporarily stored in the medium in the form of ion polarization. The ions will depolarize and the energy will be returned back to light field when the pulse exits the material. Hence, by manipulating the resonance frequency of the ions (using the linear Stark effect, for example) during the light propagation inside the crystal, the frequency of the optical pulse exiting the crystal can be changed.

To verify this concept, a ~ 1 -MHz band-pass filter where all the ions in the surrounding 18-MHz region have the same sign of the Stark effect (which is called a *frequency shifter* or *frequency shift filter*) is prepared in a 10-mm-long $\text{Pr}^{3+}:\text{Y}_2\text{SiO}_5$ crystal, as shown in Fig. 1. A 1- μs -long pulse with a frequency distribution matching the passband of the filter is sent into the crystal. It propagates with a reduced speed of $c/120\,000$ and is spatially compressed to 2.5 mm inside the crystal. According to Eq. (1), more than 99.9% of the pulse energy is in the form of ion polarization when the light pulse propagates inside the crystal [15]. An external electric field is switched on while the entire pulse is inside the crystal, shifting the resonance frequency of the ions by an amount of Δs and the pulse exiting the crystal will then also have its frequency shifted by Δs . The frequency shift is linearly proportional to the electric field applied. Since the pulse is propagating inside the transmission window of the filter, the loss can be kept very low. Furthermore, by using two crystals oriented 90° relative to each other [17] and preparing the spectral structure throughout the entire crystals, the filter could work for any spatial input mode, including scattered, randomly polarized light [9]. The solid acceptance angle of such a frequency shift filter could basically be 2π , as described later.

Another interesting feature of the present frequency shift control is that there is no strong optical field involved during the

*qian.li@fysik.lth.se

LI, BAO, THURESSON, NILSSON, RIPPE, AND KRÖLL

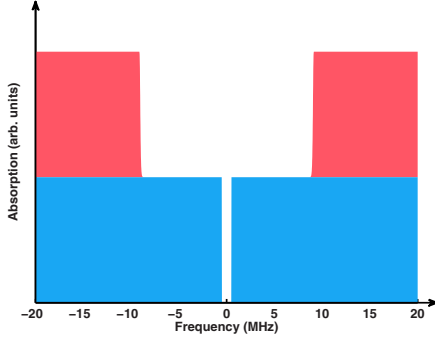
 PHYSICAL REVIEW A **93**, 043832 (2016)


FIG. 1. Frequency shift filter structure. Blue represents ions with positive sign of the Stark effect while red represents the ions with negative sign of the Stark coefficient. The material has been prepared such that all ions within the ± 9 -MHz region have the same sign of their Stark coefficient.

frequency shift process as compared to the methods mentioned above [2–5]. The frequency shift is purely controlled by an external electric field applied onto the crystal, which means that it is suitable for being integrated into strongly background-sensitive single-photon applications. Therefore, it can be used as a highly efficient frequency shifter in quantum communication, for example, for quantum memories, if the incoming photon does not match the frequency of the quantum memory device.

II. EXPERIMENT

The experiment was performed in a $10 \times 10 \times 6$ mm (crystal axes $D1 \times D2 \times b$) $\text{Pr}^{3+}:\text{Y}_2\text{SiO}_5$ crystal with 0.05%

doping concentration and the frequency shift filter structure was prepared using a $^3\text{H}_4 - ^1\text{D}_2$ transition at 2 K. This transition has an inhomogeneous linewidth of ~ 5 GHz centered at 605.977 nm [18,19]. The lifetime of the spectral hole (filter) is about 100 s and can be extended to ~ 30 min at the presence of a weak magnetic field (0.01 T) [20]. The experimental setup is shown in Fig. 2(a). A laser beam with wavelength of 605.977 nm (0 MHz in the following description) from a stabilized Coherent 699-21 ring dye laser polarized along the $D2$ axis of the crystal was split into two parts by a 90/10 beam splitter, where the stronger beam was focused onto the crystal for all the preparation and characterization of the filter and the weaker one was further split in two. One beam was sent to a photodetector (PD1) as a reference to calibrate the intensity fluctuations of the laser and the other one was used as a local oscillator for the heterodyne detection measurement. The light beams passing through the crystal and the local oscillator were overlapped on a beam splitter and sent through an optical fiber and detected by a photodetector (PD2).

For Pr^{3+} , the permanent electric dipole moment of the ground state differs from that of the excited state. Therefore, applying an external electric field, \mathbf{E} , will Stark shift the resonant frequency of the ions, compare, e.g., Ref. [21], from ν_0 to $\nu' = \nu_0 + \Delta s$, where

$$\Delta s = \frac{(\mu_e - \mu_g) \cdot \mathbf{E}}{\hbar} = \frac{\delta\mu \cdot \mathbf{E}}{\hbar}, \quad (2)$$

where \mathbf{E} is the applied electric field; μ_g and μ_e are the electric dipole moments for the ground state and excited state, respectively; and $\delta\mu$ is the difference between the excited- and ground-state dipole moments. There are four possible $\delta\mu$ orientations for Pr^{3+} , as shown in Fig. 2 (b); all four orientations of $\delta\mu$ have an angle of $\theta = 12.4^\circ$ relative to the b axis of the crystal, and the magnitude of $\delta\mu/\hbar$ is $111.6 \text{ kHz}/(\text{V cm}^{-1})$ [21]. The \mathbf{E} field is applied along the b axis and because of the symmetry of the $\delta\mu$ and \mathbf{E} field, there will be two effective Stark coefficients for Pr^{3+} , with the

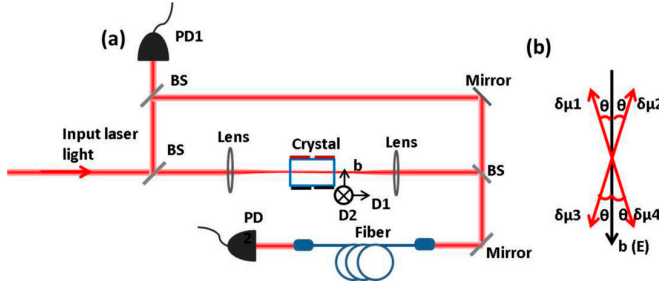


FIG. 2. (a) Experimental setup. Laser light polarized along the $D2$ axis of the crystal is divided into two beams by a 90/10 beam splitter (BS), where the stronger beam is focused to the center of the crystal while the weaker one is further split into two (one part is used as a reference beam to calibrate the intensity fluctuation of the laser and the other one is used as a local oscillator to beat with the delayed transmitted probe beam). Both the transmitted beam and the local oscillator are sent into a single mode fiber for the beating signal detection. (b) The permanent electric dipole moment difference between excited state and ground state of the Pr^{3+} ($\delta\mu_{1,2,3,4}$) relative to the electric field applied (\mathbf{E}). The electric field is along the b axis of the crystal and the angle between the dipole moment difference and the electric field is $\theta = 12.4^\circ$ for all the 4 possible $\delta\mu$.

043832-2

same amplitude but opposite signs. When an external voltage is applied across the crystal, half of the ions, those with a positive Stark coefficient, will shift to higher frequencies while the rest will shift to lower frequencies.

Optical pumping together with an electric-field-induced Stark shift were used to prepare the filter structure. In the end a ~ 1 -MHz band-pass filter surrounded only by ions with a positive sign of the Stark coefficient was prepared over an 18-MHz region in the center of the inhomogeneous profile. A sketch of the final filter structure can be found in Fig. 1. More information about how this structure was created can be found in the Appendix.

III. SIMULATION

A modified version of the Maxwell-Bloch (MB) equations for a two-level system [22–24] is used to include a Stark shift where the resonance frequency of 50% of the ions are shifted to higher frequencies while the rest of the ions are shifted an equal amount to lower frequencies when an electric field is applied. A simple and efficient way to simulate this effect is to introduce two Bloch vectors (denoted \bar{r}^A and \bar{r}^B), for the two different ion groups with opposite signs of their Stark coefficient, at each frequency and position, instead of the traditional single Bloch vector. At a particular time, τ_0 , the resonance frequency for \bar{r}^A and \bar{r}^B is shifted by $+\Delta_s$ and $-\Delta_s$, respectively. The modified MB equations are then expressed as:

$$\frac{dr_x^A}{d\tau} = -[\Delta + \Delta_s \Theta(\tau - \tau_0)]r_y^A - \Omega_i r_z^A - \frac{r_x^A}{T_2}, \quad (3)$$

$$\frac{dr_y^A}{d\tau} = [\Delta + \Delta_s \Theta(\tau - \tau_0)]r_x^A + \Omega_i r_z^A - \frac{r_y^A}{T_2}, \quad (4)$$

$$\frac{dr_z^A}{d\tau} = \Omega_i r_x^A - \Omega_i r_y^A - \frac{1 + r_z^A}{T_1}, \quad (5)$$

$$\frac{dr_x^B}{d\tau} = -[\Delta - \Delta_s \Theta(\tau - \tau_0)]r_y^B - \Omega_i r_z^B - \frac{r_x^B}{T_2}, \quad (6)$$

$$\frac{dr_y^B}{d\tau} = [\Delta - \Delta_s \Theta(\tau - \tau_0)]r_x^B + \Omega_i r_z^B - \frac{r_y^B}{T_2}, \quad (7)$$

$$\frac{dr_z^B}{d\tau} = \Omega_i r_x^B - \Omega_i r_y^B - \frac{1 + r_z^B}{T_1}, \quad (8)$$

$$\frac{d\Omega_r}{dz'} = \frac{\alpha_0}{2\pi} \left(\int_{-\infty}^{+\infty} g^A r_y^A d\Delta + \int_{-\infty}^{+\infty} g^B r_y^B d\Delta \right), \quad (9)$$

$$\frac{d\Omega_i}{dz'} = -\frac{\alpha_0}{2\pi} \left(\int_{-\infty}^{+\infty} g^A r_x^A d\Delta + \int_{-\infty}^{+\infty} g^B r_x^B d\Delta \right), \quad (10)$$

where $\bar{r}^A = (r_x^A, r_y^A, r_z^A)$, $\bar{r}^B = (r_x^B, r_y^B, r_z^B)$, g^A , and g^B are the spectral profiles (including the transmission windows) for \bar{r}^A and \bar{r}^B , respectively; Ω_r and Ω_i are the real and imaginary Rabi frequencies; Δ is the detuning; τ is retarded time; z' is the position in the one-dimensional crystal; α_0 is the absorption coefficient; T_1 and T_2 are the decay constants for the lifetime and coherence of the excited state, respectively; and Θ is the Heaviside step function which is used to describe the shift in frequency when the electric field is turned on at time τ_0 . Any function properly describing the frequency shift of the ions due to the change of the electric field could be used instead of the Heaviside function.

IV. RESULTS AND DISCUSSION

After the structure preparation, a frequency chirped pulse with a chirp rate of $1 \text{ kHz}/\mu\text{s}$ was sent into the crystal to map out the structure of the frequency shift filter. The intensity of this pulse was reduced until optical repumping of the ions was too small to affect the spectral structure. The black trace in Fig. 3(a) shows the initially created filter structure. Since the ions around the filter all have a positive sign of the Stark coefficient, the passband of the filter will shift to higher frequencies when a positive external voltage is applied, and vice versa, as can be seen in Fig. 3(a). The filter becomes narrower when higher voltages are applied onto the crystal, especially on the frequency side further away from zero frequency. There could be three possible reasons for this. One is the inhomogeneity of the electric field (Appendix) along the pulse propagation direction, which causes the frequency shift of the ions to differ slightly. While most of the ions shift the same amount in frequency, some ions shift less. Another reason is that the ions with the opposite signs of the Stark coefficient move closer to the filter as higher voltages are applied and, since the ions have a Lorentzian absorption profile, there will be some absorption caused by these ions. Both of these two effects will make the filter narrower with higher electric field and have larger effect on the frequency edge that is further away from the zero frequency. The third possible reason is that the E field applied is not exactly along the b axis of the crystal, so the projection of $\delta\mu$ of the selected ion onto the E field is no longer the same. Therefore, when a certain E field

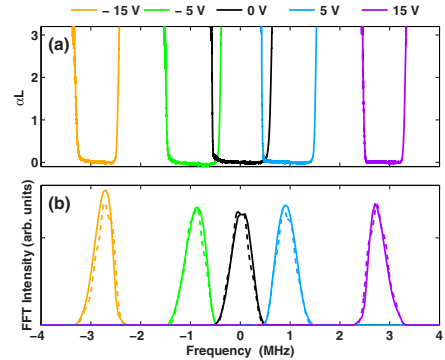


FIG. 3. (a) The passband position of the frequency shift filter when different voltages are applied. The black trace is for the filter created originally. When different voltages are applied across the crystal, the resonance frequency of the ions outside the filter shifts, and therefore the passband of the filter changes accordingly. (b) Frequency distribution of the transmitted pulse for different voltages, measured experimentally (solid traces) and simulated theoretically (dashed traces). The incoming probe pulse is at 0 MHz (605.977 nm), and different voltages are applied when the incoming pulse is completely inside the crystal. The frequency shift of the transmitted pulse follows the shift of the filter and is proportional to the external voltage applied.

LI, BAO, THURESSON, NILSSON, RIPPE, AND KRÖLL

PHYSICAL REVIEW A 93, 043832 (2016)

is applied, half of the ions will be shifted more than the rest of the ions. Since this misalignment has the same effect on both side of the hole structure, it seems unlikely to be the main reason here.

Having the frequency shift filter prepared, a 1- μ s-long Gaussian pulse with the center frequency at 0 MHz was sent into the crystal. Due to the off-resonant interaction between the optical pulse and the absorbing ions outside the filter, the group velocity of the probe pulse is slowed down to about 2500 m/s and it takes about 4 μ s for the pulse to pass through the crystal. According to Eq. (1), with this group velocity, more than 99.9% of the pulse energy is stored in the form of ion polarization when the pulse is inside the crystal. An external voltage is applied to shift the resonance frequency of the ions and the frequency of the transmitted pulse will shift as a consequence. Heterodyne detection was used to measure the frequency of the transmitted pulse. The solid curves in Fig. 3(b) shows the frequency distribution of the transmitted pulses for different voltages measured experimentally, while the dashed curves are from the theoretical simulation for the same process. The black trace is for the case where no external voltage is applied, and hence no shift is observed. A Stark coefficient of 116.7 kHz/V/cm is used in the simulation, which fits well with the literature value reported previously [21,25]. Since the frequency shift of the pulse originates from the frequency shift of the ions as the energy of the pulse is stored in the ions during the propagation inside the crystal, it is quite intuitive that the frequency shift of the pulse goes together with the frequency shift of the filter.

To illustrate the frequency shift process inside the crystal, the energy distribution just before and after the frequency shift is shown in Fig. 4, where the dark red color represents where most of the energy is stored while the dark blue shows that no energy is stored at that frequency and position (a full video of the energy flow in the crystal during the pulse propagation can be found in the Supplemental Material to this article [26]). The energy distribution is calculated by multiplying the number of ions at a specific frequency and position by the probability of them being excited and is represented by different color. It can be seen from Fig. 4(a) that the empty \sim 1-MHz channel around 0 MHz is the transmission window originally created, and even though the input pulse itself only contains energy within the \sim 1-MHz passband, the energy of the pulse is stored in the ions outside the passband. After applying an

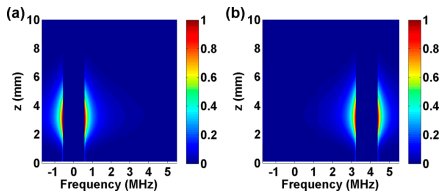


FIG. 4. The energy distribution in the ions just before (a) and after (b) applying electric field. The energy of the pulse is stored in the ions outside the \sim 1-MHz transmission window, and the frequency shift of the ions will shift the light frequency.

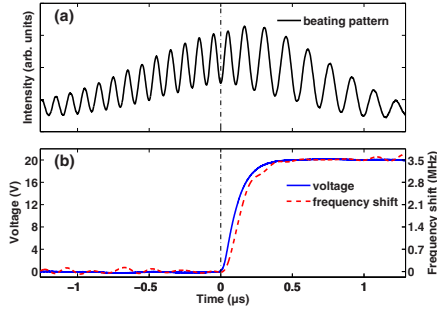


FIG. 5. (a) Beating pattern from the transmitted pulse after the crystal and the reference beam. The electric field is switched on at time $t = 0$, as indicated by the dash-dotted line. The change of beating frequency illustrates that the frequency of the transmitted pulse is changed. (b) The instantaneous frequency calculated from the beating frequency of the transmitted beam (red dashed line) is plotted together with the external voltage (blue solid line) applied onto the crystal, and the frequency shift follows the voltage change.

electric field, all the ions are shifted 3.8 MHz, as shown in Fig. 4(b), which will give a light pulse at a new frequency in the end.

To further study the frequency shift process experimentally, an external electric field was applied when half of the optical pulse had exited the crystal while the other half is still inside. As can be seen from the beating pattern in Fig. 5(a), the phase evolution of the beating pattern changes as the electric field is switched on, and the first and second half of beating pattern have different frequencies, which shows that there is a frequency shift of the transmitted pulse after the electric field is switched on. The instant frequency of the transmitted pulse is calculated as described in Refs. [27,28] and plotted together with the applied voltage as shown in Fig. 5(b). The frequency shift follows the voltage applied and the switch on time of the frequency shift filter is about 200 ns, limited by the rise time of the external voltage. It can be confirmed from the red trace of Fig. 6 that the frequency shift of the transmitted pulse is proportional to the external voltage applied and can be well controlled electrically.

Finally, we study the efficiency of the frequency shift process. The relative efficiency, i.e., $\eta_{\text{rel}} = \frac{E(V)}{E(V=0)}$, where $E(V)$ is the energy of the transmitted pulse for a specific voltage (electric field). To this end, the transmitted, frequency shifted pulse from the filter was averaged 50 times and measured directly by PD2, and the local oscillator beam was blocked (see Fig. 2). The relative efficiency was calculated by comparing the pulse area of the averaged transmitted pulse at different voltages with the case where no voltage is applied. The result is shown as the blue trace in Fig. 6. For a frequency shift of less than ± 3 MHz (applied voltage ± 17 V), the relative efficiency is above 90%. The larger the frequency shift, the lower the efficiency. This can be explained by the narrowing of the filter structure after applying the electric field as shown

043832-4

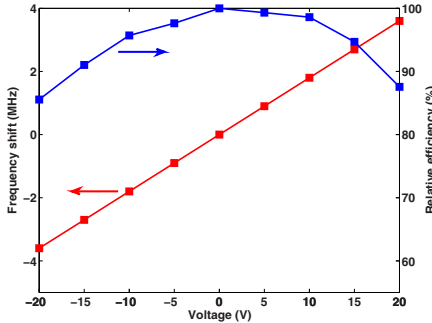


FIG. 6. Frequency shift of the transmitted pulse (red) and relative efficiency of the frequency shift (blue) for different voltages applied.

in Fig. 3. The narrowing after the frequency shift induces absorption for the outer frequency components of the light and causes the decrease in efficiency.

If we assume that the main loss inside the 1-MHz filter comes from the off-resonance excitation of the ions outside the hole and that the optical depth outside the hole is 20 for this case (estimated from Refs. [10,19,29]), then the fundamental limit on how much absorption remains in the middle of a 1-MHz inverse top-hat distribution of Pr^{3+} ions, which have a homogeneous linewidth of 1 kHz, can be calculated to be $\sim 2\%$. However, such low loss has not been experimentally demonstrated for a similar case [6].

Currently, the frequency shift is about ± 4 MHz in this experiment and is limited by our choice of hole burning technique and the existence of the two groups of Pr^{3+} with different signs of their Stark coefficient. If shifted further, then there will be absorption from ions with opposite signs of their Stark shift. Nevertheless, one can go beyond this limit. For example, by preparing another spectral hole at twice the desired frequency shift, the frequency shift can be extended to hundreds of MHz. As shown in Fig. 7(a), besides the frequency shift filter prepared at zero frequency, another wide hole is created at 200 MHz. Applying an \mathbf{E} field can shift the red ions -100 MHz while shifting the blue ions $+100$ MHz. In the end, the frequency shift filter at 0 MHz and the spectral hole at 200 MHz will overlap at 100 MHz, as shown in Fig. 7(b). Therefore, the optical pulse propagating inside the crystal can be shifted from 0 to 100 MHz in this way. We propose that the loss during the frequency shift process can be estimated as follows. Looking at Fig. 7(a), the “blue” ions which are polarized by the input pulse will need to shift towards a higher frequency until they meet the spectral hole from the “red” ions at the 100-MHz position [Fig. 7(b)]. During the shift from zero to 100 MHz before they reach the red spectral hole, the pulse in the blue transmission window can be absorbed by the “red” ions between 10 and 90 MHz [Fig. 7(a) and 7(b)]. The losses during this process will be

$$\eta \approx 1 - e^{-\alpha/2 \times L'}, \quad (11)$$

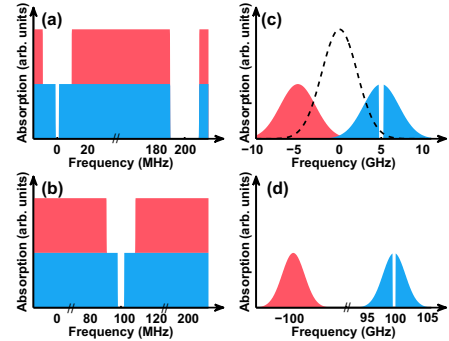


FIG. 7. Ways to make larger frequency shift. The red color stands for the ions with negative Stark coefficient while the blue ones are ions with positive Stark shift. (a) A frequency shift filter structure at 0 MHz and another spectral hole at 200 MHz away. (b) After applying a certain \mathbf{E} field, the frequency shift filter moves to 100 MHz. Using this method the frequency shift of an optical pulse could be hundreds of MHz. (c) The black dashed line is the original absorption profile with FWHM of 5 GHz. A static \mathbf{E} field can completely separate the ions with different signs of their Stark coefficient. The frequency shift filter will be prepared by simple hole burning in one group of these ions. The width of the spectral hole is exaggerated here. (d) Applying an additional \mathbf{E} field will shift the ions as well as light propagating inside the medium up to hundreds of GHz.

where $L' = v_g T$ is the distance in the crystal that the pulse propagates during the electric field switching time, T ;

$$v_g \approx \frac{2\pi\Gamma}{\alpha/2} \quad (12)$$

is the group velocity; Γ is the width of the filter transmission window; and $\alpha/2$ is the absorption coefficient of half of the ions. In Eq. (11) $\alpha/2$ is the “red” ion absorption while in Eq. (12) $\alpha/2$ is the “blue” ion absorption. Inserting Eq. (12) in Eq. (11), we get

$$\eta \approx 1 - e^{-2\pi\Gamma T}. \quad (13)$$

The loss is only affected by the width of the filter and the switch-on time of the voltage. For $\Gamma = 1$ MHz, a loss about 3% per 5 ns switching time would be achieved. So the loss can be kept low if the field switch-on is fast enough. This way, the frequency shift is only limited by the frequency range of the laser used for the structure creation.

Moreover, one can extend the frequency shift range still further by applying a large \mathbf{E} field to completely separate the ions with opposite sign of their Stark coefficients. In this way, the absorption from the other group of ions can be completely eliminated, and will no longer affect the efficiency for the frequency shift process. For instance, for a 20- μm -thick waveguide made of $\text{Pr}^{3+}:\text{Y}_2\text{SiO}_5$, a static field of 100 V will be sufficient to separate the absorbing Pr^{3+} with different signs of Stark coefficient 10 GHz apart (the inhomogeneous linewidth is about 5 GHz), as shown in Fig. 7(c). Then, by doing the

straightforward hole burning in one group of ions together with the Stark effect, frequency shifts up to a couple of hundred GHz can be achieved, see Fig. 7(d). In this case, the frequency shift can reach hundreds of gigahertz and is only limited by the breakdown voltage of the crystal (\sim MV/cm). Note that here the homogeneity of the \mathbf{E} field along the light propagation direction has to be good enough to not smear out the hole structure.

A band-pass filter can be prepared throughout the entire crystal if the preparation beam covers or scans the whole crystal [9]. It has been shown that a filter prepared in this way will work for light entering the crystal from multiple directions. The light will be transmitted and delayed if its frequency is within the passband and strongly attenuated otherwise [9]. By using special antireflection coating techniques, the input light can be coupled into the crystal very effectively, even with a high incidence angle [30,31]. Once inside the crystal, the light will be guided to the exit facet via total internal reflection (the refractive index for the crystal is $n \approx 1.8$). Therefore, the solid angle of acceptance of such a filter could be close to 2π . In the present demonstration, the input light is polarized along the $D2$ axis of the crystal since this is the axis with maximum slow light effect (energy storage). For light entering the crystal polarized perpendicular to the $D2$ axis the slow light effect would be so small that the light just passes through before there is time to change the electric field and the frequency shift cannot be achieved. This polarization restriction can be eliminated by adding an identical crystal right after the present one rotated around the light propagation axis ($D1$) by 90° relative to the first one [17]. A frequency shift filter made of two identical crystals and the same spectral structure prepared in the entirety of both crystals should be able to shift the frequency of light in any spatial mode and any polarization, including randomly scattered light. In ultrasound optical tomography, where light can be focused at an ultrasound focus deep inside a scattering medium using phase conjugation, it has been shown that the ratio between the light intensity in the focus and the background intensity can be increased by iteratively letting light passing in between the focal point and phase conjugate mirrors [32]. However, since the light will be diffracted and frequency shifted, each time it passes through the ultrasound focus, a frequency shifter, which works for randomly scattered light as demonstrated here, that is able to shift the light back to its original frequency will further improve the performance of such a scheme.

V. CONCLUSION

In conclusion, we demonstrate a voltage- (electric field) controlled optical frequency shift device capable of shifting the frequency of a light pulse by ~ 1 MHz/(V/mm). The device is based on creating a narrow semipermanent transmission window in frequency in a rare-earth-ion-doped crystal absorption line using optical pumping. This causes strong slow light effects (group velocities of a few thousand m/s) for light propagating in this transmission window. At these slow group velocities the energy of an propagating optical pulse is mainly stored as optical polarization of the ions in the material. By Stark shifting these ions, the frequency of the light pulse is shifted. The demonstrated frequency shifting

range is ± 4 MHz and the fractional pulse energy loss when applying the frequency shift is in the few to 10% range. It is proposed how the frequency range of these shifts could be extended to be limited only by the breakdown voltage of the crystal (~ 1 MV/cm) yielding a frequency shift limit of around 100 GHz. Based on related work [9,17], it is argued that these frequency shifters should have a solid acceptance angle close to 2π and thus could be used also for scattered light. As the frequency shift is controlled solely by an external electric field and does not involve any additional optical pulses, these frequency shifters can be especially suitable in weak light situation, for example, to match the frequency of weak coherent light to a particular quantum memory frequency or to shift the spectra of the qubits for the readout process [33]. Additionally, it has a potential to be integrated with other devices, which could open up on-chip applications.

ACKNOWLEDGMENTS

This work was supported by the Swedish Research Council, the Knut & Alice Wallenberg Foundation. The research leading to these results also received funding from the People Programme (Marie Curie Actions) of the European Union's Seventh Framework Programme FP7 (2007-2013) under REA Grant No. 287252 (CIPRIS) and Lund Laser Center (LLC).

APPENDIX

1. Structure preparation

For the frequency shifter to work, it is critical that the absorbing ions right outside the filter should have the same sign of their Stark coefficient. However, in $\text{Pr}^{3+}:\text{Y}_2\text{SiO}_5$, there are four possible static dipole orientations, distributed (in the $D2$ - b plane) 12.4° away from b axis [Fig. 2(b)]. For an electric field applied along the b axis, this yields two overall Stark coefficients, with the same magnitude but opposite sign. To make the frequency shifter structure shown in Fig. 1, the ions with different signs of their Stark coefficient have to be separated. This is done by combining the hole burning technique together with the Stark effect during the structure preparation process.

The sketch of a step by step absorption profile is shown in Fig. 8, where the red represents the ions with a negative sign of their Stark coefficient while the blue represents the ions with a positive sign of their Stark coefficient relative to the \mathbf{E} field. An external voltage of 88 V was applied prior to any preparation, shifting the blue ions 16 MHz and the red ones -16 MHz; the absorption profile of the interested frequency range is shown in Fig. 8(a). Then an 18-MHz-wide hole was prepared using the optical pumping scheme described in our previous paper [8,19]. The resulting absorption profile is shown in Fig. 8(b). The external field was switched off, the ions will shift back to their original position, the left two "half holes" at 0 MHz and -32 MHz, shown in Fig. 8(c), so at the region of 0 ± 9 MHz only the ions with a positive sign of their Stark shift exist. Last, the laser frequency was scanned ± 500 kHz around 0 MHz. In the end, a ~ 1 -MHz narrow hole was created with the surrounding ions within 18 MHz that have the same sign from which their Stark coefficient was created. This is the frequency shifter (frequency shift filter) and it is

SLOW-LIGHT-BASED OPTICAL FREQUENCY SHIFTER

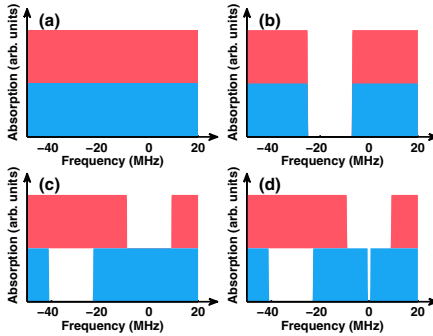


FIG. 8. Absorption profile of the ions during the preparation of the frequency shift filter. The blue and red represent absorption from ions with a positive and negative sign, respectively, of their Stark coefficient. (a) The original absorption profile when $V = 88$ V. (b) A hole of about 18 MHz was prepared by spectral hole burning when $V = 88$ V. (c) The 18-MHz hole is split in two when $V = 0$. (d) Another 1-MHz narrow hole is burnt at around 0 frequency. The 1-MHz hole which only surrounded by ions with the same sign of the Stark coefficient within the 18-MHz region is called the frequency shift filter (frequency shifter).

shown as the structure around 0 MHz in Fig. 8(d). When an external voltage is applied, the frequency shift of the ~ 1 -MHz hole will be proportional to the \mathbf{E} field.

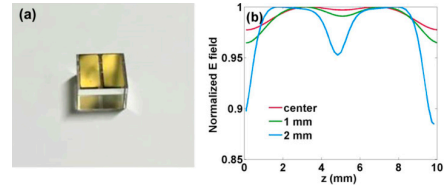
PHYSICAL REVIEW A **93**, 043832 (2016)

FIG. 9. (a) The 6-mm-thick crystal with electrodes used in the experiment. Two sets of electrodes were directly deposited onto the top and bottom surfaces of the crystal with a 0.5-mm gap between them. (b) The electric field along the light propagation axis at the center of the crystal (red) 1 mm away (green) and 2 mm away (blue) from the center. As can be seen, there is a spatial field inhomogeneity which is especially pronounced when close to the electrode surfaces.

2. Electric field

Two sets of electrodes were directly deposited onto the top and bottom surfaces of the crystal with a 0.5-mm gap between the two sets of electrodes, as shown in Fig. 9(a). Because of the two pairs of electrodes separated by a gap on each of the two surfaces, the \mathbf{E} field in the crystal will be nonuniform when an external voltage is applied across the crystal. Hence the amount of Stark shift will differ slightly for ions in different spatial positions. The \mathbf{E} field as a function of position along the light propagation path is shown in Fig. 9(b) about 0.2% inhomogeneity is shown in the center of the crystal along the light propagation path, it becomes more nonuniform when away from the center. The light propagation was close to the center in the experiment to get a better uniformity of the \mathbf{E} field.

- [1] M. Notomi and S. Mitsugi, *Phys. Rev. A* **73**, 051803 (2006).
- [2] S. F. Preble, Q. Xu, and M. Lipson, *Nat. Photon.* **1**, 293 (2007).
- [3] T. Tanabe, M. Notomi, H. Taniyama, and E. Kuramochi, *Phys. Rev. Lett.* **102**, 043907 (2009).
- [4] T. Kampfrath, D. M. Beggs, T. P. White, A. Melloni, T. F. Krauss, and L. Kuipers, *Phys. Rev. A* **81**, 043837 (2010).
- [5] D. M. Beggs, T. F. Krauss, L. Kuipers, and T. Kampfrath, *Phys. Rev. Lett.* **108**, 033902 (2012).
- [6] S. E. Beavan, E. A. Goldschmidt, and M. J. Sellars, *J. Opt. Soc. Am. B* **30**, 1173 (2013).
- [7] A. V. Turukhin, V. S. Sudarshanam, M. S. Shahriar, J. A. Musser, B. S. Ham, and P. R. Hemmer, *Phys. Rev. Lett.* **88**, 023602 (2001).
- [8] A. Walther, A. Amari, S. Kröll, and A. Kalachev, *Phys. Rev. A* **80**, 012317 (2009).
- [9] H. Zhang, M. Sabooni, L. Rippe, C. Kim, S. Kröll, L. V. Wang, and P. R. Hemmer, *Appl. Phys. Lett.* **100**, 131102 (2012).
- [10] M. Sabooni, Q. Li, L. Rippe, R. K. Mohan, and S. Kröll, *Phys. Rev. Lett.* **111**, 183602 (2013).
- [11] R. W. Boyd, *J. Opt. Soc. Am. B* **28**, A38 (2011).
- [12] J. B. Khurgin, *Adv. Opt. Photon.* **2**, 287 (2010).
- [13] R. N. Shakhmuratov, A. Rebane, P. Mégret, and J. Odeurs, *Phys. Rev. A* **71**, 053811 (2005).
- [14] A. Rebane, R. Shakhmuratov, P. Mégret, and J. Odeurs, *J. Lumin.* **127**, 22 (2007).
- [15] R. Shakhmuratov, *J. Mod. Opt.* **57**, 1355 (2010).
- [16] E. Courtens, *Phys. Rev. Lett.* **21**, 3 (1968).
- [17] C. Clausen, F. Bussi eres, M. Afzelius, and N. Gisin, *Phys. Rev. Lett.* **108**, 190503 (2012).
- [18] R. W. Equall, R. L. Cone, and R. M. Macfarlane, *Phys. Rev. B* **52**, 3963 (1995).
- [19] L. Rippe, M. Nilsson, S. Kr  ll, R. Klieber, and D. Suter, *Phys. Rev. A* **71**, 062328 (2005).
- [20] N. Ohlsson, M. Nilsson, and S. Kr  ll, *Phys. Rev. A* **68**, 063812 (2003).
- [21] F. R. Graf, A. Renn, U. P. Wild, and M. Mitsunaga, *Phys. Rev. B* **55**, 11225 (1997).
- [22] A. Thuresson, Master's thesis, Lund University, 2011.
- [23] C. J. Foot, *Atomic Physics* (Oxford University Press, Oxford, 2004).
- [24] C. S. Cornish, Ph.D. thesis, University of Washington, 2000.
- [25] M. P. Hedges, Ph.D. thesis, Australian National University, 2011.

PAPER IV

Using electric fields for pulse compression and group-velocity control

Q. Li, A. Kinos, A. Thuresson, L. Rippe and S. Kröll.

Phys. Rev. A **95**, 032104 (2017)

Synopsis of paper selected for online display of APS Physics.

Using electric fields for pulse compression and group-velocity control

Qian Li,^{1,*} Adam Kinos,¹ Axel Thuresson,² Lars Rippe,¹ and Stefan Kröll¹¹Department of Physics, Lund University, P.O. Box 118, SE-22100 Lund, Sweden²Theoretical Chemistry, Lund University, P.O. Box 124, SE-22100 Lund, Sweden

(Received 21 October 2016; published 7 March 2017)

In this article, we experimentally demonstrate a way of controlling the group velocity of an optical pulse by using a combination of spectral hole burning, the slow-light effect, and the linear Stark effect in a rare-earth-ion-doped crystal. The group velocity can be changed continuously by a factor of 20 without significant pulse distortion or absorption of the pulse energy. With a similar technique, an optical pulse can also be compressed in time. Theoretical simulations were developed to simulate the group-velocity control and the pulse compression processes. The group velocity as well as the pulse reshaping are solely controlled by external voltages which makes it promising in quantum information and quantum communication processes. It is also proposed that the group velocity can be changed even more in an Er-doped crystal while at the same time having a transmission band matching the telecommunication wavelength.

DOI: 10.1103/PhysRevA.95.032104

I. INTRODUCTION

Controlling the group velocity of light has attracted more and more attention due to its potential application in data synchronization, tunable optical buffer in optical communication [1], optical information processing, and optical switching [2]. To date, various techniques of controlling the group velocity of a pulse have been studied, such as electromagnetic-induced transparency (EIT) [3,4], coherent population oscillation (CPO) [5], stimulated Raman scattering (SRS) [6], and stimulated Brillouin scattering (SBS) [7]. More recently, group-velocity control was demonstrated in silicon-based resonators [8,9], with the target for on-chip application. However, the delay there is only typically in the range of hundreds of picoseconds. One major drawback of the above-mentioned methods for group-velocity control is their needs of a simultaneous optical pump beam which might introduce some background noise to the system, which could be especially detrimental in background-sensitive single-photon applications. It was experimentally demonstrated that the optical pulse delay can be controlled by using transient spectral hole burning at different magnetic fields [10]. However, the requirement of recreating the transient spectral hole for each specific group velocity makes it less feasible in practice. In this article, we present a technique where one spectral hole was prepared and the group velocity of an optical pulse can be solely controlled by an electric field. This is a desired feature when working with weak-light situations; for example, in quantum information and quantum communication processes.

Our technique of controlling the group velocity of an optical pulse uses the combination of spectral hole burning induced slow-light effect and Stark effect and can be described as follows: A 16 MHz spectral hole was prepared in the center of the inhomogeneous broadening of a rare-earth-ion-doped crystal, with the goal of making the edges of the hole as sharp as possible. A principle sketch of the final hole structure together with the real part of the refractive index is shown in Fig. 1(a). The blue and red colors represent ions with positive and

negative Stark coefficients, respectively. If a voltage is applied across the crystal, the resonance frequencies of the “blue” and “red” ions will shift in different directions, which leads to a narrower hole. The change of the hole width is proportional to the applied external voltage since the frequency shift of the ions is proportional to the applied voltage according to the linear Stark shift. For an applied voltage of 40 V, a sketch of the new structure, as well as the real part of the refractive index, are shown in Fig. 1(b), where in the vicinity of the left side of the hole there are only “blue ions,” while in the vicinity of the right side of the hole there are only “red ions.” The dispersion across the transmission window is much steeper than that in Fig. 1(a). This causes the group velocity of an optical pulse to be much slower when propagating in the transmission window shown in Fig. 1(b) than when propagating in a transmission window as shown in Fig. 1(a) [see Eqs. (1) and (3) in Sec. II for further information].

When a 10- μ s-long pulse with a Gaussian frequency profile is sent into the crystal, the group velocity of the pulse could be changed continuously by a factor of 20 by changing the external voltages applied across the crystal, and the group velocity decreases monotonically as the external field is increased. Furthermore, an optical pulse can be reshaped by changing the hole width while the pulse is still inside the crystal. A 1- μ s-long pulse was sent into the crystal at the presence of an external voltage of 40 V, which corresponds to a hole width of about 1 MHz. The group velocity of the pulse was small enough that almost the entire pulse was accommodated in the crystal. The electric field was then decreased rapidly, increasing the group velocity. In this way the first part of the pulse propagated a longer distance inside the crystal with a slower speed than the later part of the pulse, which caused the pulse transmitted from the crystal to be compressed in time. Another way of pulse shortening by sudden increase of the amplitude of the coupling field in an EIT scheme was proposed by Shakhmuratov *et al.* [11]. The drawback of the scheme is the necessity of the strong optical coupling field, which brings extra optical noise to the process.

Although the present experimental demonstration was carried out in Pr:Y₂SiO₅, it can be used in other rare-earth-ion-doped materials where spectral hole burning is

*qian.li@fysik.lth.se

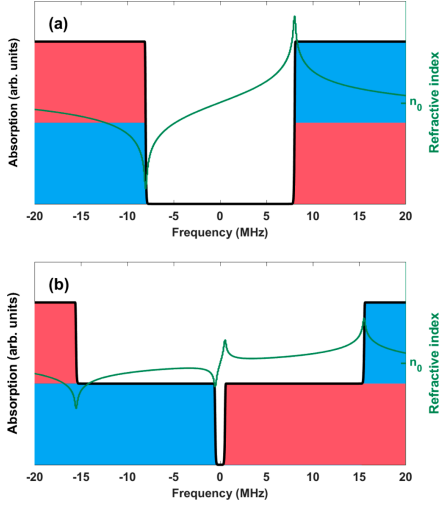


FIG. 1. A simplified sketch of the absorption structure, as well as the dispersion of the refractive index, where the red and blue color represents ions with opposite sign of their Stark coefficients while the black line shows the overall absorption. The green trace shows the real part of the refractive index over the frequency range, where n_0 stands for the refractive index of the host material and in this case $n_0 = 1.8$. (a) The original 16 MHz hole, no external voltages applied. (b) The 1 MHz spectral hole structure when an external voltage of 40 V is applied. The width of the hole as well as the slope of the dispersion changes as the external voltage is changed, which in return changes the group velocity.

possible and Stark or Zeeman effects can be applied to change the hole width. For example, in Er-doped crystals (e.g., Er:Y₂SiO₅). Er ions have an optical transition around 1.5 μm , at the telecommunication wavelength, where the fiber loss is minimum. The Stark coefficient is about 20 kHz/(V/cm) in Er:YAlO₃ [12], and 25 kHz/(V/cm) in Er:LiNbO₃ [13]. The ground-state hyperfine splitting for Er ions is much wider than that of Pr ions [14,15], a spectral hole of 575 MHz can be prepared in Er:Y₂SiO₅ according to the hyperfine splittings provided in Ref. [16]. Since the tuning range of the group velocity is only limited by the widest hole width that can be created and the external voltages applied, the tuning range of the group velocity can be much larger in Er than that in Pr.

II. GROUP VELOCITY

The group velocity v_g of an optical pulse can be calculated via the following equation:

$$v_g = \frac{c}{n + v \frac{dn}{dv}}, \quad (1)$$

where c is the speed of light in vacuum, n is the real part of the refractive index (for the phase velocity), and v is the frequency of the light pulse. When an optical pulse propagates inside a dispersive medium, in our case inside a narrow transmission window, the real part of the refractive index can change dramatically; therefore, $v \frac{dn}{dv}$ can be much higher than n itself, which in the present experiments can decrease the group velocity by four or five orders of magnitude [17,18].

Another way of interpreting the group-velocity reduction is from the light-matter interaction perspective. As shown in Refs. [19–21] (note that in Refs. [20,21], the assumption is made that the material has a refractive index of $n = 1$), the group velocity can be expressed as a temporal energy storage process of the optical pulse energy in the absorbing ions via off-resonance interaction,

$$v_g = \frac{c/n}{1 + \frac{U_c}{U_{em}}}, \quad (2a)$$

where U_c is the energy density accumulated in the excitation of the off-resonant centers and U_{em} is the energy density of the electromagnetic field propagating with phase velocity c/n in the medium in the absence of dispersion. The equation shows that, the more energy is temporarily stored in the resonance centers, the lower the group velocity of the light.

In fact, the refractive index n also originates from the off-resonant interaction but between light and the host material. Therefore, when light propagates inside a nondispersive medium, the energy density U_{em} also contains two parts: one is the energy density of the pure electromagnetic wave, U_{vac} , and another one is the energy density accumulated in the host atom, U_{host} . Similar as in Ref. [19], the energy flow across a unit cross section inside the crystal per unit time is $v_g(U_{vac} + U_{host} + U_c)$, which should be the same as the energy flow through a unit cross section per unit time outside the crystal, cU_{vac} . Then the group velocity can be expressed as

$$v_g = \frac{c}{1 + \frac{U_{host}}{U_{vac}} + \frac{U_c}{U_{vac}}}, \quad (2b)$$

hence,

$$v_g = \frac{c}{1 + \frac{U_{med}}{U_{vac}}}, \quad (2c)$$

where $U_{med} = U_{host} + U_c$ is the energy density accumulated in the medium which contains the effect from the host atoms and the resonant centers. In the case of no dispersion, the group velocity equals the phase velocity and we get $n = 1 + \frac{U_{med}}{U_{vac}}$. Thus the higher the refractive index is, the stronger is the interaction between the light and the material, hence the more energy is stored inside the material. To verify this, we can take a nondispersive material with refractive index of n , assume that we have a light beam with a certain amplitude and normal incidence that enters a material with refractive index of n from vacuum. By comparing the energy density inside and outside the material (denoted U_{inside} and U_{vac} , respectively) from the boundary condition, we get $U_{inside} = nU_{vac}$. If we make the same analogy as Courtens did in Ref. [19] that the energy density inside a material can be written as $U_{inside} = U_{med} + U_{vac}$, we get that $n = 1 + \frac{U_{med}}{U_{vac}}$. We note that Eq. (2a) is based

on the assumption that the dispersion is due only to resonance centers other than the host material, while Eq. (2c) is suitable for any general case. That is with and without dispersion and where the dispersion can come from the host atoms or other resonance centers in the material or from both. Therefore, when an optical pulse enters a medium, a certain portion of the pulse energy is stored in the off-resonant ions (atoms) of the medium, and the Bloch vectors of these ions (atoms) are lifted up slightly from their ground-state position. These ions will rephase at a later time, their Bloch vectors will point straight down again and the energy is returned back to the optical field. Intuitively, one can imagine that this process causes the light to propagate slower inside the medium.

In the case where the group-velocity reduction is mainly caused by the spectral hole burning in an absorption profile such as our case here, the group velocity v_g can be approximately calculated by [17,22,23],

$$v_g \approx \frac{2\pi\Gamma}{\alpha}, \quad (3)$$

where Γ is the width of the transmission window and α is the absorption coefficient outside the transmission window.

Equations (1)–(3) can all be used to describe the group velocity but they emphasize different aspects. Equation (1) is the formula to calculate the group velocity when one knows the dispersion, while Eqs. (2b) and (2c) are used to interpret the physical process of group velocity for the so-called material slow-light case [18,19,24]. Equation (3) provides an approximate but convenient estimate of the group velocity inside a spectral hole and is especially useful in our case here for making the first estimate of the tunability of the group velocity since it is proportional to the width of the transmission window and inversely proportional to the absorption coefficient. It is then straightforward to see that the tunability of the group velocity is proportional to the tuning range of the transmission window.

III. EXPERIMENT

The experiment was performed on a $6 \times 10 \times 10 \text{ mm}^3$ (crystal axes $b \times D1 \times D2$), 0.05%-doped $\text{Pr}:\text{Y}_2\text{SiO}_5$ crystal at $\sim 2 \text{ K}$. The top and bottom surfaces of the crystal were coated with two sets of gold electrodes indicated as the red and black lines on the crystal in Fig. 2(a) (a photo of the crystal can be found in the appendix of Ref. [18]). The energy levels involved in this experiment belong to the $^3H_4 \rightarrow ^1D_2$ transition centered around 605.978 nm with an inhomogeneous broadening of about 5 GHz and a homogeneous broadening of about 3 kHz. The hyperfine lifetime of the Pr^{3+} ion ground-state levels is about 100 s and can be extended to about 30 min at the presence of a weak (0.01 T) magnetic field [25].

A simplified setup is shown in Fig. 2(a), where a laser beam from a frequency-stabilized Coherent 699-21 ring dye laser tuned to the center of the inhomogeneous broadening was split into two parts by a 90/10 beam splitter, where the stronger beam was focused onto the center of the crystal and used for the spectral structure preparation and characterization and then measured by a photodetector (PD2) [26], while the weaker one was directly measured by another photodetector (PD1) and used as a reference beam to calibrate intensity variations.

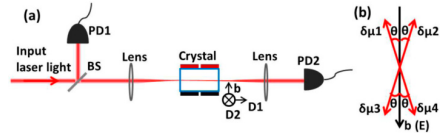


FIG. 2. Experimental setup. Laser light polarized along the $D2$ axis of the crystal is divided into two beams by a 90/10 beam splitter (BS), where the stronger beam is focused and directed along the center line of the crystal and recorded by a photodetector (PD2) while the weaker one is recorded by another photodetector (PD1) and used as a reference beam to calibrate any intensity fluctuations of the laser. (b) The permanent electric-dipole-moment difference between excited state and ground state of the Pr^{3+} ($\delta\mu_1, \delta\mu_2, \delta\mu_3, \delta\mu_4$) relative to the electric field applied (\mathbf{E}). The electric field is along the b axis of the crystal and the magnitude of the projection of the dipole moment difference onto the electric field direction is the same for all the four possible $\delta\mu$ ($\theta = 12.4^\circ$).

The permanent electric-dipole moment of the ground state is different from that of the excited state for Pr^{3+} ions and there are four possible orientations for the dipole-moment difference [18,27]. When an external voltage is applied across the crystal, the resonance frequency of the ions will be Stark shifted by Δ_s , where

$$\Delta_s = \frac{\delta\mu \cdot \mathbf{E}}{\hbar} = \pm \frac{|\delta\mu| \cos(\theta)}{\hbar} \times \frac{\Delta V}{d}, \quad (4)$$

where \hbar is the reduced Planck constant, $\delta\mu$ is the difference between the excited- and ground-state dipole moments for Pr^{3+} ions, \mathbf{E} is the electric field across the crystal (along the b axis), θ is the angle between the electric field and $\delta\mu$, ΔV is the difference in the electric potential between the top and bottom electrodes, and d is the distance between these two electrodes which in our experiment is 6 mm. The four possible $\delta\mu$ of Pr^{3+} are oriented at an angle of $\theta = 12.4^\circ$ relative to the b axis of the crystal, as shown in Fig. 2(b). The magnitude of $\delta\mu/\hbar$ is about 111.6 kHz/(V/cm) [27]. Since the \mathbf{E} field is applied along the b axis and because of the symmetry of $\delta\mu$, there will be two effective Stark coefficients for Pr^{3+} with the same magnitude but opposite signs. At the presence of a certain electric field, the resonance frequency of half of the ions, those with positive Stark coefficient (referred as blue ions), will shift to higher frequencies while the rest of the ions, those with negative Stark coefficient (referred as red ions), will shift to lower frequencies.

Originally, a 16 MHz square transmission window was created by using optical pumping. However, due to the inhomogeneity of the \mathbf{E} field inside the crystal (see the appendix in Ref. [18]) and the possible small mismatch of the electric field with the b axis of the crystal, when an electric field is applied to change the hole width, different ions see a slightly different electric field and shift slightly different amount in frequency, which smears out the sharpness of the hole edge and induces some absorption close to the edge of the hole. To compensate for this effect, the actual hole burning sequence was optimized in the following way, 16 MHz, 8 MHz, 1 MHz, and 500 kHz hole burning sequences were employed

consecutively in the presence of 0, 20, 40, and 41.5 V external voltages, followed by the same 16 MHz hole burning at 0 V in the end. This process is repeated 50 times until a hole with high transmittance and sharp edges was achieved. The sharpness of the hole was optimized by sending a frequency-chirped readout pulse after the hole creation and examine the coherent beating signal at the first hole edge. The higher the beating amplitude, the sharper the hole edge. The Rabi frequency of the hole burning sequence was kept low to avoid any power broadening and instantaneous spectral diffusion [28,29] in order to make the hole edge as sharp as possible. The whole process took about half a minute, so a 0.01 T magnetic field was applied to decrease the hyperfine relaxation rate such that the hole did not degrade much during the preparation process. A simplified sketch of the final hole structure as well as the structure at the presence of an external voltage of 40 V together with the real part of the refractive index can be found in Fig. 1.

IV. RESULT AND DISCUSSION

A. Group-velocity control

After the structure preparation, 16 Gaussian pulses, each with a full width at half maximum (FWHM) of $10 \mu\text{s}$ and a cutoff duration of $100 \mu\text{s}$, were sent into the crystal successively while the external voltage applied across the crystal was increased monotonically for each probe pulse from 0 to 42.5 V. A part of the incoming pulse (reference beam) and the transmitted pulse were measured by PD1 and PD2 shown in Fig. 2(a). By comparing the time delay of the transmitted signal and the reference beam, the group velocity of the optical pulses can be calculated for each electric field. The relative efficiency was calculated by comparing the area of the transmitted pulse at different electric fields with the area of the transmitted pulse with no external voltage (widest hole) after correction using the reference beam signal. The measurement was repeated 150 times and the result is shown in Fig. 3, where the dot represents the average value for

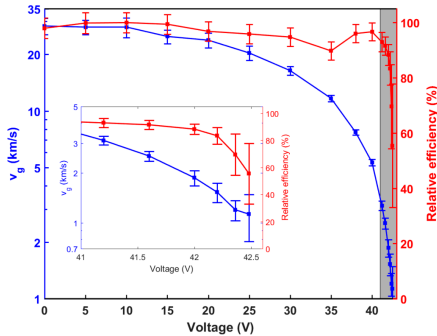


FIG. 3. The group velocity (blue) and the relative transmission efficiency (red) at different external voltages. The group velocity can be changed by a factor of 20 while keeping the relative efficiency more than 80%.

each voltage and the bars associated with the dots are one standard deviation away from the average. The gray area was zoomed in as an inset. The group velocity of the probe pulse changed from 30 to 1.5 km/s (when external voltages were changed from 0 to 42.2 V) while still having more than 80% relative transmittance. Beyond this, the absorption increases dramatically as the hole width becomes comparable to the frequency width of the pulse. 1 km/s was achieved with about 50% transmittance.

We can interpret the reduction of the group velocity from the three aspects that were discussed in Sec. II. From Eq. (1), it is clear that the steeper the dispersion, the slower the group velocity. When an external voltage is applied across the crystal the hole becomes narrower, and the slope of the dispersion becomes steeper as shown in Fig. 1. Hence $v_g \propto \frac{d\omega}{dk}$ becomes much bigger, which decreases v_g greatly.

As revealed from Eq. (2c), the more energy stored in the medium, the slower the group velocity of the light. When the hole becomes narrower, the resonant frequency of the absorbing ions are much closer to the probe frequency; therefore, the off-resonance interaction between the light and the ions becomes much stronger, which leads to more energy stored in the off-resonant ions and the group velocity decreases. For the 16 MHz hole, with group velocity of $v_g = 30 \text{ km/s}$, according to Eq. (2c), the fraction of energy temporally stored in the crystal is 99.98%, while for a group velocity of $v_g = 1.5 \text{ km/s}$, the fraction of energy stored in the crystal is 99.9991%.

We can easily estimate the tunability of the group velocity of the structure from Eq. (3), when the width of the hole changes from 16 MHz (0 V) to 0.25 MHz (estimated experimental hole width at the bottom of the hole at 42.2 V), a reduction of a factor of $\frac{16}{0.25} \times \frac{1}{2} = 32$ should be achieved (the $\frac{1}{2}$ comes from the fact that the absorption coefficient just outside the hole changes by a factor of two for these two structures; see Fig. 1). However, experimentally we only get a factor of 20 in group-velocity reduction, which is probably due to the decrease in the sharpness of the hole edge, so even though the window of full transmission is only 0.25 MHz, the full width at half maximum of the hole is actually much wider than that.

Concerning the absolute efficiency, it has been shown previously that the remaining absorption inside a 18 MHz spectral hole of a $\text{Pr}:\text{Y}_2\text{SiO}_5$ crystal with the same doping concentration as in the present experiment can be less than 0.1 dB/cm [17]. In our case this will correspond to an absolute transmission efficiency of higher than 97% for the 16 MHz spectral hole. We can then renormalize the relative efficiency according to this number to estimate the absolute efficiency for each group velocity.

In principle, as shown in Eq. (3), the tunability of the group velocity is only limited by the tunable range of the spectral hole width. Therefore, it could be greatly expanded if a much wider hole can be prepared from the beginning. For example, in $\text{Er}:\text{Y}_2\text{SiO}_5$, a spectral hole that is 575 MHz can be prepared given the hyperfine structures of the ground and excited states [16]. Therefore instead of a factor of 20 demonstrated here, a factor of 600 could be achieved ideally. Besides this, the absolute group velocity can be changed by changing the absorption coefficient at the hole edges and this

can be easily changed by changing the laser frequency to the side of the inhomogeneous absorption profile for the structure preparation process (or changing to another crystal with higher or lower absorption coefficient). The closer to the center of the absorption, the lower group velocity one can get while keeping the same tunability.

The bandwidth-delay product **BD** for such a slow-light structure can be approximately calculated by [21]

$$\text{BD} = \frac{L}{v_g} \Gamma \approx \frac{\alpha L}{2\pi}, \quad (5)$$

where L is the length of the crystal. Since the absorption coefficient can easily be changed by going to another wavelength and the length of the crystal can be altered according to the purpose of the application, the bandwidth-delay product can therefore be easily changed. A more detailed discussion can be found in Refs. [17,30].

B. Pulse compression

Group-velocity control can also be used to reshape an optical pulse in time. After the creation of the 16 MHz hole [structure shown in Fig. 1(a)], a 1- μ s-long pulse was sent into the crystal at time $t = 0$, shown as the black dashed trace in Fig. 4. When no voltage is applied, the pulse comes out of the crystal at time $\tau_1 = 350$ ns, shown as the blue trace, and the group velocity of the pulse is $v_{g1} = L/\tau_1 \approx 29$ km/s, while when the pulse enters the crystal in the presence of an external voltage of 40 V [structure shown as in Fig. 1(b)], it propagates with a much lower group velocity, $v_{g2} \approx 6.5$ km/s, and comes out of the crystal at $\tau_2 = 1.54$ μ s, shown as the green trace in Fig. 4.

Because of the low group velocity when 40 V was applied across the crystal, the 1- μ s-long light pulse was strongly compressed, from a length of 300 m long in air to about 6 mm

inside the crystal. Therefore, almost the entire pulse can be accommodated inside the crystal. If the external voltage is switched off when the pulse is just about to exit, then the first part of the pulse will go through the entire crystal with a group velocity of $v_{g2} = L/\tau_2$, while the last part of the pulse will initially propagate with group velocity v_{g2} and change to a group velocity of v_{g1} after the **E** field is switched off. Therefore, the last part of the pulse spends much shorter time inside the crystal and the pulse will be compressed in time; shown as the red trace in Fig. 4.

A possible way to estimate how much a pulse can be compressed in time might be to assume that the pulse propagates with a group velocity of v_{g2} at first, the pulse length is $l = v_{g2}\tau$, and the crystal is long enough to accommodate the whole pulse length. If the group velocity is changed to v_{g1} instantaneously just when the first part of the pulse is about to exit, it takes $\tau' = l/v_{g1}$ for the last part of the pulse to exit the crystal. Therefore, a pulse initially with a duration of τ will be changed to $\tau' = \frac{v_{g2}}{v_{g1}}\tau$. Therefore, the compression factor, defined to be the ratio of the duration of the original pulse to the duration of the compressed pulse in time, would be $\frac{\tau}{\tau'} = \frac{v_{g1}}{v_{g2}}$. Hence, the bigger the ratio of the two group velocities, the more the pulse can be compressed. In reality, the electric field cannot be changed instantaneously, so the compression factor will be smaller. However, the compression factor will always be $\frac{v_{g2}}{v_{g1}}$, if the whole pulse is inside the crystal during the time while the **E** field is changed.

If we look at the pulse compression process from the energy density point of view, the pulse first propagate in a structure as in Fig. 1(b), where the group velocity is low, the energy of the optical pulse is mainly stored in the nearby off-resonant ions. When the electric field is decreased, those ions will shift outwards relative to the hole center, constitute a wider hole, and emit light at another frequency, so the pulse coming out would have a wider frequency distribution compared with the pulse sent in. The wider frequency span may be viewed as enabling a pulse compression in time.

A relevant quantity about the pulse compression is the efficiency of the compression process, which can be calculated by comparing the pulse area of the compressed pulse with that of the uncompressed pulse from Fig. 4. If the transmitted energy for a 16 MHz hole (blue trace) is set to 100%, then the transmitted energy for the 1 MHz hole is about 96.6% while the energy transmitted for the compressed pulse is about 66%. To evaluate the energy loss during the pulse compression process, a Maxwell-Bloch simulation was performed, and the detailed information about the simulation can be found in the simulation section of Ref. [18]. Two different simulations were carried out for comparison. Case I corresponds to the actual experiment when a 1 μ s pulse is sent into the 1 MHz transmission window as shown in Fig. 1(b). Before the pulse exits, the **E** field is switched off and the transmission window changes to 16 MHz, just as shown in Fig. 1(a). In this case, if we look at the right-hand side of the hole structure there only exists red ions before the field changes so the energy will mainly be stored in the red ions, while the red and blue ions overlap after switching off the **E** field. Therefore, when light was re-emitted by the red ions, it might be resonantly absorbed by the blue ions. We expect this will cause some energy loss.

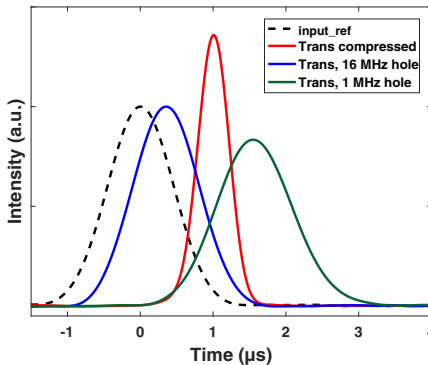


FIG. 4. Pulse compression. Dashed black trace is the reference incoming pulse, the blue trace is for 0 V, the dark green trace is for 40 V, and the red trace is for 40 V changed to 0 V just before the pulse is about to exit the crystal.

LI, KINOS, THURESSON, RIPPE, AND KRÖLL

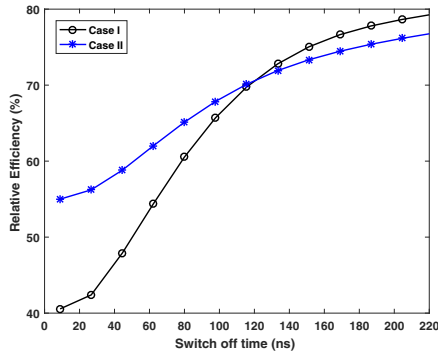
 PHYSICAL REVIEW A **95**, 032104 (2017)


FIG. 5. Pulse compression efficiency as a function of \mathbf{E} field switch off time. The black circles are from simulation case I while the blue stars are from simulation case II. See main text for the description of the two cases.

Therefore, case II is simulating a similar situation but on the right side of the hole all the ions are red ions while on the left side of the hole all the ions are blue ions as the structure shown in Fig. 1(b) if the top half part is neglected. For this simulation, there will consequently never be any overlap of the resonance frequency of the two groups of ions. Hence by comparing these two cases, the energy loss due to the overlap in resonance frequency of the two groups of ions can be mapped out.

The simulated efficiency of the pulse compression process as a function of the switch-off time of the \mathbf{E} field can be found in Fig. 5. It shows that, the slower the \mathbf{E} field is switched off, the higher is the efficiency and when the \mathbf{E} field is switched off almost instantaneously, the energy loss is 40.5% for case I and 55% for case II, respectively. The 15% lower efficiency in case I can be attributed to the overlap of the two groups of ions (red and blue) as discussed above. However, even for case II where the ions never overlap with each other, the efficiency is still only 55% when the \mathbf{E} field is switched off rapidly and this is probably due to the fact that the energy distribution of the $1\ \mu\text{s}$ pulse propagating inside a $1\ \text{MHz}$ hole and a $1/16\text{-}\mu\text{s}$ -long pulse (theoretical estimation of the FWHM of the compressed pulse according to the discussion above) propagating inside a $16\ \text{MHz}$ hole are quite different as shown in Fig. 6. When the \mathbf{E} field is switched off almost instantaneously, the ions will Stark shift to another resonance frequency accordingly and the hole changes from 1 to $16\ \text{MHz}$. However, the resulting energy distribution does not match the $16\ \text{MHz}$ structure; therefore, the rephasing process will not be complete and it is reasonable to assume that some energy would be lost due to this. As can be seen from Fig. 5, when the \mathbf{E} field is switched more slowly the energy loss due to this effect decrease for both simulation cases.

In case I, if the \mathbf{E} field is switched off in $200\ \text{ns}$, the relative efficiency one can reach is around 79% while in our experiment, only 66% was achieved. This could be due to

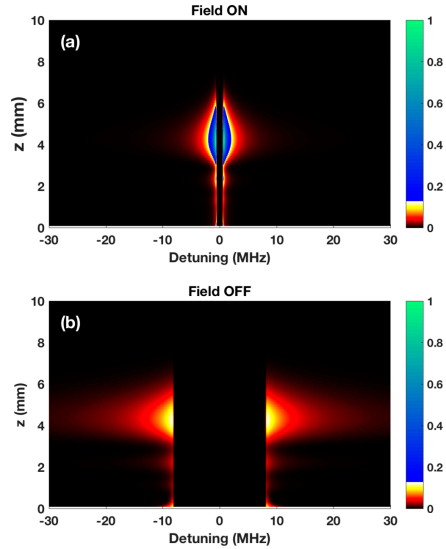


FIG. 6. The energy distribution of optical pulses propagate inside different hole structures. (a) A $1\ \mu\text{s}$ pulse in a $1\ \text{MHz}$ hole and (b) a $1/16\ \mu\text{s}$ pulse in a $16\ \text{MHz}$ hole. The color represents the relative energy stored in the ions calculated from the normalized angle of the ions' Bloch vector when optical pulses are propagating in the material. The maximum scale of 1 represents the maximum angle of the ions' Bloch vector relative to the w axis (in this simulation, for an input pulse area of $\pi/20$ this maximum angle is 2.56°), while 0 indicates that the ions' Bloch vector is pointing straight down, which means no energy is stored. The bigger the angle, the more the energy is stored in the ion. As can be seen, the energy is much more confined in frequency for a $1\ \mu\text{s}$ pulse propagating in the $1\ \text{MHz}$ hole.

absorption by ions remaining in the hole. As can be seen from Fig. 3, there is a specific absorption for each voltage when the pulse propagates inside the hole. For an applied voltage of $35\ \text{V}$, the transmission loss is about 10%. This could be minimized by further optimizing the structure preparation process.

In principle this technique can be used to stretch the pulse in time as well by having a higher group velocity at the beginning and then change to a lower one. However, this would require a crystal that is long enough to fit the entire pulse when it propagates at a higher group velocity, therefore it is practically more difficult to implement. Nevertheless, one might be able to do this with a multipass beam arrangement in a crystal or in a slow-light cavity [17].

V. CONCLUSION

In conclusion, we demonstrate a device in which the group velocity of an optical pulse can be changed continuously by a factor of 20 solely by applying an external electric field. The

energy loss of the transmitted pulse is kept below 20% over the whole group-velocity-tuning range. The device can also be used to reshape and compress the pulse. The maximum compression of a pulse depends on the ratio of the maximum and minimum group velocity with which the pulse propagates inside the crystal. The device is based on creating a semipermanent transmission window in the absorption line of a rare-earth-doped crystal using optical pumping. By Stark shifting the resonance frequency of the ions, the structure of the transmission window as well as the dispersion of the refractive index across the transmission window will be changed, hence the group velocity of the pulse propagating inside the transmission window will be changed accordingly. It is proposed that the tunable range of the group velocity can be further extended in other rare-earth-doped crystals, such as Er^{3+} -doped crystals. Because the group velocity is controlled purely by an external electric field and does not require any additional optical pulses, it can be especially useful in weak-light situations. For example, in quantum information and quantum communication processes. Moreover, since it is a solid-state device it can be integrated with other devices and could open up the way for on-chip applications.

ACKNOWLEDGMENTS

We thank NanoLund for the help with depositing electrodes on the $\text{Pr}:\text{Y}_2\text{SiO}_5$ crystal. This work was supported by the Swedish Research Council and the Knut & Alice Wallenberg Foundation. The research leading to these results also received funding from the People Programme (Marie Curie Actions) of the European Union's Seventh Framework Programme FP7 (2007–2013) under REA Grant Agreement No. 287252 (CIPRIS) and Lund Laser Centre (LLC).

APPENDIX

As can be seen from the inset of Fig. 3, the error bars for the relative efficiency become much bigger when the applied voltages are higher than 42 V (which corresponds to a hole width of less than 300 kHz). This is attributed to the 50 Hz noise in the high-voltage amplifier used for this experiment. As discussed before, the Stark shift of the ions is linearly proportional to the applied external field. The variation in the voltages applied to the crystal will cause variation in the Stark shift of the ions, which will affect the preparation process of

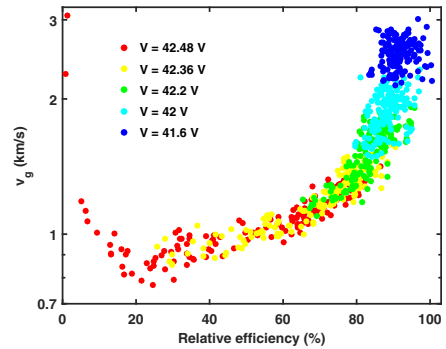


FIG. 7. The correlation of the group velocity and the relative efficiency at different external voltages.

the hole structure as well as the hole width when probing. When the width of the hole is comparable to the frequency spread of the optical pulse, a small fluctuation in the hole width can cause a dramatic change in the transmission as it changes exponentially with the number of ions inside the frequency width of the pulse. Therefore, the relative error for the transmission is much higher when the hole width is really narrow.

Since the fluctuation in the efficiency is caused by the fluctuation in the hole width, i.e., a lower efficiency is due to a narrower hole width. According to Eq. (3), a narrower hole width gives a lower group velocity as well. Therefore, the group velocity and the relative efficiency should be correlated to each other. This can be verified from Fig. 7 which shows the group velocity and relative efficiency of all 150 measurements when the applied voltages are higher than 41.6 V (i.e., hole width narrower than 500 kHz). It shows that, when the relative efficiency is higher than 20%, the group velocity is positively correlated with the relative efficiency, so that the lower the relative efficiency, the lower the group velocity. However, when the relative efficiency drops below 20%, the group velocity and the relative efficiency shows an anticorrelation.

- [1] R. Ramaswami, K. Sivarajan, and G. Sasaki, *Optical Networks: A Practical Perspective* (Morgan Kaufmann, Burlington, MA, 2009).
- [2] S. A. Hamilton, B. S. Robinson, T. E. Murphy, S. J. Savage, and E. P. Ippen, *J. Lightwave Technol.* **20**, 2086 (2002).
- [3] D. F. Phillips, A. Fleischhauer, A. Mair, R. L. Walsworth, and M. D. Lukin, *Phys. Rev. Lett.* **86**, 783 (2001).
- [4] M. Bajcsy, A. S. Zibrov, and M. D. Lukin, *Nature (London)* **426**, 638 (2003).
- [5] M. S. Bigelow, N. N. Lepeshkin, and R. W. Boyd, *Science* **301**, 200 (2003).
- [6] J. Sharping, Y. Okawachi, and A. Gaeta, *Opt. Express* **13**, 6092 (2005).
- [7] Z. Shi and R. W. Boyd, *Phys. Rev. A* **79**, 013805 (2009).
- [8] F. Liu, Q. Li, Z. Zhang, M. Qiu, and Y. Su, *IEEE J. Sel. Top. Quantum Electron.* **14**, 706 (2008).
- [9] Q. Xu, J. Shakyia, and M. Lipson, *Opt. Express* **14**, 6463 (2006).
- [10] R. P. Rajan, H. Riesen, and A. Rebane, *Opt. Lett.* **38**, 4546 (2013).
- [11] R. N. Shakhmuratov, A. A. Kalachev, and J. Odeurs, *Phys. Rev. A* **76**, 031802 (2007).

LI, KINOS, THURESSON, RIPPE, AND KRÖLL

PHYSICAL REVIEW A **95**, 032104 (2017)

- [12] Y. P. Wang and R. S. Meltzer, *Phys. Rev. B* **45**, 10119 (1992).
- [13] S. R. Hastings-Simon, M. U. Staudt, M. Afzelius, P. Baldi, D. Jaccard, W. Tittel, and N. Gisin, *Opt. Commun.* **266**, 716 (2006).
- [14] O. Guillot-Noël, P. Goldner, Y. L. Du, E. Baldit, P. Monnier, and K. Bencheikh, *Phys. Rev. B* **74**, 214409 (2006).
- [15] E. Baldit, K. Bencheikh, P. Monnier, S. Briauudeau, J. A. Levenson, V. Crozatier, I. Lorgeté, F. Bretenaker, J. L. Le Gouët, O. Guillot-Noël *et al.*, *Phys. Rev. B* **81**, 144303 (2010).
- [16] A. Orioux and E. Diamanti, *J. Opt. (Bristol, U. K.)* **18**, 083002 (2016).
- [17] M. Sabooni, Q. Li, L. Rippe, R. K. Mohan, and S. Kröll, *Phys. Rev. Lett.* **111**, 183602 (2013).
- [18] Q. Li, Y. Bao, A. Thuresson, A. N. Nilsson, L. Rippe, and S. Kröll, *Phys. Rev. A* **93**, 043832 (2016).
- [19] E. Courtens, *Phys. Rev. Lett.* **21**, 3 (1968).
- [20] R. Shakhmuratov, *J. Mod. Opt.* **57**, 1355 (2010).
- [21] R. Lauro, T. Chanelière, and J. L. Le Gouët, *Phys. Rev. A* **79**, 063844 (2009).
- [22] R. N. Shakhmuratov, A. Rebane, P. Mégret, and J. Odeurs, *Phys. Rev. A* **71**, 053811 (2005).
- [23] A. Walther, A. Amari, S. Kröll, and A. Kalachev, *Phys. Rev. A* **80**, 012317 (2009).
- [24] R. W. Boyd, *J. Opt. Soc. Am. B* **28**, A38 (2011).
- [25] N. Ohlsson, M. Nilsson, and S. Kröll, *Phys. Rev. A* **68**, 063812 (2003).
- [26] Thorlabs PDB150A.
- [27] F. R. Graf, A. Renn, U. P. Wild, and M. Mitsunaga, *Phys. Rev. B* **55**, 11225 (1997).
- [28] G. Liu, R. Cone, M. Joubert, B. Jacquier, and J. Skinner, *J. Lumin.* **45**, 387 (1990).
- [29] R. W. Equall, R. L. Cone, and R. M. Macfarlane, *Phys. Rev. B* **52**, 3963 (1995).
- [30] R. W. Boyd, D. J. Gauthier, A. L. Gaeta, and A. E. Willner, *Phys. Rev. A* **71**, 023801 (2005).

PAPER V

Development and characterization of high suppression and high tendue narrowband spectral filters

A. Kinos, Q. Li, L. Rippe and S. Kröll.

Applied optics **55**, 10442 (2016).

Development and characterization of high suppression and high étendue narrowband spectral filters

ADAM KINOS,^{1,*†} QIAN LI,¹ LARS RIPPE,^{1,2} AND STEFAN KRÖLL¹

¹Department of Physics, Lund University, P.O. Box 118, SE-221 00 Lund, Sweden

²Flatfrog, Scheelevägen 15, SE-223 63 Lund, Sweden

*Corresponding author: adam.kinos@fysik.lth.se

Received 11 October 2016; accepted 16 November 2016; posted 18 November 2016 (Doc. ID 278344); published 19 December 2016

The present work addresses critical issues in constructing high suppression, narrowband spectral filters in rare-earth-ion-doped crystals, mainly targeting the application of ultrasound optical tomography but is also applicable for areas such as quantum memories, self-filtering of laser frequencies, and other applications relying on high absorption in rare-earth-ion-doped crystals. The polarization of light transmitted through a highly absorbing crystal is experimentally analyzed. Additionally, an existing wave propagation method is used to simulate beam propagation through a spectral hole to study the high étendue requirements of ultrasound optical tomography. © 2016 Optical Society of America

OCIS codes: (070.2615) Frequency filtering; (300.1030) Absorption; (170.7180) Ultrasound diagnostics.

<https://doi.org/10.1364/AO.55.010442>

1. INTRODUCTION

Recent interest in rare-earth spectral filters based on hole burning have been seen in quantum memories [1], self-filtering of laser frequencies [2], and ultrasound optical tomography (UOT) [3]. These filters are exceptionally narrowband, which gives a strong time delay, meaning that time gating can be used to further increase the potency of the filter. These filters also have the benefit of working for arbitrary input directions (as opposed to, e.g., a Fabry–Pérot cavity), which can be important for certain applications; here we will in particular consider UOT.

Anomalies, such as tumors or low blood oxygenation in organs, surrounded by healthy tissue can be difficult to examine, especially if located deep within the body. Early noninvasive imaging of such anomalies can help in the diagnosis process of patients [3].

Several methods exist to date that try to fulfill this ambition. Ultrasound probing techniques, for example, have good spatial resolution even deep inside scattering media but lack the molecular contrast provided by optical light [4]. On the other hand, optical light has difficulties penetrating deep inside highly scattering media, such as the body, while maintaining spatial resolution. UOT is a method utilizing the benefits of both worlds, see Fig. 1(a). The ultrasound focus provides a spatially narrow region with varying local density, which, due to the acousto-optic effect, diffracts optical light. The diffracted light is in this process frequency-shifted by the ultrasound

frequency, typically in the 1–100 MHz range. However, the ultrasound absorption coefficient is 0.3 dB/(cm · MHz) [7] and limits the usable ultrasound frequency range for UOT. By examining only the frequency-shifted light, a high spatial resolution can be achieved, in addition to the good contrast benefit of the optical light [8,9].

One major obstacle that needs to be overcome in the UOT technique is the low intensity of frequency-shifted light compared with the rest of the randomly scattered light. This intensity difference, for example, depends on the ratio of volume occupied by the ultrasound and the total sample volume as well as how deep inside the scattering media the ultrasound pulse is located. Additionally, the frequency-shifted light will exit the medium in random directions emanating from a large surface area, thereby requiring high étendue analysis if a reasonable fraction of the frequency-shifted light should be collected [see Fig. 1(a)].

By utilizing narrowband spectral filters, the unshifted light can be suppressed while transmitting most of the shifted light. Good suppression filters can therefore be used in UOT to achieve a high signal-to-background ratio deep inside the tissue. A high étendue filter with 60 dB suppression might be enough to reach the depth of the human heart [3]. High étendue, high suppression filters can be created in rare-earth-ion-doped crystals, where hole burning and slow light effects [10] can give suppressions of several orders of magnitude for unshifted light with respect to shifted light, within the frequency range of a few MHz required by UOT [9].

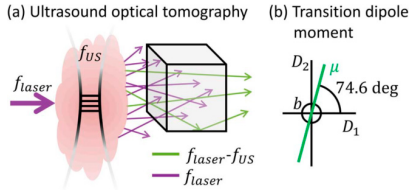


Fig. 1. (a) Schematic view of ultrasound optical tomography (UOT). An ultrasound pulse with frequency f_{US} is sent into the scattering tissue. Once this pulse has reached the desired location, a laser pulse with frequency f_{laser} is sent in. Some laser light will diffract off the ultrasound pulse and create sidebands with frequencies $f_{laser} \pm f_{US}$ (only the negative sideband is shown in the figure). Emanating from a large surface area, with random polarization and direction, the light passes through a spectral filter that strongly suppresses the light at f_{laser} and $f_{laser} + f_{US}$, while it transmits most of the light with frequency $f_{laser} - f_{US}$. This light can now be analyzed obtaining a high spatial resolution (given by the ultrasound pulse). (b) Transition dipole moment direction in $\text{Pr}^{3+}:\text{Y}_2\text{SiO}_5$, tilted 74.6 deg from the D_1 axis toward the D_2 axis [5,6].

The highest suppression value achieved to date in these crystals is around 60 dB suppression for light shifted 10.2 MHz [11], and predictions of even higher suppression have been made [11,12]. Even though this suppression might be large enough for UOT, the ultrasound frequency, and therefore the frequency shift of the light, preferably should be in the 1–2 MHz range, as the ultrasound absorption coefficient is lower for lower frequencies. In this manuscript, experiments on narrowband spectral filters have reached 53.4 ± 0.7 dB suppression for light shifted only 1.25 MHz.

The present study also more generally investigates high absorption processes inside these anisotropic spectral filter crystals by performing simulations based on an existing light propagation model [13]. Building on this approach, the light suppression as a function of incidence angle to the crystal is studied as well as the use of time gating. The crystal examined presently is a $\text{Pr}^{3+}:\text{Y}_2\text{SiO}_5$ crystal, which has its transition dipole moment lying in the D_1 - D_2 plane, as can be seen in Fig. 1(b).

By increasing the knowledge of spectral filtering in rare-earth-ion-doped crystals and thereby potentially improving the suppression of these filters, UOT techniques will in the future be able to probe deeper inside tissue in a noninvasive manner.

2. HIGH ÉTENDUE SIMULATIONS

To simulate high étendue beam propagation and investigate the filter suppression as a function of incidence angle, the theoretical framework put forth in [13] was used to simulate light propagating through a crystal. By defining the incidence angle and electric field for an incoming plane wave, the simulation calculates the total reflection and transmission through the crystal, including multiple reflections at the surfaces.

Because a spatial beam and temporal pulse can be constructed from a linear combination of plane waves, one can

perform the simulation several times and sum up the results with weights corresponding to the Fourier transform of any desired spatial and temporal profile. This is performed in the simulations presented in Section 5, where a Gaussian-shaped beam profile was used in both transverse spatial dimensions as well as in the temporal dimension.

Even though the method assumes homogeneity of the material in the transverse spatial directions (x - y plane) and also in time, in time it can be inhomogeneous in the direction of the normal to the front surface (z direction), and the absorption also can vary as a function of the light frequency. Therefore, the method can be used, not only for high étendue simulations but also for, e.g., propagation through spectral holes, materials consecutively stacked after one another, and examination of slow light effects.

3. EXPERIMENTAL SETUP

To analyze high suppression spectral filters in rare-earth-ion-doped crystals, a frequency-stable laser and a high dynamic range detection setup are required. Therefore, the experimental setup seen in Fig. 2 was constructed. The incoming stabilized laser light, at 606 nm (495 THz), can be frequency-shifted using an acousto-optic modulator (AOM, model AA.ST.200/B100/A0.5-VIS) in a double pass configuration and is used for hole burning and probe pulse creation (described in, e.g., [16]). A beam expander (not shown in the figure) is used to collimate the beam size to 1 mm, which is the size used throughout the setup. A low reflectivity beam splitter directs part of the input beam before entering the cryostat to a reference detector PD1 (Thorlabs PDB150A) and is used to calibrate for intensity fluctuations. The beam propagates along the D_1 direction of the crystal, and the polarization is aligned along the principal axis with the strongest absorption (the D_2 axis [5,6]) using a half-wave plate. Following this, a linear polarizer is used to improve the polarization purity, i.e., remove as much as possible any unwanted polarization component (in this case along the b axis). After propagating through the crystal, which sits inside a liquid helium bath cryostat at 2 K, the polarization component of the transmitted light that is to be analyzed is selected by a second linear polarizer.

To cover the large dynamic range of probe intensities obtained by propagating either inside or outside a spectral hole, the light falls upon a beam splitter after which two detectors are placed: PD2 (Thorlabs PDB150A) and PD3 (Hamamatsu PMT R943-02). To correlate the measurements of the two detectors, a signal can be used, as long as it is sufficiently strong/weak for the Thorlabs/Hamamatsu detectors to be able to record it while still not damaging them. This signal should give the same power, after the transmission and reflectance of the beam splitter are taken into account, and the two detectors can therefore be calibrated to each other.

A 10 mm long $\text{Pr}^{3+}:\text{Y}_2\text{SiO}_5$ crystal with a doping concentration of 0.05% was used. A 10 mT magnetic field was applied over the D_2 axis of the crystal to increase the spectral hole lifetime [17].

A frequency scanning pulse with a scan range of 0.5 MHz, total duration of 120 μs , and low Rabi frequency (estimated to be around 1–2 kHz) was repeatedly sent into the crystal 2100 times to create a sharp-edged spectral hole with high

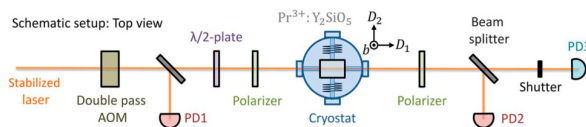


Fig. 2. Simplified experimental setup. A stabilized coherent 699-21 ring dye laser, together with an acousto-optic modulator (AOM) in a double pass configuration, is used for the spectral hole burning and probe pulse creation [14,15]. Photodetector 1 (PD1) is used as a reference detector to calibrate for laser intensity fluctuations. A half-wave plate and a polarizer before the cryostat are used to adjust the incoming polarization, while a polarizer after the cryostat is used to analyze the polarization. A 10 mm long 0.05% doped $\text{Pr}^{3+}:\text{Y}_2\text{SiO}_5$ crystal sits in a liquid helium bath cryostat at 2 K. Its axes are oriented as shown in the figure. PD2 and PD3 are low and high sensitive photodetectors, chosen to cover the large dynamic range of the transmitted probe intensities.

transmission in the center. High repetition, low Rabi frequency pulses are used to minimize the effects of instantaneous spectral diffusion [18].

Following this, 25 Gaussian probe pulses with a full width at half-maximum (FWHM) of 3 μs (unless stated otherwise) were sent into the center of the spectral hole, assigned the relative frequency of 0 MHz, to analyze the transmission properties of the profile. Afterward, still using the same structure, another 25 pulses were sent in at a detuning of 1.25 MHz (unless stated otherwise) compared with the center of the spectral hole to probe the high absorption. To make sure the structure was not significantly altered by the probe pulses, another 25 probes were sent inside followed by yet another 25 outside the spectral hole, making a total of 100 probe pulses for a single hole burning sequence. The probe pulses were separated by 200 μs , with a delay of 0.2 s between each set of 25 pulses to give the mechanical shutter, which was used to protect the light sensitive PMT detector from damage, time to open and close.

Finally, after the probing was completed, 200 frequency scanning pulses, reset pulses, were sent in at alternately positive and negative detuning compared with the hole center to shuffle the absorbing ions back toward the center and erase the hole. These pulses, with a duration of 250 μs and maximum laser power, were scanning at 37 MHz centered at 31.8 MHz and -32.8 MHz, respectively.

4. EXPERIMENTAL RESULTS

As previously mentioned, UOT light will emanate from a large surface area with a random direction and polarization. A high étendue filter will therefore collect much more light compared with a low étendue filter. Consequently, a spectral hole profile that exists spatially over the entire rare-earth-ion-doped crystal is required, and because this has previously been demonstrated by using a large beam and burning the entire crystal from the side [9], the present experiments are performed at normal incidence, both for burning of the spectral hole and probing. Furthermore, due to the high index of refraction of the crystal ($n \approx 1.8$) compared with the surrounding liquid helium ($n \approx 1$), Snell's law, combined with total internal reflection, ensures that any light that propagates into the crystal through the front surface area will exit through the back surface area, regardless of crystal length.

A schematic absorption profile (solid blue line) and the spectral distributions of the incoming probe pulses (duration 3 μs),

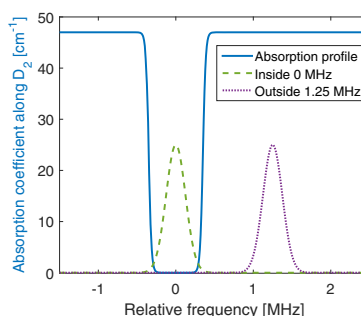


Fig. 3. Schematic absorption profile along D_2 (solid blue line), with a maximum absorption coefficient of 47 cm^{-1} [5], is shown, together with the frequency distributions of the incoming probe pulses (duration 3 μs) inside (dashed green line) and outside (dotted purple line) the spectral hole. The probe distributions are plotted against a vertical axis with arbitrary units.

both when propagating inside (0 MHz, dashed green line) and outside (1.25 MHz, dotted purple line) the hole, respectively, are shown in Fig. 3. Even though the hole burning pulse was scanning 0.5 MHz, the spectral hole it creates will be slightly wider. Therefore, the FWHM is estimated to 0.7 MHz and is shown in the figure.

Following the experimental methodology explained in Section 3, an example of the detected signals inside (0 MHz) and outside (1.25 MHz) the spectral hole can be seen in Fig. 4. The incoming polarization was horizontally aligned with D_2 , and the polarizer after the cryostat also was along the D_2 axis for Figs. 4(a) and 4(b), while it was aligned with the b axis for Fig. 4(c). As explained in Section 3, the probing consisted of four sets of 25 probe pulses each. The four sets taken with the second polarizer aligned with D_2 [seen in Figs. 4(a) and 4(b)] are detected in the order of blue, red, green, and purple. Each data presented are the mean and the standard deviation of the mean. The signals are calibrated with respect to each other, both in regards to the beam splitter splitting (that depends on polarization), the shot-to-shot intensity variation (calibrated by using a reference detector situated before the cryostat), and

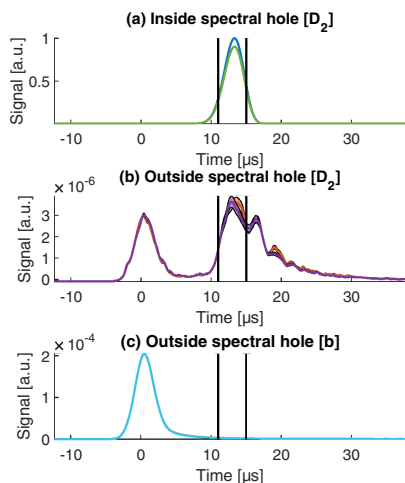


Fig. 4. Example of detected probe signals inside (0 MHz) and outside (1.25 MHz) the spectral hole, for an input pulse sent in at 0 μ s. The polarizer before the cryostat was aligned with D_2 , and the polarizer after the cryostat was aligned with D_2 for Figs. (a) and (b) and aligned with b for Fig. (c). All graphs use the same y -axis scale. The darker line shows the mean while the slightly brighter area shows the standard deviation of the mean [overlapping with the darker line for most points, except for Fig. (b) between 11–17 μ s]. The time gating used in Fig. 5 is performed between the black lines (11–15 μ s).

for different detector collection efficiency. Last, the data are normalized so that the maximum transmission amplitude inside the spectral hole is one.

As can be seen, a slow light delay of around 13 μ s is achieved when propagating inside the spectral hole. When propagating outside the hole, there are two components of the D_2 light, one that is not delayed, and one that is delayed similarly to the pulse traveling inside the spectral hole. The origin of the delayed component might be due to leakage of the probe pulse into

the spectral hole, which suggests that the spectral width of the probe is larger than expected for a temporal Gaussian with a FWHM of 3 μ s. It might be broadened in the pulse creation using the AOM, for example, due to a digitized RF signal, or it may be that our laser has a low intensity background that is broad in frequency [2]. The delayed component is lower when probing 10.2 MHz detuned from the spectral hole, which agrees with the leakage hypothesis stated above.

The b component measured inside the spectral hole is, unsurprisingly, much lower than the D_2 component and is not shown here. Contrary, the b component when probing outside the spectral hole, seen in Fig. 4(c), was found to be much larger (roughly a factor of 50) than the D_2 component. We expect to have a small b component because the linear polarizer placed before the cryostat has an extinction ratio of 10^{-5} , corresponding to a polarization angle of 0.18 deg from D_2 . If the b component, seen in Fig. 4(c), can be explained by a misalignment of the incoming polarization it would be 0.8 deg off (corresponding to an extinction ratio of $2 \cdot 10^{-4}$). This increased misalignment of the incoming polarization might be explained by the beam having to travel through two cryostat windows before reaching the crystal. However, because the transmission inside the spectral hole is almost purely D_2 , the b component outside the hole can easily be filtered out using a linear polarizer. Another option to increase the total suppression is to use two filter crystals rotated 90 deg with respect to each other around the D_1 axis, causing the b component of the first crystal to reside along the D_2 component of the second crystal [19]. Using the latter technique, good suppression is attainable regardless of the incoming light polarization, which is beneficial for UOT. Additionally, the b component is not delayed and can therefore be eliminated by time gating.

To calculate the suppression of the transmitted light outside compared with inside the hole, the D_2 signal is summed up between the two black vertical lines (at 11 and 15 μ s), as seen in Fig. 4; the suppression values shown in Fig. 5 are the time gated D_2 values.

A suppression trend was measured when the detuning for probing outside the hole was fixed at 1 MHz and the probe FWHM duration changed, which can be seen in Fig. 5(a). The suppression is monotonically increasing as a function of increased duration. This can be fully explained because the frequency distribution width of the probe pulse becomes wider

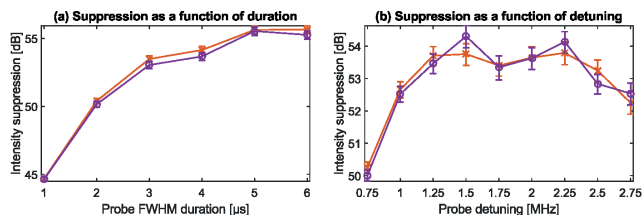


Fig. 5. Intensity suppression as a function of (a) probe FWHM duration, for a fixed detuning of 1 MHz when probing outside the spectral hole, and (b) probe detuning, for a fixed probe duration of 3 μ s. Calculated by dividing the D_2 signal area inside with the D_2 signal area outside the spectral hole, in both cases time gated between the two vertical black lines (11–15 μ s), as shown in the example in Fig. 4. The red cross data are using the first two sets of probe pulses, while the purple circle data are using the last two sets. The error bars show one standard deviation of the mean.

with decreasing duration, which leads to increased and decreased absorption for the pulse propagating inside and outside the spectral hole, respectively (see Fig. 3). A FWHM value of $3\ \mu\text{s}$ was chosen as a compromise of suppression and resolution because the shorter the pulse duration is, the less time the ultrasound pulse has to move, meaning a higher spatial resolution of UOT.

A similar suppression trend but now changing the detuning of the probe outside the spectral hole can be seen in Fig. 5(b), where the probe duration was kept fixed at $3\ \mu\text{s}$. As can be seen, the intensity suppression flattens out at a detuning of around $1.25\ \text{MHz}$, where it has reached a suppression of around $53.4 \pm 0.7\ \text{dB}$. Additionally, another measurement where the light was detuned $10.2\ \text{MHz}$ was taken, which gave a suppression of $63.2 \pm 0.6\ \text{dB}$, similar to what has been achieved previously at the same detuning [11].

The probing performed in the experiments shown so far has an estimated Rabi frequency of $25\ \text{kHz}$. Changing the probe Rabi frequency from $5\text{--}55\ \text{kHz}$ gave similar suppression values (within $\pm 2\ \text{dB}$).

5. SIMULATION RESULTS

To estimate the potential suppression of the filter in an actual UOT experiment, where the incoming light has an arbitrary input direction and polarization, an investigation of the absorption/suppression as a function of incidence angle and polarization direction was carried out. Several plane wave simulations where light propagates through the crystal were performed, and the results were summed up so that a spatial beam was achieved in both transverse directions; this was performed when propagating inside as well as outside the spectral hole. In these

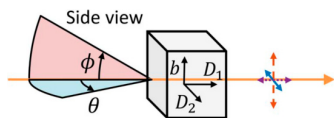


Fig. 6. Schematic view of the incidence angles θ and ϕ , located in the horizontal and vertical planes, respectively. The outgoing polarization components are using the same color notation as in Fig. 7.

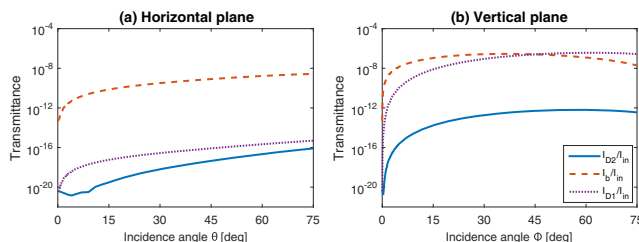


Fig. 7. Transmittance when probing outside ($1.25\ \text{MHz}$) the spectral hole, split up into transverse (blue solid line for D_2 and red dashed line for b) and normal (purple dotted line for D_1) directions to the crystal surface. The spatial angle θ is changed in the horizontal D_2 - D_1 plane, and ϕ is changed in the vertical b - D_1 plane, as seen in Fig. 6, for Figs. (a) and (b), respectively.

simulations, which are based on the methods described in [13], the crystal was oriented in the same way as in the experiments, i.e., propagation occurred along the D_1 axis with D_2 as the horizontal and b as the vertical axis. However, in contrast with the experiments, in the simulation the incidence angle was varied from the normal incidence case, as seen in Fig. 6. A Gaussian probe pulse with a FWHM of $1\ \text{mm}$ in both transverse spatial dimensions and a FWHM of $3\ \mu\text{s}$ was used in the simulations.

In Fig. 7, the transmittance of light propagating outside ($1.25\ \text{MHz}$) the spectral hole is shown for different input angles. The transmission is split into components along the transverse (D_2 and b) and normal (D_1) directions of the crystal surface. These can be seen in the blue solid (D_2), red dashed (b), and purple dotted (D_1) lines. In Fig. 7(a) the spatial angle, θ , is changed in the horizontal D_2 - D_1 plane, while ϕ is changing in the vertical b - D_1 plane for Fig. 7(b) [see Fig. 6 for a schematic view of the incidence angles].

As can be seen, light of all three polarization components exist in the crystal. This can be understood because an oscillating dipole will radiate light in almost all directions, and the electric field it generates will be perpendicular to these propagation directions. However, the ions are only phase matched in the propagation direction of the incoming light. The simulation uses several plane wave calculations with slightly different incoming angles to build up a spatial beam that propagates through the crystal; therefore, the result at, e.g., 0° incidence angle is not the same as if a plane wave would have propagated at normal incidence. Thus the interference from all the ions will, as the simulation exists of a sum of plane waves with (slightly) different input directions, for a general incidence angle create an electric field with components along all polarization directions (although some of them will be very small), which can be seen in Fig. 7.

Even though the transmission is rapidly increasing when deviating from 0° incidence angle in Fig. 7, the transmission is still relatively low for all incidence angles simulated.

Up until this point the incoming polarization has been chosen to be either s - or p -polarized light when changing the angle, but in the general case the incoming polarization is a combination of both. Because the simulation does not have any antireflection coating of the surfaces, the reflection of the s - and p -polarization components will differ according to the

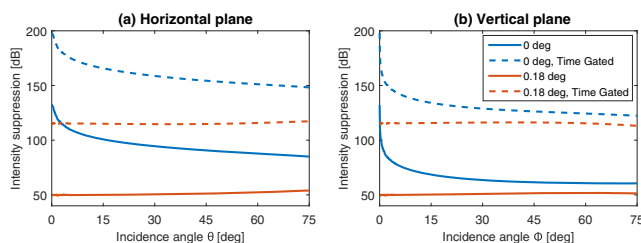


Fig. 8. Intensity suppression of light detuned (1.25 MHz) relative to centered (0 MHz) with respect to the spectral hole. (a) Incidence angle θ changes in the horizontal plane. (b) Angle ϕ changes in the vertical plane. The angles are defined as seen in Fig. 6. The blue solid line shows the suppression when the incoming polarization is perfectly horizontally aligned, while in the red solid line the polarization purity is $\frac{I_{\text{low}}}{I_{\text{high}}} = 10^{-5}$, corresponding to a polarization angle of 0.18 deg. By time gating the transmission, the dashed curves are obtained for the two different polarization purity cases (the time gating was performed between 7–9 μs , as this gave the best suppression in the simulations).

Fresnel reflection. Therefore, the polarization orientation of the electric field just inside the crystal may differ from the polarization just outside the crystal. Hence, a polarization outside the crystal aligned purely in the horizontal D_2 - D_1 plane will not for a general incidence angle be purely aligned in the horizontal plane just inside the crystal; instead it also will have a vertical polarization component. Because this vertical component is along the b principal axis, the overall transmission will be greatly increased. Fortunately, there are several ways this effect can be eliminated; here we will present three ways. First, by adjusting the incoming polarization orientation one can compensate for the difference in s and p Fresnel reflections and still get a low transmission similar to the ones shown in Figs. 7(a) and 7(b). Second, by using an antireflection coated crystal, the effect can be at least partly canceled. Finally, by using two crossed crystals, i.e., with their D_2 and b axes interchanged, placed in contact with each other, the transmission should be low regardless of incoming polarization.

By comparing the simulation results of a pulse propagating outside (shown in Fig. 7) and inside the spectral hole, one can calculate the overall suppression of the spectral filter. This can be seen in Fig. 8, both when the incoming polarization is perfectly along D_2 and when it is tilted by 0.18 deg corresponding to the polarization purity of the polarizer used in our current setup. As expected, when the polarization angle is tilted so that the b component is 10^{-5} compared with the D_2 component (0.18 deg), the suppression is also in that order. However, because this component has a negligible slow light delay, a high suppression can still be achieved by time gating, as seen from the dashed red line. It is, however, not as large as the suppression achieved when the polarization is perfectly along D_2 . We also note that the dependence on incidence angle has now almost completely vanished, and the suppression is still large, showing that the spectral filter would work as a high étendue filter.

Disregarding the large experimental b component, we also can notice that the simulation shows that it is possible to reach much higher suppression values than we were able to achieve experimentally. However, one should note that the simulation uses absorption coefficients of $\alpha_{D_2} = 47 \text{ cm}^{-1}$,

$\alpha_{D_1} = 3.6 \text{ cm}^{-1}$, and $\alpha_b = 0 \text{ cm}^{-1}$, and even though these values have been measured experimentally [5], it is possible that the absorption coefficient of crystals varies [20]. New simulations, performed with the absorption values only half of those mentioned above, show that the maximum suppression (normal incidence with a polarization along D_2) is still high, around 100 dB compared with the previous case with 130 dB. This indicates, as explained in [6], that contrary to what one would intuitively believe, the suppression or absorption in dB does not always scale linearly with the absorption coefficient or length of the crystal.

The main reason for the discrepancy between the suppression in simulations compared with experiments is most likely the leakage of the probe pulse light through the spectral hole, as explained in Section 4. However, other potential reasons for a lower suppression in experiments exist, e.g., the crystal cutting procedure can have errors in the alignment of the principal axes of the crystal to the actual sides of the crystal, so that, even when the incoming beam is perfectly normal to the front surface of the crystal, it actually deviates from the principal axes. Additionally, the experimental alignment might not be at perfect normal incidence. Another experimental difficulty is that of creating a narrow spectral hole with sharp absorption edges that is homogeneous throughout the entire crystal.

Because the random polarization of the UOT light requires filters that are insensitive to the incoming polarization, a single rare-earth-ion-doped crystal filter is not suitable, as it will attenuate the b polarization component of the light much less than the D_2 component. However, as mentioned previously, two consecutive rare-earth-ion-doped crystal filters with their D_2 and b axes interchanged can be used to suppress all incoming light regardless of polarization [19].

6. CONCLUSION

Using spectral hole burning techniques together with slow light delay, a suppression of $53.4 \pm 0.7 \text{ dB}$ was achieved for a 3 μs FWHM Gaussian probe pulse shifted 1.25 MHz compared with a pulse in the center of the spectral hole (0 MHz). Higher suppression values were obtained when pulses with

longer duration or higher detuning were used. Currently, the limiting factor to achieve higher suppression is the light leaking through the spectral hole when probing outside the hole because it was delayed similarly as the light transmitted inside the spectral hole, which makes time gating ineffective. Therefore, to further improve the performance of these filters, the origin of the leakage light has to be investigated.

The current work also uses an existing wave propagation method [13] to simulate the étendue of high suppression spectral hole filters. It is found that a relatively high suppression can be achieved even when the incoming spatial angle is changed from the normal incidence case. Furthermore, we note that a poor incoming polarization purity might limit the suppression reached, but by using time gating or two crossed crystals this limit can be overcome. Another potential solution, not investigated here, would be to use ceramic samples of similar materials because the transition dipole moment of different ions would be randomly rotated throughout the sample [21]. Ceramic samples also have the benefit of light traveling longer inside the material than in a crystal.

As the knowledge of absorption processes in rare-earth-ion-doped crystals and their dependence on polarization and propagation direction increases, the potential to construct spectral filters with high suppression values improves. As previously stated, this is important for applications such as UOT. Furthermore, narrowband spectral filtering has other potential applications areas, including, but not limited to, quantum memories [1], which are a crucial component in quantum repeaters; devices that can be used for setting up a global quantum communication network [22,23]; and self-filtering of laser frequencies, where the use of the nonlinear spectral hole burning process in rare-earth-ion-doped crystals can be used to suppress phase noise and side modes [2].

Funding. Knut och Alice Wallenberg Stiftelse; Seventh Framework Programme (FP7) (287252 (CIPRIS)); Vetenskapsrådet (VR) (Lund Laser Centre (LLC)).

Acknowledgment. The present work was supported by the Swedish Research Council, the Knut & Alice Wallenberg Foundation. Additionally, funding was received from the People Programme (Marie Curie Actions) of the European Union's Seventh Framework Programme FP7 (2007-2013) under REA grant no. 287252 (CIPRIS) and Lund Laser Centre (LLC). Finally, the authors are most grateful for useful discussions with Gerhard Kristensson.

[†]Previously publishing under Adam N. Nilsson.

REFERENCES

1. S. E. Beavan, M. P. Hedges, and M. J. Sellars, "Demonstration of photon-echo rephasing of spontaneous emission," *Phys. Rev. Lett.* **109**, 093603 (2012).
2. C. W. Thiel, R. L. Cone, and T. Boettger, "Laser linewidth narrowing using transient spectral hole burning," *J. Lumin.* **152**, 84–87 (2014).
3. A. Walther, L. Rippe, L. V. Wang, S. Andersson-Engels, and S. Kröll, "Is optical imaging of oxygenation at heart depth possible?" Manuscript in preparation (2016).
4. L. V. Wang, *Photoacoustic Imaging and Spectroscopy* (CRC Press, 2009).
5. Y. C. Sun, *Spectroscopic Properties of Rare Earths in Optical Materials* (Springer, 2005), Chap. 7.
6. M. Sabooni, A. N. Nilsson, G. Kristensson, and L. Rippe, "Wave propagation in birefringent materials with off-axis absorption or gain," *Phys. Rev. A* **93**, 013842 (2016).
7. C. Li and L. V. Wang, "Photoacoustic tomography and sensing in biomedicine," *Phys. Med. Biol.* **54**, R59–R97 (2009).
8. X. Xu, H. Zhang, P. Hemmer, D.-K. Qing, C. Kim, and L. V. Wang, "Photorefractive detection of tissue optical and mechanical properties by ultrasound modulated optical tomography," *Opt. Lett.* **32**, 656–658 (2007).
9. H. Zhang, M. Sabooni, L. Rippe, C. Kim, S. Kröll, L. V. Wang, and P. R. Hemmer, "Slow light for deep tissue imaging with ultrasound modulation," *Appl. Phys. Lett.* **100**, 131102 (2012).
10. R. N. Shakhmurov, A. Rebane, P. Megret, and J. Odeurs, "Slow light with persistent hole burning," *Phys. Rev. A* **71**, 053811 (2005).
11. S. E. Beavan, E. A. Goldschmidt, and M. J. Sellars, "Demonstration of a dynamic bandpass frequency filter in a rare-earth ion-doped crystal," *J. Opt. Soc. Am. B* **30**, 1173–1177 (2013).
12. M. P. Hedges, "High performance solid state quantum memory," Ph.D. thesis (Australian National University, 2011).
13. S. Rikite, G. Kristensson, and M. Andersson, "Propagation in bianisotropic media—reflection and transmission," *IEEE Proc. Microw. Anten. Prop.* **148**, 29–36 (2001).
14. A. Amari, A. Walther, M. Sabooni, M. Huang, S. Kröll, M. Afzelius, I. Usmani, B. Lauritzen, N. Sanguoat, H. de Riedmatten, and N. Gisin, "Towards an efficient atomic frequency comb quantum memory," *J. Lumin.* **130**, 1579–1585 (2010).
15. L. Rippe, M. Nilsson, S. Kröll, R. Klieber, and D. Suter, "Experimental demonstration of efficient and selective population transfer and qubit distillation in a rare-earth-metal-ion-doped crystal," *Phys. Rev. A* **71**, 062328 (2005).
16. L. Rippe, B. Julsgaard, A. Walther, Y. Ying, and S. Kröll, "Experimental quantum-state tomography of a solid-state qubit," *Phys. Rev. A* **77**, 022307 (2008).
17. N. Ohlsson, M. Nilsson, and S. Kröll, "Experimental investigation of delayed self-interference for single photons," *Phys. Rev. A* **68**, 063812 (2003).
18. R. W. Equall, R. L. Cone, and R. M. Macfarlane, "Homogeneous broadening and hyperfine-structure of optical-transitions in $\text{Pr}^{3+}\text{Y}_2\text{SiO}_5$," *Phys. Rev. B* **52**, 3963–3969 (1995).
19. C. Clausen, F. Bussières, M. Afzelius, and N. Gisin, "Quantum storage of heralded polarization qubits in birefringent and anisotropically absorbing materials," *Phys. Rev. Lett.* **108**, 190503 (2012).
20. A. Ferrier, B. Tumino, and P. Goldner, "Variations in the oscillator strength of the $f\text{-}7(0) \rightarrow d\text{-}5(0)$ transition in $\text{Eu}^{3+}:\text{Y}_2\text{SiO}_5$ single crystals," *J. Lumin.* **170**, 406–410 (2016).
21. N. Kunkel, A. Ferrier, C. W. Thiel, M. O. Ramirez, L. E. Bausa, R. L. Cone, A. Ikessue, and P. Goldner, "Rare-earth doped transparent ceramics for spectral filtering and quantum information processing," *APL Mater.* **3**, 096103 (2015).
22. H. J. Briegel, W. Dur, J. I. Cirac, and P. Zoller, "Quantum repeaters: The role of imperfect local operations in quantum communication," *Phys. Rev. Lett.* **81**, 5932–5935 (1998).
23. N. Sanguoat, C. Simon, H. de Riedmatten, and N. Gisin, "Quantum repeaters based on atomic ensembles and linear optics," *Rev. Mod. Phys.* **83**, 33–80 (2011).

PAPER VI

Fast all-optical nuclear spin echo technique based on EIT

A. Walther, A. N. Nilsson, Q. Li, L. Rippe and S. Kröll.

Eur. Phys. J. D **70**, 166 (2016).

Fast all-optical nuclear spin echo technique based on EIT

Andreas Walther^a, Adam N. Nilsson, Qian Li, Lars Rippe, and Stefan Kröll

Department of Physics, Lund University, 221 00 Lund, Sweden

Received 18 December 2015 / Received in final form 28 April 2016

Published online 30 August 2016 – © EDP Sciences, Società Italiana di Fisica, Springer-Verlag 2016

Abstract. We demonstrate an all-optical Raman spin echo technique, using electromagnetically induced transparency (EIT) to create the pulses required for a spin echo sequence: initialization, π -rotation, and readout. The first pulse of the sequence induces coherence directly from a mixed state, and the technique is used to measure the nuclear spin coherence of an inhomogeneously broadened ensemble of rare-earth ions (Pr^{3+}) in a crystal. The rephasing π -rotation is shown to offer an advantage of combining the rephasing action with the operation of a phase gate, particularly useful in e.g. dynamic decoupling sequences. In contrast to many previous experiments the sequence does not require any preparatory hole burning, which greatly shortens the total duration of the sequence. The effect of the different pulses is characterized by quantum state tomography and compared with simulations. We demonstrate two applications of the technique: compensating the magnetic field across our sample by monitoring T_2 reductions from stray magnetic fields, and measuring coherence times at temperatures up to 11 K, where standard preparation techniques are difficult to implement. We explore the potential of the technique, in particular for systems with much shorter T_2 , and other possible applications.

1 Introduction

Quantum technology holds great promise for the future, where several specific applications offer paradigmatic improvements far beyond what is possible using only classical systems. This includes, communication [1], encryption [2], simulations of other quantum systems such as molecules for medicine development [3] and full quantum computation [4]. To enable quantum aspects of technology it is necessary to control the coherence properties of matter, but today such control are in most cases limited to very restricted environments protecting the sensitive quantum states using cryogenic cooling or ultra high vacuum systems. For practical technological scalability however, it is clearly desirable to search for systems where coherence properties survive in ambient conditions. Very few such systems have been found, mostly related to defects in e.g. diamond [5] or silicon [6]. It is important to search for other systems that also take advantage of special benefits like the ultra-long coherence times of rare-earth ions [7]. Optical interactions with the spins are desirable for several reasons such as higher spatial resolution, better integration with other technology, and also capability of giving unique advantages related to three-level system. However, even though it has been known since the 40's that coherence properties of certain nuclear spins survive remarkably well in ambient conditions [8], optical spin measurements and manipulations in non-ideal conditions remain a difficult challenge.

Here, we demonstrate an all-optical technique based on electromagnetically induced transparency (EIT), which measures the coherence properties of a long-lived nuclear spin system. Even above liquid helium temperatures where the optical coherence is very rapidly destroyed, the nuclear spin is shown to remain coherent. The system is initialized from a mixed state by transient EIT pulses with a duration of approximately $T_{1,\text{opt}}/100$, which could be shortened even further as discussed in Section 4.4. This is much faster than previous similar techniques based on coherent population trapping (CPT) [9], since CPT require several optical lifetimes for decay. We acknowledge that similar techniques have been used in the past, e.g. non-collinearly in Pr [10] and with detunings in Tm [11], and here we use a simpler version without detunings and in a collinear arrangement. It is shown that the EIT pulses create superposition states directly from mixed states and this is characterized by quantum state tomography (QST). The EIT framework is used to derive a versatile rephasing pulse scheme, utilizing the three-level mechanic of the optical interaction of the spin qubits.

For the QST we use an ensemble qubit of rare-earth ions, and it is interesting to note that pulse parameters can be chosen such that the entire inhomogeneous optical width of the ensemble (170 kHz) is included in the EIT state. A full spin echo sequence of EIT pulses is implemented and demonstrated in two explicit examples: (i) cancellation of a dephasing mechanism by compensation of the earth's magnetic field and (ii) measurement of the nuclear spin T_2 of $\text{Pr}^{3+}:\text{Y}_2\text{SiO}_5$ for temperatures up to 11 K. The main limitation of the technique

^a e-mail: andreas.walther@fysik.lth.se

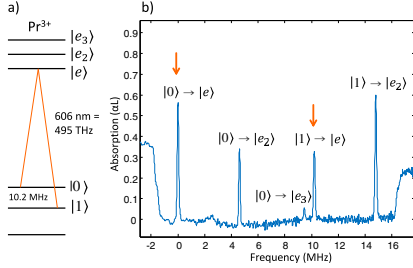


Fig. 1. (a) Level structure of the Pr^{3+} ion. The levels $|0\rangle$, $|1\rangle$ and $|e\rangle$ form the chosen A -system on which the EIT pulses operate. All transitions used in the population estimation during the experiments are visible in (b) and the EIT transitions have been marked with an orange arrow.

is the optical T_2 in relation to the EIT pulse duration. Our particular setup is limited by optical laser power, but we discuss extensions of our scheme to other systems where either higher optical power via pulsed lasers or other atomic species with larger optical oscillator strength can enable all-optical nuclear spin measurements over a broad range of optical T_2 's.

2 Theory

Consider a A -type system such as the one depicted in Figure 1a, where several levels exist but three are chosen for the EIT scheme. The existence of a bright and a dark state will now be briefly derived, but see e.g. [12] for a more detailed description. In Pr^{3+} the two involved transitions, $|0\rangle \rightarrow |e\rangle$ and $|1\rangle \rightarrow |e\rangle$ have different dipole moments, $\mu_{0/1}$, but we can assume that the corresponding laser electric fields, $\mathcal{E}_{0/1}$, can be chosen such that the Rabi frequencies are the same for both transitions, $\Omega = \mu_{0/1} \cdot \mathcal{E}_{0/1} / \hbar$. The interaction part of the Hamiltonian can then be written

$$H_{int} = \hbar\Omega (|e\rangle\langle 0| + |e\rangle\langle 1|) + c.c. \quad (1)$$

We now define an orthogonal basis set for the ground state levels, expressed in the computational one, given by:

$$\begin{cases} |B\rangle = \frac{1}{\sqrt{2}} (|0\rangle + |1\rangle) \\ |D\rangle = \frac{1}{\sqrt{2}} (|0\rangle - |1\rangle) \end{cases} \quad (2)$$

where the density matrix of each is given by $\rho = |\psi\rangle\langle\psi|$. The coupling between each of those ground superposition states and the excited state via the interaction Hamiltonian are now: $\langle e|H_{int}|B\rangle = \sqrt{2}\hbar\Omega$ and $\langle e|H_{int}|D\rangle = 0$. We see that the coupling is increased for the $|B\rangle$ state which is called *bright*, and the coupling is zero for the $|D\rangle$ state which is thus called *dark*. This

special type of interaction can be used to create a superposition state between the ground state levels even when they start in a mixed state. The density matrix of a fully mixed state can be written in the bright/dark basis as half of a contribution from each

$$\rho_{mixed} = 1/2\rho_B + 1/2\rho_D. \quad (3)$$

If a bi-chromatic π -pulse resonant with the A -levels is now applied to the mixed state, the effect is that the bright component is excited while the dark component is left untouched:

$$\rho_{total} = 1/2\rho_e + 1/2\rho_D \rightarrow \rho_{ground} = 1/2\rho_D \quad (4)$$

where the last equality is obtained by selecting the ground state levels e.g. with respect to another excited state such as $|e_2\rangle$ (although it does not have trace equal to one and is thus technically not a density matrix, it is illustrative to use it as such in this case). For the experiments presented here the state $1/2\rho_D$ represents a sufficient induced coherence, since it is enough for a signal from a spin echo sequence with a very high amplitude. This is a very efficient spin polarization operation as the duration of the full process is only that of the excited state π -pulse, which can be very short if the Rabi frequency is high enough. For other types of experiments however, one can go one step further, since the excited state population can in principle be detected, e.g. by observing the emission from this level¹. This can then be used to herald a projection onto either the excited state or ρ_D , and in the latter case a pure superposition state have been achieved.

Even though the above descriptions use optical π -pulses, because the ground states are left in a superposition state, the operation is effectively a $\pi/2$ -pulse on the nuclear spin, i.e. it implements the first pulse in the full spin echo sequence (see Fig. 2b). In order to complete the spin echo sequence and compensate for the hyperfine inhomogeneous broadening, we need a spin echo π -pulse, which can be explained in a manner similar to that in reference [10]. In words, the first waiting time, $\tau/2$, gives a dephasing of the initial Dark state, such that the resulting state can be expressed as a linear combination of the Bright and Dark state (since they form a basis). A full 2π -pulse is then applied to the new Bright state component, which has the effect of introducing a π phase shift, i.e. it flips the Bright component. Since the state has been flipped another waiting time, $\tau/2$, now rotates the state back to the original, completing the spin echo sequence.

However, we go one step further and investigate a general case, where one of the bi-chromatic components of the spin π -pulse is shifted an angle ϕ with respect to the initial $\pi/2$ -pulse. The effect of this is derived in Appendix A, showing an interesting result that the rephasing occurs at an angle of 2ϕ with respect to the original Dark state.

¹ Note that the excited state level can also be detected in a much better way by coupling the ion to a readout ion via a dipole blockade effect, e.g. as described in reference [13]. In this scheme the excited state readout could in principle still be performed much faster than the excited state lifetime.

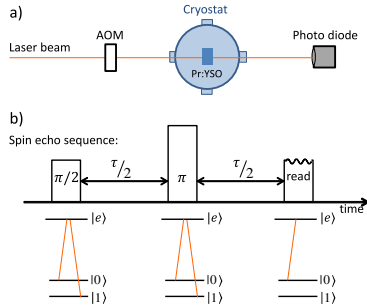


Fig. 2. (a) Simplified experimental setup. The bi-chromatic pulses are created in a single pass acousto-optic modulator (AOM). (b) The spin echo pulse sequence together with the Λ -system showing which transitions are active for each pulse. In the readout step, only one of the frequencies is active, and a beating is produced on the difference frequency if the nuclear spin state is still coherent.

Since any state on the equator plane can be reached by this general rephasing operation it constitutes a combination of the rephasing action with an arbitrary phase gate. This could be particularly convenient in dynamic decoupling schemes [14], where rephasing pulses are continuously applied and the ability to combine gates with the rephasing pulses can both save precious time in the sequence and simplify the rephasing timings, since they do not have to be extended to include another pulse in between.

To verify the operation of the sequence, optimize the pulse parameters, and to obtain the scaling for the sequence, a simulation based on the optical Bloch equations was made. A three-level system (see e.g. [15]), was simulated numerically, using detunings on both the optical levels and the nuclear spin levels to take the inhomogeneous distributions into account. In Figures 3a and 3b the path of the two components of a mixed ground state is shown, when an EIT $\pi/2$ -pulse and an EIT π -pulse is applied respectively. This figure and the simulations will be discussed further in Sections 4.1 and 4.4.

3 Experimental setup

Experiments have been performed on a $\text{Pr}^{3+}:\text{Y}_2\text{SiO}_5$ crystal with 0.05% doping concentration, cooled to about 2 K in a liquid bath cryostat. The level-structure of an individual Pr^{3+} ion is shown in Figure 1a, where each transition has about 3 kHz optical homogeneous linewidth, but where the ensemble of all Pr^{3+} ions in the crystal has an optical inhomogeneous width of about 5 GHz. The inhomogeneous width of the nuclear spin levels is about 20 kHz. In Section 4.1, where the effect of the EIT-pulses is characterized by quantum state tomogra-

Table 1. Pulse parameters for the spin echo sequence. The indices refer to the respective transition as noted in Figure 2b. Note that the optical Rabi frequencies, Ω , of the components are only approximate, since the final spin echo sequence simultaneously address Pr transitions to different excited states. The angles, ϕ , are phase shifts applied to the different frequency components to control the rotation directions (see Appendix A).

Pulse	Duration	Ω_{1e}	Ω_{0e}	ϕ_{1e}	ϕ_{0e}
$\pi/2$	2 μs	$250/\sqrt{2}$ kHz	$250/\sqrt{2}$ kHz	0	0
π	2 μs	$500/\sqrt{2}$ kHz	$500/\sqrt{2}$ kHz	$\pi/2$	0

phy, the spectral profile has first been prepared by creating an empty pit containing peaks corresponding to ions in either the $|0\rangle$ or the $|1\rangle$ ground state (the two peaks to the left and the two peaks to the right, respectively, in Fig. 1b). The optical width of the peaks is about 170 kHz and such structures can be created using the holeburning techniques described e.g. in reference [16,17]. It is ensured that the EIT pulses address the full width of the peaks by selecting a pulse duration of the pulses of 2 μs such that the corresponding bandwidth, $\delta f_{\text{bw}} \approx 1/\pi t_{\text{dur}}$, matches the peak width. Note that a high fidelity for a chosen ensemble of ions can only be achieved if all pulses in the sequence address the same frequency distribution of ions, and thus all pulses must have the same duration. Therefore the pulse area of the π -pulse is increased by having twice the Rabi frequency, rather than twice the duration (see Fig. 2b).

In total, the pulse sequence used during the experiments is summarized in Table 1.

Note that the Rabi frequencies, Ω , given in the table are only approximate and meant to represent the total Rabi frequency ($\Omega_{\text{tot}} = \sqrt{\Omega_{1e}^2 + \Omega_{0e}^2}$) at the atoms corresponding to optical π - and 2π -pulses respectively. The tomography experiment is controlled such that a Rabi frequency can be defined, but for the final spin echo sequence, several Pr transitions are involved that have different oscillator strengths, making the Rabi frequencies different. Our crystal also had a fairly high absorption, $\alpha L > 1$, and to compensate for the power drop across the crystal higher Rabi frequencies were used in this case.

A simplified experimental setup is shown in Figure 2a. Here, the laser source at 606 nm (495 THz) is stabilized to a target linewidth of 10 Hz and although the coherence created by the EIT pulses does not require a stable laser it is advantageous to ensure that the same ions are always addressed during an experiment. The bi-chromatic pulses contain frequencies separated by the hyperfine splitting in Pr^{3+} at 10.2 MHz, and are created by a single pass acousto-optic modulator (AOM) with a center frequency of 360 MHz driven by an arbitrary waveform generator with a 1 GS/s sampling rate. After the AOM the two frequency components are ensured to overlap by coupling them into a single-mode fiber before the Pr crystal. The detector is a photo diode connected to a LeCroy HRO 66Zi oscilloscope, with a segmented memory capacity as is utilized in some of the experiments described in the next section.

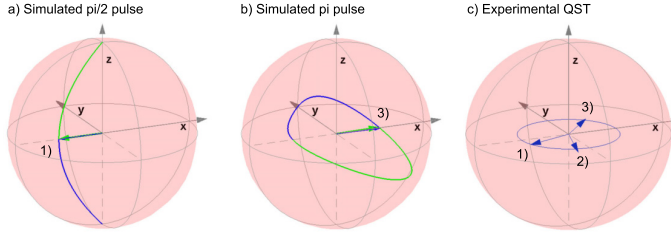


Fig. 3. (a) and (b) shows optical Bloch simulations of the paths for the two ground state components (computational basis) of an unprepared starting state subject to the bichromatic pulses. In (c) the experimental results of the quantum state tomography is displayed, where the blue circle represents the maximum attainable coherence. In both the simulated and the experimental parts the arrows corresponding to (1) is the state after the $\pi/2$ -pulse; (2) is the state after initialization with a different phase and (3) shows (1) after an additional EIT ground state rephasing π -pulse has been applied.

The amount of light deflected by the AOM for a given RF power has been calibrated to the particular laser focus at the crystal sample, allowing each of the bi-chromatic pulse components to be created with an individually specified Rabi frequency. In addition, the optical phase of each component can also be individually set, where the phase difference between the components decide the phase of the created superposition state, which is shown in Figure 3c. As can be seen in part b of Figure 2 the $\pi/2$ - and π -pulse in the spin echo sequence are bi-chromatic pulses while the final readout pulse that reveals the spin echo is a single color pulse. If ground state coherence remains in the system at the time, τ , then a readout pulse transfers the component $|0\rangle \rightarrow |e\rangle$, which leads to an excited state coherence at $|1\rangle \rightarrow |e\rangle$. This creates interference with the simultaneous readout pulse and causes a beat note at 10.2 MHz, with an amplitude corresponding to the amount of nuclear spin coherence left after time τ .

4 Results and discussion

The results section is divided into four different parts, first the EIT pulses are characterized experimentally, then we present two uses for our technique, and finally we discuss limitations to the technique and scalability to other systems, based on theoretical simulations.

4.1 Characterization with quantum state tomography

In order to show that a single EIT pulse with a duration much shorter than the excited state lifetime can create a superposition state from a fully mixed state, we characterize our pulses using quantum state tomography (QST). Even though the final spin echo sequence can be applied

without any prior preparation, we use holeburning techniques to prepare isolated peaks inside an otherwise empty spectral pit (as described in Refs. [16,17]), for these characterization experiments. Such peaks are shown in Figure 1b, where the two large peaks to the left are both transitions from the $|0\rangle$ ground state, and the two right-most peaks are both transitions from the $|1\rangle$ state.

The effect of the pulses in the spin echo sequence is simulated, with the results visualized in Figure 3. If the starting state has not been previously prepared, then it has equal components from both the two ground states and can be described as a fully mixed state (in both the computational basis as well as the Bright/Dark state basis). In the figure, two paths are shown corresponding to the two different ground state components separately, as they are affected by the same pulses. In Figure 3a the initialization paths from the spin $\pi/2$ -pulse are shown, and the two arrows show the final state after this pulse, which represents the $1/2\rho_D$ state as given by equation (4). In Figure 3b the paths of the components from the initialized state as they are affected by the spin π -pulse are shown. Keep in mind that the reason why the two different ground states end up in the same final state is because of the involvement of the third level, $|e\rangle$, through the bi-chromatic pulses, and note that this third level is not shown in the Bloch spheres in Figure 3. In our work, the π -pulse also contained an extra $\pi/2$ phase shift on the high frequency component. This has no impact on the rephasing action, as it does not matter which optical 2π -path the Bright state components are cycled through. It does however change the final spin state as we show in Appendix A and with this choice of phase the rephasing occurs opposite to the starting state as shown in Figure 3b, similar to the optical version of the echo sequence.

In order to perform QST we must first be able to estimate the population in each of the available states, visible

in Figure 1. This is done using a least square fitting procedure simultaneous for all states (although, the uppermost excited state, $|e_3\rangle$, is never involved and is thus assumed to be zero). The full quantum state density matrix can be reconstructed from the population data, corresponding to measurements with three different preceding operations that each reveal the projection onto the three axes of the Bloch sphere:

$$\rho = \frac{I + \text{tr}(X\rho)X + \text{tr}(Y\rho)Y + \text{tr}(Z\rho)Z}{2}. \quad (5)$$

The three quantities $\text{tr}(X\rho)$ etc. are obtained experimentally and correspond to the population differences in each of the three measurement cases respectively and X , Y , Z are the three Pauli matrices (for more details see e.g. Nielsen and Chuang [18]). Quantum state fidelities can then be obtained by comparing the experimental density matrix to the target ones (e.g. $1/2\rho_D$).

In Figure 3c the reconstruction from a QST in three different cases is shown. The three states are (1) EIT initialization to the x -axis; (2) EIT initialization to the y -axis by adding 90° to one of the bi-chromatic components; and (3) the initialization as in (1) followed by a rephasing EIT π -pulse. In the initialization, half of the population is lost to the excited state and if we do not perform any projective detection of this population then the maximum fidelity we can achieve is 75%. This maximum amount of coherence is represented in the figure as a blue circle with radius $1/2$. The qubit fidelities compared to the target states for the three cases are 70%, 68% and 67% respectively, which is remarkable when considering the fact that the qubit is an inhomogeneously broadened ensemble of ions. Each ion has an optical frequency width of 3 kHz, whereas the whole ensemble is 170 kHz wide. In contrast to many previous EIT experiments where the feature is narrow, we have here demonstrated spectrally broad EIT pulses, and the high fidelities indicate that the EIT effect is indeed applied to most of the population distribution.

In contrast to previous experiments with similar techniques [10,11], where only the final echo light output could be used for optimization, we have here also demonstrated the ability to optimize the atomic states directly, via QST. This allows each pulse to be optimized individually, and in addition this distinction is particularly important when considering that these EIT pulses can also be used for more general fast optical manipulation of spin qubits. For instance, the π rephasing pulse can be combined with a phase gate as shown in Appendix A, which is particularly useful for dynamic decoupling schemes. This is also applicable to pure state qubits obtained e.g. by projection or initialized through other means such as the much longer CPT pulses.

One can also note that the main loss of fidelity (compared to the target state) is not due to loss of coherence (arrow length in figure), but rather due to being off the target phase angle, especially for state (3) after the π -pulse. The arrows in Figure 3c were a result of an average of 25 experiments, indicating that the remaining phase angle is a systematic effect. The reason for this is

not known exactly, but one can suspect some experimental parameters, e.g. the two EIT components having unequal Rabi frequencies. The effect of this was tested in simulations, and it was found that with unequal Rabi frequencies, there is indeed a phase error after the π -pulse with respect to the target state. However, one would have to assume that also the initializing $\pi/2$ -pulse have the same Rabi ratio but in this case the simulations no longer support the observed data for cases (1) and (3) simultaneously. Even though other parameters were also tested we found no conclusive explanation for this behavior, which will require further study.

It is important to point out though, that the strength of the spin echo signal, i.e. the amplitude of the beat note, does not depend on the phase angle of the final state, but only the amplitude of the coherence, i.e. the arrow length projected on the equator plane. A phase error will simply shift the phase of the beat note by a constant amount, without reducing the amplitude. The fidelities however, are comparisons to specific target density matrices and do depend on the phase, therefore suggesting that the potential spin echo signal strength is actually greater than the QST fidelities imply.

4.2 Magnetic field compensation

It has been investigated recently that the presence of small magnetic fields such as the earth's magnetic field can greatly impact the coherence properties of the nuclear spin states [19]. The reason is that even for a small splitting of the hyperfine levels, δf , distributing the quantum state over different levels will cause them to beat with each other at a timescale given by $1/\delta f$. The EIT spin echo sequence can be used to compensate this splitting in real time, making it a practical lab technique. For $\text{Pr}^{3+}:\text{Y}_2\text{SiO}_5$, the strongest magnetic g-factor has been measured to be 12 kHz/100 μT [20], and although there may exist stray magnetic fields in our cryostat, we believe that in the present experiments the earth's magnetic field gives the largest contribution to the splitting. In Lund, where the experiments were carried out, the vertical component of the earth's magnetic field is dominant at about 50 μT , which then gives a splitting of about 6 kHz. The expected nuclear spin T_2 is about 500 μs [21], but such a splitting would give a beat minimum after 85 μs , drastically limiting the coherence properties.

In order to compensate for magnetic fields in any spatial direction, three pairs of Helmholtz coils with 10 turns each and a radius of 10 cm, was added to the setup. A fast update rate of the experiment was achieved and depend on two things, the fast EIT sequence, and the ability to use a segmented memory on an oscilloscope. A chain of 30 spin echo sequences with increasing wait time, τ , was pre-programmed into the memory of an arbitrary waveform generator. An oscilloscope with a segmented memory was then used to store only the readout pulses, carrying the resulting beating, in each spin echo sequence. A master trigger was used at the start of the whole chain, followed by secondary triggers at each readout pulse. This enables

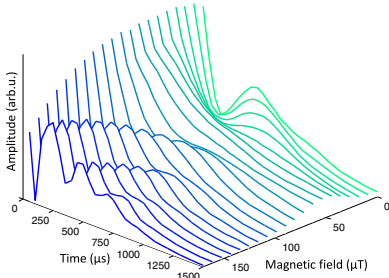


Fig. 4. Coherence decay curves for the nuclear spin vs. the magnetic field in the vertical direction, which was the most sensitive one in our setup. The two other directions were kept at compensated values. The longest (and smoothest) decay occurs at a compensation field of about 50 μT , which corresponds to the local vertical component of the earth's magnetic field.

high temporal resolution capable of resolving the beating, while at the same time allowing the results from the full chain to be stored simultaneously in the memory. The data was analyzed in real time, extracting the 10.2 MHz beat amplitude using a Fourier algorithm, allowing a full 30 point T_2 decay curve to be displayed at a 1 Hz update rate. This enabled real time tuning of the coil currents in order to compensate for the background magnetic field components in all three directions. The update rate was in our case mostly limited by the oscilloscope master trigger rate, since the spin echo sequence itself plus scramble pulses at the end to reset holeburning effects, requires only 150 ms to run the 30 points in a set.

In Figure 4 the result of coherence decay curves at 2 K, for 20 different vertical magnetic field levels is shown, taken while the magnetic field in the two other directions were compensated. The values of the magnetic field axis in the figure is obtained by estimating the field produced by an applied current to our Helmholtz configuration. This estimation gives a compensation in the vertical direction of about 50 μT , which matches the earth's magnetic field component in this direction. Off the compensation point, the beatings due to the quantum interference between the split hyperfine states are clearly visible. The oscillation frequency matches the one expected from the sizes of the splittings well, and the fully compensated curve also matches the expected T_2 value well. However, some effects of excitation induced dephasing is observed, and this is discussed in more detail in the next section.

4.3 High temperature nuclear spin T_2

Above temperatures of approximately 5 K the coherence time, T_2 , of the optical transitions decreases very rapidly as a function of temperature, $T_2 \propto 1/T^7$, due to non-resonant two-phonon interactions [22]. It is known that the

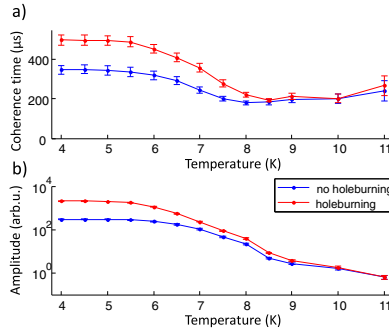


Fig. 5. Coherence time of the nuclear spin as a function of temperature in two cases in (a), with and without holeburning before the EIT sequence. The difference between the two curves is discussed in the text. In (b) the signal level of the Raman beating is shown as a function of temperature, predictably decreasing as the optical linewidth increases. For both figures, the error bars correspond to a 95% confidence interval.

nuclear spin coherence of Pr^{3+} does not follow this rapid decay, although the difficulty of preparing a spin polarization when the optical line is broad has limited previous measurements up to only 6 K [21]. To extend this we apply a spin echo sequence with our EIT pulses. The combination of EIT interactions being naturally less affected by optical fluctuations and a sensitive Raman beating measurement enables us to obtain signals up to 11 K, corresponding to optical linewidths $(11/6)^7 = 70$ times broader than previous measurements.

Figure 5 shows the temperature dependence of the coherence time and beating amplitude respectively. Each point in the figures is evaluated from an average of 25 decay curves similar to the one at 50 μT displayed in Figure 4. From such averages, each with 30 different delay times, exponential decay functions with three different parameters were fitted: amplitude, T_2 and a general offset. The error bars represents the uncertainty of the fitting estimation of those parameters, and correspond to a 95% confidence interval.

The lowest point in the figure at 4 K is taken with the sample submerged in a liquid helium bath, but all other points are taken with cooling through a helium gas flow otherwise in vacuum. The temperature on the x-axis is the one reported by the cryostat, which has previously been verified by a probe mounted directly at the sample. As can be seen in Figure 5b, the signal level of the Raman beating decreases strongly with temperature after about 6 K as expected, due to the optical broadening. After about 8 K it is no longer possible to do spectral holeburning and the signal has decreased about two orders of magnitude. Related to this, we see that the T_2 curve in a) displays some curious features, which are now discussed.

The blue curve represents measurements by the EIT spin echo sequence alone on an unprepared sample, while the red curve represents the case when the spin echo sequence was preceded by a preparatory holeburning pulse emptying a 2 MHz absorption region at a frequency corresponding to the $|0\rangle \rightarrow |e\rangle$ transition of the A -system. While this does not affect the action of the EIT sequence itself, it reduces the total amount of ions involved in the experiment, which can remove dephasing caused by other excited ions. Two processes could explain this behavior, either instantaneous spectral diffusion (ISD) from optically excited ions affecting the nuclear spin states, or non-equilibrium resonant phonons. Such phonons are created when the optically excited state decay down to a different, and more probable, Stark level, which then decays down to the ground state by releasing phonons that can be resonantly absorbed by the nuclear spin states, destroying their coherence [23]. Effects from the standard ISD dephasing can normally be mitigated by reducing the excitation power of the laser, however in this case we have used EIT pulses with a Rabi frequency set to match a π pulse area on the optical transition. If this would be a concern, one could avoid these mechanisms e.g. by using a sample with lower doping concentration or go further out to the edge of the inhomogeneous profile, where the same excitation power would excite fewer ions. The behavior after 8 K where the two curves overlap, is due to the fact that when holeburning is no longer possible the same results should be obtained for both sequences. This also indicates that the apparent decrease of the T_2 during the temperature range 6–8 K is not due to an actual decrease of the spin T_2 but rather increased dephasing from larger optical excitation. Therefore, we can conclude that as far up in temperature as we can measure, the nuclear spin is not destroyed by thermal effects but remains coherent.

4.4 Scaling to other systems

Even though we have only demonstrated this technique in the particular case of $\text{Pr}^{3+}:\text{Y}_2\text{SiO}_5$, we argue that it can be applied generally over a broad range of systems. In order to determine the limiting factors, optical Bloch simulations for different system parameters were performed. It was found that the signal strength of the Raman beating remains constant until the optical coherence time becomes shorter than the duration of the excitation EIT pulse. In Eu^{3+} systems e.g., where the starting linewidth is more narrow this occurs at much higher temperatures. From the relation between T_2 and temperature given in reference [24] it is estimated that it is feasible to reach above 20 K. This would enable the very recent measurements of reference [25] to be implemented all-optically by the method used in the present work.

Outside of rare-earth systems, atomic vapors are also considered for quantum memories, and these systems often involve optical excitations that are dipole allowed, giving much shorter excited state lifetimes in the order of tens of ns, but at the same time having much higher oscillator strengths, allowing π -pulses with a much shorter duration.

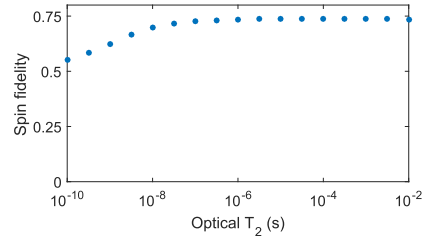


Fig. 6. Fidelity of the nuclear spin that is left at the end of the EIT spin echo sequence as a function of the optical T_2 of the system from simulations. Note that without a projective measurement tracing out the excited state as discussed in Section 2, the maximum fidelity is 0.75. Since any amount of coherence is enough to achieve a signal from a spin echo sequence, the result shows viability of the method down to at least 100 ps.

This enables our method to work for systems with a broad range of T_2 times, as we will now analyze in more detail.

Quite generally, the Rabi frequency is directly proportional to the transition dipole moment, μ , which in turn causes the duration of a π -pulse to be inversely proportional to it: $T_\pi \propto 1/\mu$. At the same time, T_2 of a transition is upper limited by $2T_1$, which is inversely proportional to the square of the transition dipole moment, i.e.: $T_2 \propto 1/\mu^2$ (see e.g. [26]). Combining these two relations gives

$$T_\pi \propto \sqrt{T_2}. \quad (6)$$

If we take as a simple assumption that the achievable laser intensity is roughly constant for different time scales, then the signal level of the EIT sequence can be simulated for different time scales given the constraints of equation (6). In Figure 6 we have plotted the achievable nuclear spin fidelity (without projective measurements) when limited by a laser intensity similar to the one in our experiments, which is approximately 100 mW focused to a spot with about 70 μm diameter. The simulations show that the cutoff in this figure for lower times occur when the optical T_2 becomes shorter than the duration of the EIT pulses, where the duration is set by the desire to reach a π pulse area using the available intensity.

While high fidelity spin polarization is achievable as long as the optical T_2 times is above 10 ns, obtaining a signal from a spin echo sequence can be achieved as long as there is some amount of coherence induced in the system. This allows the EIT spin echo method to be used down to about 100 ps, which covers most, if not all, systems that could be interesting for quantum information purposes.

However, keep in mind that this result contains the simple restriction of constant laser intensity. When targeting system with short lifetimes, pulsed lasers are often available that can deliver much higher peak intensities, which will further extend the scheme. A special case of this may be when short pulsed lasers are used to target A -systems where the laser is not bi-chromatic but two of

the levels are covered by the inherently broad (but still phase coherent) spectrum of the pulse. In this case, an EIT superposition can also be initiated [27] and used as a coherence probe. Although, the readout mechanism would have to be different than the beating used here, e.g. a rotation onto the population of the states.

5 Conclusions

We have described and experimentally demonstrated a fast and efficient all-optical spin echo technique to generate a coherent ground state spin superposition from a mixed state. The method is based on EIT and is particularly useful e.g. in higher temperature settings or when short and fast sequences are needed. The created dark superposition states have been characterized by quantum state tomography and demonstrations of the spin echo sequence has been performed for two selected cases. Firstly, an accurate and real time compensation of the background magnetic field components in all three directions. Secondly, the nuclear spin T_2 of Pr^{3+} was measured by all-optical means up to a temperature of 11 K. Comparisons to simulations show this to be limited by the optical power of the laser. Possibilities to further extend this by means of e.g. pulsed lasers were discussed. The method can be used in a wide variety of systems, since even though the optical T_2 must be longer than the pulse duration, the useful regime was shown to be achievable in most cases.

Author contribution statement

A.W. planned and carried out most of the work, and also wrote the manuscript, A.N.N. wrote the code for and performed the simulations, Q.L. carried out some of the experiments, L.R. and S.K. contributed by discussions throughout the planning, analysis and writing stages.

This work was supported by the Swedish Research Council, the Knut & Alice Wallenberg Foundation. The research leading to these results also received funding from the People Programme (Marie Curie Actions) of the European Union's Seventh Framework Programme FP7 (2007-2013) under REA grant agreement No. 287252 (CIPRIS) and Lund Laser Center (LLC).

Appendix

We now derive a general case of the rephasing mechanism of an EIT-based π -pulse. As mentioned in the main text, the Bright and Dark states are described by (following the vector notation of Nielsen and Chuang [28], without normalization to keep it brief and clear):

$$|D\rangle = \begin{bmatrix} 1 \\ -1 \end{bmatrix}, |B\rangle = \begin{bmatrix} 1 \\ 1 \end{bmatrix}. \quad (\text{A.1})$$

Changes and rotations that only affect the equator-plane of the Bloch sphere representation, i.e. the phase of states, can then be described by a rotation matrix (Sect. 4.2 of Ref. [28]):

$$R_z(\theta) = \begin{bmatrix} e^{-i\theta/2} & 0 \\ 0 & e^{i\theta/2} \end{bmatrix}. \quad (\text{A.2})$$

After the initial pulse of the spin echo sequence, all ground state population is in the Dark state, and due to the inhomogeneous distribution of our ensemble this state will experience a dephasing due to a detuning, δ :

$$|\Psi\rangle_{\text{dephased}} = R_z(\delta) \cdot |D\rangle = \begin{bmatrix} e^{-i\delta/2} \\ -e^{i\delta/2} \end{bmatrix}. \quad (\text{A.3})$$

Since the Bright and Dark state represents a basis for the Bloch sphere, the new dephased state can be expressed as a linear combination of $|B\rangle$ and $|D\rangle$ components. However, the original choice of phase angle for what constitutes Bright and Dark state respectively is arbitrary and just corresponds to our reference frame. Any two vectors on the equator plane pointing in opposite directions corresponds to a Bright/Dark basis for a bi-chromatic light field with an associated phase relation between the frequency components. Such a basis can be obtained by a rotation of the original Bright/Dark basis by an arbitrary angle, ϕ :

$$\begin{cases} |D\rangle_{\text{rot}} = R_z(\phi) |D\rangle = \begin{bmatrix} e^{-i\phi/2} \\ -e^{i\phi/2} \end{bmatrix} \\ |B\rangle_{\text{rot}} = R_z(\phi) |B\rangle = \begin{bmatrix} e^{-i\phi/2} \\ e^{i\phi/2} \end{bmatrix} \end{cases} \quad (\text{A.4})$$

We intend to exploit this point, by choosing a new phase angle between the bi-chromatic components for our rephasing pulse compared to the initial $\pi/2$ -pulse (see Tab. 1). To easily describe the operation of the rephasing pulse we express the state in equation (A.3) as linear components of the rotated basis:

$$|\Psi\rangle_{\text{dephased}} = a |D\rangle_{\text{rot}} + b |B\rangle_{\text{rot}}, \quad (\text{A.5})$$

i.e. we solve the set of equations:

$$\begin{bmatrix} e^{-i\delta/2} \\ -e^{i\delta/2} \end{bmatrix} = a \begin{bmatrix} e^{-i\phi/2} \\ -e^{i\phi/2} \end{bmatrix} + b \begin{bmatrix} e^{-i\phi/2} \\ e^{i\phi/2} \end{bmatrix}, \quad (\text{A.6})$$

where the coefficients a and b are required to be complex. The solution is given by:

$$\begin{cases} a = \frac{1}{2} (e^{-i\delta/2} e^{i\phi/2} + e^{i\delta/2} e^{-i\phi/2}) \\ b = \frac{1}{2} (e^{-i\delta/2} e^{i\phi/2} - e^{i\delta/2} e^{-i\phi/2}) \end{cases} \quad (\text{A.7})$$

The spin π -pulse can be implemented by an optical 2π -pulse, since a full rotation between two of the levels in a Λ -type scheme causes a π phase shift on the rotated

state, which is the Bright state here. The new state can thus be described:

$$|\Psi\rangle_{\pi} = a|D\rangle_{rot} - b|B\rangle_{rot} = \begin{bmatrix} e^{-i(\phi-\delta/2)} \\ -e^{i(\phi-\delta/2)} \end{bmatrix}. \quad (\text{A.8})$$

In the final step of a spin echo sequence, a waiting time equal to the time it was allowed to dephase before occurs. During this time the state rephases by a rotation in the same direction and by the same amount as earlier:

$$|\Psi\rangle_{rephased} = R_z(\delta) \cdot |\Psi\rangle_{\pi} = \begin{bmatrix} e^{-i\phi} \\ -e^{i\phi} \end{bmatrix}. \quad (\text{A.9})$$

Here we see that a rephasing always occurs (δ is canceled out), but the final state is shifted by an angle of 2ϕ , i.e. twice the angle of the π -pulse components. This result represents an interesting opportunity since it allows the rephasing pulse to be combined with an arbitrary phase gate operation, as discussed in Section 2.

In the special case of $\phi = 0$, we see that the rephasing occurs at our original Dark state:

$$|\Psi\rangle_{rephased, \phi=0} = \begin{bmatrix} 1 \\ -1 \end{bmatrix}. \quad (\text{A.10})$$

In our experiments evaluated by the quantum state tomography in Figure 3c, we make use of another special case with $\phi = 90^\circ$:

$$|\Psi\rangle_{rephased, \phi=90^\circ} = \begin{bmatrix} 1 \\ 1 \end{bmatrix}. \quad (\text{A.11})$$

This is opposite to the starting state (neglecting the global phase factor) and is similar to the case of the optical photon echo sequence rephasing.

References

1. H.J. Kimble, Nature **453**, 1023 (2008)
2. Hoi-Kwong Lo, Marcos Curty, Kiyoshi Tamaki, Nat. Photon. **8**, 595 (2014)
3. I.M. Georgescu, S. Ashhab, F. Nori, Rev. Mod. Phys. **86**, 153 (2014)
4. T.D. Ladd, F. Jelezko, R. Laflamme, Y. Nakamura, C. Monroe, J.L. O'Brien, Nature **464**, 45 (2010)
5. G. Balasubramanian, P. Neumann, D. Twitchen, M. Markham, R. Kolesov, N. Mizuochi, J. Isoya, J. Achar, J. Beck, J. Tessler, V. Jacques, P.R. Hemmer, F. Jelezko, J. Wrachtrup, Nat. Mater. **8**, 383 (2009)
6. W.F. Koehl, B.B. Buckley, F.J. Heremans, G. Calusine, D.D. Awschalom, Nature **479**, 84 (2011)
7. M. Zhong, M.P. Hedges, R.L. Ahlefeldt, J.G. Bartholomew, S.E. Beavan, S.M. Wittig, J.J. Longdell, M.J. Sellars, Nature **517**, 177 (2015)
8. N. Bloembergen, E.M. Purcell, R.V. Pound, Phys. Rev. **73**, 679 (1948)
9. C.G. Yale, B.B. Buckley, D.J. Christle, G. Burkard, F.J. Heremans, L.C. Bassett, D.D. Awschalom, Proc. Natl. Acad. Sci. **110**, 7595 (2013)
10. B.S. Ham, M.S. Shahriar, M.K. Kim, P.R. Hemmer, Phys. Rev. B **58**, R11825 (1998)
11. A. Louchet, Y. Le Du, T. Brouri, F. Bretenaker, T. Chanelière, F. Goldfarb, I. Lorgère, J.-L. Le Gouët, Solid State Sci. **10**, 1374 (2008)
12. M. Fleischhauer, A. Imamoglu, J.P. Marangos, Rev. Mod. Phys. **77**, 633 (2005)
13. A. Walther, L. Rippe, Y. Yan, J. Karlsson, D. Serrano, A.N. Nilsson, S. Bengtsson, S. Kröll, Phys. Rev. A **92**, 022319 (2015)
14. E. Fraval, M.J. Sellars, J.J. Longdell, Phys. Rev. Lett. **95**, 030506 (2005)
15. A. Imamoglu, J.E. Field, S.E. Harris, Phys. Rev. Lett. **66**, 1154 (1991)
16. L. Rippe, B. Julsgaard, A. Walther, Yan Ying, S. Kröll, Phys. Rev. A **77**, 022307 (2008)
17. A. Amari, A. Walther, M. Sabooni, M. Huang, S. Kröll, M. Afzelius, I. Usmani, B. Lauritzen, N. Sangouard, H. de Riedmatten, N. Gisin, J. Luminescence **130**, 1579 (2010)
18. M.A. Nielsen, I.L. Chuang, *Quantum Computation and Quantum Information* (Cambridge University Press, United Kingdom, 2000) Eq. 8.148, Chap. 8.4.2.
19. G. Heinze, S. Mieth, T. Halfmann, Phys. Rev. A **84**, 013827 (2011)
20. J.J. Longdell, M.J. Sellars, N.B. Manson, Phys. Rev. B **66**, 035101 (2002)
21. B.S. Ham, M.S. Shahriar, M.K. Kim, P.R. Hemmer, Opt. Lett. **22**, 1849 (1997)
22. D.E. McCumber, M.D. Sturge, J. Appl. Phys. **34**, 1682 (1963)
23. Y.S. Bai, R. Kachru, Phys. Rev. B **46**, 13735 (1992)
24. F. Könz, Y. Sun, C.W. Thiel, R.L. Cone, R.W. Equall, R.L. Hutcheson, R.M. Macfarlane, Phys. Rev. B **68**, 085109 (2003)
25. A. Arcangeli, R.M. Macfarlane, A. Ferrier, P. Goldner, Phys. Rev. B **92**, 224401 (2015)
26. R.C. Hilborn, Am. J. Phys. **50**, 982 (1982)
27. P.R. Berman, Phys. Rev. A **72**, 035801 (2005)
28. M.A. Nielsen, I.L. Chuang, *Quantum Computation and Quantum Information* (Cambridge University Press, United Kingdom, 2000)



Qian Li has been a Ph.D. student in division of Atomic Physics at the Physics Department of Lund University since 2012.

All the work presented in this thesis was accomplished with the help of this ring dye laser, which worked amazingly most of the time while it enjoyed little breaks every now and then.